Udforskning af nye nano strukturerede materialer til fremstilling af hydrogen

Vesborg, Peter Christian Kjærgaard

Publication date:
2010

Document Version
Publisher's PDF, also known as Version of record

Photocatalysis in μ-reactors and related activities

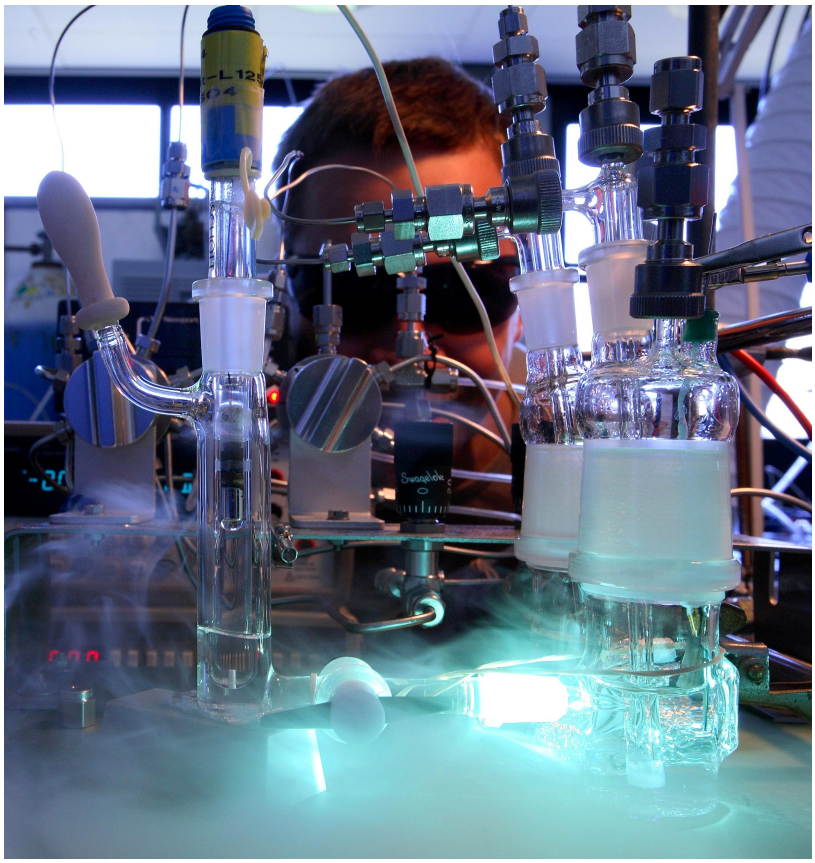

Ph.D. Dissertation by

Peter C. K. Vesborg

January 2010

Center for Individual Nanoparticle Functionality
Technical University of Denmark

Front page picture:
Two-compartment photoelectrochemical cell. Illumination is deliberately misaligned to light up the cell while liquid nitrogen and water provide the smoke effect.

Preface

This thesis is submitted in candidacy for the Ph.D. degree from the Technical University of Denmark (DTU). The work presented has been carried out from October 2006 to January 2010 at the Center for Individual Nanoparticle Functionality (CINF) in the department of Physics, under the supervision of Professor Ib Chorkendorff. The original title for the project was "Exploration of new nano-structured materials for hydrogen production", but since only a small fraction of my time has been spent on activities covered by that description the title of the project was changed along the way.

I wish to express my appreciation of the friendliness and helpfulness of the many students and staff at the department in general and at CINF in particular. It has been a real pleasure to do research and also to socialize with all of you. I am grateful to Ib, my advisor, for general guidance and for entrusting me with the freedom to also do fun (and on rare occasions also useful) "wild" experiments. I would also like to thank Professor Jørn Bindslev Hansen for letting me play with his sputtering chamber and for helping me to get it to cooperate.

Kgs. Lyngby, January 18th, 2010
Peter C. K. Vesborg

Abstract

This thesis presents work on the development of materials, and of experimental test methods for photocatalysis and photoelectrocatalysis. It also presents progress towards electrochemical synthesis of ammonia at near room-temperature. The materials discussed in relation to photocatalysis and photoelectrocatalysis include films of TiO_2 nanotubes, thin-films of Ta_3N_5 and of TaON and surface-treated p-type silicon.

Anodic growth of nanotubes of TiO_2, in ethylene glycol solutions containing fluoride ions, is shown to be influenced by the concentration of molecular oxygen in the electrolyte. Oxygen increases the speed with which the nanotubular film grows, and it is demonstrated how this effect can be utilized to grow uniform films of nanotubes on large non-conducting glass substrates.

Various strategies for synthesis of tantalum nitride (Ta_3N_5) and tantalum oxynitride (TaON) thin-films, for use as photoanodes, are presented. In particular, it is shown to be possible (although difficult) to grow TaON films using reactive sputtering.

Photocathodes for water splitting, which are based on p-type silicon, are presented. Very recent results indicate that treatment of the silicon surface with transition metal-chalcogenide cubanes can provide the surface with catalytic activity towards hydrogen evolution, and at the same time offer some degree of protection against oxidation of the silicon.

A new generation of μ-reactor is also presented, along with a discussion of its usefulness in photocatalytic measurements. It is shown how the high sensitivity and quick time response of these reactors provide information about how a photocatalyst performs. As an example, it is demonstrated that the μ-reactor is a convenient tool for measuring both photocatalytic activity and chemical selectivity. The new μ-reactors are also used to study photooxidation of CO over four orders of magnitude in intensity (90 $\mu W/cm^2$ to 645 mW/cm^2, λ = 367 nm) over TiO_2 nanotubes and P25 photocatalysts, and turnover is shown to scale with light intensity to the power of 0.84.

The μ-reactors are also used to record an action spectrum for CO oxidation for TiO_2 nanotubes, and relevant quantum efficiencies are calculated and discussed (both Incident Photon to Product Efficiency and Absorbed Photon to Product Efficiency). Prospects for further improvement of the μ-reactors including electrochemical μ-reactors are also discussed.

Finally, a condensed account of activity in the project to synthesize ammonia electrochemically is presented. The objective with that chapter is to document the reasoning behind the many gradual changes and improvements in the experimental approach, and also to to present a few ideas for future efforts.

Resumé

Denne afhandling omhandler arbejde med udvikling af materialer og eksperimentelle testmetoder inden for fotokatalyse og fotoelektrokatalyse. Den præsenterer også fremskridt mod elektrokemisk lavtemperatur syntese af ammoniak. Blandt de materialer der behandles i forbindelse med fotokatalyse og fotoelektrokatalyse er TiO_2 nanotubes, tyndfilm af Ta_3N_5 og TaON samt overfladebehandlet p-type silicium.

Det vises, at anodisk vækst af TiO_2 nanotubes i flourid-holdig ethylenglykol elektrolyt, påvirkes af koncentrationen af molekylær oxygen i elektrolytten. Det vises, at oxygen øger hastigheden hvormed nanotube-filmen gror, og det demonstreres hvorledes denne effekt kan bruges til at gro ensartede film af nanotubes på store ikke-ledende glassubstrater.

Forskellige strategier for syntese af tyndfilm af tantalnitrid (Ta_3N_5) og tantaloxynitrid (TaON) til brug som fotoanoder præsenteres. Specielt vises, at det er muligt (men vanskeligt) at gro TaON film ved reaktiv sputtering.

Fotokatoder til spaltning af vand, som er baserede på p-type silicium, præsenteres. Helt nye resultater indikerer, at behandling af siliciumoverfladen med kubiske overgangsmetal komplekser både kan forsyne overfladen med aktive centre hvor hydrogenudvikling katalyseres, og at denne overfladebehandling kan give en vis beskyttelse mod oxidering af siliciummet.

En ny generation af μ-reaktorer præsenteres sammen med en diskussion af deres anvendelighed i forbindelse med fotokatalytiske målinger. Det vises hvordan disse reaktorers høje følsomhed og hurtige responstid kan give nyttig information om hvordan en fotokatalysator yder. Eksempelvis demonstreres, at μ-reaktormålingerne er et nyttigt værktøj til måling af fotokatalytisk aktivitet såvel som kemisk selektivitet. De nye μ-reaktorer bruges endvidere til at studere fotooxidation af CO over fire størrelsesordener i lysintensitet (90 $\mu W/cm^2$ til 645 mW/cm^2, $\lambda = 367$ nm) over TiO_2 nanotubes og P25 fotokatalysatorer, og det vises at omsætningen skalerer med lysinten-

siteten i 0.84 potens. μ-reaktorerne bruges også til at optage et "action" spektrum for CO-oxidation for TiO_2 nanotubes, og relevante kvantevirkningsgrader udregnes og diskuteres (både "Incident Photon to Product Efficiency" og "Absorbed Photon to Product Efficiency"). Fremtidsperspektiverne for yderligere udvikling og forbedring af μ-reaktorerne, herunder også elektrokemiske μ-reaktorer, diskuteres.

Afslutningsvis præsenteres en sammenfatning af de aktiviteter, der har fundet sted i forsøgene på elektrokemisk syntese af ammoniak. Formålet med dette kapitel er dels at dokumentere baggrunden for de mange gradvise ændringer og forbedringer i den eksperimentelle tilgang, dels at præsentere nogle idéer til fremtidig udvikling af ammoniakprojektet.

List of Included Papers

Paper I
Controlled Directional Growth of TiO_2 Nanotubes
Su-il In, Yidong Hou, Billie L. Abrams, Peter C. K. Vesborg and Ib Chorkendorff
Accepted - Journal of The Electrochemical Society (2010).

Paper II
Highly sensitive silicon microreactor for catalyst testing
Toke R. Henriksen, Jakob L. Olsen, Peter C. K. Vesborg, Ib Chorkendorff, and Ole Hansen
Review of Scientific Instruments **80**, 124101 (2009).

Paper III
Anodic bonding with cooling of heat-sensitive areas
Peter C. K. Vesborg, Jakob L. Olsen, Toke R. Henriksen, Ib Chorkendorff, and Ole Hansen
Review of Scientific Instruments **81**, 016111 (2010).

Paper IV
Gas phase photocatalysis in μ-reactors
Peter C. K. Vesborg, Jakob L. Olsen, Toke R. Henriksen, Ib Chorkendorff, and Ole Hansen
Submitted

Paper V
Quantitative measurements of photocatalytic CO-oxidation as a function of light intensity and wavelength over TiO_2 nanotube thin films in μ-reactors
Peter C. K. Vesborg, Su-il In, Jakob L. Olsen, Toke R. Henriksen, Billie L. Abrams, Alan Kleinman-Shwarsctein, Ole Hansen and Ib Chorkendorff
Submitted

Other Publications

Paper VI
Transient behavior of Cu/ZnO-based methanol synthesis catalysts
Peter C. K. Vesborg, Ib Chorkendorff, Ida Knudsen, Olivier Balmes, Jesper Nerlov, Alfons M. Molenbroek, Bjerne S. Clausen and Stig Helveg
Journal of Catalysis **262** 65 (2009).

Paper VII
Dynamics of surface exchange reactions between Au and Pt for HER and HOR
Billie L. Abrams, Peter C. K. Vesborg, Jacob L. Bonde, Thomas F. Jaramillo and Ib Chorkendorff
Journal of The Electrochemical Society **156**, B273 (2009).

Contents

Anyone who believes exponential growth can go on forever in a finite world is either a madman or an economist
- Kenneth E. Boulding, economist at University of Colorado, Boulder

Chapter 1

Introduction and Background

1.1 Introduction

Over the past three years I have worked with a range of fields including: Non aqueous electrochemistry, aqueous electrocatalysis and corrosion, gas phase photocatalysis, MEMS [1] technology, μ-reactors, gas phase photocatalysis, photo-electrocatalysis as well as various synthesis techniques.

Since the main motivation for all the projects has been (solar) energy harvesting and storage I will present my personal perspective on current and future energy supply in the following introductory sections. Thus, anyone not interested in my subjective perspective on these matters may choose to jump directly to section 1.3.

1.1.1 The energy problem

> *The greatest shortcoming of the human race is our inability to understand the exponential function*
> - Albert A. Barlett, physicist at University of Colorado, Boulder

Human population is growing exponentially - in fact growth has been hyper-exponential in the past 300 years. Before technological advances made it possible to cultivate the land world population was stable at about 5 million individuals [1, 2]. From about 5000 BC until around 1700 AD the world population grew exponentially doubling every ∼1000 years so that by 1700 AD world population had reached about 650 million. The industrial revolution coupled with rapid advances in agricultural technology, and later on in medicine, meant that by 1800 AD the time for the world population to double, t_2, had fallen to about 200 years. By 1927, t_2 was only 125 years and the population had reached 2.000 million. In the early 1900s the modern world was taking form. Great advances such as modern medicine decreased infant mortality and ammonia synthesis, which enabled artificial fertilizers, vastly increased agricultural output.

[1] Micro Electro-Mechanical Systems

It was also around the turn of the century that the energy needed to power civilization could no longer be supplied by sustainable sources (e.g., wood and peat) making mankind addicted to fossil fuel - at the time mainly coal. By 1974, world population had reached 4.000 million i.e., it had doubled in only 47 years.

At the time of writing the world population has reached 6.797 million and is still doubling every 50 years or so. It seems worthwhile for the well-meaning engineer to carefully consider the irony of the fact that not only is the world population growing exponentially, but the rate of growth ($1/t_2$) is 20 times higher than it was in pre-industrial times - before the engineer really started to help solve society's problems!

Even if the growth of the world population could be frozen at the current level, ~6.800 million people, we would still face increasing resource consumption as the poorest 5.800 million people strive to reach the same material standard of living as the richest 1.000 million people enjoy today.

Focusing on one particular (albeit essential) resource, viz. energy, it can safely be stated that modern society of today is entirely dependent on fossil fuel. World total energy consumption was 11295 MTOE/yr (Million Ton Oil Equivalent / year) in 2009 [3]. This was distributed: 34.8% Oil, 29.2% Coal, 24.1% Natural gas, 6.4% Hydro electric and 5.5% Nuclear fission. Thus, fossil fuel corresponds to a combined 88.2%. Wind, solar, biomass and other "alternative" sources are not included due to lack of high quality data [2]. The biggest consumers of energy are: US: 20.3%, PRC: 17.7%, EU: 15.3%, Russia: 6.1% and Japan: 4.5%.

1.1.2 Oil

It is a indisputable fact that the dominating role of oil is ending. Coal has consistently been the fastest growing source of primary energy since 2002. In this same period of time global oil production has been almost constant at around 3900 MTOE/yr and there is a hefty, ongoing debate over whether oil production has peaked already or how soon it will happen. Without going into this controversial topic in any detail the famous Hubbert prediction deserves mention. After an initial publication in 1949 in *Science* [5], M. King Hubbert, who was a geophysicist working for Shell, predicted in 1956 [6] that US oil production would peak between 1965 and 1970 (in fact, it did indeed peak in 1970 at about 470 MTOE/yr and is presently down at about 213 MTOE/yr (lower 48 states) [7] [3]) and that global oil production would peak around year 2000 at 1700 MTOE/yr (in fact in 2000 the production was 3600 MTOE and not quite at its peak yet so Hubbert was off the mark by a factor of 2 in production and by 4-10 years with his prediction - 50 years into the future). As with Texan production, the Norwegian production is also famous for following Hubbert's curve [4] closely (It peaked in 2001 at 162 MTOE/yr and is now 114 MTOE/yr).

[2] Wind electricity produced in 2008 has been estimated [4] to be 155 TWh = 13.3 MTOE/yr $\leq$ 0.12% of World energy supply.

[3] Production in Alaska peaked in 1988 at 101 MTOE/yr and is now down to 34 MTOR/yr

[4] Hubbert's curve is the logistic distribution function (derivative of the logistic function): $\frac{d}{dt}\left(\frac{Q_{max}}{1+ae^{bt}}\right) = Q_{max}\left(\frac{abe^{bt}}{(1+ae^{bt})^2}\right)$ where Q_{max} is the total amount that eventually will be recovered and t is time.

For the North Sea area as a whole, production peaked in 2000 at 288 MTOE/yr and is now 185 MTOE/yr [5] [8, 9].

Another fact worth mentioning is that the energy input required to extract, transport and refine the oil into consumer products is (on average) significant and increasing. The usual term for this is Energy Returned On Energy Invested, EROEI. Increasing EROEI is a consequence of the "easy (oil) first" principle - i.e., that increasing amounts of energy is required to find and extract the oil e.g., horizontal drilling, deep water oil rigs, CO_2 injection, oil shale (or tar sand) transport and processing and so on, and/or that grades are becoming heavier/less clean requiring more process hydrogen and energy for cracking, hydrogenation, de-sulphurization and other refinery processes needed to make petroleum products. EROEI is inherently hard to estimate - or even define, but some observers claim that oil extraction has seen EROEI for US oil extraction drop from ∼100 in 1930 to 40 in 1970 and further down to 14 today [10]. The numbers are uncertain, but EROEI is certainly dropping - even in Saudi Arabia [10]. The implication of this is that if oil extraction follows the Hubbert curve then there is much less *available* energy on the decreasing side of the peak than there was on the increasing size because an increasing fraction of the energy available is used for extraction/upgrade purposes. In other words, the drop in *available* energy output will be faster than its initial increase despite the symmetry of Hubbert's curve [6].

1.1.3 Gas and coal

It seems that there is a general consensus that natural gas and particularly coal will peak later than oil. It seems inevitable, therefore, that energy companies will continue to accelerate the construction of Gas To Liquids (GTL) plants (and Coal To Liquids (CTL) in the longer term) to meet demand for liquid fuel for cars, airplanes and ships. It will be interesting to see if capacity expansion in these areas will be fast enough to offset the inevitable future rapid drop in oil supplies. If not, the global economy will be in an entirely new situation: Chronic "oil crisis".

In any case, gas will also peak within the a couple of decades leaving only coal as "easy" energy to cover society's needs. The energy challenge humanity has created for itself, starting now and continuing 5 to 10 decades into the future, is tremendous.

1.2 Direct solar harvesting

> *I'd put my money on the sun and solar energy. What a source of power! I hope we don't have to wait until oil and coal run out before we tackle that.*
> - Thomas Alva Edison, 1931.
> In discussion with his friends, Henry Ford and Harvey Firestone.

[5] Danish oil production peaked in 2004 at 19.1 MTOE/yr and is now at 14.0 MTOE/yr.

[6] Note also that EROEI has nothing to do with market price of the commodity. Willingness of the market to pay more money for energy can *never* make energy available from any source which has an EROEI ≤ 1.

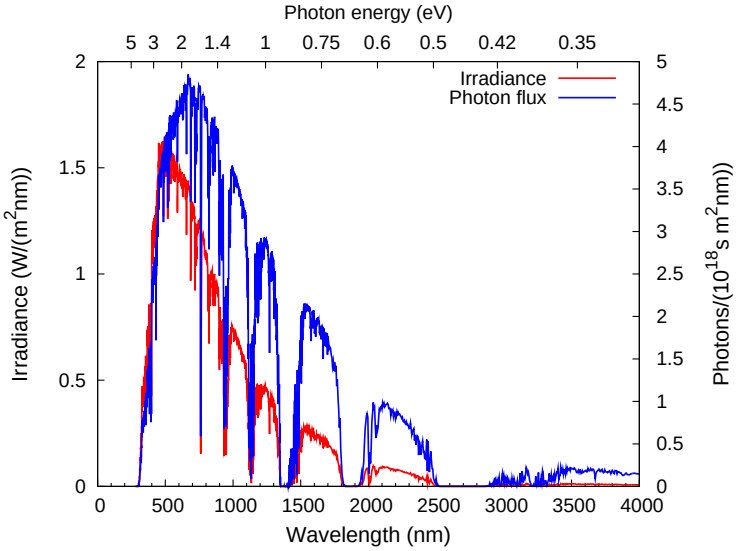

Figure 1.1: Standard AM1.5G (ASTMG173) terrestrial insolation in units of Power/(Area×Wavelength interval) and in Photons/(Area×Time×Wavelength interval).

The sun is an immense thermonuclear reactor. Every second it converts 560 million tonnes of hydrogen to helium. In the process, 4.2 million tonnes of mass converted into energy (3.8×10^{26} W). At the orbital distance of the earth this corresponds to a energy flux of 1336 W/m^2(the extraterrestrial solar constant). Multiplying by the projected area of the earth the total power we receive from the sun is 1.73×10^{17} W (173000 TW) outside the atmosphere (11000 times current human consumption). On average 51% of this light reaches the surface of the earth unabsorbed and unscattered. This (important) effect of the atmosphere is taken into account in the so-called "air mass XX" spectra (AM-XX). The (terrestrial) photovoltaic industry always perform benchmark tests against AM1.5. The AM1.5 spectrum is chosen to represent an "average" conditions in the "lower 48" states in the US averaged over one year. The receiving surface in the AM1.5 definition is tilted 37° towards the equator [7]. Two versions of AM1.5 exist. AM1.5G (Global) is the total radiation hitting the standard surface (direct radiation from the sun plus scattered radiation from the atmosphere). AM1.5G is the incident flux integrated over the entire 2π hemisphere of the sky. By contrast, AM1.5D (Direct) is only the component coming directly from the sun. Since Rayleigh scattering is proportional to photon frequency (energy) to the power of 4, the extra light in AM1.5G (compared to AM1.5D) is mostly in the blue-violet-UV part of the spectrum (the sky is blue!).

The AM1.5G spectrum is shown in Fig. 1.1. The many "missing" intervals in the spectrum are mainly due to absorption in H_2O and CO_2. Figure 1.2

[7] Some further assumptions such as total water vapour column of 1.42 cm and a total ozone column of 0.34 cm may be found at the NREL website [11] (`rredc.nrel.gov/solar/spectra/am1.5/`). The currently accepted standard spectra are found in ASTM-G-173-03 (AM1.5) and ASTM-E-490-00 (AM0.0)

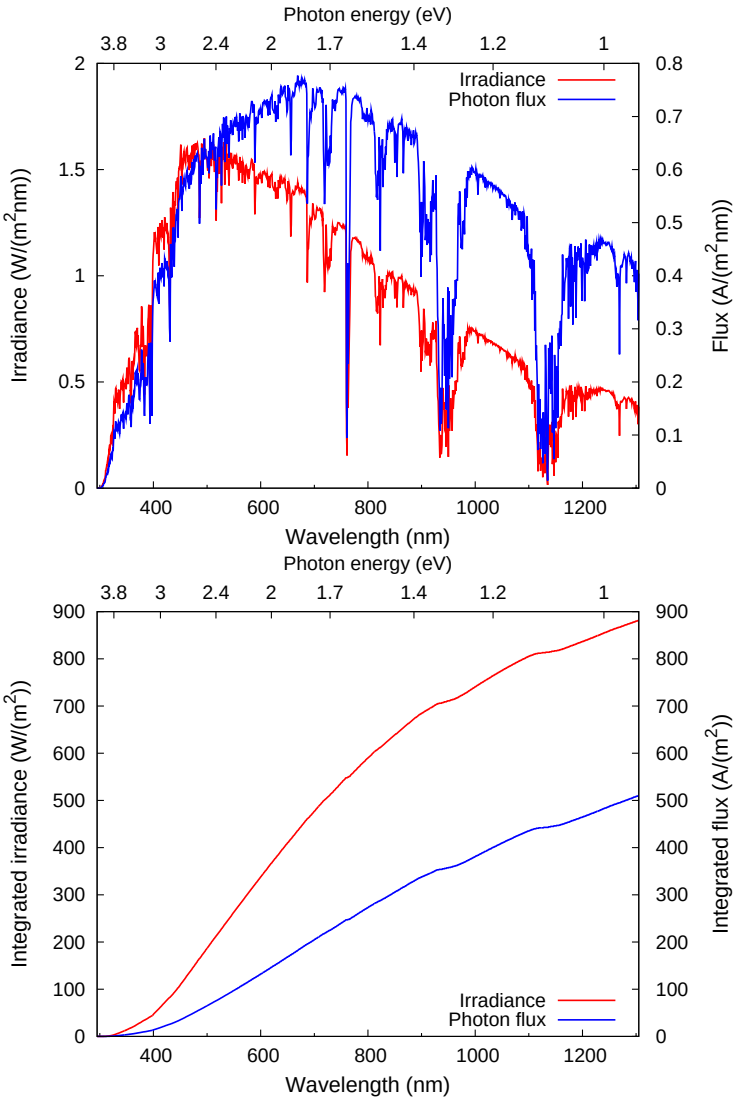

Figure 1.2: Top graph is a closeup of the $\lambda < 1300$ nm region of the AM1.5G spectrum. Photon flux is converted to Ampère (by division by $6.24{\times}10^{18}$ (photons/s)/A) i.e., photocurrent for a device capturing 100% of the photons. Bottom graph shows integrated irradiance and photon count (in A). If integration were extended to $\lambda = 4000$ nm the irradiance and photon flux would be 1.00 kW/m^2 and 691 A/m^2 respectively.

shows a closeup of the high-energy region of the spectrum up to 1300 nm. I have converted photon flux to units of Ampère/m^2 to facilitate comparison with achieved photocurrents. As an example, consider a typical silicon solar cell which (under AM1.5) has a short-circuit current of $J_{sc} = 33$ mA/cm^2. Since silicon has an (indirect) bandgap of about $E_g = 1.1$ eV it can be read off the graph that the theoretical maximum short circuit is about 45 mA/cm^2. The record device (the "PEARL" made at the University of New South Wales) achieves a short circuit current of 42.7 mA/cm^2 (and a peak efficiency of 25%) under AM1.5G [12].

While there are many ways to convert solar radiation into useful forms I will not discuss any indirect techniques (such as hydroelectric, wind, wave or biomass). Nor will I discuss solar-thermal conversion, but restrict myself to select techniques using band-gap excitation of semiconducting materials. This represents the most direct way to harvest solar energy, since the energy of the individual photons are used.

1.2.1 Photovoltaics

The most successful approach to direct solar harvesting, by a large margin, has been photovoltaics (PV). The earliest PV devices followed Edmond Becquerel's 1839 discovery of photocurrent and lead to selenium based solid-state devices of 1 to 2% efficiency. The first silicon-based solar cell was developed in 1941 by Russel Ohl working for Bell labs [13, 14] and by 1954 4% efficiency had been achieved using Czochralski-silicon.

One commercial market has been totally dominated by this technology since the 1960s - namely the satellite and space industry. Striving for high power/mass ratios (as opposed to power/price ratio) this industry has developed exotic InGaP-GaAs-InGaAs triple-junction cells and ultra-efficient single-crystal silicon cells to deliver 35.8% and 22.4% respectively under standard "1 sun" illumination [15, 16]. The former is based on scarce materials (more on this later) and is very expensive to produce and therefore only relevant for aerospace applications and mobile electronics where price is a non-issue, but the latter is being commercially marketed by Sunpower Corporation for large-scale terrestrial energy harvesting [8].

Taking latitude, atmospheric scattering, absorption, cloud cover and other weather phenomena into account maps can be drawn showing the annual incident solar energy/area and by multiplying this with an average performance ratio [9] the annual energy produced/W$_{\text{peak/nameplate}}$ of installed solar panels can be made. Such a map for Europe is shown in Fig. 1.4 and in Fig. 1.5 for the USA.

There are two traditional problems with PV. The first is the (lack of) storage of the produced energy. The second is the cost. Given that any PV technology

[8] Sunpower sells whole solar *panels* with efficiencies above 19%!

[9] The performance ratio averages the combined effects that 1), panels are assumed mounted on non-tracking mounts i.e., the irradiance is rarely perpendicular to the panels, and 2), that effective panel efficiency depends on the spectrum of the light and the intensity of the light (Crystalline silicon panels, generally, loose efficiency at $<$ "1 sun" irradiance whereas thin-film panels, generally, gain efficiency at $<$ "1 sun" irradiance). The factor of 0.75 used in the map of Europe (Fig. 1.4) is appropriate for crystalline silicon panels.

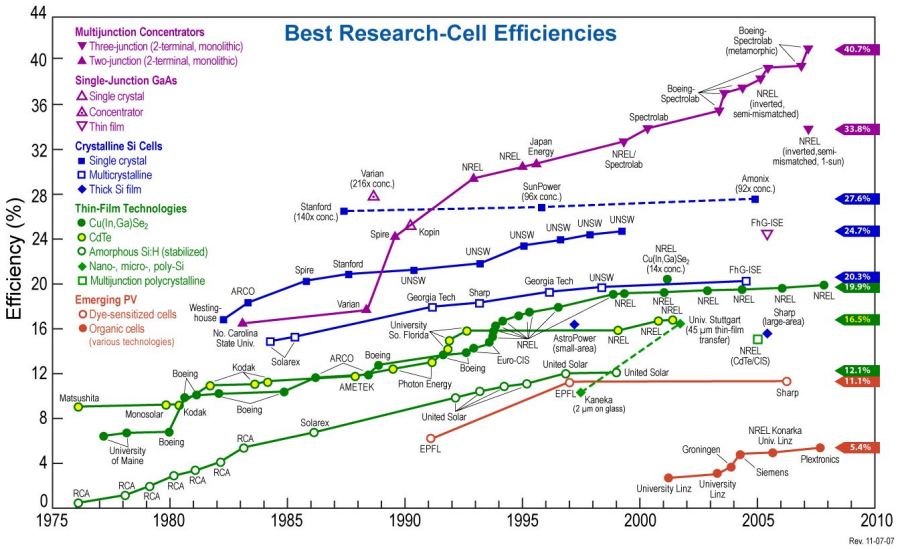

Figure 1.3: Historical record efficiency levels of different photovoltaic technologies. Adapted from [17]

inherently has no storage ability it is amazing how many PV technologies co-exist which all compete over price. Sunpower's non-conventional and expensive, but efficient, cells represent one end of the spectrum. Most of the market (∼85% currently goes to "traditional" Si-based cells with their intermediate price and performance (∼2.7 $\$/W_{peak}$, $\eta_{panel} \sim 13-16\%$). The thin-film technologies (mainly CdTe, amorphous-Si (a-Si) and CuInS/CuInGaSe (CIS/CIGS)) with their lower efficiencies and cost ($\eta_{panel} \sim 7-12\%$, ∼2.0 $\$/W_{peak}$) have a market share of almost 10%, but are growing even faster than silicon. Other technologies such as (string-ribon silicon, polymeric cells or "Grätzel" Dye-Sensitized Solar Cells (DSSC)) currently have very minute market penetration. A (not perfectly up to date) history of best verified *research-device* efficiencies of different PV technologies is shown in Fig. 1.3. As a rule, commercial modules (when they exist) achieve 60 to 75% of the efficiency of the tiny research cells.

Right now, the market (i.e., "Wall Street") seems to favor the emerging thin-film technologies, presumably because thin-film has a strong leadership in power/price ratio. CIGS startup companies with ambitious market goals and (according to themselves) very promising efficiencies and low production costs receive large influxes from venture companies. For example, companies like Solyndra, Nanosolar, Miasole and Solopower have all received over $200 million each (Solyndra and Nanosolar more than $500 million each) without selling any products yet! Perhaps even more impressive is the fact that the World's (by far) largest CdTe-panel producer, First Solar Inc., had a market valuation of ∼$24 billion (and a price/earning of over 30), until the stock market slide of 2008 and it still has a valuation of more than $10 billion. First solar has consistently been able to lead the world in power/cost and now claims production costs of 0.83 $\$/W_{peak}$ (was 1.08 $\$/W_{peak}$ in 2008) and it has increased the average

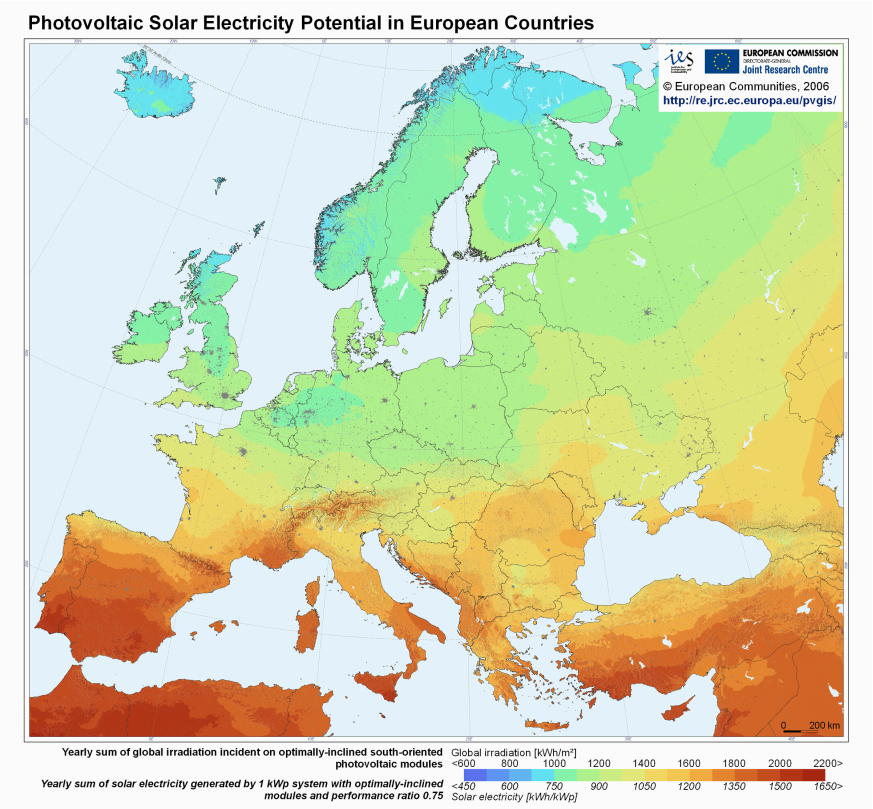

Figure 1.4: Resource map for photovoltaic installations in Europe. In Denmark an annual production of 0.85 kWh of electricity can be expected for each W_{peak} of installed power while in e.g., Portugal more than 1.5 kWh can be expected from the same installation. Southern Span, Italy and Turkey receive about 2.0 kWh/(m^2yr). Adapted from [18]

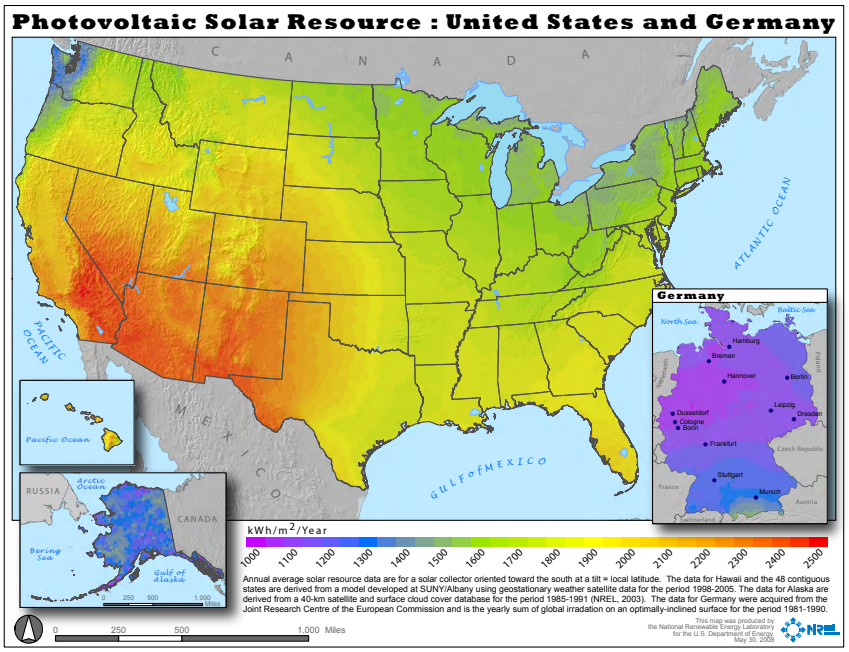

Figure 1.5: Resource map for photovoltaics in the USA (with an insert showing Germany for comparison). The best locations in the US have 10 to 20% higher annual insolation than the best areas in Europe (∼2.4 kWh/(m^2yr)) and the *worst* area in the lower 48 states (western Washington) is at least as good as southern Germany. Still, Germany is the World's largest market for photovoltaics! Adapted from [19]

module efficiency from 7% in 2003 to 11% today (which is a world record for commercial CdTe and 66% of the NREL record device [10]). In 2009 First Solar also surpassed Q-cells (German solar cell manufacturer) and became the world's largest PV producer with a nominal production capacity of 1100 MW_{peak}/yr. This all sounds promising, but as First Solar expands production, it will hit an insurmountable ceiling: The availability of tellurium on which its technology is entirely dependent since it cannot be substituted in CdTe.

Without going into detail, global production of Te is between 200 and 600 tonnes/yr (depending on source [20, 21] and [22, 23]) and CdTe technology currently consumes about 100 tonnes Te/GW_{peak} and it cannot be expected to go below 50 tonnes Te/GW_{peak} due to the ($\sim$5 μm) absorber thickness required to absorb a high fraction the light, which is essential for high efficiency. Since global Te production cannot be increased beyond 900 tonnes/yr at the most (essentially no matter what price is offered [11]) a maximum of 18 GW_{peak} could ever be produced on a yearly basis (corresponding to perhaps 3.4 GW continuous power (assuming an optimistic 20% capacity factor) i.e., 2.5 MTOE/yr - rather insignificant in the global perspective [12]). CIGS does does not fare much better, unfortunately. Supplies of gallium are limited (reported production in 2008 was 95 tonnes - half that of platinum) and since it is a by-product of aluminium production (only) it can only be increased by increasing recovery ratios which may prove uneconomical. CIS-cells (without gallium) will eventually hit a limit due to the dependence on indium - a by-product of zinc production *only* with an annual primary supply [13] of 570 tonnes in 2009. Assuming that all other uses for indium could be discontinued (not probable) this amount corresponds to about 29 GW_{peak} worth of CI(G)S produced each year giving about 4.0 MTOE/yr contribution (assuming 20% capacity factor and that indium consumption can be brought down to 20 tonnes In/GW in the future) - also quite insignificant.

The unfortunate conclusion is that for any solar harvesting technology to really make an impact on global energy supply it *must* be scalable to many thousand square kilometers of panel produced every year as may be seen by the following:

$$\text{Annual PV energy [MTOE/yr]} = \frac{\text{(peak power)} \times \text{(capacity factor)}}{\text{continuous power/(MTOE/yr)}} \tag{1.1}$$

Where peak power is land area times insolation times PV efficiency. For 1 km^2 of 10% efficient panels in a good location with 1 kW/m^2 solar constant and a

[10] NREL (National Renewable Energy Laboratories) currently hold the world record for research (less than 1 cm^2 in size) CdTe and CIGS cells at 16.6% and 19.9% 1 sun efficiency, respectively.

[11] This is because no primary Te mines exist. All Te is made as tiny amounts of *byproduct* of other metals - mostly copper. The situation resembles that of rhodium with is only made as a byproduct of platinum and therefore has zero supply flexibility regardless of price. A detailed analysis of alternative Te sources and the feasibility of direct Te mining may be found in Green [21].

[12] Of course, if the PV electricity is replacing fossil fuel in a conventional power plant then one may divide by the efficiency of the power plant - say 40% - so that CdTe PV may replace 6 MTOE/yr of fossil fuel.

[13] Primary supply is output from mines i.e., excluding recycled material.

capacity factor of 20% one finds:

$$\text{Annual PV energy} = \frac{(1\ \text{km}^2 * 1\ \text{GW/km}^2 \times 0.1) \times (0.2)}{(1.37\ \text{GW/(MTOE/yr)})} = 0.014\ \text{(MTOE/yr)} \tag{1.2}$$

An area of 1000 km^2 of PV only gives on the order of 14 MTOE/yr - roughly 5% of the annual *growth* in world energy consumption. We therefore need 20.000 km^2 of 10% efficient PV erected *every year* just to keep up with current growth rates of energy consumption. Currently, CIGS panels contain 3000 kg/km^2 of indium.

1.2.2 Photocatalysis and photoelectrocatalysis

The introductory remarks in the previous section about the scale of the problem and the hopelessness of relying on anything but the must abundant materials of course also applies to any approach to solar harvesting - also photocatalysis and photoelectrocatalysis. The latter technologies are much less efficient than PV (generally far below 10%), but they solve at least one serious drawback of PV - namely energy storage. Energy storage is a whole topic in its own right and many technologies compete. Compressed Air Energy Storage (CAES), flywheels and pumped hydro are the usual "physical" approaches while chemical storage is even more of a jungle: Various electrolyzer-fuel cell (water splitting) concepts along with batteries (and flow batteries) like lead-acid (or lead-carbon acid), sodium chloroaluminate "ZEBRA" and sodium-sulphur "NaS", ZnBr and Vanadium-redox are the "usual suspects". In general, all battery technologies offer higher electricity-to-electricity efficiency than water splitting concepts, but "solid" batteries like lead-acid have limited cycle life and flow batteries are more expensive and the experience-base with these is limited. Prices range from 150 to 200 $/kWh of storage for the cheapest lead-acid batteries up to $\geq$ 800 $/kWh for fancy Li-ion batteries, so capital costs and depreciations (due to limited cycle life) are significant. In short - storage of (PV) electricity is a major problem.

Most researchers in photo(electro)catalytic solar harvesting attempt to spilt water:

$$\begin{array}{lrcl} \text{anode:} & 2\text{H}_2\text{O} & \rightarrow & \text{O}_2 + 4\text{H}^+ + 4e^-, \\ \text{cathode:} & 4\text{H}^+ + 4e^- & \rightarrow & 2\text{H}_2, \\ \text{overall:} & 2\text{H}_2\text{O} & \rightarrow & 2\text{H}_2 + \text{O}_2 \end{array} \tag{1.3}$$

If this reaction could be made to work in practice it would solve half of the energy storage problem - namely the conversion of solar energy into chemicals [14]. Even if hydrogen is not used directly in fuel cells for making electricity it is

[14] The other half - going from hydrogen back to electricity in a fuel cell presents a problem of its own. Sadly, low temperature PEM fuel cells cannot be a large-scale solution due to their mediocre efficiency (about 60%) and their dependence on platinum as electrocatalyst. Currently the best *research* cells need 0.4 g Pt/ kW output, i.e., 0.4 tonnes Pt/GW [24]. World production of Pt is 200 tonnes/yr i.e., 500 GW of electricity (360 MTOE/yr) is a hard limit (100% Pt utilization, 100% of the *time* - defeating the "storage" purpose). High temperature fuel cells (SOFC) might be useful on a large scale with their higher efficiency (>70%) and zero PGM requirement, but huge amounts of zirconium and yttrium and lanthanum would be needed for their construction. The DTU-Risø 2G cell gives 1.3 W/cm^2 and is about 400 μm thick [4]. This gives approximately 100 tonnes Zr/GW, 10 tonnes Y/GW, 10 tonnes La/GW and 1500 kg Sr/GW.

still useful as an important feedstock for chemical processing (not least for the upgrade of coal to liquid fuels). The reaction has some obvious merits (abundant reactant, no toxicity, reasonable redox potential ($\Delta G^{\ominus} = 1.23$ eV) compared to the solar spectrum (Fig. 1.2)), but it also has some drawbacks (main product is hydrogen which is less useful than a liquid fuel and making the worthless byproduct, oxygen, without large energy loss (overpotential) and without PGM-based (Platinum Group Metals (Ru, Rh, Pd, (Os), Ir, Pt)) catalysts is a major challenge).

Fusion energy will be needed in the long run, and unless we can control it in a practical way here on earth, our only option is to get it from the sun by harvesting its photons.

1.3 Dissertation overview

In the following chapters I will present and discuss selected projects and results. For the sake of brevity, I will not present much theory about any subject or experimental technique, but instead refer to the literature [25–28].

The first project is on growing TiO_2 nanotubes (TiO_2 NTs) on non-conducting supports. TiO_2 NTs have attracted much interest in recent years in the photocatalysis community. We had the idea to grow them inside our newly developed μ-reactors in order to characterize their activity. The project led to a practical method of growing the TiO_2 NT film directly on non-conducting supports. The work also resulted in a new "discovery", viz. that the growth of TiO_2 NTs may be controlled by molecular oxygen.

The second project is about photoelectrodes for water splitting (photoelectrolysis). This was supposed to have been my main project, but ended up being a side project. I will present results on preparation techniques of tantalum-based photoanodes (inspired by work in Kazunari Domen's group at Tokyo Institute of Technology) and some more recent results from using p-type silicon in combination with platinum-free co-catalysts as a photocathode for hydrogen evolution.

The third project covered is about carrying out photocatalytic reactions in μ-reactors. This builds on years of experience in our own group with μ-reactors, but I am very happy with the technological advances we have made in the past two years. I will discuss in which ways we have evolved the μ-reactor platform and how I think it could be made even more useful in the future. Naturally, I have carried out a number of photocatalytic experiments in these reactors and I will also discuss the outcome thereof.

Finally, selected topics from my so-called "side-project", electrocatalytic ammonia synthesis, are discussed since that project has taken a great deal of my time. The experimental approach to this problem (in terms of methodology) has changed a great deal over the last three years and the reasons for these changes are outlined along with some conclusions.

Chapter 2

TiO_2 nanotubes

2.1 TiO_2 nanotubes

When titanium is immersed in an electrolyte and subjected to an anodic bias a thick film of TiO_2 will grow on the metal. The thickness depends primarily on the voltage and to a lesser extent on the time of anodization. The conventional picture of this process is that the oxide has some characteristic "break-down" field strength (on the order of V/nm) above which the oxide grows. For aluminium it is accepted that the ionic current seen with fields above the breakdown threshold is due both to oxygen ions migrating down to the metal-oxide interface and to metal ions migrating to the oxide electrolyte interface, but only the former ions contribute to growing the oxide thicker since the latter ions are dissolved in the electrolyte upon arrival at the surface. The same is believed to be true of anodic growth of TiO_2 [29].

In most electrolytes this process results in dense films with little structure, but in electrolytes containing fluoride ions, F^-, oxide dissolution competes with oxide growth and this may result in complex structures growing on the metal. In 1995 Masuda and Fukuda reported that aluminium could form self-organized pores [30] and in 1999 Zwilling et al. reported that anodization of titanium in F^--containing electrolytes resulted in porous surfaces [31] and they observed nanotubes [32], but didn't call them by that phrase. A few years later, Grimes's group at Penn State University also used fluoride-containing electrolytes to prepare anodize titanium and called the resulting structures nanotubes (Gong et al. [33]).

The interest in TiO_2 nanotubes has been strong since they were first reported because their geometry could in principle be advantageous for a number of applications. One example is DSSC's (Grätzel solar cells). In this application the dye molecules are anchored on nanoparticles of TiO_2 where they may inject an electron into the conduction band after absorbing a photon. Since a layer several μm in thickness is required for complete absorption of the light the layer of TiO_2 must be hundreds of nanoparticles "thick" and injected electrons must *diffuse* to the front electrode. This diffusion over hundreds of nanoparticles must

happen without the electrons recombining with holes in oxidized dye molecules [1] or reducing I_2 in the electrolyte to I_3^- along the way in order to get an external current from the cell. The promise of TiO_2 nanotubes is that they potentially offer the same order of magnitude of surface area for dye absorption as the nanoparticles while improving electron collection, since electrons no longer must to hop from one nanoparticle to another hundreds of times. Another example, where films of TiO_2 could be useful, is for self cleaning/sterilizing windows since they presumably have the photooxidizing activity of TiO_2 nanoparticles (see chapter 5), but are more transparent (due to lower scattering) and mechanically stable.

Since 2001 the technique for growing TiO_2 NTs has evolved to become quite versatile. For instance, the thickness of the tubular walls may be controlled by the temperature of anodization (lower temperatures giving thicker walls) and anodization voltage affects overall size with larger voltage resulting on tubes that are longer, thicker and have thicker wall thickness. Voltage ramping during anodization has been used to grow tapered TiO_2 NTs. Perhaps the biggest "knob" on the process is the composition of the electrolyte. Initial experimentation used water-based electrolytes, but Macak et al. suggested that electrolytes with lower diffusion rates would give smoother NTs and showed this with a glycerol-based electrolyte [34]. Electrolytes based on organics such as ethylene glycol, DMSO [2] or formamide with very little water content ($\leq 3\%$) have been preferred in recent years and have enabled TiO_2 NTs hundreds of μm in length to be grown [35].

The literature on nanotubes contains very little concrete mechanistic information and the explanations given for NT formation is nearly always qualitative. A recent exception from Schmuki's group (Thebault et al. [29]), shows a finite element model of ionic concentration profile away from the growth-zone at the bottom of the tubes (not least the pH gradient) and links this to experimental data for dissolution rates of TiO_2 in HF-containing electrolytes as a function of pH (reproduced in figure 2.1). The figure illustrates why acidity is always tuned to pH ≥ 5 when long NT's are sought. At low pH the chemical dissolution of the TiO_2 catches up with field assisted growth and therefore the tubes are limited to < 600 nm in length for water-based electrolytes. Neutral or alkaline conditions, however, do not result in clean TiO_2 NTs because or the increased rate of hydrolysis at higher pH which results in unwanted "debris" (thought to be hydrous titanic oxide [36]) seen in electron microscopes as particles inside on on the NT film. As mentioned, modern electrolytes for forming TiO_2 NTs are generally not based on water and they have a low concentration of fluoride and as high a pH as is allowable without too much debris formation. In our group we have stuck with a known recipe [37] of 2% water and 0.3% NH_4F in ethylene glycol. The problem tackled by our group was how to grow the TiO2 NTs on *non-conducting* supports.

[1] Dye molecules which have injected an electron after absorbing a photon, but which have not yet been reduced by an I_3^- ion.

[2] Dimethyl sulphoxide: $(CH_3)_2SO$

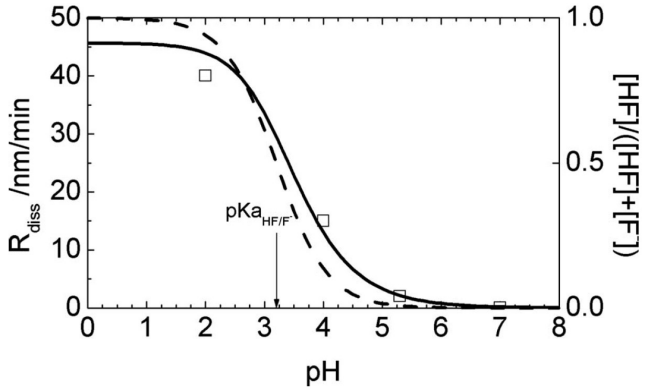

Figure 2.1: TiO_2 dissolution rate (solid curve, left ordinate) and fraction of fluoride present as HF (dashed curve, right ordinate) as a function of pH. The electrolyte aqueous 1 M $(NH_4)_2SO_4$ with $0.5\%_{mass}$ NH_4F. (Adapted from [29])

2.2 Growing TiO_2 nanotubes on non-conducting supports

In order to get a TiO_2 NT film into the μ-reactor (see chapter 4) we wanted to grow the film directly on what would later become the inside of the pyrex lid. To get well-defined thickness of titanium on a well-defined area was not a problem with access to the photolithographic and sputter coating facilities in the Danchip cleanroom. The problem was how to anodize the entire film without losing electrical contact prematurely - i.e., before all metal was converted.

Grimes' group had reported unsuccessful attempts at converting thin-films of titanium: "Anodization of single layer titanium films was not successful as the metal layer in contact with the electrolyte surface was rapidly etched away, thus breaking electrical contact with the submerged portion of the film undergoing anodization before nanotubes could be formed."(Mor et al. [36]) The problem may be seen in Fig. 2.2. Mor et al. speculated that the loss of contact was due to non-uniform electric fields near the electrolyte surface enhancing the chemical dissolution rate relative to the field-assisted oxidation process. Their remedy was to either grow the NT film until contact was lost and then thermally oxidize the remaining metal in a furnace (giving a nanotubes-on-bulk oxide structure) or to deposit an extra titanium layer of at least 400 nm thickness, where the sample would penetrate the electrolyte surface to prevent loss of contact [36].

Su-il In (Post Doc. in our group) found that by immersing the entire Ti-film into the electrolyte (away from the surface), and by contacting the lowest part of the titanium film with a titanium wire to apply the bias, the film would become transparent at the top first (furthest away from the contact point) and then gradually anodize completely so that contact was not lost before the entire metal film had been converted. A schematic illustration of the method may be seen in figure 2.3. While this "bottom-contact" method solved the problem of

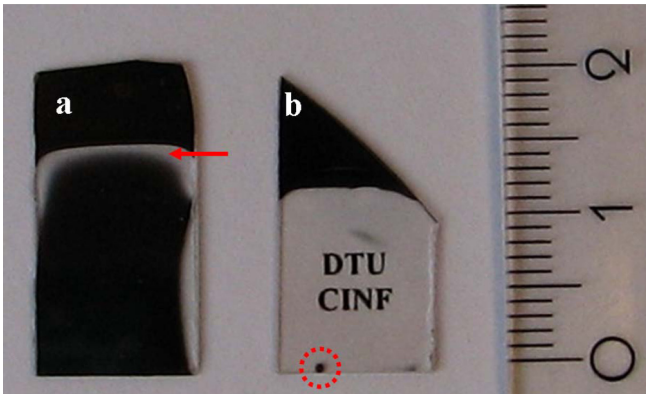

Figure 2.2: The left photograph shows how contact is lost (when all metal is converted) near the electrolyte surface (red arrow) when electrical contact as attempted above the surface. The picture on the right shows the result of contacting the metal film as far from the electrolyte surface as possible (bottom contact). Only the contact point (red dashed circle) is unconverted.

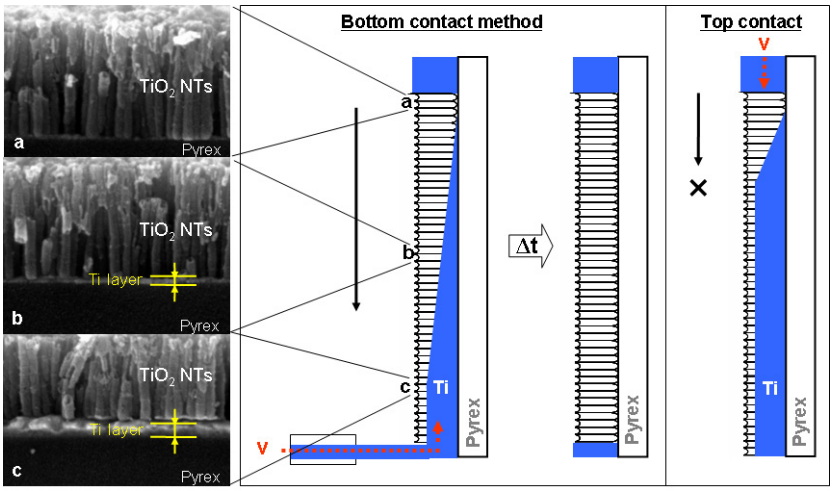

Figure 2.3: Schematic showing the "bottom contact" anodization method. The wire carrying the anodic current to the film touches the film furthest away from the electrolyte surface (deepest point). The wire (blue line at the bottom) is made from a valve metal (Al, Ti, Zr, Nb, Hf, Ta, W) - we always use Ti - to prevent oxygen evolution and excessive corrosion. The SEM (Scanning Electron Microscope) pictures show cross sections of a film where anodization was terminated before completion to show thickness gradient of the unconverted titanium metal. The central figure shows the finished film after completed conversion and the figure to the right shows a conceptual picture of premature contact loss when voltage is applied from above the electrolyte surface.

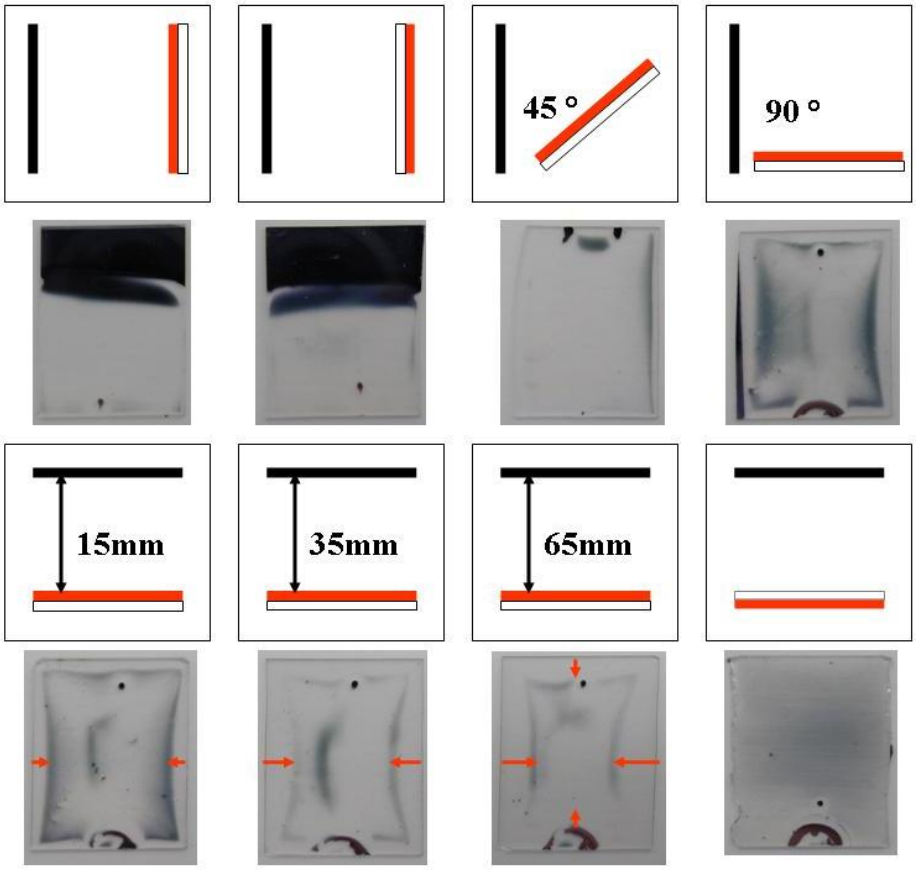

Figure 2.4: Photographs of samples that have been anodized in various geometries. The black line symbolizes the counter electrode and the red line is the titanium. The white rectangle is the pyrex support. The small dark dot in all but the third photograph is unconverted Ti at the point where the film was contacted by the Ti wire. The unconverted semicircle in all but the first two pictures shows where the clip holding the sample in place was covering the Ti film.

growing a homogenous, full-thickness TiO_2 NT film on pyrex it was a puzzle to us why it worked. Therefore a large effort to investigate the phenomenon was launched while the patent application [Patent application I] for the process was being written. It seemed impossible that gravity could play a role and the exact placement and geometry of the (carbon paper) counter electrode (CE) was also quickly ruled out (by experiments) as the reason why the film grew "downwards". If the film was placed horizontally a few centimeters below the surface with the CE above or below then the film would not grow either towards or away from the contact point. Instead it would become transparent in pincushion or barrel (concave or convex) shapes (see photographs in Fig. 2.4), but seemingly be *almost* homogeneously oxidized. We began to suspect that molecular oxygen could play a

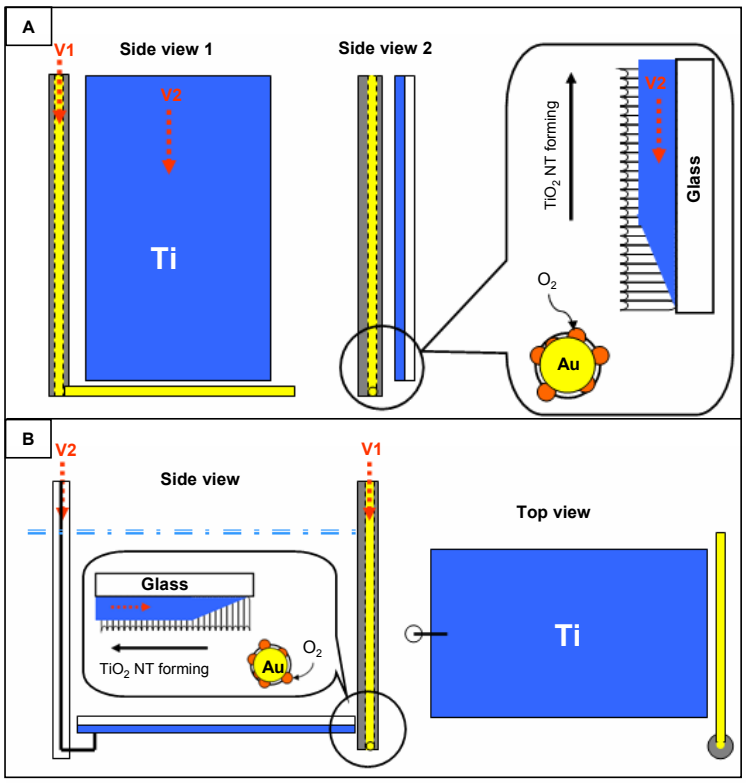

Figure 2.5: Schematic of the experiments using a gold wire (auxiliary anode) as a line-source of molecular oxygen. In **A**, the sample is standing vertically in a de-aerated electrolyte and the un-insulated Au wire acting as a source of oxygen below the sample. In this case (were voltage is applied from above) anodization proceeds upwards. In **B**, the sample is horizontal with the gold wire to the right. In this case anodization proceeds towards the left - away from the oxygen source.

role and carried out a number of experiments to investigate the theory. The tip of a syringe needle with air was brought within a couple of millimeters of the sample such that a tiny air bubble was near the titanium surface when anodization was started. Invariably, this resulted in the film becoming transparent near the bubble before the rest of the film. We also tried using a gold wire as a linear source of oxygen in the horizontal anodization geometry. In this experiment the gold wire was placed within a few millimeters of the sample (opposite the titanium contact wire) and a positive voltage of a few volts was applied (with respect to the CE) such that oxygen bubbles appeared on the gold wire surface. The geometry is shown schematically in Fig. 2.5. The gold wire with the bubbles clinging to it was than disconnected from the voltage source (before bubbles got large enough to dislodge and rise to the surface) and the anodization of the film begun in the usual way. In this case the anodization would finish first (evidenced by the sample becoming transparent) close to the gold wire and then progress towards the contact point resulting in complete anodization just like the bottom con-

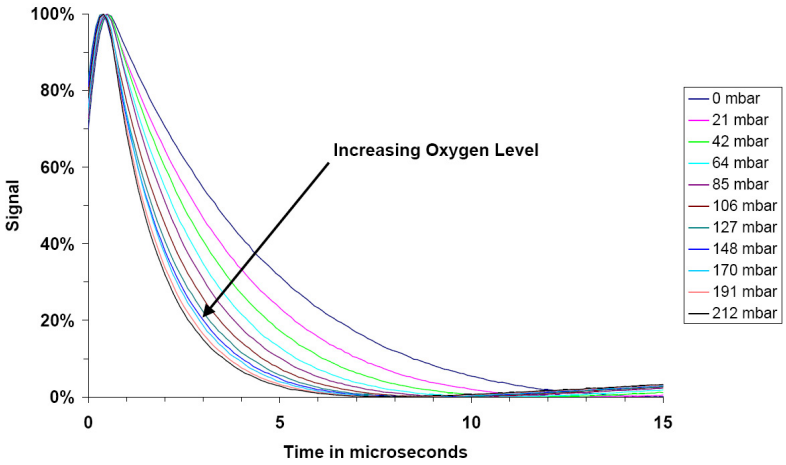

Figure 2.6: Fluorescence decay of Oxydots. It is seen the time constant for decay depends strongly on O_2 concentration - particularly in the limit of low concentration. Adapted from Oxysense "White paper" available at oxysense.com

tact method (Fig. 2.3) had done. It was quite evident, that O_2 was playing a role.

2.3 The role of molecular oxygen

Elucidating the role of molecular oxygen for the anodization process proved to be very difficult. For one thing, considerable effort went into the (seemingly simple) process of getting the electrolyte properly de-aerated before experiment start-up. Bubbling with argon (scientific, 99.9999%) seemed logical, but the problem of affecting electrolyte composition (by water or perhaps even NH_3 and HF escaping) during hour-long bubbling necessitated the use of a pre-bubbler (also filled with electrolyte solution) to saturate the argon beforehand. Measuring O_2 concentration in both the headspace over the electrolyte and down in the electrolyte was accomplished with a OxySense Model 210T oxygen sensor using "Oxydots" inside the electrolysis vessel. Each Oxydot is a Ru-amine dye in a siloxane matrix which fluoresces orange when (and some microseconds after) it has been illuminated with blue light, but the fluoresce is strongly quenched by O_2. This makes for a non-invasive *time* measurement (as opposed to measuring an absolute magnitude of some signal) (see Fig. 2.6) and it is sensitive down to 0.03% O_2 in gas phase and 15 ppb O_2 in liquid phase. Using this unit we found that when the electrolyte had been bubbled so that the oxygen level in all depths was at essentially the detection limit, and air then was introduced in the headspace the oxygen concentration would *not* increase with time and depth in the manner expected for simple 1D diffusion from a fixed surface concentration

[3] i.e., as an error function. Instead, after a few minutes induction period (at 2 cm in depth) the oxygen concentration would increase *far* more rapidly than expected and then slow down. This puzzling behavior, where the effective diffusion constant seemed two orders of magnitude higher than the textbook value for oxygen in water, which at 20°C (293 K) is roughly $D = 2.0 \times 10^{-5}$ cm^2/s was never fully understood. Ib suggested that maybe microscopic argon bubbles suspended in the viscous glycol effectively turned it into a cheese-like structure, and that only a small volumetric fraction of gas bubbles (with their *much* higher diffusivity compared to the liquid) would be needed to significantly enhance overall (average) diffusion [4]. The diffusion anomaly was not investigated further.

Having learned that oxygen plays a key role in the anodization I suggested to use O-18 labelled O_2, instead of air, in the syringe experiment followed by Secondary Ion Mass Spectroscopy (SIMS) on the grown film to see if oxygen from O_2 was incorporated into the film. This experiment was done along with an experiment using 2% O-18 labelled water (instead of 2% regular water) in the electrolyte. The latter experiment would show if water was the only source of oxygen to the film. As it turned out (Fig. 2.7), the ethylene glycol is the main source of oxygen early in the process, as evidenced by large amounts of O-16 in the upper 100 nm of the film, which in the de-aerated, $H_2{}^{18}O$ electrolyte could only originate from the glycol. Down through the film it becomes more rich in O-18, probably because the water molecules diffuse down through the tubes faster than the glycol molecules.

Unfortunately the former, more important, experiment with labelled O_2 was inconclusive. No O-18 was detected in the film (Fig. 2.7), but that cannot rule out that O_2 might play a *catalytic* role where it is consumed - and then remade from water - over and over as the film grows. The (speculative) idea is sketched in Fig. 2.8. The model assumes that an oxygen vacancy may spontaneously form on the TiO_2 surface (at the bottom of the tube) due to the strong electric field. This assumption is consistent with the generally accepted picture of how anodization proceeds as presented in section 2.1. The second assumption needed is more bold. Namely that sometimes a vacancy can develop which for some reason (e.g., steric hinderance) cannot be filled by oxygen in a water molecule (which is angled at 104.5°), but that it can be filled by an oxygen atom sitting in an O_2 molecule. If these assumptions are correct then partial charge transfer from the O_2 to the strongly biased surface can be imagined to take place (step B in Fig. 2.8) and then a water molecule can donate two electrons (by making two protons) via the O_2 now sitting on the surface. The final step is that the outer oxygen atom from the original O_2 molecule and the oxygen from the water form a new O_2 molecule and the process can repeat itself. If this model is correct then

[3] Fick's diffusion law in 1D is: $\frac{\partial C}{\partial t} = D\frac{\partial^2 C}{\partial x^2}$, where C is concentration and D is the diffusion constant. The impulse response function of this is a Gauss function which may be integrated to give the solution for the boundary condition of constant (oxygen) concentration at the surface, C_s. The solution is the complementary error function: $C(x,t) = C_s\left(erfc\left(\frac{x}{2\sqrt{Dt}}\right)\right)$

[4] One may estimate by how much the effective diffusion length is shortened by the existence of bubbles of "infinite" diffusivity. If the volumetric fraction of bubbles is called b, then the effective diffusion distance becomes: $x^* = x(1 - 2r\sqrt[3]{\frac{b}{4/3\pi r^3}}) = x(1 - 2\sqrt[3]{\frac{b}{4/3\pi}})$, where x is the diffusion distance in the absence of bubbles and r is the radius of the bubbles. 1 $\%_{\text{vol.}}$ of bubbles, i.e., $b = 0.01$ lowers the effective diffusion distance by 13%). Certainly a substantial effect, but not nearly enough to account for the observed diffusion enhancement

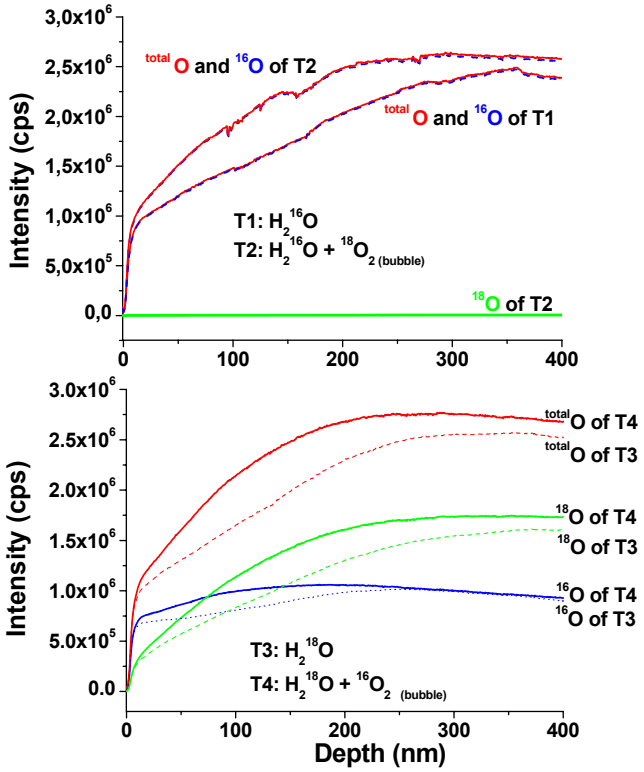

Figure 2.7: SIMS data for two experiments. The top graph shows a sample exposed to a bubble of O-18 labelled O_2 (T2) compared with a similar non-labelled experiment (T1). No O-18 is found in the film. The bottom graph shows a sample anodized in de-aerated with 2 % O-18 labelled water (T3) and a similar experiment including a non-labelled O_2 bubble. These experiments show that near the surface of the tubes O-16 (from ethylene glycol) predominates whereas deeper in the film water becomes the predominant oxygen source as evidenced by the O-18 signal.

there is no overall consumption of O_2 in the anodization process - O_2 merely facilitates transfer of oxygen from water (or glycol) to the surface. If this is true then it is not a surprise that no O-18 was detected by SIMS in the experiment with a labelled O_2 bubble, since the total amount of O-18 incorporated into the film should only correspond to the two original (labelled) O-atoms (i.e., one monolayer) as the oxygen-atoms after each turnover, are replaced by O-16. Add to this that the labelled "layer" will be the top layer (grown first), which is exposed to the HF in the electrolyte for the entire duration of the experiment (about 40 minutes) so if chemical etching rates are anything like what they are in the aqueous system (Fig. 2.1) that oxide would soon be dissolved leaving no O-18 to detect.

In conclusion, we failed to find experimental evidence to prove (or disprove) our hypothesis of why oxygen works the way it does. That, however, does not subtract from the fact that we found that molecular oxygen *does* play an

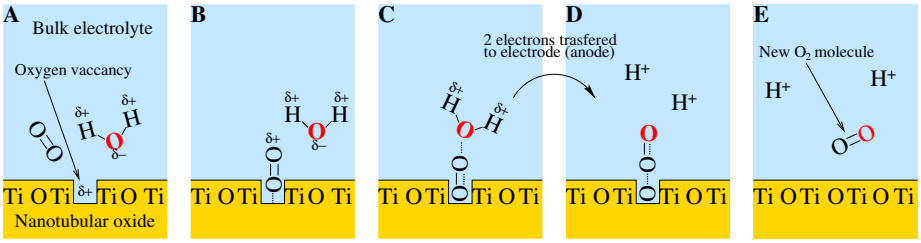

Figure 2.8: One idea for the catalytic role of oxygen during anodization. **A**: A surface oxygen atom has migrated into the bulk due to the strong field leaving a surface vacancy behind. **B**: An absorbed O_2 molecule occupies in the vacancy and donates negative charge to the oxide film. **C**: The the lone-pairs on the oxygen atom of a water molecule is attracted to the absorbed oxygen molecule's net positive charge. **D**: The hydrogen atoms of the water molecule donate their electrons to the anode and migrate away as protons while the oxygen atom of the water molecule forms covalent bonds to the outer atom of the original oxygen atom. **E**: The bond between the oxygen atoms of the original oxygen molecule is broken and the surface vacancy is healed while a new O_2 molecule is formed. The high field may form a new surface oxygen vacancy and the process repeats, $\rightarrow$ A.

important role in the anodization, and that we have shown that this method may be used to grow homogenous, transparent layers of TiO_2 NTs over large *non-conducting* samples (full 4-inch wafers were successfully anodized, [Paper I]). If transparency is desired, but electrical conductivity is not needed (as with self-cleaning windows) our anodization method may turn out to be useful.

Chapter 3

Photoelectrocatalysis

3.1 Overview and common experimental techniques

I have been involved in work on several different kinds of photoelectrodes and this section serves to introduce each kind and give a brief background about each. The objective of all the work with photoelectrocatalysis has been to make photoelectrodes for water splitting (photoelectrolysis).

Initial testing of any new photoelectrode was always carried out in crude "open beaker" electrochemical cells. In these simple experiments the photoelectrode is placed in front of a planar glass window of a modified 100 ml glass beaker and electrolyte (typically H_2SO_4, $HClO_4$, KNO_3 or NaOH depending on the nature of the electrode) is added. A counter electrode (e.g., carbon paper or perhaps a Pt gauze) and a reference electrode is also placed in the beaker and experiments may begin. These early experiments are typically cyclic voltammetry (CV) under illumination (often chopped at about 1 Hz), to get a feel of photocatalytic performance and an estimate material specific parameters such as the flat-band potential, U_{FB} [1]. However, the observation that a given sample exhibits a photocurrent does not prove that it is spilling water. Consider e.g., a TiO_2-based photoanode which shows an anodic photocurrent when illuminated. Even if hydrogen is collected at the counter electrode in stoichiometric amounts it still is not conclusive evidence of photocatalytic water splitting. The oxygen must also be collected and quantified. Otherwise, the photocurrent could be caused by a reaction like: $Ti + 2\ H_2O \rightarrow TiO_2 + 4\ H^+ + 4\ e^-$ (i.e., corrosion of metallic Ti or sub-stoichiometric oxide)) instead of water oxidation: $2\ H_2O \rightarrow O_2 + 4\ H^+ + 4\ e^-$. In order not to be fooled by such photocurrents that do not represent photocatalytic water splitting we have developed the cell seen in the photograph Fig. 3.1. The cell, which is made from pyrex glass, has two main compartments - one for the photoelectrode and one for the counter electrode -

[1] The flat-band potential may often be estimated simply by the applied potential at which the photocurrent has decayed to (almost) zero. This is because U_{FB} is the potential one must apply to eliminate the space-charge (and therefore band bending) that results when the Fermi level of the semiconductor equilibrates with that of the electrolyte when the sample is immersed. In the absence of band-bending (to separate photogenerated electrons and holes) the photocurrent drops dramatically due to recombination [27, 38, 39].

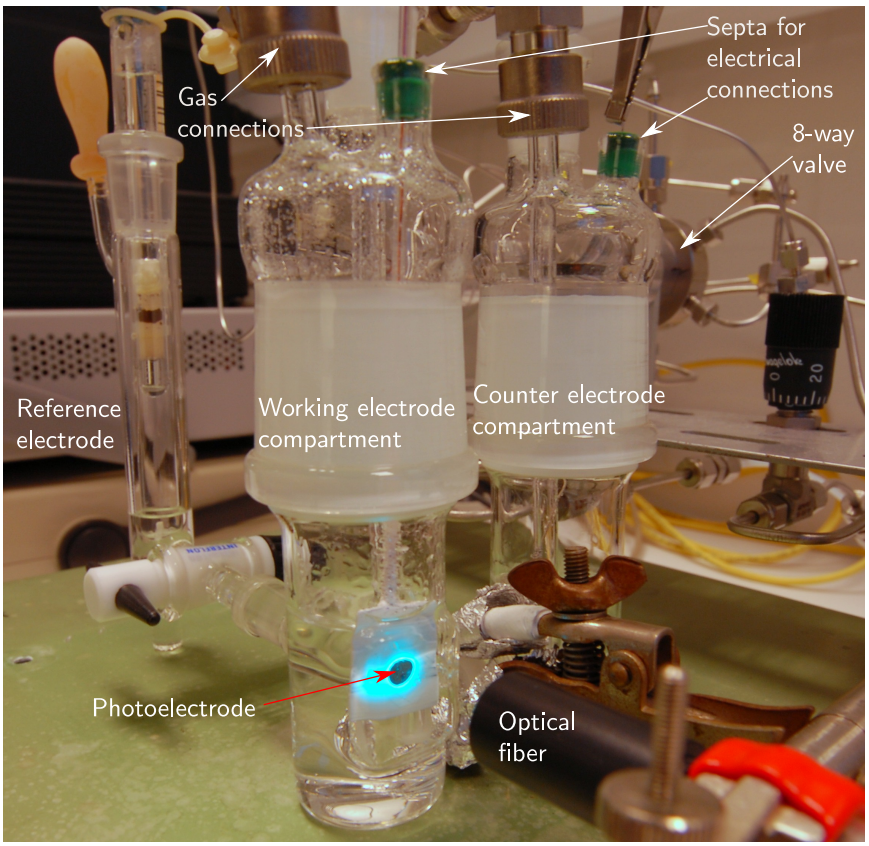

Figure 3.1: Photograph of the compartmentalized cell for Photo-ElectroChemical (PEC) experiments. The in foreground, the compartment for the working (photo)electrode is seen. To the left, the reference electrode appendix may be seen and to the right the counter electrode compartment is seen. The two main compartments are separated by a glass frit. The two compartments may be simultaneously bubbled with different gasses if needed.

and they are separated by a glass frit, which allows ions to pass, but minimizes gas migration from one compartment contaminating the other compartment [2]. The compartment for the photocathode is also fitted with a planar glass window to minimize diffraction of the incident light and with a reference electrode compartment (via a lapped stopcook). Each electrode compartment is closed off via a glass lid (lid and cell mate using standard taper glass joints) and each lid has two electrical feedthroughs (GC-style septa, Supelco) for electrode connections and two gas connections - one for input and one for output gas (Swagelok "UltraTorr" fittings). The gas fittings connect to the gas handling using 1/16 inch stainless steel tubing (thin tubes give mechanical flexibility),

[2]For example, when using a photoanode which evolves oxygen and a platinum counter electrode which evolves hydrogen then oxygen diffusing into the counter electrode compartment would react with the hydrogen over the platinum causing a loss in both oxygen and hydrogen product which leads to an apparent loss in Faradaic efficiency.

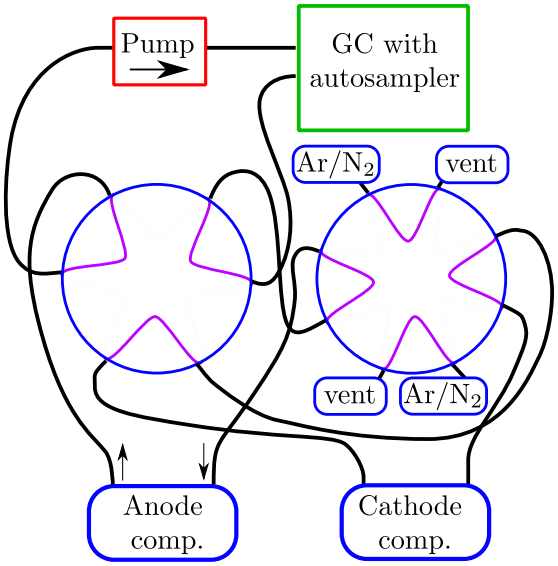

Figure 3.2: Schematic of the gas circulation system for the compartmentalized photoelectrocatalysis cell. The 6-way valve chooses which of the two compartments is under analysis by the GC (Gas Chromatograph). Gas from that compartment is continually circulated through the sampling-loop of the GC-autosampler. In the figure, the anode-compartment of the cell is being analyzed. The 6-way valve also serves to seal the other compartment. The 8-way valve is used before the experiment starts to flush both compartments with suitable gasses (typically argon, but it could also be different gasses e.g., oxygen in the anode compartment and hydrogen in the cathode compartment to minimize chemical bias due to sub-atmospheric partial pressure of a reactant or product species). The flush-gas is bubbled through the electrolyte to replace other dissolved gasses and clean the headspace.

which is also the material that the entire external gas system is made in order to make everything as airtight as possible [3]. The gas handling system (seen in Fig. 3.2) features two multi-way valves: A six-way valve to select which compartment is being sampled by pumping gas through the sampling loop of a GC and an eight-way valve, which either flushes both compartments (potentially with different gasses) or seals one compartment off and allows sampling of the other. The system shown in Figs. 3.1 and 3.2 has been used to quantify oxygen and hydrogen from electrolysis and photoelectrolysis of small currents and is practical to work with.

3.2 TiO_2 based photocathodes

Any energy capture technology based on band-gap excitation using TiO_2 as absorber has an inherent disadvantage: The high bandgap, E_g, of TiO_2 which is

[3] The only parts of the system which are not either glass or stainless steel are the four small (silicone) septa and the (Viton) O-rings in the UltraTorr fittings

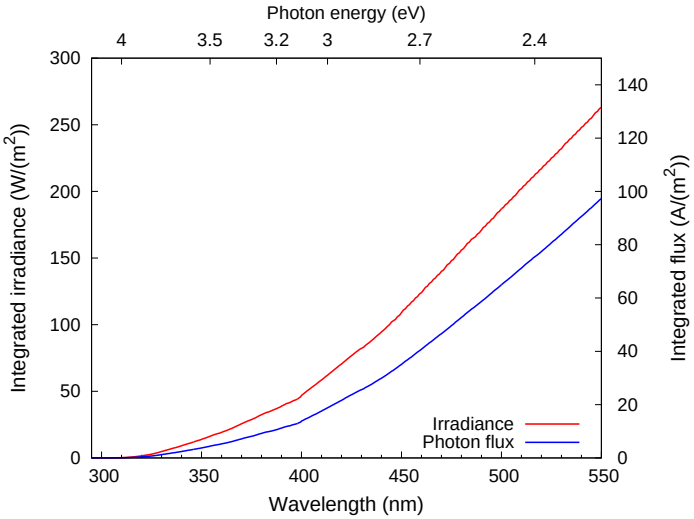

Figure 3.3: Closeup of the high energy region of the AM1.5G (ASTMG173) terrestrial solar spectrum. It may be read off the graph, for example, that the limiting photocurrent for a material with a $E_g = 3.0$ eV is only about 1.9 mA/cm^2.

usually said to be 3.0 eV for the rutile phase and 3.2 eV for the anatase phase. This means, in a "best-case" scenario where all incident solar photons above E_g could be captured and used (all losses are ignored), that rutile would only utilize light with $\lambda < \sim$413 nm and $\lambda < \sim$387 nm for anatase. This corresponds to a maximum photocurrent under AM 1.5G illumination of 1.88 mA/cm^2 and 1.06 mA/cm^2 respectively (Fig. 3.3). These currents give rise to a theoretical maximum energy efficiency [4] of 1.88 mA $\times$1.23 V/(100 mW/cm^2) = 2.3% (and 1.3%) respectively. For this reason I have only used TiO_2 samples as references for comparison (and teaching) and not done any serious work on making TiO_2 photoanodes.

3.3 Tantalum-based samples

Kazunari Domen's group at the University of Tokyo has been studying water splitting for more than 20 years, and in the last decade they have established that many nitrides and oxynitrides not only absorb visible light, but are able to drive either hydrogen evolution (HER) or oxygen evolution (OER) with decent turnover rates in the presence of suitable co-catalysts and (perhaps) sacrificial electron donors or acceptors. Domen's group reported that the very simple system (only one type of metal) of tantalum, oxygen and nitrogen showed stable activity for water splitting [40–42]. In particular, they reported that suspensions of nanoparticles of TaON ($E_g \approx 2.5$ eV) or Ta_3N_5 ($E_g \approx 2.1$ eV) both could be made to split water under visible illumination, but only with sacrificial reactants (Ag^+ ($AgNO_3$) and methanol for OER and HER respectively). From Figs. 3.3

[4] For a TiO_2 photoanode-based device capturing all photons with $E_{ph} > E_g$ and operating at zero external bias. Highly unrealistic!

and 1.2 we see that limiting photocurrents of TaON and Ta_3N_5 are 6.2 mA/cm^2 and 12.5 mA/cm^2 respectively

Since most of the published work from Domen's group was on nanoparticles in suspension and since, generally, the quantum efficiency for OER was much higher than HER with TaON catalysts I wanted to attempt making photoanodes based on these (n-type) tantalum(oxy)nitride compounds. If I could successfully make and contact such thin-films, a thorough study of the effect of thickness (absorbtion versus charge transport) and co-catalysts (e.g., RuO_2) would be possible. There were a few papers by Domen's group about tantalum-based photoanodes available from which to get inspiration [43, 44]

3.3.1 Thermal conversion of tantalum to (oxy)nitride

According to the literature, tantalum oxide converts into oxynitrides first and later pure nitrides when treated at high temperature in nitrogen-containing atmospheres [45–47]. It is generally accepted that temperatures above 600°C (873 K) are needed, which limits the choice of substrate. Treatment in N_2 is thought to give mainly the TaN phase which is not interesting as a photocatalyst [5]. The general procedure for producing Ta_3N_5 [6] from Ta_2O_5 is treatment in dry NH_3, preferably at $T \in [720 \ldots 850]$°C (993 to 1123 K) (presumably, H_2/N_2 mixtures could also work). Making the simple oxynitride, TaON, is accomplished by treatment (also preferably at $T \in [720 \ldots 850]$°C) in wet NH_3 i.e., NH_3 that has been bubbled through a saturated solution of NH_3 in water at room temperature. Both these procedures have been used in Domen's group and I have successfully made both compounds this way (as evidenced mainly from X-ray diffraction (XRD), not shown). Ta_3N_5 power looks deep-red, much like Fe_2O_3 (as one might expect from the similar bandgap), while TaON powder looks orange.

Making the powders was easy. Making films on metallic substrates was a different story: Having read claims in the literature that only tantalum oxide would be converted into (oxy)nitride under reaction conditions - not metallic tantalum, I initially thought that making thin-film of an (oxy)nitride on metallic tantalum would not be so hard [7] [43, 44]. The idea was that I would grow an oxide layer of suitable thickness on the metal (either thermally in air or by anodization) and then carry out the conversion to (oxy)nitride afterwards. Suffice it to say that metallic tantalum is *not* unaffected by the treatment, but it is not converted into dense, adherent (oxy)nitride either. This negative result is not surprising in the light of the observation by Gavrilyuk et al. that upon exposure to air at 500 to 600°C the surface bulges up and "...the oxidation products on the surface of the tantalum being transformed into a white powder, which readily separates from the metal." [46]. Somehow, the Japanese group

[5] TaN is a metallic conductor and has a dull, grey-metallic appearance. It is not quite as stable to corrosion as the famed oxide (Ta_2O_5) which gave tantalum its name, but nonetheless still so stable that it is being investigated as electrode/support for high-temperature (> 100°C) water electrolyzers and fuel cells (Part of the Hycyle project [48]).

[6] Ta_3N_5 is a formal stoichiometry. Measurements of actual samples indicate that the true composition is more like $Ta_3N_{4.7}$ depending on synthesis temperature [47].

[7] I forgot my own law: "Nothing is as easy as it ought to be."

avoided such problems in their recent work. Below is a description of some of the issues encountered in this project and which steps were taken to overcome them:

Metallic tantalum "attacked" by NH_3 The problem was thought to be due oxygen leaking into the tube furnace and/or feed gas through plastic tubing, etc. Therefore as much tubing as practically possible (but not all) was changed to stainless steel. Experiments with very high NH_3 flow rates were carried out in order to decrease the oxygen concentration for a given leak rate and also to lessen any back-diffusion of oxygen from the exhaust line. The problem was never fully understood.

Hydrogen embrittlement Hydrogen (from the NH_3) may diffuse into the tantalum lattice at high temperature, and this is thought to be what sometimes causes foil-samples, which were planar when they were placed in the furnace, to become twisted and distorted in shape when they have been treated. Various measures to mitigate this were implemented along the way. It became standard procedure that the warm-up and cool-down ramps were completed in an inert atmosphere of helium or argon. The warm-up in an inert should facilitate removal of residual water (see previous point) while cool-down in an inert would allow time for the hydrogen to diffuse back out and hopefully also stress-anneal the metal.

In a further effort to alleviate the first two problems attempts to shorten the time in reactive gas as much as possible were also carried out. Figure 3.4 shows an example of a measurement on one sample with thermally grown Ta_3N_5 on Ta. The experiment is typical in being "quick and dirty" - just to get an order of magnitude of the quality of the sample and, as the tiny photocurrent shows, the sample is quite bad. Samples such as this, with a visibly non-adhering film of nitride, exhibit photocurrents, which are three to four orders of magnitude too low to be interesting and therefore not worth the effort to characterize properly.

3.3.2 Anodization of tantalum

One aspect of the preparation of tantalum-based samples was particularly easy and fun and that was growing tantalum oxide by anodization. Plain water works fine as electrolyte, although I typically added a little soap as surfactant. The most beautiful (interference) colors can be achieved on the surface of the tantalum in this manner [8]. The success of aqueous anodization gave me one of my more "wild" ideas of the project: If anodization in water gives oxide films, then anodization in liquid NH_3 might give nitride films? Naturally, such an idea had to be tested so I condensed about 40 ml NH_3 in a ethanol slush-ice bath and added a bit of metallic sodium to make it conductive (solvated electrons). Anodization was attempted in this electrolyte at about -55°C (218 K), at various potentials (up to 60 V), and with various concentrations of sodium (from a blue solution and all the way to a metallic, copper colored solution), but without a convincing effect on the tantalum [9].

[8] When trying this experiment "at home" one should not omit to anodize a sample to exactly 30 volts. It results in a spectacular dark-violet/dark-purple surface. Similar effects are well-known for thin-films of SiO_2 or Si_3N_4 on silicon.

[9] Nevertheless, it was an interesting experiment.

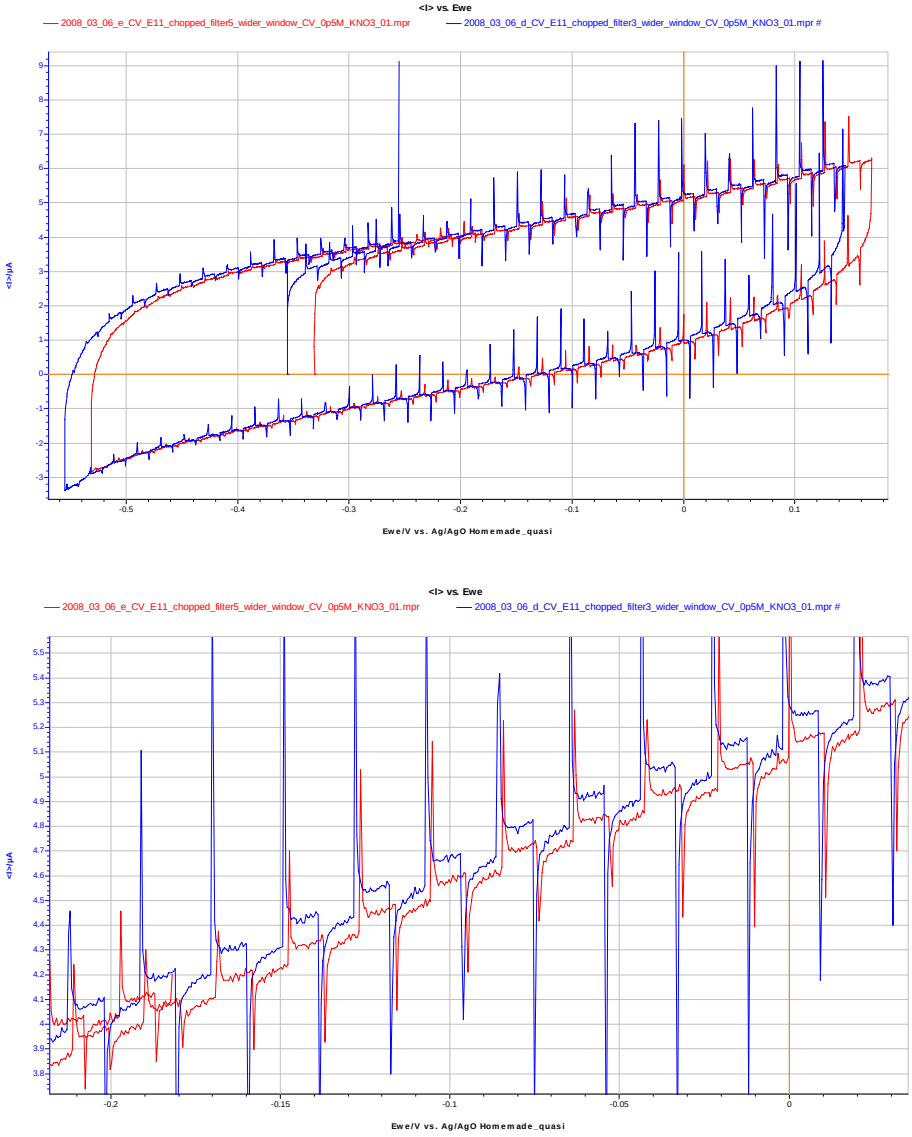

Figure 3.4: Cyclic voltammograms under chopped illumination of a Ta_3N_5 sample without any co-catalyst in a 0.5 M KNO_3 electrolyte. Divisions in the abscissa grid are 0.1 V apart and in the ordinate the divisions are 1 μA (0.05 V and 0.1 μA in the lower graph). The blue trace is using a 420 nm cut-on (high pass) filter in the beam of a Xe-lamp and the red trace is using a 515 nm filter (see Fig. 5.8 on page 77). The sample exhibits anodic photocurrent (even with the 515 nm filter) as expected (n-type material), but the photocurrent is very low (about 0.1 μA). The pH of the electrolyte is close to neutral and the homemade AgO/Ag reference electrode has potential of about +0.35 V vs. RHE (Reversible Hydrogen Electrode), so, on this scale, the reversible potential for HER/HOR is -0.76 ± 0.1 V.

3.3.3 Reactive sputtering of tantalum

As an alternative approach to making tantalum (oxy)nitride thin-films I wanted to try reactive sputtering. Reactive sputtering is a term that covers sputtering in a non-inert atmosphere so that the sputtered material may react with the reactive gas. In my case the initial idea was to sputter Ta_3N_5 by using a mixture of nitrogen and argon as the sputtering gas. The question was whether nitrogen would be reactive enough to achieve the desired stoichiometry. Of course it might also be possible to grow TaON in a mixture of argon, oxygen and nitrogen. Oxygen was expected to be much more reactive than nitrogen, but I thought that if a sufficiently low oxygen/nitrogen ratio in the gas was used the resulting oxygen to nitrogen ration should be 1:1 as in TaON.

For this sputtering project I talked to Jørn Bindslev (professor at DTU physics) about the possibility of using his Physical Vapour Deposition (PVD)-chamber (Alcatel) for these experiments. He was quite optimistic about the project and was very supportive all along. The Alcatel chamber is fitted with a large butterfly valve to control pumping speed. It is pumped by an oil diffusion pump (ODP) with a liquid nitrogen trap. The chamber has no load lock and the "lid" is lifted off the chamber whenever samples or targets need to be changed. The lid seal with the walls is accomplished by a large O-ring. For these reasons the base vacuum is about 2×10^{-5} mbar - high vacuum, but certainly not ultra-high vacuum. The chamber itself is fitted with an evaporation source (for gold), a DC magnetron sputter source (used in this work) and an RF sputter source (for sputtering non-conducting targets). The DC magnetron target is quite large (about 10 cm in diameter) and fortunately Jørn had a tantalum sample on hand.

The very first experiments were just about igniting the plasma and keeping it on in pure argon. This seemingly simple task was not entirely trivial. In order to get decent base-line deposition rates for pure Ta the target itself had to be machined down by the workshop and a new grounding ring [10] had to be made. After a few iterations, however, Jørn measured reasonable deposition rates (using the in-chamber quartz oscillator) and we were ready to start experiments with adding nitrogen to the argon. Figure 3.5 shows a (sputter) depth-profile of the Auger electron signal [11] of an early attempt at growing Ta_3N_5 by reactive sputtering. During profiling, the sputtered area is 1×1 mm^2 and the Ar^+ ion current was 2.30 μA, as seen in the bottom of the plot. According to the instrument calibration [12] this should result in a sputtering rate of about 200 ML/min (assumed yield: 3.5 Ta/Ar) and with a monolayer thickness of 2.8 Å this gives 56 nm/min. Judging from the depth profile, therefore, layer 1 (Ta) takes $16 - 11 = 5$ minutes to sputter, making the thickness estimate 280 nm. This is *very* different from the thickness estimated during deposition from the change in quartz crystal resonance frequency (Inficon), which was only

[10] The grounding ring is a metal ring that is grounded to the chamber and which has a lip that protrudes radially inward a few millimeters around the target and a few millimeters above the target surface. It serves as anode during sputtering so the geometry is important.

[11] Recorded with a primary energy of the e-beam of 5 kV and a sample current of 1.2 μA by John Larsen (CINF).

[12] Calibration was carried out (years ago) by sputtering through a sample made by anodizing Ta to 66.6 V, which yields an oxide 100.0 nm thick (confirmed by Rutherford Backscattering).

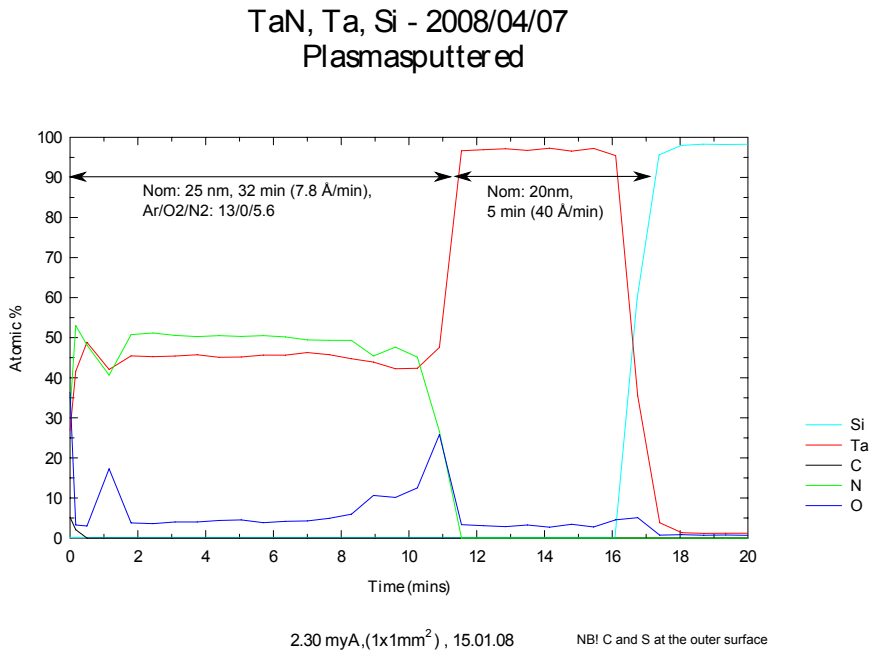

Figure 3.5: Auger-based sputter-profile of an early sample. The parameter is sputter time in the analysis chamber and the traces are atomic abundances. The substrate is silicon (light-blue trace) and in this case 2 layers are sputtered onto the sample. Layer 1 (11-16 minutes) is (almost) pure tantalum (red trace) deposited in a plasma of pure argon. Layer 2 (0-11 minutes) was deposited over 32 minutes with argon and nitrogen flows of 13 sccm and 5.6 sccm respectively. According to the Auger analysis layer 2 contains about 50% N, 45% Ta and 5% O (i.e., almost TaN stoichiometry). $p_{total} = 2.5$ Pa

20 nm. To reconcile this factor of 14 in difference it was decided to deposit tantalum on a silicon sample with photo-resist patterns to allow lift-off and subsequent thickness measurement with a profilometer. A nominal (Inficon) thickness of 103 nm pure Ta was deposited and measured to be 335 ± 10 nm with the profilometer i.e., a factor of 3.25 higher than nominal thickness. This means that all nominal thicknesses (of Ta) should be multiplied by a factor 3.25 and that nominal thicknesses for TaN should be multiplied by $3.25 \times \rho_{\mathrm{Ta}}/\rho_{\mathrm{TaN}} = 3.95$ [13]. The stoichiometry seen in Fig. 3.5 is determined in each point by comparing the Auger signal amplitude of the relevant peaks in the spectrum. As an example, an overview spectrum is shown in Fig. 3.6. This example shows a sample after 30 seconds of sputtering (i.e., about 5 nm) below the surface. The figure illustrates that the Auger cross-section of oxygen and nitrogen is much higher than that of tantalum. The relative sensitivity factors used are: C: 0.140, N: 0.230, O: 0.400,

[13] It also implies that the real sputtering rate in John's chamber (1×1 mm^2) is 3.25×20 nm/5 min = 13 nm/min = 47 ML/min (i.e., far below the expectation of 200 ML/min) according to observed sputtering time of the Ta-layer in Fig. 3.5 and also confirmed by later measurements on thicker Ta layers. This corresponds to a suspiciously low sputter yield of about 0.85 Ta/Ar, which is not understood.

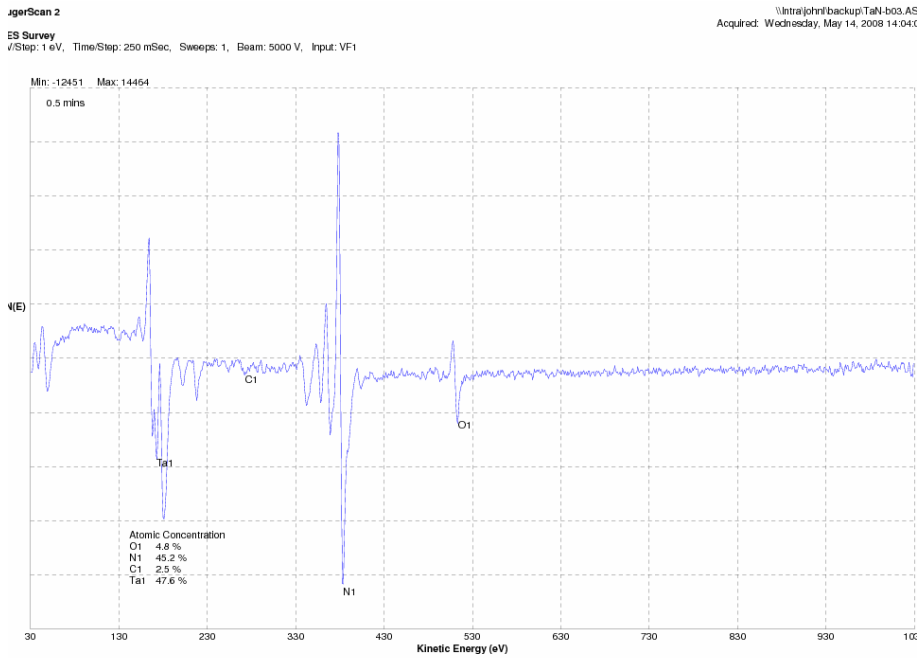

Figure 3.6: Auger survey scan of a similar sample to that shown in Fig. 3.5 after 0.5 minutes of sputtering. The tantalum, nitrogen and oxygen peaks are clearly seen, but the carbon signal is already very weak. The estimated atomic concentrations estimated from these signals are seen in the lower left corner of the plot (4.8% O, 45.2% N, 2.5% C, 47.6% Ta).

Si:0.280, Ta:0.136. [14]

Figure 3.5 illustrates the general phenomenon that when N_2 (or O_2) is added to the sputtering gas, the deposition rate drops drastically - presumably due to passivation of the target surface. In the case of Fig. 3.5 the rate drops from about 40 Å/min to 7.8 Å/min upon changing from pure Ar to 30% N_2 in Ar. Another observation is that even when adding nitrogen the resulting film is sub-stoichiometric in nitrogen ($\sim Ta_3N_{3.3} \neq Ta_3N_5$). In later depositions lower Ar/N_2 ratios were attempted, but without much improvement on the N/Ta ratio in the resulting films and with increasingly unstable plasmas. Also, the oxygen content of the films could never reliably be brought below about 4% (also seen in the film in Fig. 3.5 [15]) so for these reasons it was decided to also try making TaON films, where residual oxygen would be a non-issue. Figure 3.7 shows the (final) attempt at growing Ta_3N_5 in the Alcatel (second layer) with the Ar/N_2

[14] These values are default in the Φ MACS (Multiple-Technique Analytical Computer System) manual from 1985, and they reproduce e.g., the stoichiometry of known substances like Ta_2O_5 quite well.

[15] At that time, this residual oxygen was thought to be due to finite base pressure of the Alcatel, but in hindsight it is more likely to be due to residual oxygen in the nitrogen (even though it was N5 i.e., 99.999%). It is also possible that background water in the Auger-chamber could chemisorb on the sample during sputtering, giving a false background signal, but since the base pressure of the Auger-chamber is 10^{-10} mbar this is a small contribution.

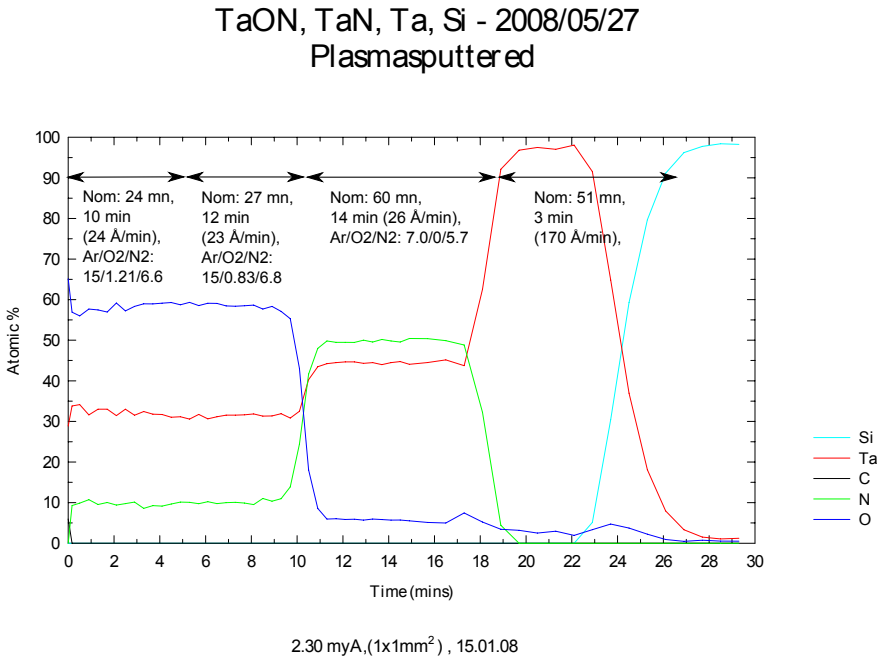

Figure 3.7: Auger-profile of a sample with four layers (settings on the PVD). Layer 1 is pure Ta grown in Ar. Layer 2 is an attempt at Ta_3N_5 with the lowest Ar/N_2 ratio allowed by the PID unit of the Alcatel (45% N_2 in Ar). Layer 3 and 4 represent the first attempts at growing TaON. The difference is the O_2 content. Despite the fact that the N_2/O_2 ratio in the gas is 8.2 and 5.4 in layers 3 and 4 respectively the resulting, films contain barely 10% nitrogen and almost 60% oxygen. $p_{total} = 2.5$ Pa

ratio set to the lowest ratio the gas controller of the Alcatel would allow. Even with this mix of 45%N_2 in Ar, the resulting film contains only 50%$_{at.}$ nitrogen. The third and fourth layers represent the first attempts at hitting the TaON composition. Even though the gas led to the chamber had much more N_2 than O_2, the resulting films are very rich in oxygen and poor in nitrogen. This clearly demonstrates the higher reactivity of oxygen in the sputtering process. Layers 3 and 4 are so similar (approximate composition $Ta_3O_5N_1$) despite different oxygen pressures that *much* lower oxygen concentrations are needed to reach the desired TaON. Subsequent experiments of pushing the lower limits O_2-flow of the Alcatel gas controller failed to bring the oxygen content in the films sufficiently down, so it was decided to substitute the pure oxygen with a premixed N_2/O_2 mixture and, if necessary, dilute that further with pure N_2. For this reason, a bottle of 1% O_2 in N_2 was acquired and hooked up on the "O_2"-line of the Alcatel. Figure 3.8 shows an early sample made using pure Ar (for interlayers of "pure" Ta) and Ar/(1%-O_2)mix mixtures. The sample has 6 layers. Layers 1,3 and 6 are pure Ta, layers 2,4 and 5 are attempts at making TaON. Unlike the other Auger-sputter profiles, this profile was made sputtering over a 2×2 mm^2 area, so the sputtering times should be divided by 4 when comparing with the other

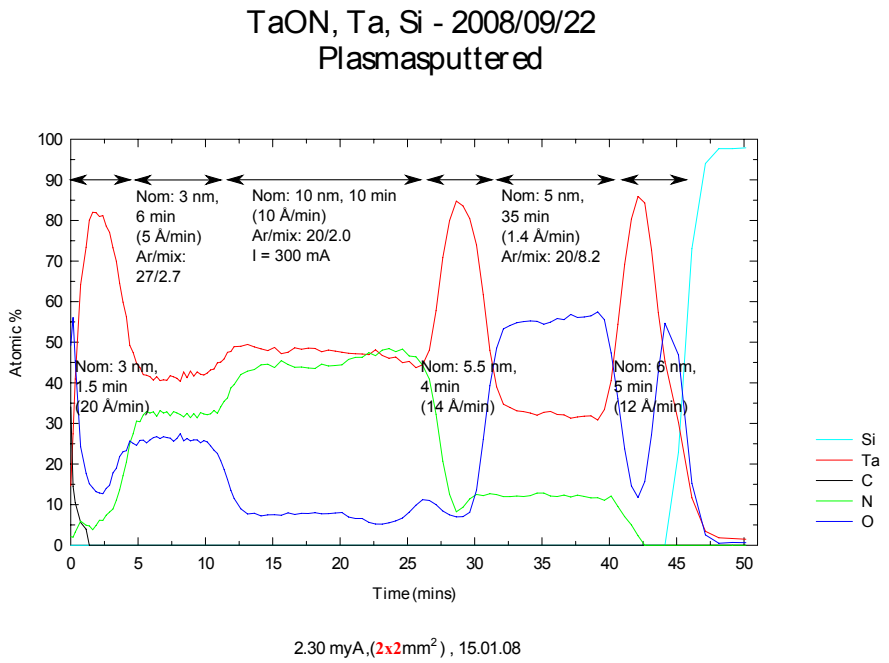

Figure 3.8: Auger-profile of a sample with 6 different layers. This sample was the first attempt at using a premixed O_2/N_2 (1% O_2) gas as source of both oxygen and nitrogen for growing TaON films. Layer 2, which grew very slowly (< 1.5 Å/min), is almost an oxide with its very small nitrogen content. Layer 4, which was grown at higher plasma power and with higher Ar-content and with a much higher deposition rate, was almost the opposite of layer 2 in that it had a high nitrogen content and a very low oxygen content. Layer 5 was grown with the same gas composition as layer 4, but at base plasma-power came close to the desired composition, TaON, despite its slightly too high Ta content. p_{total} = 2.5 Pa (layers 1-3), p_{total} = 3.9 Pa (layers 4-6)

samples. The second layer of the film grew with a very low rate. The mixture ratio was Ar/mix = 20/8.2 corresponding to $Ar/O_2/N_2$ = 20/0.082/8.1, but surprisingly, the composition was quite similar to what was seen in the earlier sample made with higher oxygen content (Fig. 3.7). I am convinced that this is due to the abnormally low deposition rate, where the target has time to oxidize despite the small partial pressure of oxygen. This explanation seems plausible when comparing with layer 4, which was grown with a higher argon concentration, but - more importantly - grown at a 7 times higher rate. Despite the fact that the N_2/O_2 ratio is fixed at 99 this film contains *much* more nitrogen and less oxygen - in fact the oxygen content of this film is below the target concentration (it is only 5-7%). The growth rate of this film was increased by turning up the plasma power supply (and running at a slightly higher pressure (p_{total} = 3.9 Pa)). The whole business of running the plasma at above-minimum power, however, was thought to be highly unattractive because the plasma typically became unstable

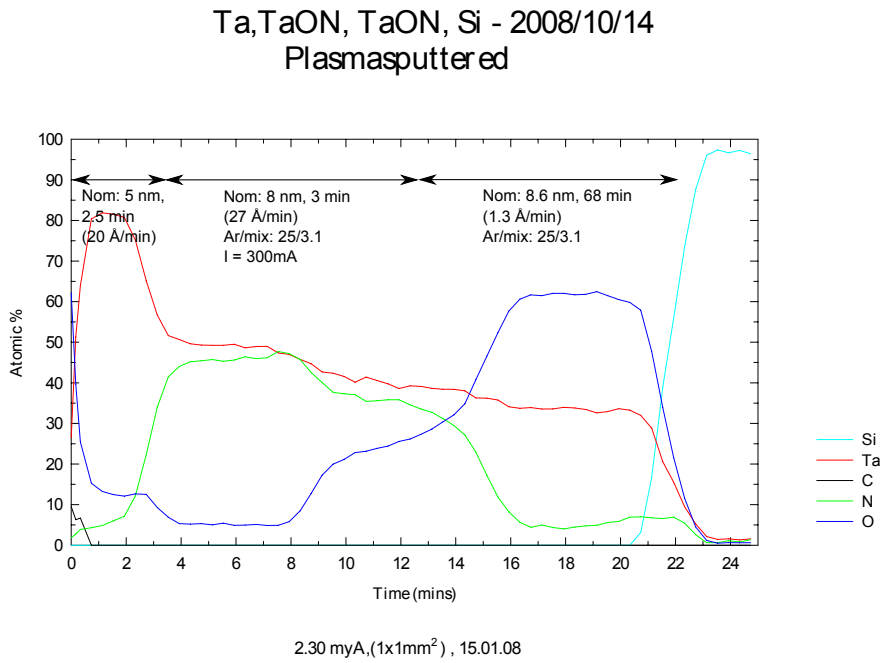

Figure 3.9: Auger-profile of a sample prepared with conditions close to those in Fig. 3.8, but with a slightly lower Ar/mix ratio in an attempt to bring down the Ta content down a bit compared to layer 5 in Fig. 3.8. The result was a miserably low deposition rate which results in a too high oxygen/nitrogen ratio in the film. Nevertheless, at a certain depth in the sample (corresponding to about 14 minutes of sputtering in the Auger-chamber) the composition is very close to being TaON, so it seems that it indeed is possible to grow TaON by reactive sputtering. $p_{total} = 3.9$ Pa

and sample-to-sample reproducibility would become worse. Layer 5 was grown with the same Ar/mix ratio as layer 4, but at the minimum-power setting. In this case the deposition rate was depressed by a factor 2 to about 5 Å/min and the resulting film gained in oxygen content as one would expect at this point. Actually, the stoichiometry of this film ($TaO_{0.5}N_{0.65}$) - quite close to the target composition - was encouraging despite the apparent sensitivity on deposition rate which was a real problem for reproducibility (there is no "knob" to control deposition rate on the Alcatel).

Essentially the same conclusions about the importance of deposition rate can be drawn from data in Fig. 3.9 where it looks like there are four films, but in reality there are only three. Layer 1 started out with a very high oxygen concentration and a *very* low deposition rate, despite it having almost exactly the same nominal parameters as in the case of layer 5 in Fig. 3.8, but it took more than an hour of sputtering at a miserable rate before the stoichiometry started changing. About at the same time I became impatient and increased the

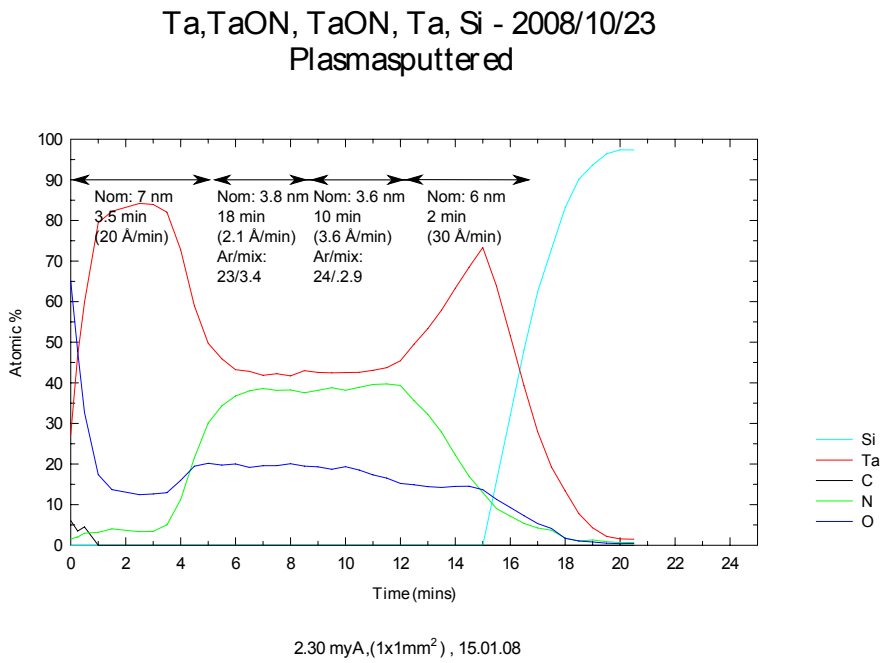

Figure 3.10: Auger-profile of another sample grown with the 1% O_2 in N_2 mix. For some reason, the sputter-profile seems "scrambled". This is most pronounced with layer 1 where the Ta-signal is mixed with the Si-signal over almost 5 minutes of sputtering. The reason for this is not clear. Layers 2 and 3 were grown with a Ar/mix ratios of 8.3 and 6.8 respectively and, as expected, the resulting deposition rate is higher than layer 5 in Fig. 3.8 (where Ar/mix was 10). In spite of this the oxygen content is lower and the N<Ta. $p_{total} = 3.9$ Pa

plasma power which eventually resulted in a too high deposition rate and too low oxygen content of the film.

The final, relevant sputter profile is seen in Fig. 3.10 which shows another attempt at growing TaON using the 1% O_2 in N_2 mixture in Ar at minimum power. Given the results in Figs. 3.8 and 3.9 it would seem that a deposition rate of about 5 Å/min gives the best results and that the Ar/mix ratio should be below 10. Two such conditions were tried with the sample shown in Fig. 3.10, but the resulting film had a surprisingly small oxygen content. The reason for this is not clear.

It is evident from the samples shown in Figs. 3.5, 3.7, 3.8, 3.9 and 3.10 (and many other other samples not shown) that gas composition certainly is not the only important parameter. Deposition rate can have a dramatic influence as evidenced by the fact that the same gas composition can give both $Ta_7O_{12}N$ and $Ta_{10}ON_9$ when the deposition rate is increased 20 times (Fig. 3.9). Apart from the many problems linked to overcoming the limitations of

the gas controller unit of the Alcatel [16], a major issue was sample-to-sample reproducibility. I think this is mostly linked to the fact that in DC-sputtering mode, the power of the plasma could not be controlled in any reliable way. Sometimes the power could be increased by increasing the sputtering voltage, but a stable plasma essentially never results. I suspect that this is due to the surface oxidation/nitridation state of the target changing (competition between the reactive gasses which passivate the target and the sputtering which cleans the target).

The plan for the project with reactive sputtering of TaON was that once stoichiometry was under control the next step would be to make a heater stage so that samples could be heated to control and promote crystallinity of the TaON film, but since stable growth of TaON with reasonable deposition rate was never achieved the plans for a heater stage remained just that. Unfortunately therefore, the technology never matured to the point were samples fit for photocurrent measurements could be produced, so it has yet to be verified whether photoanodes can indeed be made in this manner.

As an outlook for reactive sputtering, the project has convinced me that it is possible to deposit a multi-component mixture of a well defined stoichiometry (such as TaON) by reactive sputtering, but *only* with a PVD machine (with stable plasmas) where parameters (such as deposition rate and plasma power, gas composition and pressure) can be controlled with precision within a wide parameter space, where oscillations in any of these parameters are negligible and where it can be ensured that the plasma and the target have reached steady-state conditions before the sample is exposed to the plasma.

Given such a PVD chamber I think that materials like TaON could be made much more controlled and (importantly) on a much wider range of supports than what is possible with the thermal route which, given its temperatures $> 750°C$ (1023 K) and harsh environment (wet NH_3).

3.4 Photocathodes

In our group we have also been working on photocathodes for some time. In particular Billie Abrams and Yidong Hou (both Post Docs. at CINF). Our approach is based on p-type silicon in the form of wafers, since we have access to the Danchip cleanroom at DTU, which is an excellent facility for top-down processing of silicon wafers. Photoelectrodes based on silicon is an old concept and much work has already been done by other groups. Our approach has been to combine our group's experience with nano-structured molybdenum sulphide compounds as HER catalysts [49–52] with the silicon's ability to capture photons. One traditional problem with using silicon as a photoelectrode is that it forms a surface oxide (SiO_2), which is an excellent insulator and this kills the activity. This particular problem is naturally most pronounced when n-type silicon is employed as a photoanode, but it is also a problem for photocathodes since, according to the Pourbaix diagram for the Si/H_2O-system, a potential of

[16] Aside from its internal limits on maximum and minimum gas flows for the Ar, N_2 and O_2 channels the gas-controller also had a nasty habit of oscillating the gas flows - particularly when running more gasses simultaneously.

≈ -1.0 V is needed to prevent corrosion at pH = 0 and ~ -1.2 V is needed at pH = 4 [53]. The key challenge, therefore, is to find a coating for the silicon which prevents oxidation and which at the same time is a good HER catalyst.

In 2005 and 2006 the theory group at CAMd used their descriptor based approach[17] [54] for finding HER catalysts and came up with (amongst others) a new platinum-based system [55] and a PGM-free system: The Mo-edge of MoS_2. The latter may be hydrated in four steps, and while the first hydration binds too strongly according to the calculation the second hydrogen as a differential binding ΔG_{H} of $\sim$0.08 eV and therefore satisfies the criterion of $\Delta G_{\mathrm{H}} \approx 0$ [49, 56]. The inspiration source which led to the investigation of MoS_2 was nature: The reactive centers in the enzymes nitrogenase and hydrogenase are excellent HER catalysts despite that fact that they contain no PGM atoms. They contain more earth abundant elements - notably iron, molybdenum and sulphur. It was later confirmed experimentally that MoS_2 was active for HER and that activity indeed scales with the edge length (as opposed to terrace area) corroborating the computational conclusion [50, 52]. MoS_2 is by no means the only system with potential for HER/HOR activity. Going away from the dichalcogenides (MoS_2, WS_2, $MoSe_2$, (Co)Mo_2,...), of which a few were tested, there is also a family of cubanes which deserve attention.

The cubanes, generally, contain a cubic core stabilized by surrounding ligands. A cube has eight corners and so too has the core in the cubane complex. Typically, there are four corners with metal atoms[18] and four corners with non-metal atoms. The metal atoms also complex-bind organic ligands. Konrad Herbst (scientist at Haldor Topsøe A/S) has synthesized a whole range of cubanes using some of which our group recently demonstrated that cubane-type Mo_xS_y entities immobilized on electrode surfaces can have HER activity [51].

In the present work with silicon-based photocathodes we have had the most success with one particular cubane, namely a complete cubane with three molybdenum atoms, one copper atom and four sulphur atoms in the cubic core. Each molybdenum atom binds a methylcyclopentadienyl group and the copper atom binds a chloride ion [57]. The structure is seen in Fig. 3.11. We have recently filed a patent covering the use of such cubanes with p-type silicon for photocathodic hydrogen evolution [Patent application II].

3.4.1 Sample preparation and cubane deposition

As synthesized, the cubanes are dissolved in a methanol-dichloromethane mixture and from a stock solution we dilute with more solvent to the concentrations needed for deposition. The silicon we use for making samples is boron-doped (p-type) with a nominal resistivity of 2 Ωcm and polished to be (100) terminated. The choice of doping level was not based on any deep analysis. Upon immersion

[17] A necessary, but not sufficient, condition for a good hydrogen evolution/oxidation catalyst is that the change in free energy of absorption is close to zero at 0 V vs. NHE. The condition may be written as $G(\mathrm{H}_2(g) + 2^*) \approx G(2H^*) \approx G(2H^+) + 2e^- \Rightarrow \Delta G_{\mathrm{H}} \approx 0$. Therefore ΔG_{H} may be used for computational screening for potential HER and HOR catalysts - as a descriptor for activity.

[18] Cubanes with atoms in all eight corners are called complete. Incomplete cubanes have only three metal atoms and therefore one of the eight corners is unoccupied.

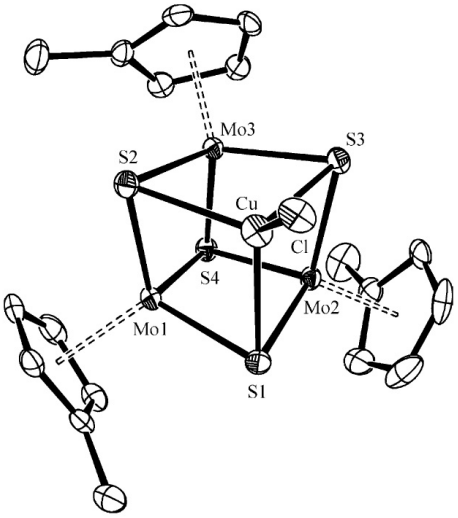

Figure 3.11: Structure of the Mo_3CuS_4 cubane. The shown entity is actually a cation with charge +1. The counter ion is *p*-toluenesulphonate. (Adapted from [57])

of the silicon in the electrolyte Fermi-level equilibration results in a space-charge layer in the silicon is formed. Usually, the ideal situation is that the effective depth of the space-charge layer (where the bands bend to aid in electron-hole separation) is matched to the penetration depth of the solar light and this depletion depth is controlled by the doping concentration. In our case the doping density (corresponding to a resistivity of 2 Ωcm (300 K)) is about 5×10^{15} (boron atoms)/cm^3 i.e., not a very high doping density. The depth of the depletion layer may be estimated [58]: $d \approx \sqrt{\frac{2\epsilon_0 \epsilon_r N_a \phi}{eN_a(N_a+N_d)}}$ where ϵ_0 and ϵ_r denote the vacuum and relative permittivity, respectively and N_a and N_d is the volumetric concentration of acceptor and donor states, e is the electron charge and ϕ is the surface potential (band bending) due to the space charge. Taking ϕ to be 0.5 V and using the relative permittivity of silicon ($\epsilon_r = 11.7$) and $N_a = 5 \times 10^{15}$ cm^{-3} $>> N_d$ I find that $d \approx 360$ nm. The question is how this compares to the penetration depth of the light.

Figure 3.12 shows data for the absorbance of silicon and the resulting limiting photocurrent under solar radiation. Given that the silicon photocathode in a silicon-based PEC device should absorb >95% of the photons up to at least 1000 nm (1.24 eV) ($\alpha \approx 100$ cm^{-1}, Fig. 3.12) the effective silicon thickness must be on the order of ∼130 μm according to Lambert-Beer's law. In other words the required thickness of silicon is orders of magnitude higher than what can be "reached" with the band bending. For this reason a high carrier lifetime which allows the minority carriers to diffuse to the space charge region would be paramount in a planar sample.

The individual samples are made by dicing wafers into 16 mm by 20 mm pieces. Electrical contact to the (backside) of the silicon is established by a

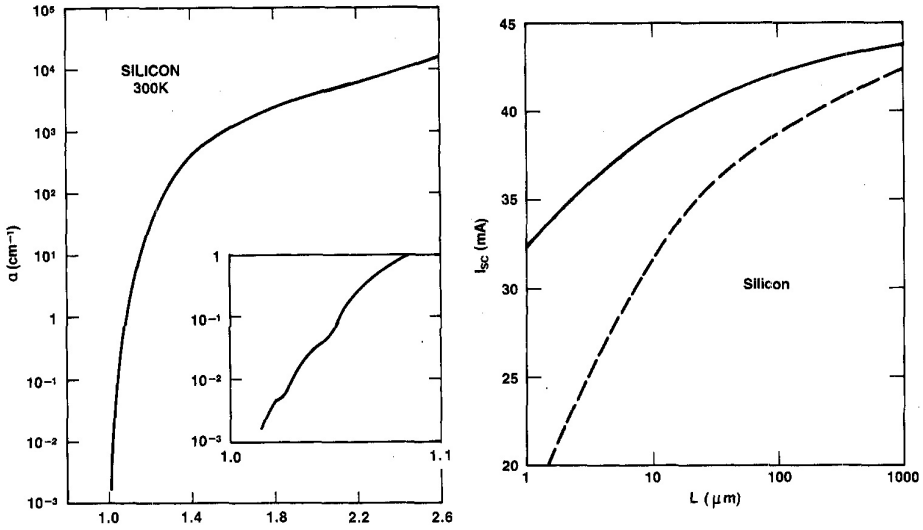

Figure 3.12: The graph on the left shows the absorption coefficient of silicon as a function of photon energy and the graph to the right shows short circuit current as a function of silicon thickness (under AM1.5G). The solid curve shows silicon with a textured surface (zero reflection losses) and the dashed curve shows silicon with a planar surface-air junction. (Adapted from [59])

variant of the procedure used in the Lewis-group [19]: A patch on the backside of the silicon sample is scratched with a diamond while exposed to an In-Ga eutectic which wets the exposed silicon. A Cu wire is then dipped in the In-Ga mixture and fastened in place with fast-drying silver paint. Mechanical stability and isolation of the contact are achieved by coating the contact in Loctite Hysol 1 C epoxy adhesive. These silicon samples are prepared for cubane deposition by sonication in an ethanol/water mixture, to remove organics, and rinsed in 18 MΩcm water. Then the sample is treated with a 1% HF solution at room temperature to remove native oxide from the surface and leave it hydrogen terminated. This monolayer of hydrogen stabilizes the surface against oxidation by air, but only for a short time. Therefore, it is important that the cubanes are deposited on the surface very soon after the HF dip before the surface re-oxidizes. We have explored various avenues for depositing the cubanes. Initially, we used simple "drop-casting" of a known volume of cubane solution of known concentration on the H-terminated silicon and flashing off the (volatile) solvent. The advantage of drop casting is good control of the total deposited amount, but the main problem with drop cast samples has been that the cubanes are unevenly distributed. Recently, we have started to electrodeposit the cubanes on the H-terminated silicon. In this electrophoretic deposition method the sample is sealed to a small PTFE (Teflon) vessel with an 8 mm O-ring so that the sample becomes the bottom of the cell. Then the cubane-solution is added to the vessel and the counter electrode introduced (we currently use the end face of a graphite rod) and a voltage is applied between the sample and the counter electrode

[19] Nathan Lewis' group at Caltech

in this two-electrode deposition cell. The experimental parameters we have varied are: Concentration of the cubane solution, deposition time and deposition voltage. We have not tried any fancy pulsed deposition techniques (only simple chronoamperometry) and we have also kept the temperature of the cell and electrolyte at room temperature. Experience so far is that for planar samples the optimum concentration of the cubane solution is between 5 and 20 μM and the optimum bias during deposition is between -5 and -15 V. Deposition time seems less important but we typically deposit for five minutes.

3.4.2 Sample testing

Electrochemical testing of the samples is carried out in the compartmentalized cell shown in Fig. 3.1. The electrolyte was 0.1 M $HClO_4$ and the counter electrode was a platinum gauze. As a reference we have used a commercial $Hg/HgSO_4$ electrode or a platinum wire in the WE-compartment since it is being bubbled with hydrogen anyway (in this manner the platinum wire is a reversible hydrogen electrode at the pH of the electrolyte (~ 1)). The working electrode was illuminated in a spot of approximately 8 mm in diameter corresponding to the spot where the cubanes were deposited. Most experiments have been carried out using a 1 kW Xe lamp filtered with a 645 nm cut-on filter so that only red (and infrared) light hits the silicon[20]. The main experiment is cyclic voltammetry in the dark and with illumination, but we also do chronoamperometry at relevant voltages to see the time-evolution of the photocurrent. Figure 3.13 shows a series of measurements on samples which were similarly prepared except that the concentration of the cubane in solution was changed. In this case there is a broad maximum in activity around 10 μM. We do not yet know what surface concentration of cubanes this corresponds to [21], but a simple calculation gives an upper estimate: The volume of cubane solution in the deposition vessel is 0.25 ml, and if the cubane concentration is 10 μM and the deposition area 0.25 cm^2 this gives an upper limit of 6×10^{15} cubanes/cm^2 - i.e., about 5 to 10 monolayers considering the size of an individual cubane. It seems, therefore, that within an order of magnitude (which could be explained by less than 100% of the cubanes being deposited) the maximum activity is associated with a monolayer of cubanes on the Si(100) surface.

Figure 3.13 also shows that there there is a (small) photocurrent associated with the applying positive potentials to the silicon sample. In this case the sample is evolving hydrogen and providing a photovoltage at the same time (energy harvesting), but the current and hence efficiency is miserable. Nathan Lewis' group have done much work on silicon photocathodes - often using platinum as the surface HER catalyst and they have measured respectable photocurrents at up to +0.3 V vs. NHE at pH 1.3 and even higher positive bias at neutral pH [60]. Our system is clearly performing much worse, but it is also free of scarce

[20] One reason why we have not used blue and green light is that in a final two-photon device, the photocathode would be series connected to a photoanode which would likely have a higher bandgap (1.8 eV to 2.2 eV). The green, blue and ultraviolet part of the spectrum should therefore be reserved for the anode - ideally in such a way that the "natural" current of the photocathode and photoanode is the same since the series-connection will force the currents to be equal and therefore they should be matched.

[21] This is currently under investigation with XPS (X-ray Photoelectron Spectroscopy), but the quantification is tricky.

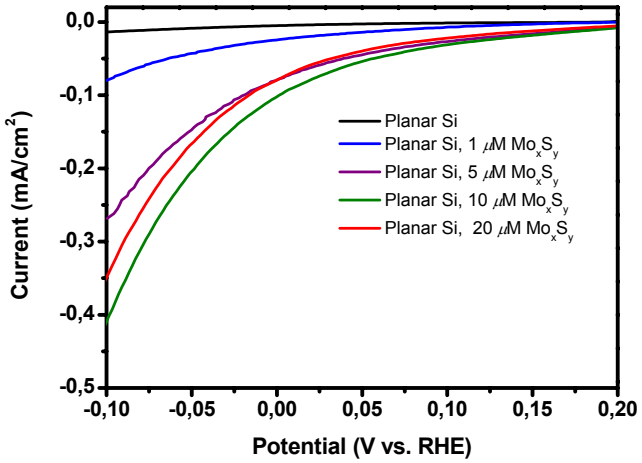

Figure 3.13: Figure showing the photocurrent as a function of the concentration of the depositing solution. Deposition in a solution with a concentration in the 5 to 20 μM range is clearly better than in the 1 μM solution, which again is clearly better than the pure solvent. Note that there is a cathodic photocurrent (albeit tiny) at slightly positive bias. Similar scans in the dark (not included) show essentially zero current on this scale. (Preliminary data)

elements and could potentially be improved greatly (one promising avenue of improvement is explored in section 3.4.4).

3.4.3 Stability

The stability of the cubane coated samples is surprisingly good. Since the oxidation of silicon is strongly downhill in energy [22] the expectation was that an electrode left in air would quickly oxidize (perhaps under the cubane layer) and become inactive. Indeed samples with *very* low loading of cubanes de-activate in air. The rate of deactivation is currently being investigated, but stability is higher than it is for plain, H-terminated samples. Drop cast samples with a high loading of cubanes can maintain activity for weeks in air, but on the other hand their activity is one order of magnitude worse than a freshly prepared low-loading sample (electrophoretically deposited). Under HER conditions (i.e., hydrogen atmosphere and a potential of ∼0 V) cubane coated samples are stable - even with those with a low loadings and high activity. Conversely, under HER conditions the (much less active) H-terminated samples quickly deactivate.

3.4.4 Structured samples

While the result, viz. that cubane treatment of the planar silicon surface can improve photocatalytic hydrogen evolution currents manyfold and that activity does not quickly degrade, is encouraging the measured photocurrents are orders of magnitude below a reasonable target of a finished two-junction device. A

[22] $Si + O_2 \rightarrow SiO_2, \Delta G^{\ominus} = -850.7$ kJ/mol= 8.82 eV

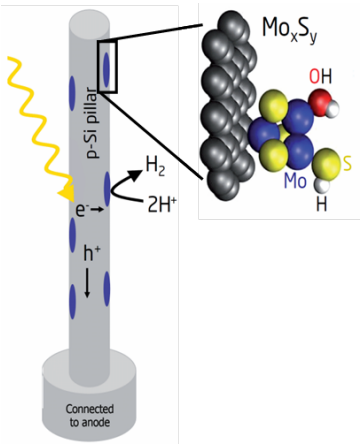

Figure 3.14: Schematic representation of one orthogonalization concept. Absorption of light may occur in the length axis of the silicon rods and so does majority carrier transport. Minority carriers, on the other hand, transfer radially in the rods to the surface which is coated with cubanes.

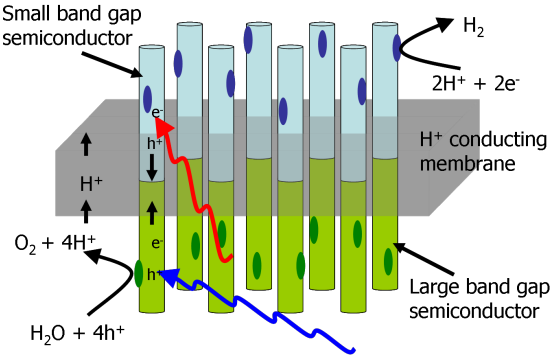

Figure 3.15: The "dream-device". A photocathode and a photoanode (matched to yield similar photocurrents under solar illumination) sit on either side of ion-conducting membrane (e.g., H^+ conducting). The photoelectrodes operate with no external (electrical) bias so they must (together) provide enough potential to drive the water splitting reaction (including overpotentials). The ion-conducting membrane serves to provide physical separation of hydrogen and oxygen products. (Nathan Lewis, 'Helios' concept)

reasonable minimum overall current for a practical water splitting device under AM1.5 illumination is perhaps 5 mA/cm^2 (corresponding to 23 l H_2/m^{2}h). Indeed, studying Fig. 1.2 reveals that a silicon photocathode absorbing all photons where $\sim 680 < \lambda < \sim 1000$ nm in conjunction with a photoanode absorbing all photons where $\sim 400 < \lambda < \sim 660$ nm ($E_g \approx 1.75$ eV), could in principle deliver almost 38 mA/cm^2 if we disregard the unavoidable black-body and Auger recombination losses [59]. Including these losses brings this figure down to perhaps 60% i.e., about 22 mA/cm^2. Currents approaching these values could naturally never be realized in a practical cheap PEC device, but it sets the benchmark against which to compare a given technology. Clearly, a photocathodic current of less than 0.5 mA/cm^2 at the reversible hydrogen potential (Fig. 3.13) is nothing to get overly excited about, even if it doesn't include platinum and is stable.

The obvious thing to try to in order to improve the photocurrent is to "orthogonalize" the system. This means to structure the surface in such a way that light absorption occurs in one direction (orthogonal to the photoelectrode), as in the case of the planar sample, yet allow the electrochemistry to take place in depth in the system. Such a concept, based on silicon pillars, is shown in Fig. 3.14. The

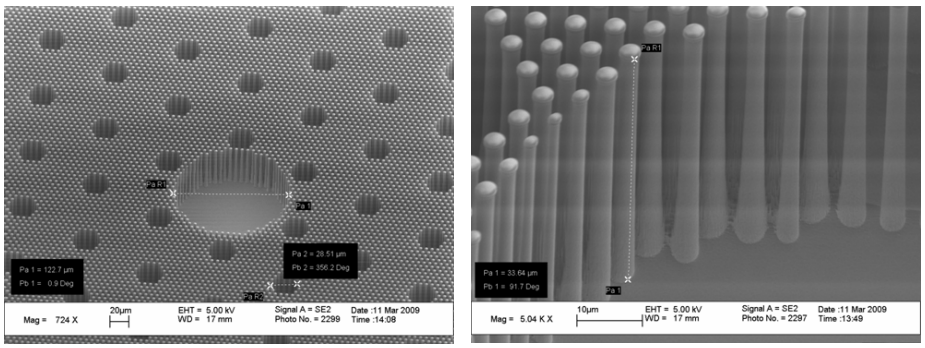

Figure 3.16: Low resolution and medium resolution SEM micrographs of the silicon pillars (made by Christian Damsgård, Post Doc. at DTU Nanotech). The current design features rods that are 40 μm in length and about 3 to 4 μm in diameter and placed in a hexagonal lattice with a lattice constant of about 6 μm. This configuration is almost certainly not optimized, but nevertheless the enhancement in photocurrent over planar samples is considerable.

main advantages of orthogonalization are that the minority carriers must only transfer a distance of about the radius of the pillars, as opposed to the characteristic penetration depth of light, which may be orders of magnitude higher, and that the total surface area available for (potentially sluggish) electrocatalysis can be increased many times [23]. Fig. 3.15 is a conceptual illustration of a two-photon water-spiltting PEC device with an (ion conducting) membrane separating the photoanode from the photocathode so that O_2 and H_2 products are physically separated. Figure 3.16 shows some SEM micrographs of our current structured silicon cathodes. These structures were defined by conventional photolithography and etched using an advanced dry-etch process - i.e., a top down process. The structures are not optimized at all. It is just a proof-of-concept to confirm that photocurrent may be increased by orthogonalization. A comparison between the photocurrent may be seen in Fig. 3.17. At the reversible potential the figure shows that the photocurrent of the sample with pillars and cubane coating is about 1.5 mA, which is some 200 times higher than planer, H-terminated samples. The pillared, cubane-coated sample exhibits cathodic photocurrent at applied bias of up to +150 mV (not fantastic, but not bad either - considering that the system contains no platinum group metals). Another interesting thing to note in Fig. 3.17 is that the H-terminated, but pillared sample has almost 50 times higher photocurrent at the reversible potential than the planar sample despite the fact, that the increase in geometric area is only $\sim$ 6 times. The other 8 times enhancement is probably due to lower recombination losses and

[23] In the orthogonal configuration it becomes more realistic to achieve the "ideal" doping density. Namely if the doping density is chosen so that the the band bending depth (depletion depth) corresponds to (slightly less than) the radius of the pillars then the charge separation in the pillars should be most effective. And if the pillars must be $\sim$130 μm long to absorb the red light and if they are structurally sound with an aspect ratio of 100, i.e., they must be 1 μm in diameter, then the doping level should be chosen to correspond to a depletion thickness of $\sim$600 nm, which is very reasonable and close to the currently used doping density.

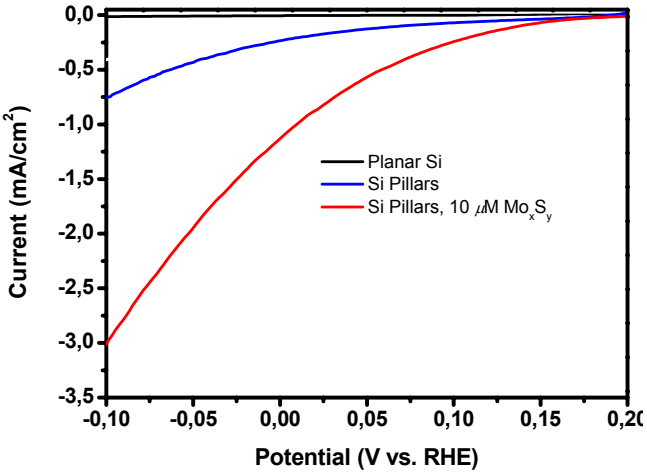

Figure 3.17: Comparison between photocurrents of planer (H-terminated) silicon, silicon with pillars like Fig. 3.16 and silicon pillars coated with cubanes. The latter sample shows a very respectable current (on the order of 1.5 mA) at the reversible potential and cathodic current extends up to almost + 150 mV. The H-terminated, but pillared sample also has a significant photocurrent. (preliminary data)

lower optical reflection losses in the pillared structure, which shows how much geometry matters.

The photocathode project has only recently obtained a high-priority status and therefore most of the experiments that are "obvious" to do have not yet been carried out. We are still in the process of evaluating techniques for characterizing the surface of samples. For example, we are optimistic that the XPS will be able give us quantitative information about coverage and qualitative information about oxidation states (of the metal atoms and chalcogen atoms in the surface coating), but other spectroscopic techniques like ISS, AES (Ion Scattering Spectroscopy and Auger Electron Spectroscopy) may also prove useful. Microscopic techniques like TEM or STM (Transmission Electron Microscopy and Scanning Tunnelling Microscopy) could perhaps also yield information. The XPS data which we have so far has been puzzling. While high-loading (drop cast) samples show large Mo, Cu and S signals with the right Mo/Cu ratio (3), the low-loading, electrophoretically loaded samples (the most active ones) show *emph* very small Mo-signals and the Mo/Cu ratio is also far below the nominal value. As a double check, we have depostied pure Cu using our electrophoretic method (from solutions of $CuCl_2$ in the same solvent that we use for the cubanes), but these samples are vastly inferior to the ones prepared from the cubane solution so, as expected, Cu alone does not work. In any case, the most pressing issue with this project is to find out why the cubanes work in the first place and what gives rise to the apparent stability of the samples. With an understanding of these fundamental questions we should be able to go about optimizations of the system in a more rational way.

Chapter 4

μ-reactors

4.1 Background

At DTU physics (ICAT/CINF) there has been an ongoing μ-reactor project for many years. The term μ-reactor, in this context, covers a chemical reactor with dimensions in the μm range. The small dimensions offer a number of advantages for catalyst characterization as compared to conventional macroscopic reactors such as tubular plug-flow reactors. One advantage to measuring catalytic activity in μ-reactors is that the small dimensions give high temperature uniformity (even when highly endothermic or exothermic reactions are studied, because of the high surface-to-volume ratio) and what's more temperature may be changed quickly and precisely. Heaters and thermometers can also be incorporated directly into the structure using MEMS techniques. A μ-reactor may also be designed to keep concentration gradients small and well-defined, which makes extraction of kinetic data easier.

In our group, the approach to μ-reactors has been to use standard clean-room techniques (notably UV-lithography, wet etching and Reactive Ion Etching (RIE)) to define flow channels, reactor chamber and gas interfacing holes in silicon wafers with 16 μ-reactors on each 4 inch wafer. Our μ-reactors, therefore, are made of silicon and catalytic passivation is achieved by a thin layer of thermally grown oxide as the last processing step.

The state of the art in the group in 2006 - the "old" design (Fig. 4.1) - was a "sniffer" design meaning that the entire main flow went through the reactor, but only a very small fraction of this flow (controlled by the sniffer) was led to the QMS (Quadropole Mass Spectrometer) for detection. Jakob Lind Olsen, Toke Riishøj Henriksen and I started our PhD work at about the same time. Toke's project was to develop and manufacture a new generation of μ-reactors with much improved sensitivity, and Jakob's project was to test these and use them for measuring heterogeneous catalysis. My involvement in the μ-reactor project started almost a year later [1]. By that time the first version of the new

[1] During the first year of my PhD I was mainly occupied with the electrolytic ammonia project (chapter 6) and with thermal treatment of tantalum and photoanodes in general (chapter 3)

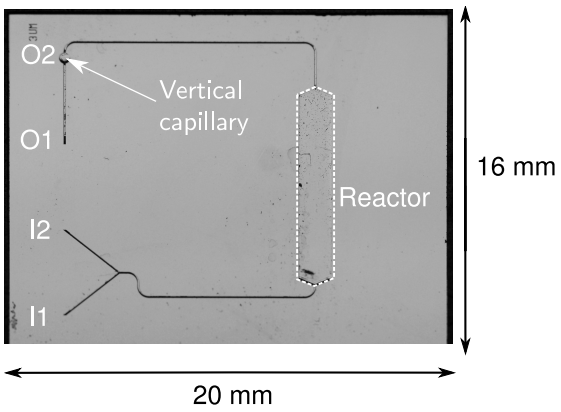

Figure 4.1: The "old" μ-reactor design. The design has a relatively large reactor volume (4.05 μl) and a "sniffer" design where all the gas from the MFCs goes through the reactor, but only a tiny fraction is diverted into the QMS for detection. Gas is let in via I1 and I2 and out via O1 and O2. O1 leads the main flow to a pressure controller and O2 leads gas from the reactor to the mass spectrometer for detection.

generation of μ-reactors was ready for testing. For (mostly) historical reasons, Jakob decided to use CO-oxidation over platinum as the test reaction. In parallel, it was decided to also try photocatalytic CO oxidation - after all the new reactors had a transparent (see Fig. 4.2) pyrex lid and a large frontal reactor area (1 cm in diameter) - well suited for illumination. This potential usefulness for photocatalysis was the reason why I got involved in the μ-reactor project.

4.2 Overview of the μ-reactors

The current version of the μ-reactor is seen in Fig. 4.3. There are two inlets (I1 and I2) and two outlets (O1 and O2) through which the μ-reactor exchanges gas with the outside world (through a gas-interface manifold) and apart from these four holes the μ-reactor is sealed with a pyrex lid. The photograph in Fig. 4.3 shows a bonded μ-reator i.e., the structures are seen through the pyrex lid. After gas enters the μ-reactor, via the inlets, the two gas streams are mixed by diffusion in the meandering structure. Then the (main) flow goes to the outlet (O1), and a small flow of the mixed gas is diverted through the circular reactor chamber and ultimately to the QMS via the flow-restricting capillary seen immediately in front of the outlet to the QMS. The main-flow channels, i.e., the two inlets, the mixing structure and the first outlet channel, are etched ~300 μm deep to minimize pressure losses. The main flow can be more than 20 sccm [2] and this makes regular mass flow controllers (MFCs) useful for mixing the reactant gas from pure component gasses. The reactor chamber and the QMS-outlet (O2) channel and capillary are only etched 3 μm deep. This keeps the reactor volume down to 240 nl (which makes the time constant for gas in the reactor chamber shorter) and is highly important for cooled-bonding (see

[2] Standard Cubic Centimeters per Minute

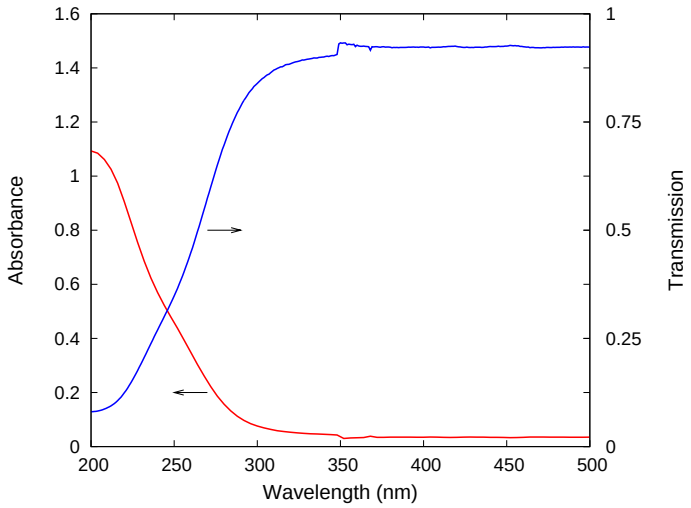

Figure 4.2: Measured absorbance (and corresponding transmission) of the pyrex lids used to seal the μ-reactors as a function of wavelength. Above ∼330 nm the transmission is nearly constant at ∼92%. 50% transmission occurs at 264 nm and 10% transmission occurs at 215 nm so experiments well below 300 nm are possible (although a correction for pyrex absorption must be made in that case).

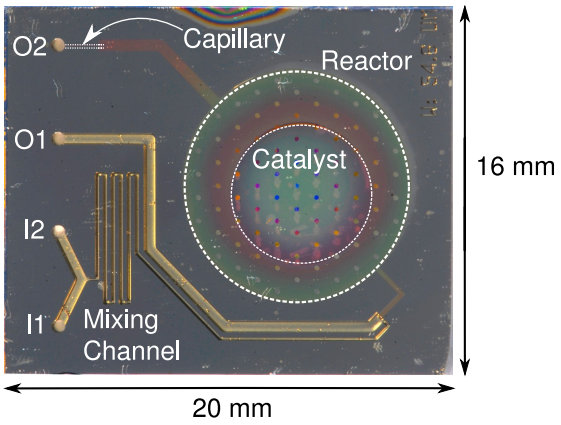

Figure 4.3: Top view of the μ-reactor (new design) where main parts are indicated. I1, I2, O1, and O2 mean the same as in Fig. 4.1. The reactor chamber has a volume of 240 nl.

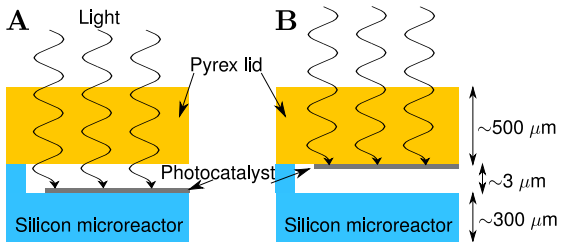

Figure 4.4: Partial cross sections of two different μ-reactors loaded in two different ways and a photograph of a μ-reactor. Sketch A shows that when photocatalyst is deposited on the silicon reactor the illumination is frontal - i.e. light is incident from the same side as the reactants - while sketch B shows that photocatalyst deposited on the Pyrex lid (as in the examples in this paper) is effectively illuminated from behind.

section: 4.4). Finally, two different capillary widths are available: 54.5 μm for large reactor flows and 5.6 μm for small reactor flows. The former is useful for experiments where fast time-response is required or when turnover becomes too high with the narrow capillary. Conversely, the narrow capillary chips are useful when turnover is lower, or when catalytic experiments at elevated pressures are carried out, to avoid excessive gas flow into the QMS.

Figure 4.4 illustrates the two principal ways in which photocatalyst may be loaded into the μ-reactor. If the photocatalyst is deposited on the bottom of the reactor chamber, illumination is frontal in the sense that reactants and light reach the photocatalyst from the same side. On the other hand, if the photocatalyst is deposited on the lid, then illumination is from behind - i.e., reactants and light reach opposite sides of the catalytic layer. To date, most experiments have been carried out with the photocatalyst on the lid (back illumination). The main reason for this is that the transparency of the pyrex lid makes it possible to carry out UV-VIS absorbance measurements on the photocatalytic film in transmission mode using a spectrophotometer. In general, this way of measuring absorption of the catalyst is far more convenient (but not necessarily more accurate) than diffuse reflectance using an integrating sphere, which is necessary for non-transparent samples (such as the μ-reactor).

4.3 Early experiments

The first photocatalytic experiment we tried with the new μ-reactors was CO-oxidation. This is (at least in principle) a very simple reaction involving only two elements: $CO(g) + O_2(g) \rightarrow CO_2(g)$. Initial experiments were with Degussa P25 photocatalyst [3], to make sure we were using an effective catalyst. As it turned out, the CO-oxidation over P25 experiment worked in the first try! Figure

[3] Today, Degussa is called Evonik, and their venerable P25 catalyst is now called "Aeroxide®TiO_2 P 25". It is a nanopowder of TiO_2 of BET surface area 50 ± 15 m^2/g, average (primary) particle size is 21 nm, tapped density is 130 g/l. The crystalline phases in "P25" are often claimed to be anatase and rutile and their ratio often quoted as 4:1 (from X-ray diffraction quantification), but recently, physical isolation of the phases indicate that there is also an amorphous phase and that the ratio is 78:14:8 (anatase:rutile:amorphous) [61].

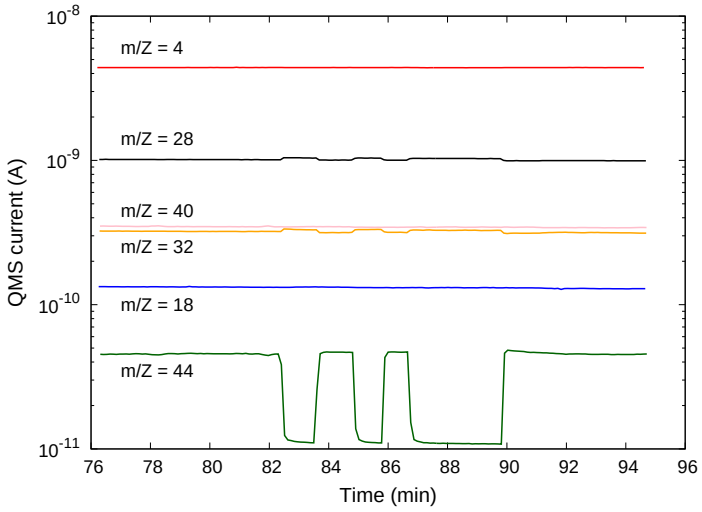

Figure 4.5: One of the first measurements of photooxidation of CO over P25. The reactant gas is a premix of He (90%), CO(5.0%), O_2 (2.5%) and Ar (2.5%) and the light source is a small, 4 W Hg-lamp. The light is on to begin with, but turned off briefly at times 82.2 min, 84.6 min and 86.6 min. Clear response in CO_2 and CO and O_2 may be seen. The finite CO_2 signal when the light is off is due to CO-oxidation on the QMS filament.

4.5 shows an early experiment of photooxidizing CO in a μ-reactor over P25 catalyst. In this case, the reactant was a premix with 90% and only 5% CO and the light source was not very intense (1.75 mW/cm^2 between 310 and 390 nm). The reason why CO_2 only drops a factor of five or so when the light is turned off, is that it cannot drop below the background level, which is due to CO and O_2 reacting on the filament of the QMS - it is *not* due to dark reaction (as confirmed by various experiments including comparison with empty μ-reactors, heating of TiO_2-loaded μ-reactors etc.). After the first experiments with P25 in the μ-reactors it was realized that μ-reactors are an almost ideal platform for testing small thin-films of photocatalyst - at least for gas-phase reactions.

In parallel with the early photocatalytic experiments, Jakob and I did a rather thorough study of thermal CO-oxidation over small platinum circles (deposited on the inside of the pyrex lids) in an attempt to find the practical detection limits of the system for thermal catalytic experiments [4]. We demonstrated that catalytic CO-oxidation at only 300°C (573 K) could be observed for polycrystalline platinum films with areas down to 15 μm^2 (much lower catalyst area than reported for other high-sensitivity reactors [62, 63]). The catalytic results were published along with a detailed description of the μ-reactor and its fabrication

[4] Experiments where temperature is scanned inherently have worse detection limits for catalytic turnover than isothermal photo-experiments. The reason is that the conductance of the reactor-capillary system changes with temperature meaning that all signals measured in the QMS change with temperature (even with an empty reactor with zero turnover), but since the "memory" of the QMS is not the same for all gasses it is not always trivial to subtract non-constant background signals when looking for a small catalytic contribution to a signal.

and with calculations and measurements of the capillary flow as the first paper published by the current μ-reactor group [Paper II].

The experiments with thermal CO-oxidation also led to several technological developments of the μ-reactor experimental platform including a complete re-design of the gas interface manifold (to a UHV-style (Ultra High Vacuum) welded stainless steel construction with "VCR" connectors), a fixture for holding the four O-rings which seal to the μ-reactor (I1, I2, O1 and O2), (fixing the O-rings to avoid uneven-compression and over-compression when mounting a μ-reactor), an auxiliary manifold for argon blanketing of the O-rings (to avoid diffusion of O_2 and N_2 through the O-rings, which would otherwise detrimentally affect signals at m/Z = 14, 16, 28 and 32, particularly when the μ-reactor is heated), μ-reactor lids with integrated thermometers (RTDs) and - not least - locally cooled bonding (section 4.4). We also switched from Viton to Kelrez as the O-ring material because of Kelrez' superior high-temperature stability [5]. All these developments significantly improved the versatility of the system as a whole, although (with the exception of "cold-bonding" and the improved gas interface manifold) they are not really critical for photocatalytic experiments since these typically are carried out at room temperature.

4.4 Anodic bonding

A critical aspect of the entire μ-reactor technology used in our group is the ability to make all the necessary flow-structures with photolithography combined with chemical and physical etching processes in silicon (standard MEMS techniques) and then seal the entire structure including the reactor chamber after loading the catalyst with a "lid" of some kind. This lid must provide a hermetic seal and be capable of withstanding elevated temperatures and potentially aggressive gasses without mechanical failure or contamination of the catalyst. For photocatalysis it must also be transparent in the relevant wavelength range. These demands led to the use of a technique known as "anodic bonding" or "Mallory bonding" (so-named after the company where it was invented in the late 1960's) [64]. Anodic bonding can be used to bond two materials together with electrostatic attraction, and for many materials combinations also covalent bonds. One material must be electrically conductive while the other must be an ionic conductor at elevated temperature. The materials are cleaned and placed in intimate contact. Then they are heated (high enough for ionic conductivity) and a large negative voltage is applied to the ionic conductor. This causes ions to migrate and the resulting internal field forces the two materials together. The electrostatic contact pressure can be very large (GPa range [65, 66]) if the distance is small enough i.e., if the contacting surfaces are smooth and free of dust and dirt. Chemical bonds between the two materials generally form so the bond is permanent, also when external high-tension and heating are removed. Many materials may be bonded by this method, but a major restriction of course is that the two materials must have a reasonable match of thermal expansion coefficients. The material combination which has seen most use is the silicon-glass system [65]. In our case

[5] Kelrez was chosen despite its *much* higher price and its (in our experience) higher diffusion-leak rates for oxygen, since argon-blanketing of the O-rings eliminates the problem anyway.

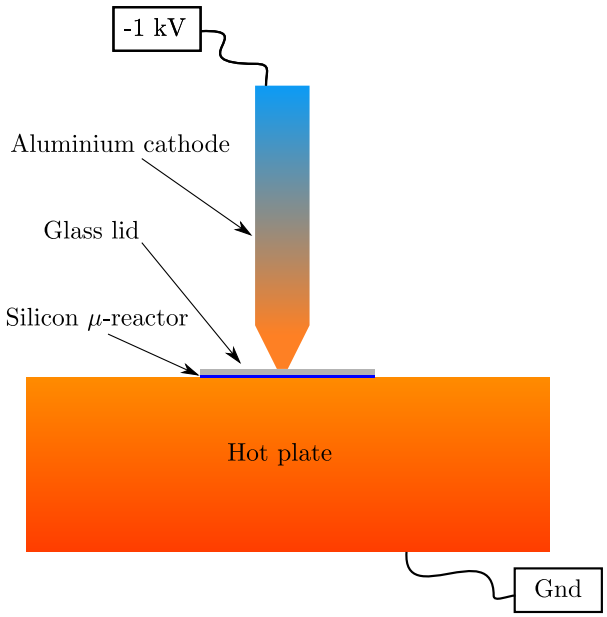

Figure 4.6: Basic setup for "hot bonding". The silicon chip is lying on a grounded hotplate with the pyrex lid on top. A high-tension cathode is touching the glass from the above while the hotplate heats from below.

we bond silicon (chips with flow channels) with thin pyrex lids to complete the μ-reactor. The most mobile cation in pyrex is Na^+, but to achieve reasonable mobility it must be heated to at least 300°C (573 K)) and preferably 350°C (623 K), in our experience.

The conventional approach to bonding (which was used by us) is to place the stack consisting of the chip with the lid on top on a hotplate and touch the lid with a long, thin high-tension cathode. Figure 4.6 shows a sketch of this "hot-bonding" arrangement. This setup is very easy to operate and it has the advantage that one visually may see how bonding progresses (the bonded area is clearly distinguishable from un-bonded areas - see Fig. 4.7). The hot bonding method has obvious appeal in its simplicity and robustness and for years it was the only approach taken to seal (previous designs of) μ-reactors in our group. This is in spite of the fact that nanoparticulate gold catalysts (notorious for sintering) have been studied. For this purpose, therefore, sealing had to be done using elastomeric (Viton) membranes and other troublesome techniques - basically due to the lack of a room-temperature sealing technique.

4.4.1 The need for cold-bonding

After quite a few μ-reactors had been bonded both with TiO_2 nanotubes (chapter 2), nitrogen-doped TiO_2 nanotubes, as well as with TiO_2 films made by reactive sputtering, it was realized that results for photocatalytic activity were surprisingly un-reproducible. Samples that were similarly prepared would not always lead to

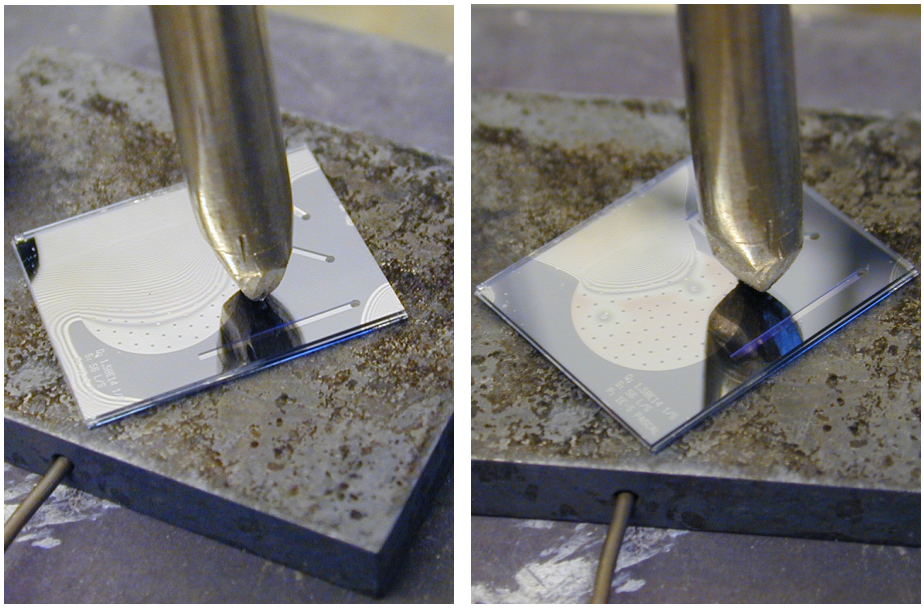

Figure 4.7: Photographs from a typical "hot bonding" procedure. The first picture shows the stack after a short time where less than half of the lid has bonded and the second picture (taken later) shows the bonding process nearing completion. Notice how clearly the 3 μm-deep flow structures are visible in the bonded areas and the "Newton rings" visible outside the bonded areas.

μ-reactors of similar photocatalytic performance - not even to within a factor of 2. After some time we came to suspect that the anodic bonding process, which, at the time, was not carried out as a standardized procedure, could be the reason for the lack of reproducibility.

4.4.2 Locally-cooled anodic bonding

In an attempt to minimize the thermal budget of the catalyst in the reactor chamber of the chip, I had the idea that it might be possible to keep the central part of the reactor lid cool while heating the rest of the "sandwich" to a sufficiently high temperature to complete the anodic bonding. The trick would be to apply intense heat from the glass-lid side, while touching the central part (reactor) with a "cold finger" on the Si-side taking advantage of the enormous difference in thermal conductivity of silicon and pyrex. Actually, in terms of heat flow, this is an inversion of the regular hot-bonding technique, where heat flows from the silicon to the glass. For practical implementation of the heated cathode scheme the idea was to use cheap, commercial quartz-halogen lamps serving a heating elements embedded in drilled holes in a top electrode (made from aluminium) since quartz (unlike glass!) remains non-conductive up to *very* high temperatures. The latter is necessary since it is far more practical to have the glass at high voltage and the cold finger grounded than vice versa, because of the hassle of maintaining the liquid circulating coolant at high voltage!

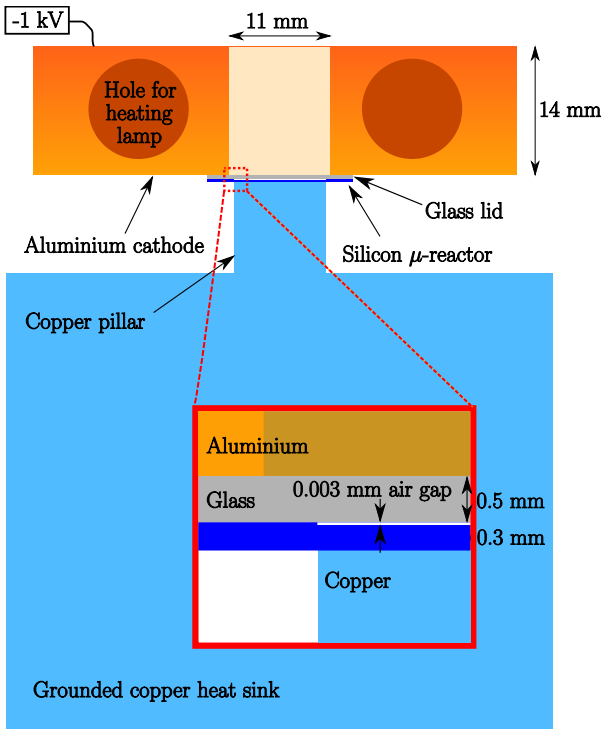

Figure 4.8: Cross-section of the current incarnation of the setup for locally cooled bonding. The silicon chip is supported on a grounded "cold finger" made of copper (using heat-sink paste) so that (only) the reactor area touches the copper. The lid is placed on top of the reactor and with the heated aluminium cathode on top. The entire glass surface except the reactor area is in contact with the aluminium.

The scheme could potentially work because of the radial symmetry of the cooled area (making frozen-in thermal stress a smaller problem due to the lack of stress-concentrating corners) and because of the large XY dimensions of the structure (mm) compared to the very shallow reactor chamber (μm). In effect, the heat-flow outside the cooled region is axial in the pyrex and radial in the silicon (within the cooled region it is opposite). A schematic (of the present incarnation) of the system is seen in Fig. 4.8 and as a photograph in Fig. 4.9. Currently, we heat the cathode to about 475°C (748 K) using two 150 W halogen lamps (Osram). At the same time, we keep the copper support cooled by flowing cooling liquid (ethanol-water mixture) through the copper support. If the cooling fluid is kept at about 0°C (273 K) it results in the copper block being about 10°C (283 K) which, in turn, means that the tip of the cold finger is about 40°C (313 K) (at a typical heat flow of the order of 200 W). The result is that the center of the μ-reactor is below 50°C (323 K). This has been verified by steady-state heat calculations; both numerical (Finite Element Analysis) (Figs. 4.10 and 4.12) and analytical calculations on a "simplified" geometry ([Paper III]) and even measured experimentally using a four-point RTD measurement (Fig.

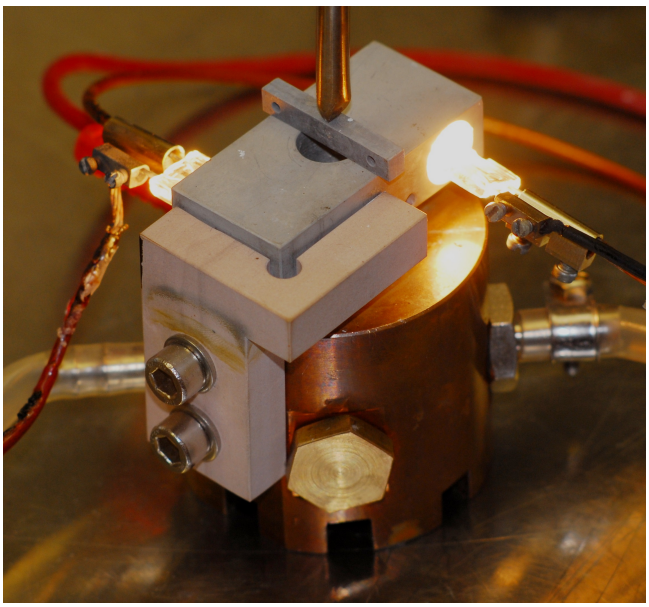

Figure 4.9: Photograph of the current "cooled-bonding" setup in action. Temperature of the aluminium cathode is controlled by the voltage drop over the two (series connected) quartz lamps (normally 18 V). To facilitate alignment of the cathode exactly over the cold finger, a support (stop) is mounted on the Cu-block, and the cathode rests against it. This stop must be able to withstand the heat from direct contact with the cathode and insulate against the high tension, and it is therefore machined from a piece of ceramic (Macor). There is condensation on the plastic tubing, which supplies the Cu-block with coolant fluid. Once bonding is over, it is important to remember to turn off the coolant flow because otherwise the Cu-block will become as cold as the fluid, and the whole setup becomes a wet mess due to condensation.

4.11). For the measurement we used our standard RTD μ-reactor lids, which incorporate a 100 nm thick platinum 4-terminal resistor structure, and contact pads for making the four connections, as detailed in [Paper II]. For measuring the temperature inside the μ-reactor during bonding, we turned the lid "upside down" so the Pt RTD was inside the μ-reactor. As a result, the measured RTD temperature corresponds to the temperature inside the reactor. The temperature of the aluminium top cathode was also recorded using a K-type thermocouple. The measurements are plotted in Fig. 4.11 and the (FEA) calculated temperature as a function of radius inside the reactor chamber is shown in Fig. 4.12. It is seen that the cathode stabilizes at ~475°C (748 K) while the RTD temperature inside the reactor only reaches 45°C (318 K). The agreement with the FEA calculation is very good.

After the method became operational I carried out an experiment where I loaded a μ-reactor with P25 by spin-coating a slurry onto the pyrex lid. The lid was then bonded to a chip using this method with local cooling of the

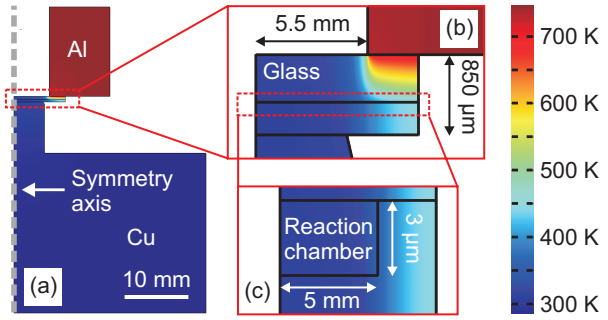

Figure 4.10: Geometry and colour plot of the calculated steady state temperature distribution from the FEA made by Toke. The geometry is an axially symmetric approximation to the real cooled-bonding setup. (a) The entire geometry with equal scale on both coordinate axes. The vertical, dashed, grey line signifies the symmetry axis. The silicon and the glass chip are stacked between the aluminum cathode and the copper heat sink. (b) Magnification of the silicon and glass chip. A high temperature gradient is observed in the part of the Pyrex lid outside the reaction chamber. (c) Magnification of the reaction chamber. The temperature in the chamber is seen to be close to room temperature as a result of the cooled bonding fixture. Note that in (b) and (c) the scaling of the x-axis and the y-axis is different.

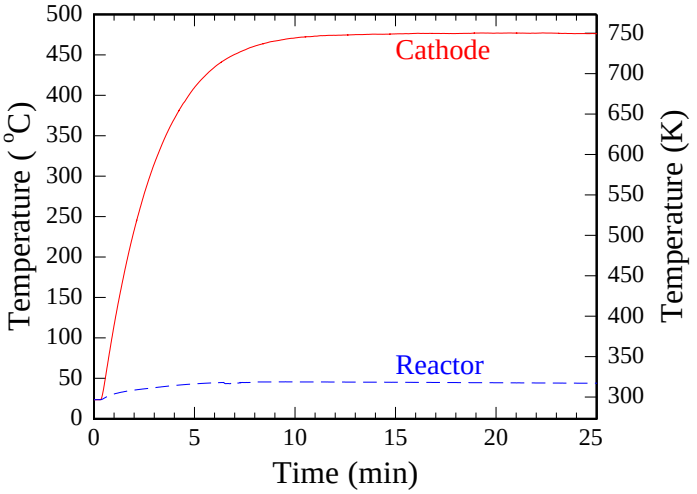

Figure 4.11: Thermocouple measurement of the aluminium cathode temperature (full red curve) and RTD measurement of the reactor chamber temperature (blue dashed curve). The RTD temperature measures the temperature on the pyrex surface (inside the reactor) and the platinum structure probes the central ∼3 mm of the reactor area.

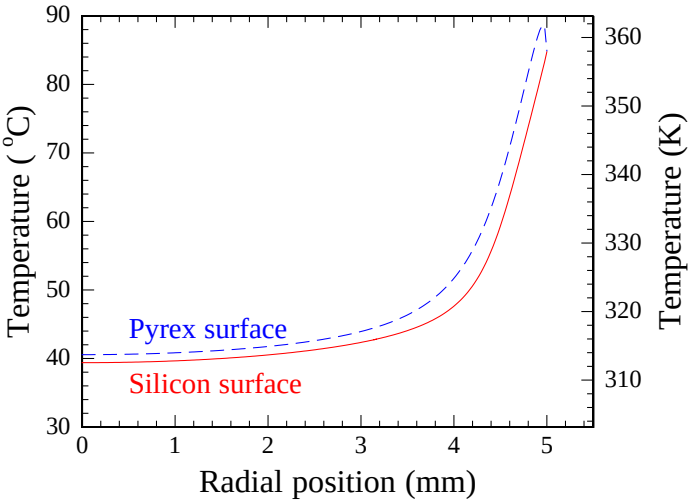

Figure 4.12: Steady-state temperature distribution in the reaction chamber as computed in the FEA. The temperature in the chamber as a function of radial position is shown. The radial position is the distance from the center axis of the chamber (the symmetry axis). In the plot, the temperature in the top of the chamber adjacent to the Pyrex is shown (blue dashed curve) as well as the temperature in the bottom of the chamber adjacent to the silicon (red full curve).

reactor area (and catalyst) and the μ-reactor measured the activity. Then I hot-bonded the sample [6] in the conventional way (i.e., heated it to ∼330°C (603 K) while applying −1 kV to the lid) and remeasure its activity. The hot bonding procedure had led to ∼5x loss in activity! Then, I exposed the μ-rector to air over a weekend and re-tested it. Activity had recovered up to about 80% of its original (cold-bonded) level. Normally, the reproducibility of repeated measurements on the same μ-reactors is very good, so this behavior is highly unusual. One would think that an oxide-catalyst, such as P25, would withstand ∼330°C (603 K) for extended periods without ill-effect (considering that P25 is produced at *much* higher temperatures). Possibly the electrical bias plays a role - e.g., by somehow driving contaminants onto the TiO_2 surface? However, time was not invested in repeating this experiment (or the corresponding experiment with heating, but without applying high tension after cold-bonding and initial testing) and we still do not have a clear understanding of how and why hot-bonding affects P25 (or similar) photocatalyst. We just decided to be pragmatic and make it standard procedure to cold-bond photocatalyst μ-reactors.

In conclusion, the bonding method with local cooling has the disadvantages of being slightly more cumbersome and have a slightly lower lower success rate compared to conventional hot bonding, but for sensitive catalysts it is a necessary procedure to follow.

[6] Of course, the sample was already bonded by the cold-procedure, but I carried out the hot-bonding as if it weren't.

4.5 Liquid-phase reactions in μ-reactors

This section gives a brief overview of a pet project of mine which, however, has not yet matured beyond concepts and test structures.

4.5.1 Motivation

As discussed in section 3.1, the best way to show that observed current corresponds to a given electrocatalytic or photoelectrocatalytic reaction (not to side reactions or worse - to corrosion) is to collect and analyze products. However, the traditional approach is either to use a macroscopic cell (similar to our two-component cell, Fig. 3.1) with a highly sensitive measurement technique or to place a capillary "sniffer" as close to the electrode surface as possible and then use e.g., a mass spectrometer to analyze the substances (electrolyte, reactants and products) caught by the sniffer. The first option has the disadvantage that the macroscopic size of the cell severely limits sensitivity, unless high currents ($\sim$mA) can be achieved. The main disadvantage of the second approach is that the sniffer only probes the products - it cannot quantify these products since only a small fraction is captured.

If, on the other hand, it were possible to carry out the (photo)electrocatalytic experiments in a structure like our μ-reactors then the fact that any molecule in the reactor-area of the chip eventually enters the QMS will give built-in quantification of (volatile) components. Of course this means that the "wet" μ-reactors must include provisions for introducing electrolyte and also at least two electrodes (of which one could be a photoelectrode) and preferably also a third (reference) electrode.

4.5.2 Wet μ-reactor design

No reports were found in the literature about electrocatalysis or photoelectrocatalysis in reactors resembling our μ-reactors. Undeterred, some preliminary feasibility experiments were carried out using the existing μ-reactors with a few minor modifications:

1. A through-hole was added in the center of the reactor. The purpose of this was to provide an inlet for electrolyte.

2. The reactor was coated with a hydrophobic fluorosilane (FDTS [7]) layer, except for a circular area of 8 mm in diameter in the center of the reactor area.

3. Pyrex lids were prepared with 50 nm thick platinum electrodes and these were also coated with FDTS, expect in a circular area corresponding to the un-coated area on the reactor.

The idea of these modifications, which is illustrated in Fig. 4.14, was that the hydrophillic nature of an oxidized silicon surface and the pyrex surface would draw in electrolyte via capillary forces, but that the liquid would not breach the 1 mm wide hydrophobic belt in the perimeter of the reactor area

[7] FDTS (per-FluoroDecyl-Tri-chloroSilane) may be seen in Fig. 4.13.

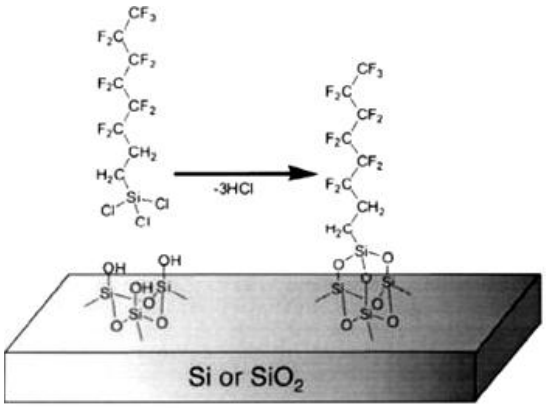

Figure 4.13: Mechanism for FDTS CVD (Chemical Vapour Deposition). FDTS coated surfaces are very hydrophobic (water contact angle $\geq 110°$).

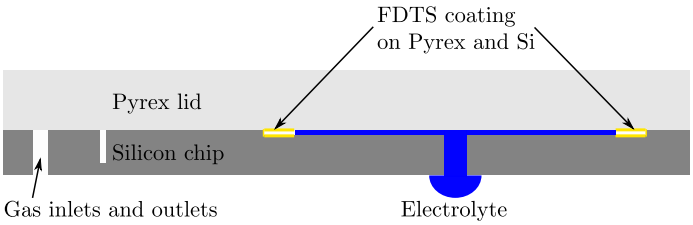

Figure 4.14: First approach for containing electrolyte using the slight modifications of the existing μ-reactors.

and therefore not block any of the gas flow channels. The platinum electrodes (two parallel strips, 1 mm apart) on the inside of the Pyrex lid would serve as cathode and anode during electrochemistry. After receiving these modified components from Toke, Jakob and I soon tried them out in the setup. We found that getting the electrolyte to enter the chip, although sometimes tricky, was always possible. The hydrophobic perimeter, however, was not always effective everywhere. At the time we were hot-bonding our chips (section 4.4) and the thermal stability of FDTS was limited at the temperatures required for anodic bonding. If the cooled-bonding technology (section 4.4.2) had been available when those experiments were performed, this problem would probably have been a non-issue. In any case, a few reactors, into which liquids could successfully be introduced, were bonded. We did a few experiments with electrolysis of water in these μ-reactors and saw hydrogen and oxygen in the QMS proving the concept.

One lesson learned from these preliminary electrolysis experiments was that the maximum current that could be applied before gas bubbles would form around the electrodes was extremely small. This is of course due to the limited solubility of H_2 and O_2 in water and their slow, two-dimensional diffusion out to the hydrophobic perimeter, where they are carried to the QMS by a stream of Ar. The radical solution to this problem was to fundamentally change the design of the "wet" μ-reactors so that mass transport of products in the electrolyte would take place in the z-direction, as opposed to the radial direction in the existing

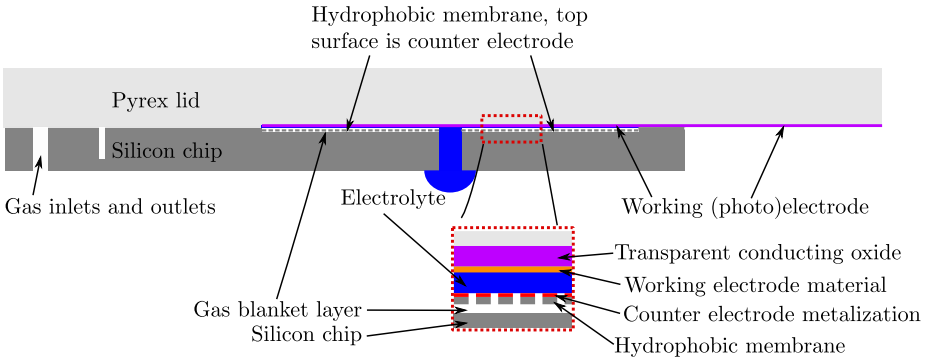

Figure 4.15: Our current approach to "wet" μ-reactors. The reactor compartment now has three separate levels. The lowest is the gas transport layer. The middle layer is a porous membrane which allows gas to pass, but not liquid, as it is coated with a strongly hydrophobic fluorosilane. The top layer is the electrochemical cell. The counter electrode metal is deposited on top of the membrane and the working electrode is deposited on a conducting inter layer (e.g., ITO (Indium-Tin Oxide)) on the pyrex lid.

(but modified) wet μ-reactors.

Figure 4.15 shows the basic idea. The reactor compartment of the chip was to be divided into a electrochemical cell, containing the electrodes and electrolyte at the top, and a gas transport layer at the bottom. These two layers would be separated by a gas-permeable membrane, which, at the same time, would be impermeable to the electrolyte (by making it hydrophobic with an FDTS coating). The membrane may also serve as counter electrode if the top surface is coated with a metal (e.g., Pt [8]). In this arrangement, the cathode to anode distance would only be the height of the top compartment (a few μm) and, at the same time, this would also be the maximum distance that products would need to diffuse. The latter in particular should enable experiments with currents in the mA-range (see section 4.5.3).

The key component of the "wet" μ-reactor is the hydrophobic membrane. Our approach has been to use a SOI (Silicon On Insulator) i.e., a silicon substrate with an oxide of a well-defined thickness (5 μm) and a silicon layer (also of known thickness - e.g., 30 μm) on top. The idea is to define the shallow features of the chip (including the flow-limiting capillary) in the top layer in the usual way and then etch a fine honeycomb pattern of holes *through* the top silicon layer down to the buried oxide. Then proceed to wet-etch the oxide between the top silicon (membrane) and the bottom silicon (substrate) for sufficiently long time to allow gas to pass everywhere under the honeycomb membrane (using buffered HF), but not so long as to completely remove the oxide support structures. A successful test structure of this kind, made by Toke, can be seen in Fig. 4.16.

[8] In water electrolysis one would want to avoid the back reaction $2\ H_2 + O_2 \rightarrow 2\ H_2O$, which runs at room temperature over PGM surfaces one might choose e.g., Au as the counter electrode since it is inert for the reverse reaction.

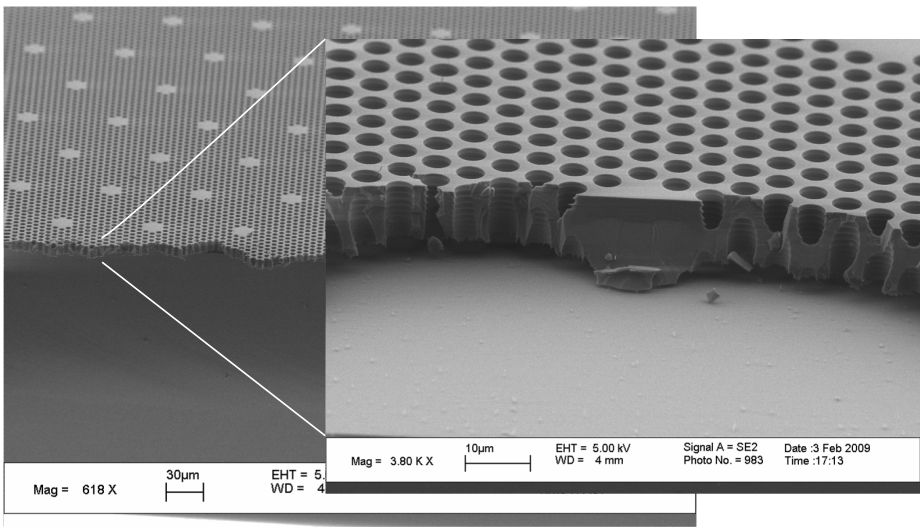

Figure 4.16: SEM micrographs of test structures of the hydrophobic membrane. The individual holes are "drilled" by more than ten polymer depositing/etching cycles in an ASE (Advanced Silicon Etcher) machine. This can actually be seen upon close inspection of the high-resolution micrograph.

4.5.3 Expected detection limit and limiting current

Experience shows that, in gas-phase experiments where the background QMS signals are low, there is a practical detection limit of about 5×10^{10} product molecules/s which is equivalent to 10 ppm of the total chip flow. In a (photo)electrochemical water splitting experiment the carrier gas entering the QMS through the capillary is expected to be saturated with water vapor (31 mbar at room temperature), thus for a main flow at 1 bar of 5×10^{15} molecules/s of carrier gas this gives a water flow of 3.1×10^{13} molecules/s. Such a high flow will inevitably give a high signal on m/Z = 2 due to cracking. The signal at m/Z = 2 is of the order of 1% of the m/Z = 18 signal - so the inevitable background at m/Z = 2 will correspond to a H_2 flow of about 3×10^{11} molecules/s. Assuming that the (photo)electrochemically evolved hydrogen must be at least as high as the background for quantitative detection the corresponding current is $I_{H_2,\min} = 2$ (electrons/molecule) $\times\ 3 \times 10^{11}$ (molecules/s) $\times\ 1.602 \times 10^{-19}$ (A $\cdot$ s/electron) ≈ 96 nA. A similar calculation can be made for oxygen, but in that case the main source of background is not expected to be cracking in the QMS but instead from oxygen diffusing in through the water injection hole in the reactor. With careful blanketing with e.g., Ar or He it should be possible to obtain a lower background of m/Z = 32 than m/Z = 2, in which case the expected minimum current needed for quantifiable product detection remains $\sim$100 nA.

If the thickness of the electrolyte layer, l, taken to be 3 μm (height of the regular reactor chamber) and the working electrode is taken to be the oxygen evolving anode then the upper limit on the current (before bubbles can form)

is 8.8 mA/cm^2, at room temperature. Fick's law says: $J = -D\frac{\partial\phi}{\partial x} = -D\frac{\phi_0}{l}$, where J is flux, D is the diffusion constant (2.01×10^{-5} cm^2/s for O_2 and 5.11×10^{-5} cm^2/s for H_2 at 25°C (298 K)) and ϕ_0 is the limiting solubility of the gas (1.24×10^{-6} mol/cm^3 for O_2 and 8.00×10^{-7} mol/cm^3 for H_2). Plugging in the numbers for oxygen gives $J_{\text{limit}} = -2.05\frac{1.24}{0.0003}8.3 \times 10^{-8}$ mol/cm^{2}s which is the same as 8.8 mA/cm^2. The same calculation for hydrogen gives a limiting current of 14.4 mA/cm^2 (i.e., 6.9 mA and 11 mA respectively for the 0.78 cm^2 of the reactor). The limiting currents increase slightly with temperature due to higher diffusivity, but not much since the limiting solubility drops. This simple estimate shows that the "wet" μ-reactors should be able to bridge the gap up to practical (photo)currents of over 1 mA, and beyond 1 mA a conventional reactor like the one discussed in 3.1 may be used. Of course experiments are always easy - on paper - in practice the concept sketched in Fig. 4.15 has not yet been realized. However, Toke is currently working on the first batch and we hope to test a complete μ-reactor of this new "wet" kind within a few weeks.

Chapter 5

Photocatalysis

5.1 Photooxidation of CO over TiO_2 catalysts

As mentioned in the previous chapter, the very first experiments with photocatalysis in the μ-reactors were conducted using P25 as photocatalyst. It was deposited as an aqueous slurry directly on the silicon chip with a pipette. This crude method was fine in a binary "Does it work?, Yes/No" experiment, but for any quantitative experiment an alternative means of depositing the catalyst was needed for two reasons. The first reason, is that good control of the amount of deposited catalyst is *very* hard to get in practice in the manual pipette procedure. The second reason is that the deposited catalyst films are visibly non-uniform. Non-uniformity need not be an issue when doing conventional thermal catalysis, but it is a major concern in photocatalysis where even illumination (uniform catalyst excitation) is required.

5.1.1 Powdered photocatalysts

In order to improve the catalyst loading procedure a small project on spin-coating colloidal photocatalyst onto the sample was carried out. The aim was to come up with an experimental recipe for reproducible deposition of different thicknesses. The bottom line of the project is that when using P25 photocatalyst it is a major hurdle to minimize the size of the agglomerates in the solution. However, on a more macroscopic (μm)-scale quite uniform films of approximate thickness from 200 nm to at least 1000 nm can be deposited by spin-coating with a stock solution of $5\%_{\text{mass}}$ P25 in pure water. The solution is sonicated while a small volume of ($\sim$100 μm) is withdrawn and transferred to the sample which immediately is spun up to 6000 RPM [1] for 10 seconds. In order to deposit catalyst only within the area of the glass that will mate with the reactor-area of the chip, the glass is protected from deposition using clean-room "blue-tape" (SWT20, Nitto Scandinavia A/S) This procedure is repeated if a film thicker than 200 nm is desired, and we speculate that thinner films could be deposited using more dilute solutions, but that has yet to be confirmed. It must, however, be admitted that the spin-coating technology is not perfected - largely due to a lack of interest in (commercial) photocatalyst powders. One particular problem is the buildup of

[1] Rotations Per Minute

a (very narrow) rim of higher film-thickness around the edge of the hole in the blue film which defines the deposition area.

Up till now, all quantitative experiments carried out in the μ-rectors (section 5.2, page 72) have been carried out on thin-film samples (either sputter-deposited or electrochemically grown) which are easier to characterize.

5.1.2 TiO_2 NT thin films

As soon as the method for growing TiO_2 NT films on the pyrex lids had been developed (chapter 2) it was used for growing films on the pyrex lids for the μ-reactors. Early tests were promising. Turnover was high and time response was fast with both simple light-sources, such as our small 4 W Hg-lamp, and with more elaborate Xe-source illumination. Su-Il was interested in activity data for a series of nitrogen-doped samples (slightly yellow in color) which he had prepared, so some effort was spent measuring on such samples and comparing these with otherwise similar, but undoped, samples. At that time, all samples were still being hot-bonded (see section 4.4) so the results for individual tests should be taken with a grain of salt. Nonetheless, the general result was that the undoped samples were far superior to the nitrogen-doped samples in the presence of UV-light, but even when using 400 or 420 nm cut-on (high pass) filters N-doped samples were not really better than undoped samples.

5.1.3 The effect of water

Another observation made in early 2009 was that when photooxidizing CO, it seems that the presence of water has a strong, inhibiting effect, which has also been reported by Einaga et al. [67]. When the μ-reactor mounted on the gas interface manifold is changed, the newly mounted μ-reactor generally contains absorbed water. The initial CO-oxidizing activity is also low, but as the μ-reactor is illuminated, and continually flushed with dry reactant gasses activity increases and reaches a stable plateau after some time. It is therefore mandatory to make sure that the μ-reactor has reached steady state activity before performing measurements. This is a trivial matter of simply observing the CO, CO_2, and possibly O_2 (and H_2O), signals under chopped illumination until they reach steady state levels. To speed up the drying process (particularly for samples with thicker films) a hot air gun is often used to heat the reactor to $\sim$100°C (373 K) after it has been mounted in the gas interface manifold. When the water signal no longer shows a prompt reaction upon heating the μ-reactor for a few seconds, it is because the μ-reactor is dry and activity, generally, is stable.

5.1.4 Responsiveness

From our earliest photoexperiments in the μ-reactors we noted that the system is very responsive to changes in illumination. Figure 4.5, which shows one of the first experiments, demonstrates this phenomenon - viz.that the signals respond quite rapidly after the light has been toggled. The ability to turn reactivity on and off nearly instantly (by turning illumination on and off) may be used to measure the effective time constant of the μ-reactor in an experiment optimized

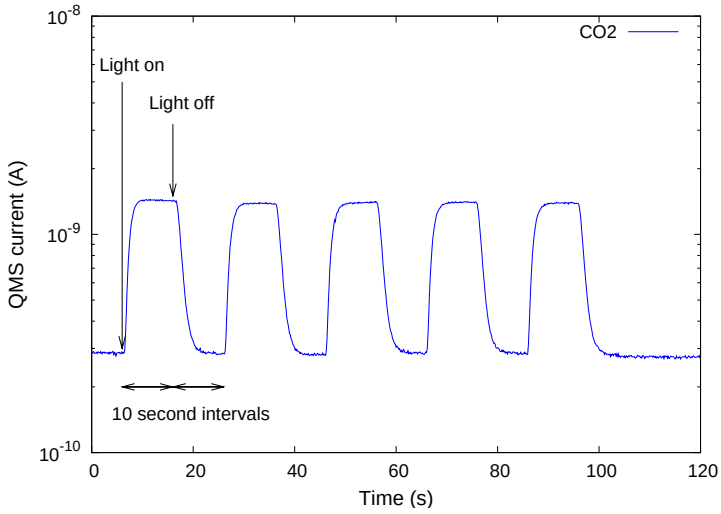

Figure 5.1: Experiment to test the response time of the system. The CO_2 signal is sampled at 10 Hz and the light is toggled every 10 s. It may be seen that the CO_2 level takes only $\sim$ 2 s to reach 90% of the steady state level.

for speed [Paper IV]. Such an experiment with fast sampling of the CO_2 (m/Z = 44) and using a μ-reactor, with a wide capillary, is shown in Fig. 5.1. The figure shows that the (new) steady state signal is reached within a few seconds after the light is toggled and this speed is one of the μ-reactors greatest benefits since it allows fast collection of data under different operational conditions (such as changing illumination intensity or wavelength - see sections 5.1.6 and 5.2.3). The responsiveness may also give useful information about the intrinsic time constants of the μ-reactor system and possibly about mass-transport of reaction products through photocatalyst films.

5.1.5 Parameter space

One of the great advantages of the μ-reactor being a flow reactor with fast time response is that it is quite easy to map out a big space of operational parameters. After we had switched from pre-mixed CO-O_2-Ar-He for CO-oxidation to individual MFCs (Mass Flow Controllers) for CO, O_2 and Hr/Ar, it seemed obvious to try out different CO/O_2-ratios and pressures to see which parameters gave the highest turnover, or best light/dark signal ratio etc.

Figure 5.2 shows (raw) data from such an overnight experiment, where four different total pressures (0.2, 0.5, 1.0 and 2.0 bar) are tested, and at each pressure 6 different CO/O_2-ratios (0.007(6), 0.026, 0.067, 0.25, 1.0, 3.0 - in all cases with 25% Ar in the feed) - i.e., 24 different conditions - are tested in 24 hours (all at room temperature). In this case the catalyst is 400 nm TiO_2 nanotubes on the pyrex lid (see chapter 2). All channels follow zig-zag trajectories because every second point is with illumination and every second point is without illumination

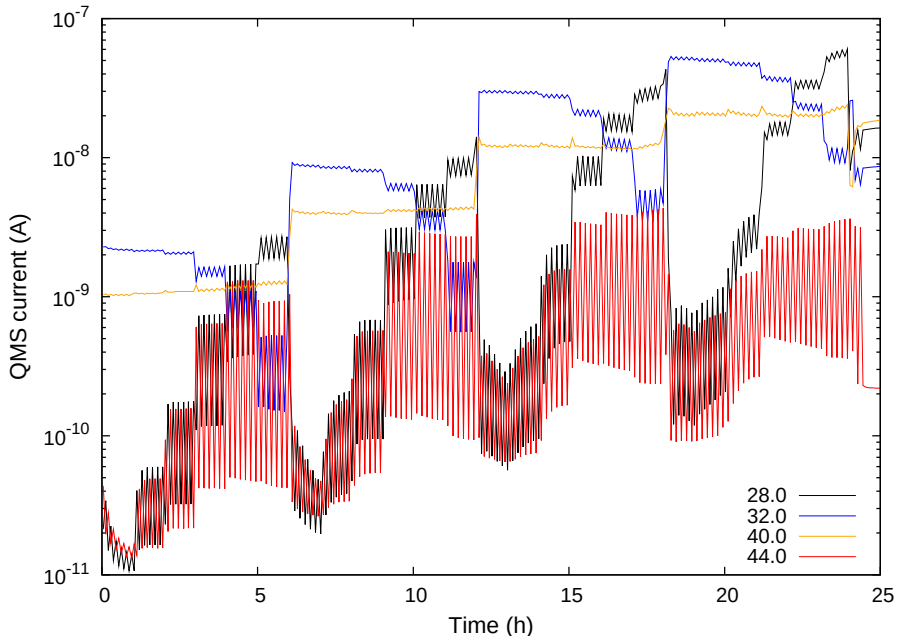

Figure 5.2: Overview plot of an experiment to map out parameter space for photocatalytic CO-oxidation in the μ-reactor. The data falls into 4 groups of constant pressure in the reactor: 0-6 h: $p = 0.2$ bar, 6-12 h: $p = 0.5$ bar, 12-18 h: $p = 1.0$ bar, 18-24 h: $p = 2.0$ bar. Six different CO/O_2-ratios (0.007(6), 0.026, 0.067, 0.25, 1.0, 3.0) are tested at each pressure. The catalyst was a 400 nm thick film of TiO_2 nanotubes. Light source: 1 kW Xe-lamp with 285 nm filter (see Fig. 5.8 on page 77).

[2]. Many things can be learned from the data. For one thing, this sample does not perform better at 2 bar, than at 1 bar - not by any measure. For pressures below 1 bar, however, conversion increases with pressure and this could indicate that site blocking becomes important at or about 1 bar while at low pressures the catalyst is starved of reactants. It is also clear that the highest ratio between CO_2-signal with the light on and with the light off (dark signal is due to reaction on the QMS filament) is obtained when the CO/O_2-ratio is close to stoichiometric. Especially at reduced pressures, the CO/O_2-ratio 1:1 (i.e., slightly lean in CO) results in high light/dark signal ratios.

Focussing more on the CO_2-signal, Fig. 5.3 shows the level when the light is

[2]One might think that the argon signal should be stable, but in general it also is affected when the light is toggled. The reason for this is twofold: At low turnover (in this experiment when there is very little CO in the feed) the Ar signal drops when the light is switched on because the μ-reactor heats up slightly when illuminated, which then depresses flow through the capillary (see [Paper II]). Conversely, at high turnover (in this experiment when the mixture is close to stoichiometric) the argon flow is increased as the light is switched on. The reason is that the reaction consumes gas (0.5 O_2 + 1.0 CO $\rightarrow$ 1.0 CO_2) and since the reactor is isobaric, more reactant gas will be drawn into the reactor chamber as oxygen is consumed. In this manner the gas in the reactor chamber is enriched in argon and therefore the QMS signal goes up. At intermediate turnover these two effects almost cancel each other out, as seen in Fig. 5.2 (third mixture ratio, second pressure group: 0.5 bar, $CO/O_2 = 0.067$).

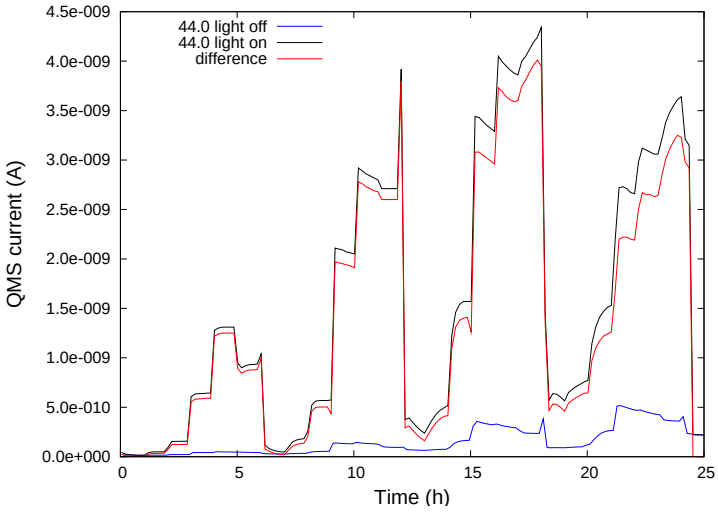

Figure 5.3: Plot of the CO_2 data from Fig. 5.2 on a linear scale. Instead of the zig-zag curve I have plotted a curve for when the light is on (black), another for when the light is off (blue) and a third (red) showing the difference. This way of plotting the data clearly illustrates that nothing is gained by going above 1 bar in pressure. It also shows that the system equilibrates faster at lower pressures. At 0.2 bar the plot clearly shows that at the 3:1 CO/O_2-ratio CO_2 output drops because the reaction is starved of oxygen.

on, off and the difference between on and off on a linear scale. This plot makes it evident that at high pressures it takes longer for the signals to stabilize every time the mixture ratio is changed. This is because of the internal volume of the tubing between the MFCs and the gas-interface manifold. From this data it would seem attractive to conduct experiments at sub-atmospheric pressures (perhaps 0.5 bar), but the benefit compared to 1.0 bar is not very big. There is a practical advantage to conducting experiments at or slightly above 1.0 bar, viz.that when the μ-reactor is changed and the tubing is at or above atmospheric pressure no air is sucked into the tubes, which means that measurements on a newly mounted reactor can start much sooner. This is an advantage when measuring on several μ-reactors in one day, but not important when μ-reactors are mounted for longer periods. The compromise decided upon, on the basis of this data, was to settle on 1.0 bar and a 1:3 CO/O_2-ratio for future experiments with CO-oxidation over TiO_2 in various forms.

5.1.6 Intensity study

Motivation

CINF recently purchased an industrial high-power UV-LED source (Hamamatsu model LC-L2) fitted with a focusing lens assembly (Hamamatsu L10561-220) suited for areas of 8 mm in diameter. The peak wavelength is ~367 nm and the

FWHM [3] is ∼9 nm. In our setup an average irradiance on the sample μ-reactor of ∼645 mW/cm^2 at full power was measured using a calibrated spectroradiometer (International Light model RPS-900R). The unit may be electronically tuned down to 10% of full power. Combined with simple neutral density (ND) filters of optical density 1.0 and 2.0 (Newport corp.) a few extra orders of magnitude in light intensity are made available so this light-source seems ideal for studies of how photocatalytic turnover scales with light intensity.

We thought it worthwhile to study this dependence because when we use our monochromated Xe-lamp to characterize the photocatalytic performance as a function of illumination wavelength (action spectrum - see section 5.2.3) the irradiance on the sample increases by almost eight times when the wavelength is increased from 300 nm to 400 nm. This means that two parameters (wavelength *and* irradiance) are effectively being scanned simultaneously; if the turnover is strongly non-linear in irradiance for a given sample the action spectrum must be corrected for that. Another reason why a measurement of turnover as function of irradiance might be interesting is that it gives mechanistic insight. For example, it is often claimed that in the limit of low light intensity (where mass transport is not a limiting factor) turnover should scale linearly with incident photon flux. Furthermore, it is claimed that at higher irradiance levels turnover becomes proportional to the square root of irradiance due to substantial carrier recombination. Experimental support for this was found by Egerton and King [68] by oxidizing isopropanol to acetone over rutile TiO_2 and commercial pigments in the liquid phase while varying irradiance over five orders of magnitude. Later, however, Ohko et al. [69] studied the same reaction in gas phase over a TiO_2 thin film at very low light intensities (45 μW/cm^2 down to 36 nW/cm^2 - the latter corresponding to only 6.6×10^{10} photons/(cm^{2}s)) and found turnover to be proportional to (irradiance)$^{0.8}$ over their 3.5 orders of magnitude in irradiance (as long as the isopropanol concentration was above 10 ppmv).

Results

We calibrated the actual output of the Hamamatsu LED unit with all the filters and at all power settings using the spectroradiometer to obtain exact extinction of the individual ND (Neutral Density) filters (which at 367 nm is not equal to their nominal values). Then two different μ-reactors, one with P25 and one with TiO_2 NTs, were tested for CO-oxidation activity. For both samples the light intensity is almost constant over the thickness of the sample due to the thin layers used and the proximity of the 367 nm central wavelength to the band edges. This is especially true with the nanotube μ-reactor since its absorption edge is at ∼380 nm, so in simple transmission, only about 10% is absorbed at 365 nm (see Fig. 5.6 on page 74). Figure 5.4 shows data for measured CO_2 production where the constant background signal has been subtracted as a function of measured irradiance (centered at 367 nm) for the two different μ-reactors from 90 μW/cm^2 to 645 mW/cm^2. For comparison, integration of the AM1.5G spectrum (Fig. 3.3) in the 10 nm interval from 365 to 374 nm gives 0.67 mW/cm^2. The data are presented in a log-log plot, so if turnover were proportional to illumination

[3] Full Width at Half Maximum

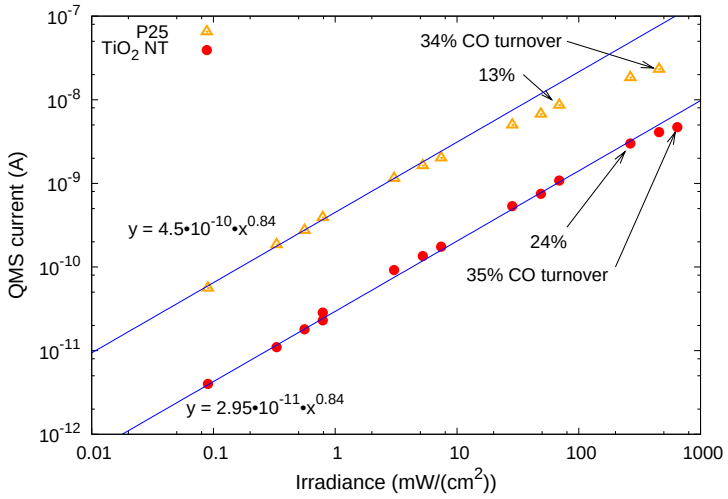

Figure 5.4: Background-corrected m/Z = 44 (CO_2) QMS signal as a function of measured irradiation on the reactor with $\lambda = 367$ nm peak wavelength. For the nanotube μ-reactor it is seen that, except for the highest illumination intensities where the effective feed gas composition is altered by high turnover in the reactor (final two data points where well over 10% of the CO is photooxidized to CO_2), the turnover vs. illumination intensity is very well described by a power function. The apparent slope (power) is 0.84 meaning that a doubling of the light intensity only results in a factor 1.79 times more turnover. This relation holds true over four orders of magnitude of light flux - from moderate to very high flux (90 μW/cm^2 to 645 mW/cm^2 = 1.7×10^{14} to 1.2×10^{18} photons/(cm^{2}s)). Also in the case of P25 it seems that the turnover is proportional to illumination intensity to the power of about ~0.84. At intensities above ~5 mW/cm^2 the power law fails (or changes to a lower power), but it cannot be ruled out that this is due to mass-transport limitations in the P25 film.

intensity the data would fall on lines of slope 1. For the μ-reactor with TiO_2 NTs it is remarkable that the turnover vs. intensity falls on a straight line over four orders of magnitude (of course as a substantial fraction of the available CO is converted in the final couple of data points the linearity fails). Turnover is *not* proportional to irradiance (slope $\neq 1$), but rather to irradiance raised to the 0.84 power (the reaction is of order 0.84 in irradiance). For P25 the same slope is seen at moderate irradiance up to about 1 mW/cm^2, but above 5 mW/cm^2 the slope is lower. This could be due to a change in mechanism, but it could just as well be due to mass-transport limitations.

To ensure that the slope of 0.84 is not somehow an artifact of the illumination wavelength being close to the band edge a similar experiment was conducted at 254 nm (strong line in the Hg spectrum) with the nanotube sample, although the illumination could only be varied over one order of magnitude for practical reasons. The result was that the turnover seemed proportional to irradiance to

the 0.75 ± 0.06 power.

Discussion

As mentioned in the above motivation, the non-linearity of photocatalytic conversion in irradiance for CO oxidation and other gas (and liquid) phase photocatalytic reactions over TiO_2 have previously been reported in literature. Peral and Ollis note for acetone oxidation in gas phase that $r \propto I^{0.7\pm0.1}$ (I is irradiance and r is rate) over one order of magnitude and conclude that they are in the "transition regime" between the values of 0.5 (recombination dominated) and 1.0 (light limited) [70]. Aguado et al. report that for one of three different colloids they test for formic acid decomposition in liquid phase they find that $r \propto I^{0.78\pm0.2}$ (the two other colloids have even lower exponents) [71]. Einaga et al. who study CO oxidation at high light intensities (~1 to 10 W/cm^2) find that $r \propto I^{\sim0.7}$ for TiO_2 (and $r \propto I^{\sim0.5}$ for platinized TiO_2) [67]. Hwang et al. find $r \propto I^{0.73\pm0.1}$ for CO oxidation over platinized TiO_2 (~0.03 to 3 mW/cm^2) [72]. Even Ohko et al., who measure isopropanol oxidation in the gas phase over three orders of magnitude at what they call "Extremely low" light intensities and arrive at $r \propto I^{0.8\pm0.04}$, conclude that they are in a "transition region" between the two asymptotic values [69].

Considering that Ohko et al. measure $r \propto I^{0.8\pm0.04}$ with I from 36 nW/cm^2 to 45 μW/cm^2 [69], and that we measure $r \propto I^{0.84\pm0.03}$ with I from 90 μW/cm^2 to 645 mW/cm^2 (albeit for a different kind of TiO_2 film and a different reaction) it seems unreasonable that the combined seven orders of magnitude in light intensity where $r \propto I^{\sim0.8}$ is just a "transition region" between the low light limit, where supposedly $r \propto I$, and the recombination dominated region, where supposedly $r \propto I^{0.5}$. A related question is whether anyone has really ever measured $r \propto I^{1.0}$?

Egerton and King show that only one pigment (out of the three commercial pigments plus rutile that they test) shows $r \propto I^1$ at low light intensities [68], and this conclusion is based on only two data points - the rest of the data for that pigment at higher intensities shows $r \propto I^{\sim0.5}$ as does the data for the other two pigments. I would hesitate to conclude that turnover can never be truly proportional to incident photon flux, but it appears that it is hard to find a (TiO_2-based) photocatalyst and a probe-reaction where this can be measured in practice.

5.2 Quantitative measurements in the μ-reactors

Plots like those shown in Figs. 4.5 and 5.1 are just plots of raw QMS currents. Another example is shown in Fig. 5.5 which is a screen-dump from LabVIEW program used to control the setup and QMS. In order to make quantitative statements about catalyst performance we would need to convert from units of Ampère (current measured on the electron multiplier of the QMS) to units of molecules/s - i.e., to count the molecular flows going through the reactor chamber. This would give the same quantitative information about turnover that the electrical current gives in (photo)electrochemistry, but with the added

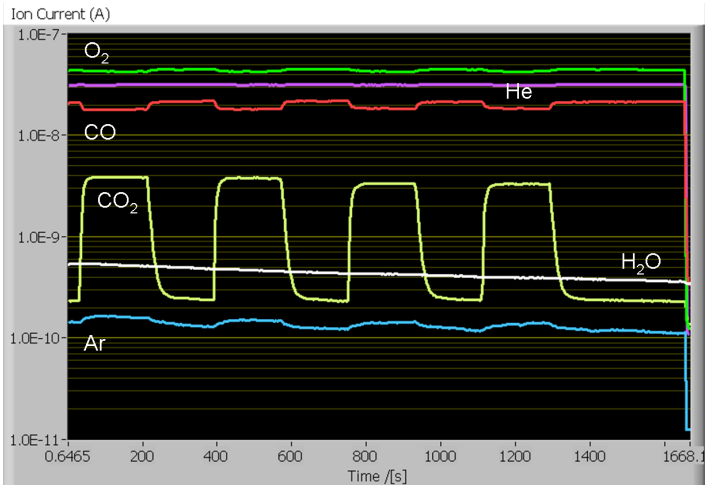

Figure 5.5: Raw data drawn directly from the mass spectrometer for a CO-oxidation experiment. Labels have been superimposed to show what the which gasses the different channels are probing. The particular measurement shown is CO-oxidaiton over TiO_2 nanotubes, but early measurements using P25 were similar.

bonus of solid proof about which reactions are occurring [4].

5.2.1 Optical characterization of samples

The first experiment to perform on a sample is to measure the optical absorption properties. This is best done before the sample is bonded to seal the μ-reactor. If the photocatalyst is deposited on the Pyrex lid it is particularly convenient since in that case the sample can be mounted in the sample beam of a standard, double-beam UV-VIS spectrophotometer. In this case a blank Pyrex lid is generally placed in the reference beam so that the apparent absorbance is only due to the photocatalytic coating on the sample. Figure 5.6 shows such a measurement. The red '+' symbols are the raw absorbance data. Of course the sample will not only absorb, but also scatter light (but the instrument will not distinguish the two) so therefore I have made a naïve fit of the scattering (using the apparent absorption at photon energies well below E_g) and subtracted that scattering component to get the "corrected" absorbance data (blue '+' symbols). The difference between the uncorrected and corrected data is substantial near E_g, but insignificant for $E_{ph} >> E_g$ since in that case, absorption is essentially 100%.

5.2.2 Calibration procedures

There are four steps to perform to get the calibration to convert from QMS currents to molecular flows, but step 1 must in principle only be done once and

[4] When measuring a current in electrochemistry and particularly in photoelectrochemistry it is of prime importance to know which reaction(s) the current corresponds to (see section 3.1).

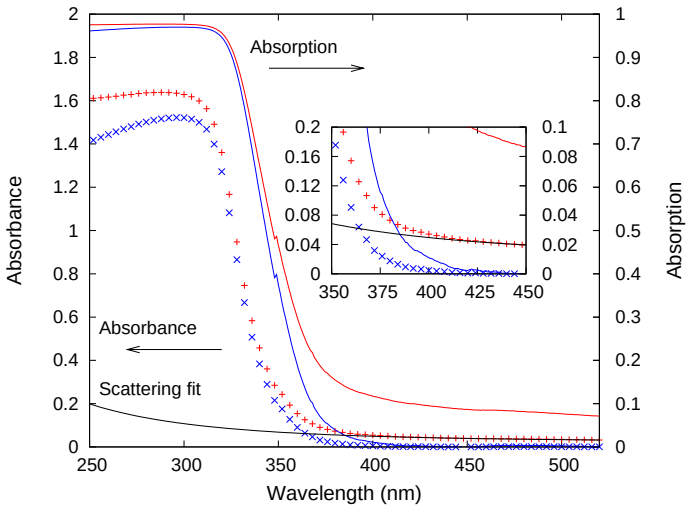

Figure 5.6: Absorbance ($A = \log(I_0/I)$) - red plus signs, left ordinate - of a sample with TiO_2-NT's measured against a blank Pyrex lid in the reference beam. The black curve is a fit ($A_{\text{scattering}} = C_1/\lambda^4 + C_2$) to the data above 400 nm as a simple model of the the scattering losses. Subtraction of the fit from the absorbance is plotted with blue crosses and represents the "scattering corrected" absorbance. The right ordinate is the resulting absorption ($1 - I/I_0$) - red and blue solid curves. Again, the blue curve is the "scattering corrected" data. The inset shows a close-up of the band edge region. For instance it can be read off the blue curve that only below 385 nm does the nanotube film absorb more than 2% of the incident photons. Scattering (black line) is probably overestimated at short wavelengths since scattered photons have a high absorption probability due to short absorption length, but the error due to this is insignificant since raw and corrected absorbance remain essentially equal at short wavelengths (both above 95 %).

then only steps 2-4 (which are very quick) have to be repeated with every new μ-reactor [Paper V]:

1. Measure the molecular flow of a "reference" μ-reactor by pumping down a known volume fitted with a baratron through the capillary of the reference μ-reactor (see [Paper II]). Call this flow R_{flow}. The unit is [molecules/s].

2. Find the molecular flow of the sample μ-reactor, S_{flow} [molecules/s]. This is conveniently done by comparing the QMS current of a suitable gas component (this *inert* internal reference is typically He measured at m/Z = 4) of the sample μ-reactor with the reference μ-reactor using the same gas mixture. This gives the relation

$$S_{\text{flow}} = R_{\text{flow}} \frac{S_{QMS}(inert)}{R_{QMS}(inert)} \tag{5.1}$$

where $\frac{S_{QMS}(inert)}{R_{QMS}(inert)}$ is the ratio of measured QMS currents [Ampère/Ampère] of the inert gas in the sample μ-reactor to the reference μ-reactor. This

simple method of swapping the sample with the reference reactor is much faster and more convenient than doing a pump-down experiment (step 1) with every sample μ-reactor.

3. Measure the QMS signal for every interesting component, n, in a known gas mixture to find a set of calibration constants, C_n, (sensitivity factors):

$$C_n = S_{\text{flow}} \frac{f(n)}{S_{QMS}(n)} \tag{5.2}$$

where $f(n)$ is the fraction of the n$^{\text{th}}$ component of the gas ($\sum f(n) = 1$ where summation is over all components) and $S_{QMS}(n)$ is the QMS current measured for the n$^{\text{th}}$ component. Each calibration constant is the ratio of the molecular flow to the measured QMS current of a given gas, n. They capture differences in ionization probabilities etc. In general, they are equal within 50% of each other - except for He which has a low ionization cross section.

4. Now the molecular flow of each gas component, n, is given by

$$S_{flow}(n) = C_n S^*_{QMS}(n) \tag{5.3}$$

where $S^*_{QMS}(n)$ is the QMS signal that has been corrected for background in the QMS (including cracking and reaction on the filament). In the case of CO (photo)oxidation this is easy since, in the dark, there is no reaction (verified in separate experiments) so the dark CO_2 signal (m/Z = 44) is the background and in the above equation $S^*_{QMS}(\text{CO}_2) = S_{QMS}(\text{CO}_2) - S_{QMS-\text{dark}}(\text{CO}_2)$

The order of magnitude for molecular chip flow is 5×10^{14} molecules/s - i.e. 10^{-9} moles/s for μ-reactors with the small capillary (with $p = 1$ bar) and an order of magnitude higher for μ-reactors with the large capillary. Implicit in the calibration is the assumption that the QMS is linear (i.e. a 10 times reduction in pressure of a given gas component in the QMS results in a signal that is exactly 10 times lower). A linearity calibration of the mass spectrometer has been carried out and there is no reason to suspect any non-linearity leading to a systematic instrumental error. Generally, I also see mass balance for carbon and oxygen: CO + CO_2 = constant and 2 O_2 + CO + 2 CO_2 = another constant.

5.2.3 Action spectra, IPPE and APPE

Using a monochromatic and tunable light source it is common practice in photoelectrocatalysis to measure photocurrent (possibly under some electrical bias) at different wavelengths. The result - photoactivity as a function of wavelength - is known as the “action spectrum”.

Taking advantage of the fast time response and the (calibrated) high sensitivity of the μ-reactors we recorded the chemical equivalent of the photocurrent action spectrum for a TiO_2 NT sample, again using CO-oxidation as a probe reaction.

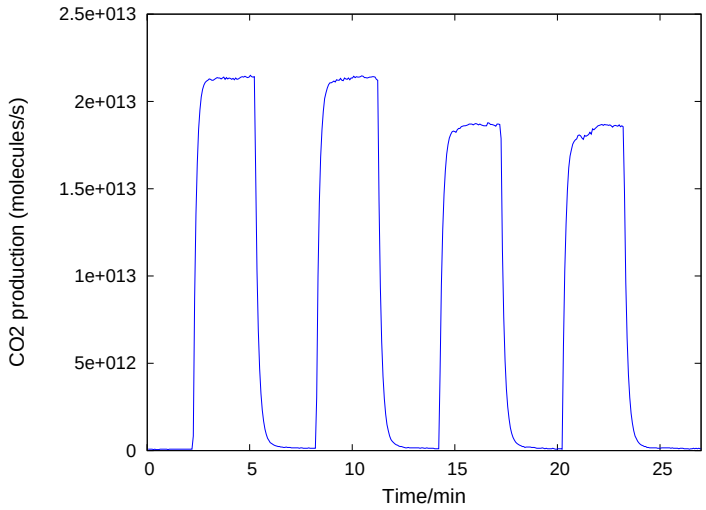

Figure 5.7: Calibrated version of Fig. 5.5 (CO_2 signal only) where the ordinate now has units of molecules/s (and is plotted on a linear scale).

Xe-source

Our work-horse light source consists of an (ozone free) 1 kW Xe-arc source (Newport model 66924) equipped with a water filter to absorb unwanted long-wave light ($\lambda \gtrsim 1000$ nm) and often a "hotmirror" is also used to eliminate the strong lines in the Xe spectrum between 750 nm and 1000 nm [5]. The lamp is fitted with an electronic shutter which is controlled by a computer using LabVIEW and the optical output is coupled via a quartz fiber bundle through a collimating lens onto the sample μ-reactor. The actual irradiance incident on the μ-reactor (measured by putting the probe of a calibrated spectroradiometer in place of the μ-reactor) is seen in Fig. 5.8. Evidently, the unfiltered Xe-output follows (reasonably well) the solar (AM1.5G) spectrum multiplied by 35, except in the 330 nm to 370 nm region when the hotmirror is in place. The plot also shows what the spectrum looks like when various cut-on filters are introduced in the beam. Interestingly, some filters (in particular the 285 nm and 400 nm filters) have significant transmission below the nominal cut-on wavelength while others (e.g., the 420 nm filter) do not. This underlines the importance of this kind of actual measurement [6]

For the purpose of the action spectrum measurement the Xe lamp was used as a basis for a (wavelength) tuneable lightsource shown schematically in Fig. 5.9. In this application the hotmirror was removed from the Xe lamp which instead was fitted with a monochromator (Newport Cornerstone 260) and

[5] Unfortunately the hotmirror also reflects around the second harmonic of the cut-off lavelength (which in our case is 700 nm), so therefore interval from 330 nm to 370 nm is also cut out of the spectrum (Fig. 5.8).

[6] In the photocatalysis literature, claims of "visible light activity" are sometimes seen based on observed activity under light filtered by e.g., a 400 nm filter, but without an accompanying measured spectrum, however, as Fig. 5.8 shows, such an experiment could lead to wrong conclusions due to UV-leakage.

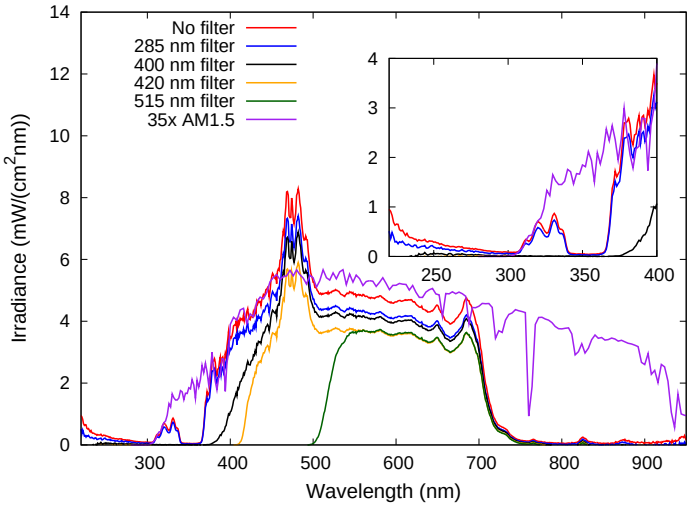

Figure 5.8: Measured irradiance on the μ-reactors of the Xe-light source with hotmirror alone (no filter) and with various filters from Newport (cut-on: 285, 400, 420, 515 nm).

appropriate optics for F-number matching. In this case both the monochromator and shutter are controlled from the lab computer using LabVIEW so that the whole measurement may be pre-programmed.

In order to measure the light irradiated onto the μ-reactor the spectroradiometer was used. The raw measurements of the monochromated output of the Xe light source at every wavelength used are presented in Fig. 5.10. With this instrumental configuration the FWHM is on the order of 9 nm and the peak irradiance is around 40 μW/cm^{2}nm for central wavelengths in the relevant range (∼300 to 370 nm). As a reference, AM1.5G is also shown in Fig. 5.10 and it is seen that its irradiance is of the same order of magnitude. No effort was made to keep irradiance constant over the wavelength interval. Given the results of the intensity study such extra refinements might be relevant for very accurate characterization, but for the purpose of demonstrating the technique it was considered unnecessary - not least since irradiance is constant to within a factor of two in the wide 310 nm to 370 nm interval. Figure 5.11 shows the same data as Fig. 5.10, but converted to photons flux spectrum (instead of energy flux) and also the integrated photon flux at each wavelength setting. For example, at the 330 nm setting the integrated photon flux is 5×10^{14} photons/(cm^2 s).

The raw measurement of photocatalytic CO_2 production at these monochromator settings may be seen in Fig. 5.12. The abscissa is time (as is always the case for μ-reactor QMS data), but of course it really corresponds to wavelengths starting from 290 nm and up to 400 nm (the monochromator setpoint is changed in 5 nm increments while the shutter has turned off the light). The fact that the μ-reactor is a *flow* reactor with very high sensitivity is what enables a well resolved action spectrum to be recorded in only 135 minutes.

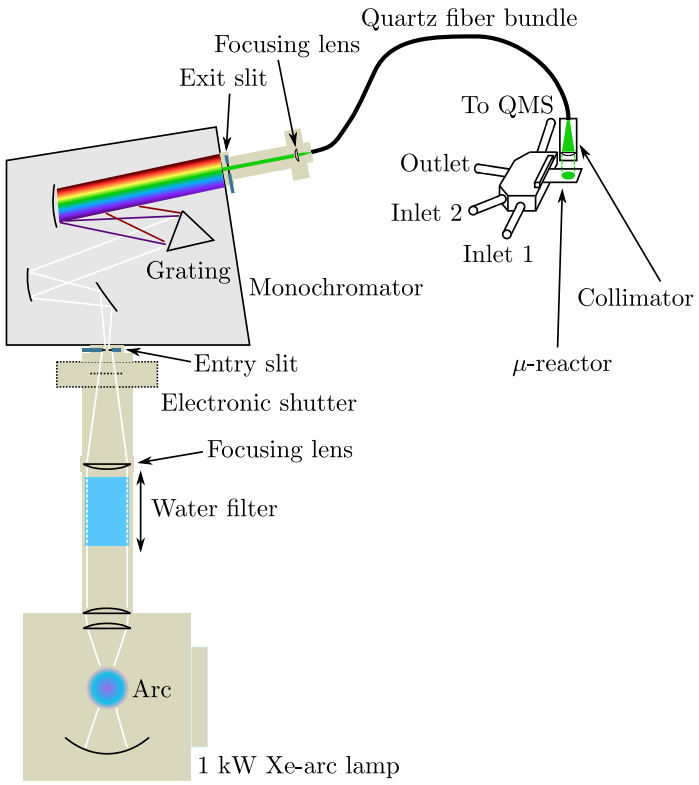

Figure 5.9: Schematic of the monochromated Xe-arc source used for measuring action spectra. The irradiance of the system at all relevant settings (choice of wavelength, slits and grating) is measured by putting the measuring head of a calibrated spectroradiometer in the place of the μ-reactor. This irradiance measurement is carried out immediately before or after the actual measurement on the μ-reactor.

The next logical step, of course, is to subtract the background signal and use the calibration procedure described in section 5.2.2 to find the true turnover as a function of time. Then, taking an average of the turnover at each wavelength and plotting it as function of wavelength is what is represented by the red '+' symbols in Fig. 5.13. Clearly, maximum turnover occurs in the wavelength interval 325 nm to 345 nm for this sample. Peak turnover occurs at 330 nm and is about 1.45×10^{12} CO_2/s. Without anything to compare with, such a number

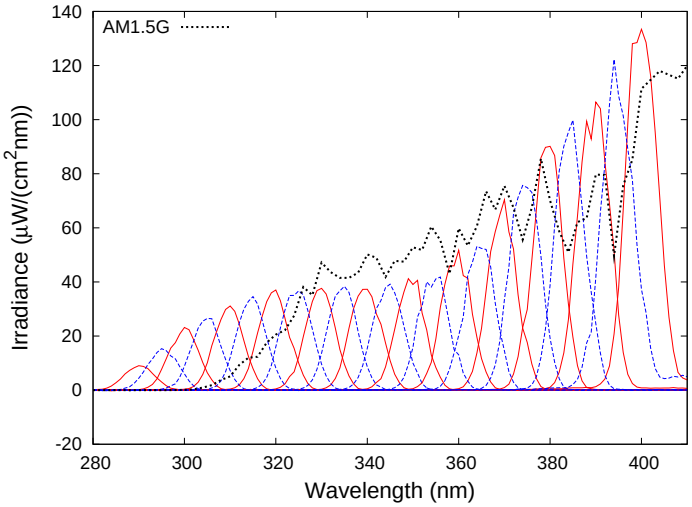

Figure 5.10: Irradiance spectra measured at the μ-reactor surface for all the monochromator settings used for recording action spectrum. For clarity, every other wavelength measurement $(290, 300, 310, \ldots)$ is plotted with solid, red and every other wavelength $(295, 305, 315, \ldots)$ in dashed, blue. Note that in the wavelength interval (310 to 370 nm) the irradiance is constant within a factor 2. AM1.5G (dotted, black line) is included for comparison.

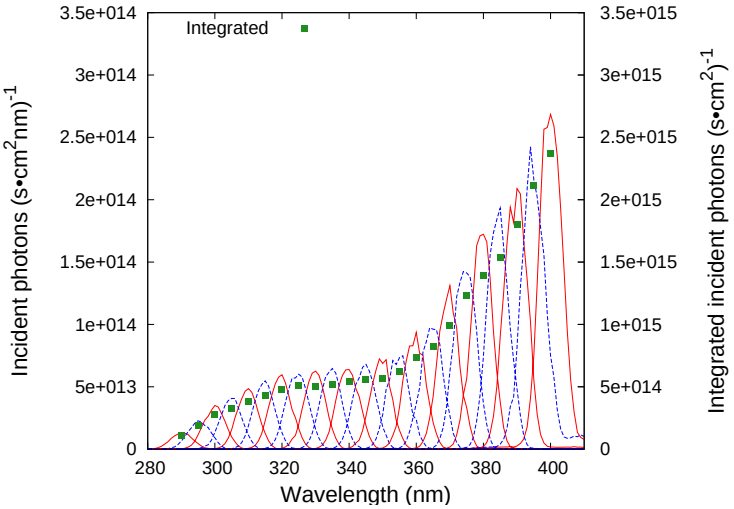

Figure 5.11: Data from Fig. 5.10, but converted to photon flux density (instead of energy flux density). The green squares show the integrated photon flux density at each monochromator setting (second ordinate). This photon flux density is on the order of $5 \times 10^{14}/(\mathrm{cm}^2\ \mathrm{s})$ in the relevant wavelength range < 375 nm.

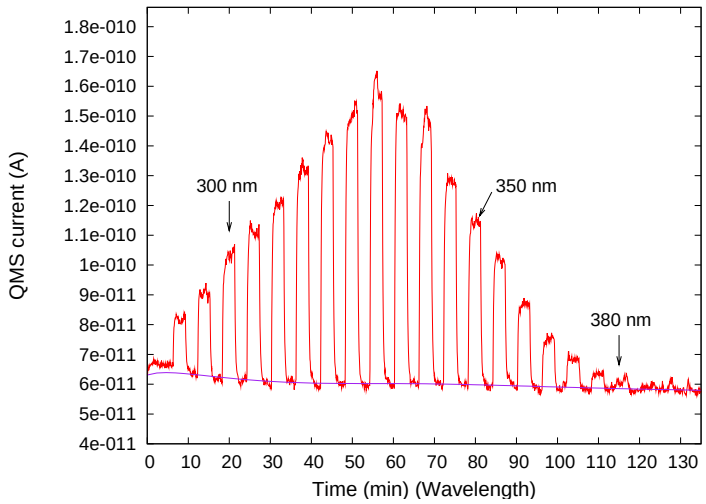

Figure 5.12: Raw CO_2 (m/Z = 44) action spectrum data. The wave length is incremented in 5 nm steps from 290 nm every 12 minutes while the shutter is toggled every 6 minutes. The blue line shows the fitted background signal in the QMS.

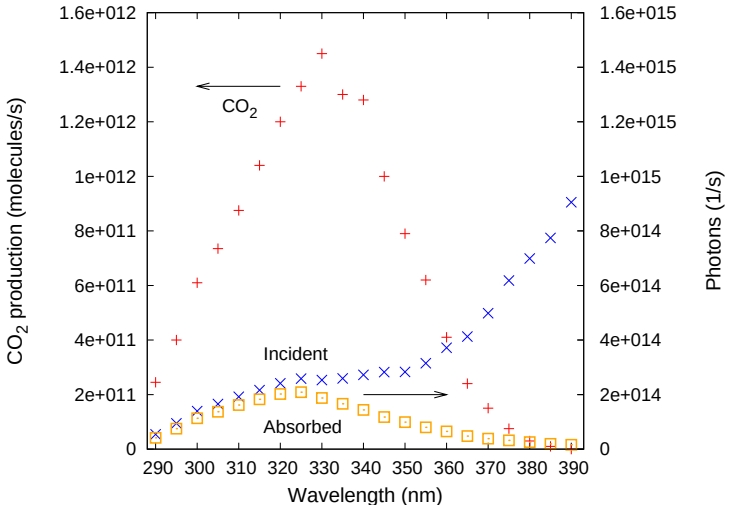

Figure 5.13: Background corrected CO_2 (From Fig. 5.12) converted to units of molecules/s as described in section 5.2.2 (red + symbols). Also shown (right ordinate) is the integrated incident and absorbed photons/s (data from Fig.5.11 multiplied by the active photocatalyst area).

is quite meaningless. The obvious thing to compare with is photon flux [7] which is why I have co-plotted the incident photons over the catalyst area (blue circles) and also the best estimate for the number of photons absorbed by the TiO_2 NT film (black squares). To find the latter, the UV-vis absorption measurement of the lid (before bonding) has been used and corrections for losses due to scattering and reflection and absorption in the Pyrex have also been carried out (for details see [Paper V]). The final step, to assess how well the photocatalyst works at different wavelengths, is to divide the turnover by incident photons, or by absorbed photons. The former gives the Incident Photon to Product Efficiency (IPPE), which is the chemical equivalent of the Incident Photon to Current Efficiency (IPCE) measured in photoelectrocatalysis, and the latter is the Absorbed Photon to Product Efficiency (APPE), which is an internal quantum efficiency for the catalyst and the reaction. Both the IPPE and APPE are plotted in Fig. 5.14. It may be seen that the IPPE drops off quite rapidly for wavelengths above 340 nm. This is because above this wavelength a substantial fraction of the photons penetrate the 400 nm thick film unabsorbed. The highest value for the IPPE (about 0.5%) for this reaction occurs in the 325 nm to 335 nm interval. Below 325 nm, there is a small drop in IPPE with decreasing wavelength, which we interpret as a signature of the back-illumination - namely that at lower wavelengths most of the absorbtion will take place near the glass lid (away form the reactants). This means that, on average, the reaction occurs deeper inside the nanotubes so reactants and products must diffuse longer and turnover rates must locally be higher. A consequence of this explanation is the prediction that if the same measurement were conducted with frontal illumination there should be no such drop in IPPE for decreasing wavelength - indeed IPPE might even continue to increase slightly with photon energy if mass-transport is an issue. Such experiments (comparing frontal and back illumination for different film thicknesses and wavelength) are currently being carried out.

Looking at the APPE the picture is a little different. Here it is seen that there is a broader maximum in APPE from 330 nm up to 360 nm, and in this interval the APPE reaches 0.8%. The drop in APPE with decreasing wavelength may be understood in the same way as the drop in IPPE, and the reason why the activity drop is steeper in the case of APPE is that, here, it is *given* that the photon is absorbed, while for IPPE there is still a little gain in terms of the fraction of absorbed photons as wavelength is decreased - even below 330 nm,

[7] In traditional heterogeneous catalysis one would divide by surface area (or sites) to get a *turnover frequency*. In photocatalysis the term has less meaning (since it is highly illumination dependant), but it can be estimated (to within a factor of ~ 3) for the purpose of the exercise: The area with nanotubes is 8 mm in diameter. Assuming that the film is 400 nm thick, and that the tubes have an outer diameter of 40 nm, an inner diameter of 20 nm and a roughness factor of 2 then each NT has a surface area of $A_{\mathrm{NT}} \approx r\pi(d_i + d_o)l = 2\pi(20+40)400 = 0.15\ \mu\mathrm{m}^2$. The number of NTs within an 8 mm diameter is $N = A_t/A_{\text{unit cell}} = (\pi/4)(8\ \mathrm{mm})^2/(\sqrt{3}/4 \times d_o^2) = 7.3 \times 10^{10}$ nanotubes with a total area of $\sim$110 cm^2. This means that in this experiment at 330 nm the turnover frequency is on the order of 10^{-5} or 20 turnovers/(nanotube·s). Incidentally the number of CO molecules entering a nanotube every second may be estimated by the collision number, $\frac{v_{avg}N}{4V}$, since the inner diameter of the nanotubes is below the mean free path in the gas mixture ($\sim$ 100 nm at 1 bar). For a reactor pressure of 1 bar (1/7 bar of CO) and T=300 K I find that $\sim 1.3 \times 10^{11}$ CO molecules enter a nanotube every second, but only 20 get oxidized. At 35% conversion (last datum in Fig. 5.4 at 645 $\mathrm{mW/cm}^2$ and $\lambda = 365$ nm) turnover is 2.8×10^{13} CO/s i.e., 380 turnovers/(nanotube×s) or a turnover frequency of $\sim 3 \times 10^{-4}$.

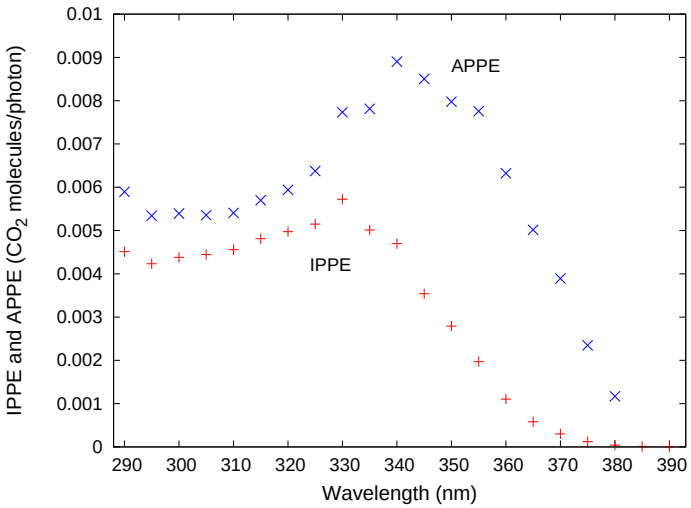

Figure 5.14: Incident Photon to Product Efficiency (IPPE) and Absorbed Photon to Product Efficiency (APPE). Up to ∼340 nm one CO_2 molecule results for every ∼200 photons incident on the reactor. At wavelengths above approx 340 nm the IPPE quickly drops off reflecting the fact that many photons pass the TiO_2 nanotube layer unabsorbed. Considering only the fraction of photons absorbed, the APPE, it is clear that higher wavelength may well induce turnover - up to ≈380 nm. The APPE has a broad maximum at 345 ± 15 nm where the efficiency is about 0.8%. The APPE data at 290 nm and particularly above 370 nm is very uncertain. This is because APPE is calculated as conversion divided by absorbed photons and in the extremes of the plot both denominator and numerator are close to zero.

which acts against the back illumination effect. Going up in wavelength there is also a clear drop in APPE, but while it was expected for IPPE, it is less obvious why it occurs in the APPE. One possible explanation is that not all excitations are "created equal". For instance, if inter-band states exist in the material then low-energy photons have a greater likelihood of exciting an electron into such states than of exciting an electron to the conduction band where it is free to move. In the former case the electron-hole pair has a higher risk of recombining without inducing any photocatalysis than in the latter case.

5.3 Other reactions

While we think that CO oxidation is a useful and practical reaction for assessing the quality of a photocatalyst it does have some drawbacks. One major concern is its sensitivity to the presence of moisture (section 5.1.3), since in any real application the catalyst would almost certainly be exposed to water. For example, when mineralizing any organic molecule which contains hydrogen water is even a product!

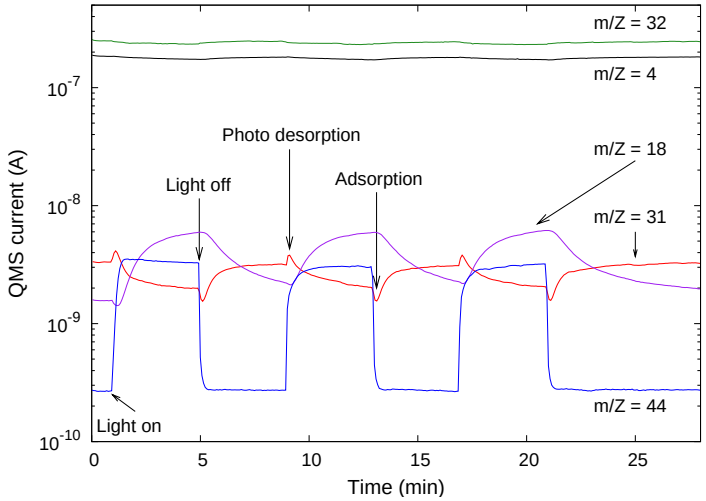

Figure 5.15: Photooxidation of methanol over P25 photocatalyst. m/Z = 31 is the main signal from methanol and m/Z = 18 is the main peak from water. It is clear that the while the CO_2 signal responds quickly to illumination the methanol signal. The water signal in particular takes much longer to respond. Notable photo desorption and (re-adsorption upon switching off the light) of methanol is observed.

In consideration of this we have conducted photooxidation of a few simple organic compounds in the μ-reactors (mainly methanol [Paper IV] and methane) while in our "macro-reactor" we have also oxidized acetone. Figure 5.15 shows an example where we are oxidizing methanol ($CH_3OH + 3/2O_2 \rightarrow CO_2 + 2H_2O$). The CO_2 signal behaves in the usual way for CO oxidation i.e., it increases when the light is turned on and vice versa. As expected, the methanol signal (measured on m/Z = 31 - i.e., ions CH_3O^+) behaves inversely (decreases when the light is turned on). The methanol signal, however, also shows a quick increase before the larger, steady-state decrease as the light is turned on and when the light is turned off the methanol signal has a quick dip before it goes back up to its higher steady state level. Apparently, the methanol is photo-desorbing and re-adsorbing i.e., the equilibrium coverage with illumination is smaller than in the dark. Since the experiment was conducted with a weak light source (of ~2.4 mW/cm^2, UV-only) the total temperature increase of the μ-reactor is *well below* 1 K as the light is turned on, so methanol desorption is not a thermal effect [8]. It is very interesting to see how the water signal responds to illumination. Clearly, water is produced by the reaction as expected, but it takes a long time before steady-state is reached after illumination is toggled. In the experiment the light was toggled every four minutes, and this is not nearly enough to obtain steady water signals - while the CO_2 signal still stabilizes within a minute. As a consequence of this behavior any experiment with water will inherently take longer time to carry out than a corresponding CO experiment.

[8] The setup is perfectly capable of carrying out TPD (Temperature Programmed Desorption) experiments so in principle any thermal effect could be quantified, but this was not pursued.

Water splitting ($2H_2O \rightleftarrows 2H_2 + O_2$) is of course a classic (but difficult!) reaction in the field of photocatalysis. The main problems are that TiO_2 doesn't really work since electrons in the conduction band are not reducing enough to drive the HER reaction ($2H^+ + 2e^- \rightleftarrows H_2$) and also since the water splitting reaction is strongly uphill ($\Delta G^{\ominus} = +1.23$ eV/electron (4.92 eV/oxygen molecule)) and prone to running backwards, so a system is needed which catalyzes HER and OER, but not HOR or ORR. In the early 1980's Domen ran the water splitting reaction using $SrTiO_3$ particles as the semiconductor, since $SrTiO_3$ has a conduction band high enough to run the HER and using NiO-covered Ni as a co-catalyst [73]. Fabio Dionigi (PhD student at CASE) has recently tried to run this reaction in the μ-reactors with catalyst prepared similarly following Domen's papers, but without measurable turnover so far. Judging from Domen's papers it is also quite optimistic to expect measurable turnover since Domen reported *very* low activity [9] for this reaction and this catalyst.

Another reaction which would be interesting to try is PROX i.e., PReferential OXidation of CO in the presence of (a large surplus of) H_2. The hope would be that a photocatalyst could achieve high selectivity towards CO oxidation [10]. This reaction is also on our "to-do list".

A final reaction, which we are keen on trying out, is NO (nitric oxide) decomposition (DeNOX model reaction). This particular reaction has also been studied by Rusu and Yates (over TiO_2 (110) at low temperatures), who found that N_2O (nitrous oxide) to be the primary product [74].

5.4 Macro-reactor

Despite its advantages, the μ-reactor system is unsuited for certain types photocatalytic experiments. There are three main reasons for this: Firstly, that the QMS used for detection in the μ-reactor system is orders of magnitude less sensitive towards organic compounds compared with a GC fitted with a flame ionization detector (FID). Secondly, that the ultra-small reaction chamber of the μ-reactor cannot accommodate any catalyst unless it either is in the form of a sub-micron powder or is deposited directly on the lid or reactor surface as a thin-film. The third and final reason is that for reactions where the rate is extremely low a batch-reactor (as opposed to a flow reactor like the μ-reactor)

[9] Domen reports a rate of 4.4 μl/h and 2.2 μl/h (hydrogen and oxygen respectively) for 2 g (!!) of catalyst under illumination from a 450 W high-pressure Hg-lamp [73]. This is equivalent to 1.5×10^7 H_2 molecules/s for each μg of catalyst under quite intense UV-illumination. In general, the detection limit of the μ-reactor is between 1 and 10 ppm of the total capillary flow (depending on high high the background of the signal of interest is in the QMS). With 1 bar in the μ-reactor and using the small capillary the reactor flow is on the order of 5×10^{14} molecules/s (see section 5.2.2) leading to a detection limit for hydrogen or oxygen of about 5×10^9 molecules/s, hence we need *at least* 670 μg of catalyst in the μ-reactor to be able to see turnover on the oxygen signal. Since the volume of the μ-reactor only is 240 nl, the catalyst must be packed with an effective density of 2.8 g/ml. This is an order of magnitude higher than what can realistically be expected (the "tapped density" of P25 is only 0.13 g/ml according to its data sheet) so it is quite ambitious to measure water splitting with Domen's catalyst in the μ-reactors.

[10] From a practical application, where H_2 for a PEMFC must be reduced from e.g., 1000 ppm to < 20 ppm one would need an APPE $> 10\%$ since the electrical cost to run the UV-source would otherwise consume a significant fraction of fuel cell's production.

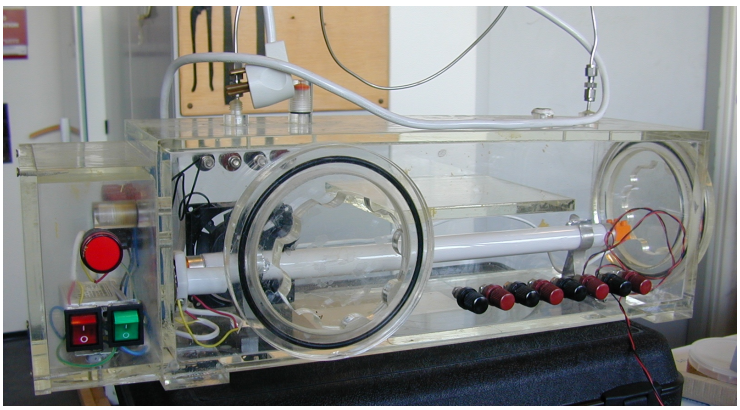

Figure 5.16: Photograph of the old photocatalytic batch reactor, "the incubator". The internal volume is approximately 25 l. The box is made of acrylic and can accommodate several different light sources and rather large photocatalytic surfaces.

can sometimes be necessary in order to obtain a quantifiable amount of product.

For these reasons our group has also employed big photocatalytic reactors for various purposes. The first of these (nicknamed "the incubator") is a large closed box (25 l volume) made from acrylic and with a built-in fan for forced mixing. A photograph of the incubator is seen in Fig. 5.16 It uses an internal light source and we detect turnover either by using a small commercial combined $CO/H_2O/CO_2$ measuring unit inside the box or by hooking the box up to a GC using an external pump and circulating gas through the sampling loop of the GC. In general terms, the incubator is not an ideal system. The main problem is its polymeric construction and its large volume. These "features" result in a reactor which is almost impossible to get really clean since it cannot be baked or evacuated, and many species of interest can (and do!) diffuse into and out of the acrylic walls and that leads to a pronounced, but unpredictable "memory effect" [11].

In order to address the problems of the incubator, yet retain its versatility towards photocatalyst and reaction, we came up with a very simple design which we called the "macro-reactor". It is made up, simply, of two 6 inch Conflat (CF) viewport flanges with a double-sided conflat spacer flange in between and can be seen in Fig. 5.17. The purpose of the spacer is to provide space to weld on interfaces (gas inlet and outlet, thermocouple and electrical feedthrough) to the reactor. The macro reactor uses external light sources such as low-pressure Hg-lamps or arrays of UV-LEDs (Light Emitting Diode). The GC is used to measure turnover (again by pumping the gas from the reactor via the sampling-loop of the GC). The macro-reactor can (just) accommodate a sample as large as a 4 inch wafer, and the total volume (including gas circulation tubing) is about 300 ml. So while it is much smaller than the incubator it is 10^6 larger than the μ-reactor. The macro reactor has proven highly useful for experiments with "difficult" reactions

[11] The last experiment carried out in the incubator affects the current experiment.

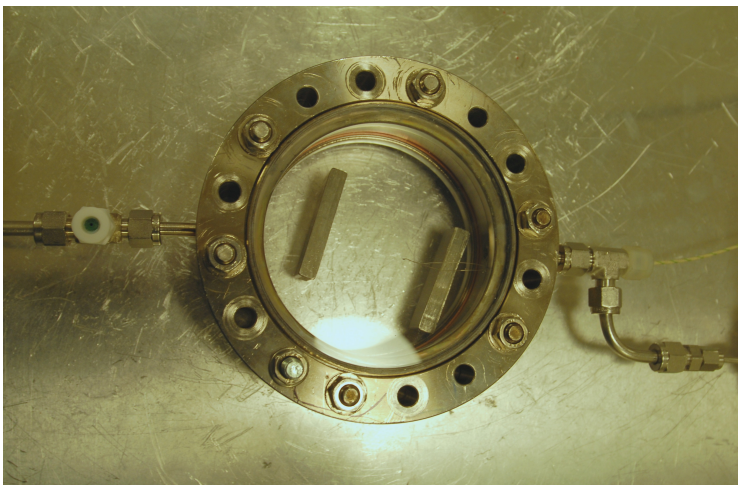

Figure 5.17: Photograph of the new batch reactor (the "macro-reactor"). All components (except the injection septum seen to the left of the reactor) are UHV-compatible so the system can be evacuated and baked if necessary. Gas is circulated using an external pump to a GC for detection. Total volume of the system is 300 ml.

such as photocatalytic CO_2 reduction ($CO_2 + 3H_2 \rightleftarrows CH_4 + 2H_2O$), but it has also been used successfully for methane oxidation.

Chapter 6

Electrochemical ammonia

This chapter deals with my "side-project": Electrochemical ammonia. As it turned out, I spent a significant part of my time on this project and carried out many interesting experiments (as well as a few frustrating ones). However, I never really managed to conclusively demonstrate that it is possible to make ammonia electrochemically which is why nothing about this project has been published so far. My intention with this chapter is to document some of the noteworthy points about the project and present experimental tricks and tips as well as lessons learned so that mistakes are not repeated. It is not intended to give a comprehensive overview of the topic, nor to describe in any detail the many experiments carried out.

6.1 Motivation

The motivation behind the project is to find an alternative to the extremely important industrial Haber-Bosch process, viz:

$$3H_2 + N_2 \overset{\text{Fe}}{\leftrightarrows} 2NH_3, \quad P = 150 \ldots 300 \text{ bar}, \quad T = 450 \ldots 500°C \tag{6.1}$$

One reason to seek an alternative route is that the Haber-Bosch plants are *very* big units. A modern plant produces about one million tonnes NH_3/yr, and the total annual world production is about 100 times as big so each plant is huge. Decentralized NH_3 production would be advantageous - perhaps especially in developing countries where infrastructure for transporting fertilizers to remote areas might be inadequate: Nitrogen fixation is also a potential strategy for storage of surplus renewable (intermittent) electricity in useful chemical form [1]. The hope is that an electrochemical process can be found which will render it possible to fixate N_2 at low pressures (preferably ambient) at low, or at least moderate, temperatures. Enzymes can do it, so it *is* possible.

[1] Another dream reaction for this purpose is electrochemical fixation of CO_2 as methanol or other simple organic molecules.

6.2 Background

There are two main strategies for making ammonia electrolytically. One is to activate nitrogen on a cathode surface and react it off by hydrogenation. In this case current is being carried by protons. The other strategy is to reduce N_2 to nitride (N_3^-) anions which carry current and serve as a source of reactive nitrogen at the anode. The latter approach has been popular in Japanese groups after Goto and Ito showed, very convincingly, that nitride ions can be made from N_2 gas in a molten salt (KCl, NaCl eutectic) electrolyte at 450°C (737 K) over a nickel cathode [75]. Goto and Ito used the process to grow a film of TiN on a Ti anode, but later Murakami et al. showed that a similar strategy could be used to make NH_3. They used a LiCl-KCl-CsCl eutectic and a nickel-sponge cathode to make 8×10^{-6} mol NH_3, corresponding to a current efficiency of 72% at 400°C (673 K)[76]. The former strategy has been shown to be theoretically possible [77], and (initially) based on claims of success in the literature [78], this approach has been the focus of the efforts of the CAMd/CINF group (formerly CAMP/ICAT, and now also CASE).

The electrochemical ammonia project was the very first project I started working on at CINF. It was all along intended to be my side project (with photocatalysis as the main project). I was the third person to run the electrochemical NH_3 synthesis project at CINF, following two Post Docs. (John Davis and Tatiana Morante). John tried to reproduce the result of Marnellos and Stoukides and of Kordali et al. ([78, 79]) who were both claiming successful electrochemical ammonia synthesis in two different cell designs at low pressures and temperatures. Both strategies were thoroughly tested in cells copying those from the papers, but none could be made to work convincingly. Although ammonia was produced at a rate comparable to that of Kordali et al. (0.1 μg/(cm^{2}h) vs. 0.2 μg/(cm^{2}h)) the same "activity" was seen when nitrogen feed *was swapped for argon* leading to the conclusion that trace-amine species in the Nafion electrolyte of the Kordali cell or perhaps degradation of the membrane itself, was giving the ammonia signal. In any case (as is the case for *all* reports of (near) room temperature electrochemical ammonia synthesis) the rates were exceedingly low [2]. Boucher et al. explain many of the pitfalls in investigating ammonia synthesis in general and photocatalytic ammonia synthesis in particular [80, 81].

6.3 Catalysts and electrolytes

During the past three years time I have worked with only two cathode materials, namely molybdenum nitride (Mo_2N) and barium nitride (Ba_3N_2), although the current work at CAMd (by Post Doc. Anthony Goodrow) indicates that tungsten nitride is also worth consideration. In all cases the choice of of materials is guided by DFT calculations on the free energies of the various intermediate states involved. As an example, consider Mo_2N which is seen in Fig. 6.1. The potential energy landscape of the complete cycle (starting from a nitrogen vacancy in the Mo_2N surface, a nitrogen molecule and six protons and electrons and going to two ammonia molecules and a new surface vacancy) is shown in Fig. 6.2. The

[2] To the point where detection of product without contamination from materials or environment and without interference from other species becomes a major problem.

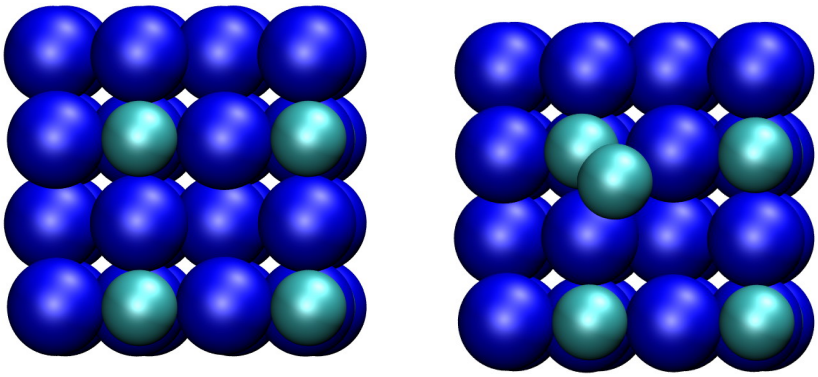

Figure 6.1: Renderings of the atomic arrangement of a surface of Mo_2N made by Eva M. Fernández (then, Post Doc. at CAMd). The large, blue spheres are Mo-atoms, while the smaller turquoise spheres represent N-atoms. The figure on the left shows the virgin surface while the figure on the right shows the surface where the top-left N-atom has been removed (e.g., hydrogenated away as NH_3) and replaced by an adsorbed N_2 molecule.

energies shown are calculated, lowest energies for each intermediate step and as such do not include any activation barriers (we consider thermodynamics only - not kinetics). The figure reveals that absorbing and dissociating the N_2 molecule should be no problem on this surface. Once dissociated, the hydrogenations are (relatively) easy to carry out and the only real thermodynamic barriers seem to be getting the product molecules to desorb, but at no more than 0.5 eV this should not present any problem in practice. In other words, the material looks promising. A possible problem, however, could be competing hydrogen evolution. At -0.63 V the HER should run easily, so the current efficiency could be very low because of this. Another, more practical, problem could be to make a surface like that shown in Fig. 6.1 and keep it clean since trace oxygen (or perhaps even water) would bind to the surface stronger than nitrogen and poison the activity [3].

The need for a proton conducting electrolyte which does not contaminate the catalyst surface with hydroxyl groups or oxygen and which preferably can operate from room-temperature and up to at least 150°C (423 K) was what led to the choice of an ionic liquid electrolyte. In general, the term "ionic liquid" [4] refers to pure compounds which are liquid at (or near) room temperature and are almost entirely ionic in character. This also means that they have exceedingly low vapour pressures. The ions, generally, have high stability towards electrochemical oxidation or reduction so the "electrochemical window" of the ionic liquids can

[3] Both these problems (competing HER and oxygen poisoning) are unfortunately general in nitrogen fixation. No known enzymes can hydrogenate nitrogen selectively without also making H_2 which, of course represents a huge waste of energy for the organism and oxygen poisoning of the active surface is a major problem since essentially any surface that is reactive enough to bind N_2 will bind O_2 even stronger. In the industrial Haber-Bosch process cleaning the feed gas from residual oxygen (water) is a major issue and much energy (literally) is spent on this to avoid catalyst deactivation.

[4] Also sometimes referred to as "room-temperature molten salts".

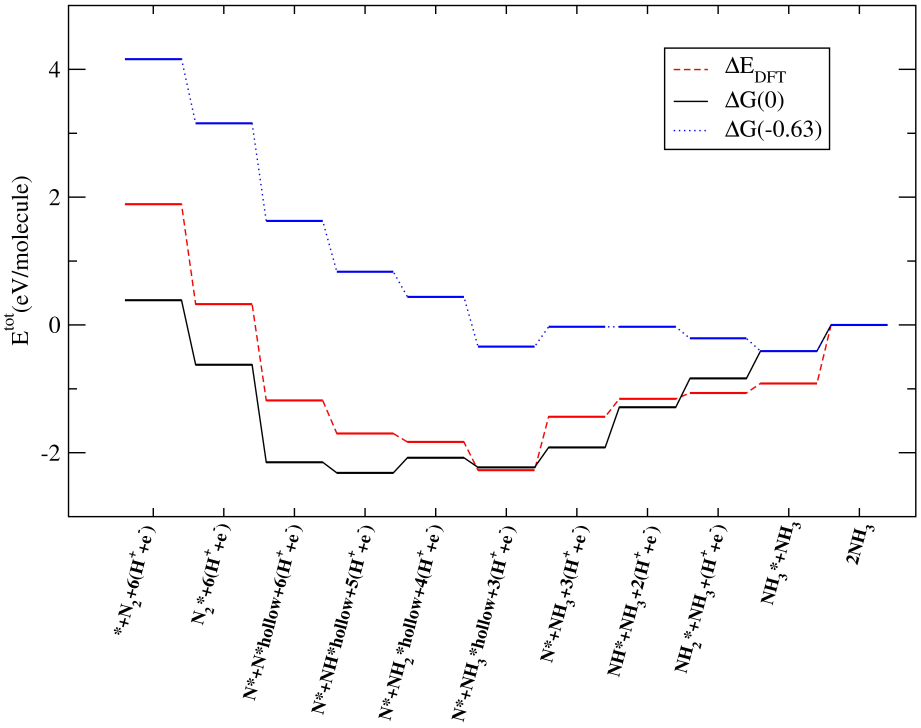

Figure 6.2: Energies of the ammonia synthesis process over a Mo_2N surface as calculated by Eva M. Fernández (then Post Doc at CAMd). The $*$-symbol represents a nitrogen vacancy in the Mo_2N surface. The curves for ΔG take into account the entropy changes and are shown for cathode potentials of 0 V and -0.63 V vs. a hydrogen electrode. The first two steps (absorbing *and dissociating* the N_2 molecule are clearly downhill). In the next the steps the first nitrogen is hydrogenated (potential dependent steps) and then the first NH_3 molecule desorbs (slightly uphill). Then the second N-atom is hydrogenated and it is seen that the first hydrogenation step is more reluctant than it was with the first nitrogen (this time U $= -0.63$ V is needed for the hydrogenation to be unhindered). Finally, the second NH_3 is desorbed and that is also uphill by about 0.5 eV.

be up to four volts wide [5]. The cation which must be extremely electropositive can be as simple as Li^+, but is usually a simple organic. In our case is is 1-ethyl-3-methylimidazolium (known as [EMI]) i.e., the electron donating species is the imidazole-group (containing two nitrogen atoms). The anion must be very electronegative. Simple cations include BF_4^- and PF_6^-, but in our case it is the bis(trifluoromethylsulphonyl)imide i.e., $N^-(SO_2CF_3)_2$ (known as [TFSI] or [Tf2N]). Both ions may be seen in Fig. 6.3. Exactly why this particular electrolyte ([EMI][TFSI]) was chosen (by my predecessor) is not known to me, but I suspect it is due to fact that it is hydrophobic and has a low viscosity (for

[5] This is an important reason why they have been used in some lithium-ion battery chemistries where the electrochemical stability of the electrolyte often limits the maximum open-circuit voltage obtainable.

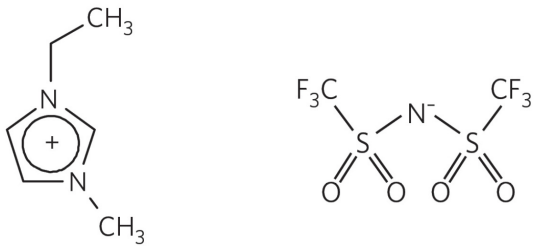

Figure 6.3: Components of the ionic liquid used as electrolyte in this work. (Adapted from [82])

an ionic liquid), making it easy to work with. There may well be better choices available. Nevertheless, the electrolyte is (the) one parameter which I have kept constant in all my experiments.

6.4 Brief history of early experiments

When I started working on the ammonia project I used an optical (infrared) NH_3-detector with a 0 to 5000 ppm dynamic range. The unit was very noisy (short term RMS noise of > 50 ppm NH_3) and random long term drift. Unaware of the fact that it was broken, I tried to use it for a few months, but eventually it was sent for repair where the measurement chamber was replaced since it was contaminated with "acid" - apparently from previous (mis)use. The repaired and calibrated unit enabled easy and convenient measurements of ammonia in a gas flow.

These early experiments were carried out using a small glass vial with a septum (PTFE-coated silicone) lid and using syringe needles to get gas into and out of the cell. Gas connections were made using flexible silicone tubing and flow direction was controlled by three-way valves of polycarbonate and the flows (of N_2, H_2 and sometimes Ar) were controlled using two MFCs. Essentially all experiments were "batch" experiments in the sense that the cell was run a constant potential (chronoamperometry) for a certain time or until a certain total charge had been passed. During this time the cell was supplied with a small flow of hydrogen and nitrogen and a freeze-trap (stainless steel tube down-stream of the electrochemical cell) was used to capture any ammonia product. A simple drawing of one of the ways these experiments were carried out can be seen in Fig. 6.4. The batch experiment consisted of two distinct phases ("synthesis" (accumulation of product) and "flush" (detecting product)). Both phases are shown in Fig. 6.4, which also shows an experimental configuration where the anode is kept in the outer "compartment" of the cell to minimize loss of ammonia due to oxidation on the platinum anode. This configuration, however, means that the protons must diffuse longer (giving lower cell currents at any given temperature). It also means that the air-tightness of the system is determined by the outer septum alone. An alternative configuration is seen in Fig. 6.5 where the inner vial is closed (and therefore contains both the anode and cathode) allowing the outer glass vessel to be filled with purge gas, to minimize any leakage

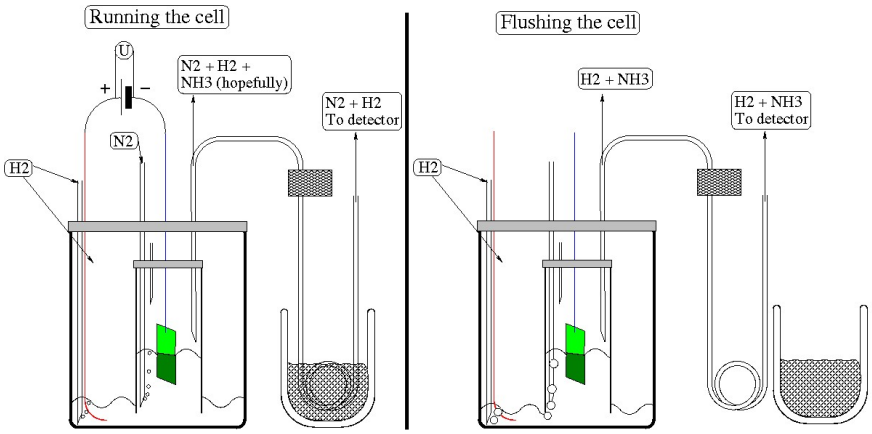

Figure 6.4: Sketches of one way of doing batch experiments in the "old" NH_3 setup. The sketch on the left shows the state of the cell during ammonia synthesis is seen. H_2 is bubbled into the outer compartment, which also houses the platinum anode. Protons may then diffuse to the inner cell, to which a flow of N_2 is also led. Hopefully, nitrogen is then reduced on the cathode in the inner cell and product ammonia is carried out of the cell by a stream of surplus H_2 and N_2 and into a freeze trap, which is cooled by ethanol slush ice (or liquid nitrogen). Ammonia should then be captured in the freeze trap, while hydrogen and nitrogen pass the trap and continue through the infrared detector and out the vent (via six meters of 1/8 inch OD tubing to prevent back-diffusion). The sketch on the right shows how the cell and freeze-trap are flushed after a suitable time (or charge) has passed. The electrolyte is bubbled through with a high flow of H_2 and the freeze trap is thawed (e.g., by means of hot water).

of atmospheric oxygen into the inner cell. A myriad of different experiments with various tricks and experimental configurations such as those shown in Figs. 6.4 and 6.5 to solve different problems where carried out over approximately one year. I will not describe any of the experiments in detail, but I have drawn a rough time-line (Fig. 6.6) which features key dates and events in the ammonia project. There are actually two lines in the figure. The top one shows major changes/advances in the experimental setup. For instance, it shows in which period I used the noisy NH_3 detector when it came back after it had been repaired and when I switched to using a QMS as my primary detector (more about this in section 6.5). It also shows that by February 2008 I started using my new "UHV-style" setup, which was completely free of polymers or elastomers - an all-stainless steel and glass construction (see section 6.5). The lower line in the figure shows when I was using which cathodes and it also shows a couple of noteworthy experimental results.

6.4.1 Some results

After I got the NH_3 detector back from repair I had pretty much settled on an experimental method. I used this to carry out a number of experiments and

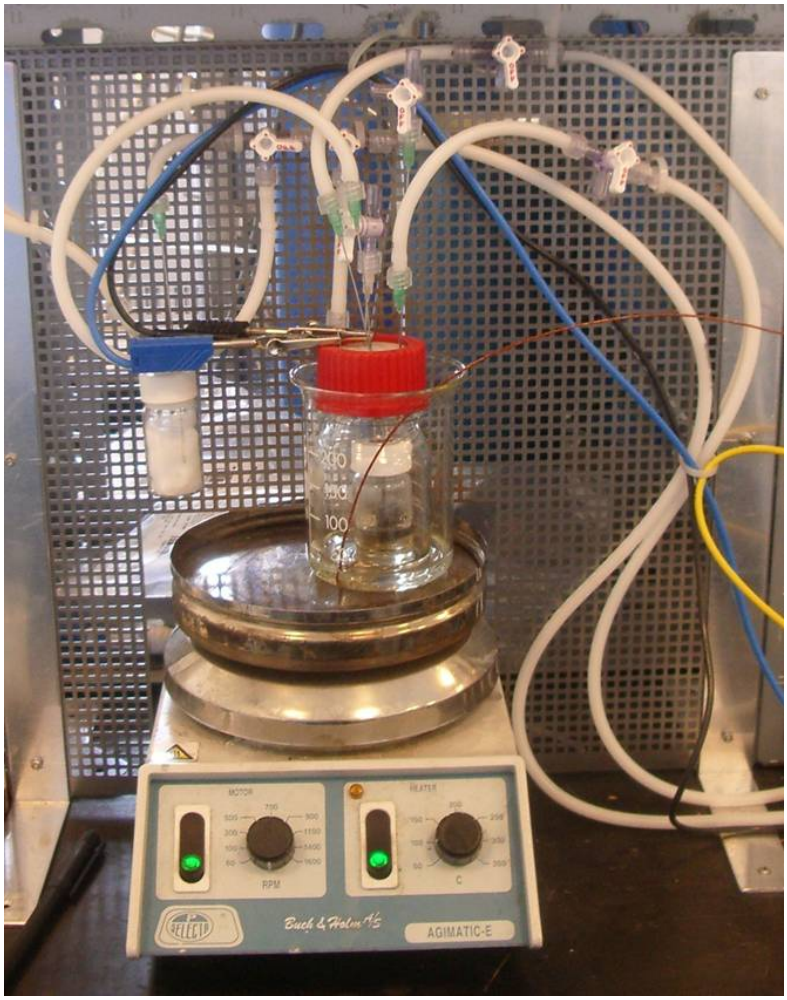

Figure 6.5: Photograph of one particular 'incarnation' of the old setup. The cell (inner glass vial), in this case is entirely contained inside the outer glass vial (i.e., it contains both a cathode and an anode unlike the configuration shown in Fig. 6.4). This vial sits inside a larger glass (with the red GL45 cap), which is continually purged with argon. The purpose of this outer container is to minimize the leakage of air through any possible leak in the septum of the inner cell. The outer glass container stands in an open beaker with some silicone oil to help transfer heat from the hotplate below. A thermocouple is used to measure the temperature of the silicone oil.

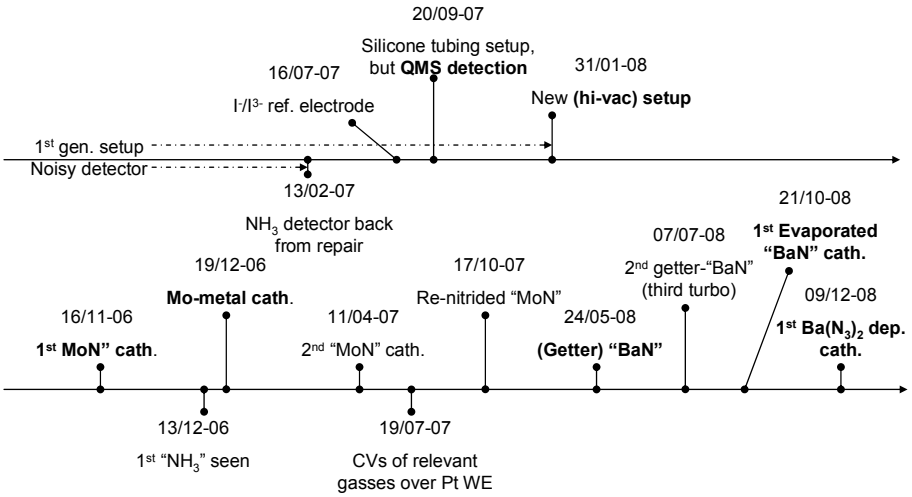

Figure 6.6: Chronological overview of my ammonia experiments. The top line represents major events in the experimental setup while the lower line represents notable changes in catalyst (cathode) and a few experimental results.

control experiments, in an attempt to make sure that I was was not getting any "false positives". The quick summary of an experiment was a follows:

- Purge the electrolyte with a N_2/H_2 mixture (30 sccm/ 4.5 sccm) and heat the electrolyte to $\sim$90°C.
- Freeze the trap [6].
- Apply potential and wait a suitable amount of time while keeping the trap frozen and the electrolyte temperature approximately constant (chronoamperometry).
- Unfreeze the trap and set N_2 to zero and the H_2 flow to 15 sccm and record the resulting ammonia peak with the infrared detector.

Several attempts at making ammonia using a molybdenum foil convinced me that metallic Mo does not work as a cathode for this reaction [7]. There was simply never any difference in ammonia signal between attempts at making ammonia over molybdenum, and control experiments with e.g., no current passed. After this was established I was ready to start doing experiments with nitrided Mo-foils once again, and I used a virgin piece (which had been lying around for over

[6] Preferably the trap should be frozen with liquid nitrogen to minimize ammonia loss, but that cannot be done if one also wants to perform a reference experiment using argon instead of nitrogen since argon liquifies in the trap (highly problematic when the trap is thawed)! On the other hand, using a slush ice of ethanol instead of liquid nitrogen is only practical at T≈ -110°C (163 K), but at this temperature ammonia has a finite vapour pressure (on the order of 0.1 to 0.5 Pa), hence some ammonia will be lost in this case.

[7] No-one had predicted that metallic Mo should work, quite the contrary, but it is sometimes nice to know what "no-activity" looks like - particularly for a complicated experiment such as this.

Results. 2nd Mo_2N cathode.

Date yr/m/d	Gasses	Voltage (V)	Time (h, min)	Charge (μAh)	Peak height ppm	Note
07/04/23	H_2 + N_2	-2.0	5,20	-138	∼30	a (†)
07/04/25	H_2 + N_2	0	5,10	∼ 0	[1;2]	Ctrl
07/04/26	H_2 + N_2	-1.0	4,45	-20	[1.5;2.5]	b
07/05/01	H_2 + N_2	-2.0	4,45	-137	∼ 5	†
07/05/02	H_2 + N_2	-2.0	4,45	-169	∼ 6.5	†
07/05/23	H_2 + N_2	-2.0	5,00	-148	[6;6.5]	†
07/05/24	H_2	-2.0	4,10	-142	< 1	Ctrl
07/06/04	H_2 + N_2	0	5,00	∼ 0	[1.5;2.5]	Ctrl
07/06/05	H_2 + N_2	0	5,20	∼ 0	[1.0;2.5]	Ctrl
07/06/22	H_2 + N_2	-2.0	5,50	-92	∼ 4	c (†)

a, Abnormally large NH_3 peak. Possibly because this is the first experiment with this electrode?

b, Lower voltage experiment. At this voltage (and total charge) the peak is not significantly different from some of the reference experiments.

c, Total charge is quite small. The reason is unknown.

Table 6.1: Collection of data from the last two months of experiments with the infrared NH_3 detector. The peak height is measured as the difference between the stable offset level before flushing (while the freeze trap is still frozen) and the peak in the NH_3 signal, which occurs a few minutes after the trap is thawed. The experiments marked with a † symbol are the main experiments where NH_3 synthesis is attempted and they give a peak height of about 6 ppm, whereas the control experiments generally give a peak of less than 2.5 ppm. There is a difference, but it is not big enough to be convincing.

six months, but had not earlier been used electrochemically). The result of the experiments with this foil are summarized in table 6.1. The table shows data and experimental parameters from a series of ten experiments using the "old" (silicone tubing, glass vial) setup and a nitrided Mo-foil as the cathode. The first observation is that the very first experiment using this electrode gave rise to an abnormally large peak. In fact, integrating the area of this peak (200 ppm×minutes) and multiplying it by the gas flow rate, when flushing the cell and freeze trap (15 sccm), the total amount of NH_3 turns out to be 3.0 μl, which corresponds to a current efficiency of 7.7% - not bad at all! Later experiments attempting to repeat this (i.e., the 07/05/02) experiment, however, showed significantly lower NH_3 signals (and a correspondingly lower current efficiencies of about 1%). Assuming that the good result from the 07/04/23 experiment is not an artifact of some kind this could indicate that the virgin electrode has some nitrogen, which may be irreversibly hydrogenated away, leaving a less active (but truly catalytic) surface behind. However, since the wetted surface in these experiment was on the order of 2 cm^2 in area (i.e., $\sim 2 \times 10^{15}$ sites in the absence of roughness) and 3.0 μl corresponds to 8×10^{16} NH_3 molecules, so this explanation alone is not satisfactory. Of course it is also possible that something is just wrong with the 07/04/23 data. In any case, this enhanced apparent, activity of virgin electrodes certainly begs for more investigation.

After the experiments, summarized in table 6.1, were carried out I started using the QMS in place of the optical detector. The reason for the change in detector was that we had to verify that any water contamination in the gas (i.e., captured in the freeze trap) was not being mistaken for ammonia - i.e., that we were misinterpreting the measurement. Indeed we knew, that the infrared detector had have some cross-sensitivity towards water vapour. The idea was that a mass spectrum of the contents of the freeze trap would prove (or disprove) the presence of ammonia - and it would also allow isotope labelled experiments - e.g., to see if indeed a virgin electrode contributes nitrogen to the ammonia, or if every N-atom comes from N_2. As it turned out, getting conclusive evidence of ammonia using a QMS was even harder than imagined, due primarily to cross-talk with water on m/Z = 16 and 17. Even m/Z = 15 is problematic due to the low signal of ammonia on this channel and the background from N_2 (due to naturally occurring N-15) and CH_3 from organic junk (like roughing pump oil) or trace ionic liquid. To date, the body of data in table 6.1 is still the best experimental "evidence", that we have for electrolytic ammonia.

6.4.2 CVs of relevant gasses over a Pt WE - a short digression

One of the challenges of doing electrochemistry in a non-aqueous electrolyte is that many familiar concepts (like pH) change their meaning and there are no well known standard reference electrodes available. Case in point: Fig. 6.2 tells us that no electron transfer steps are uphill in Gibbs free energy if the potential is below -0.63 V (vs. H^+/H_2/Pt at pH = 0, 1 bar H_2 and T = 298K), but how is the potential measured (or even defined) in the ionic liquid? Obviously, hydrogen pressure and temperature are experimental parameters, but pH? Also, when using metallic "quasi"-reference electrode for three electrode experiments the reference potential drifts over time in an un-predictable way.

The effect is seen in Fig. 6.7, which shows repeated CVs of the ionic liquid saturated with nitrogen using a Pt-wire as a quasi reference electrode and using a homemade reference electrode based on the I^-/I_3^-/Pt system [8].

Having made a working, practical reference electrode I went on to compare the CVs of gasses relevant to the project i.e., hydrogen and nitrogen and argon, but also oxygen and water to know what features to look out for. In Fig. 6.8 I have collected five such CVs for comparison.

[8] The electrode was made by dissolving [EMI]I and I_2 in [EMI][TFSI] (the ratio if [EMI]I to I_2 is 4:1 so that the I^-/I_3^- ratio becomes 3) and placing the solution in a glass tube terminated by a glass frit (the tube with frit was salvaged from a retired commercial Ag/AgCl reference electrode) with a thin Pt-wire dipping into the electrolyte. Such an electrode has a potential of −0.21 V vs. ferrocenium/ferrocene [83].

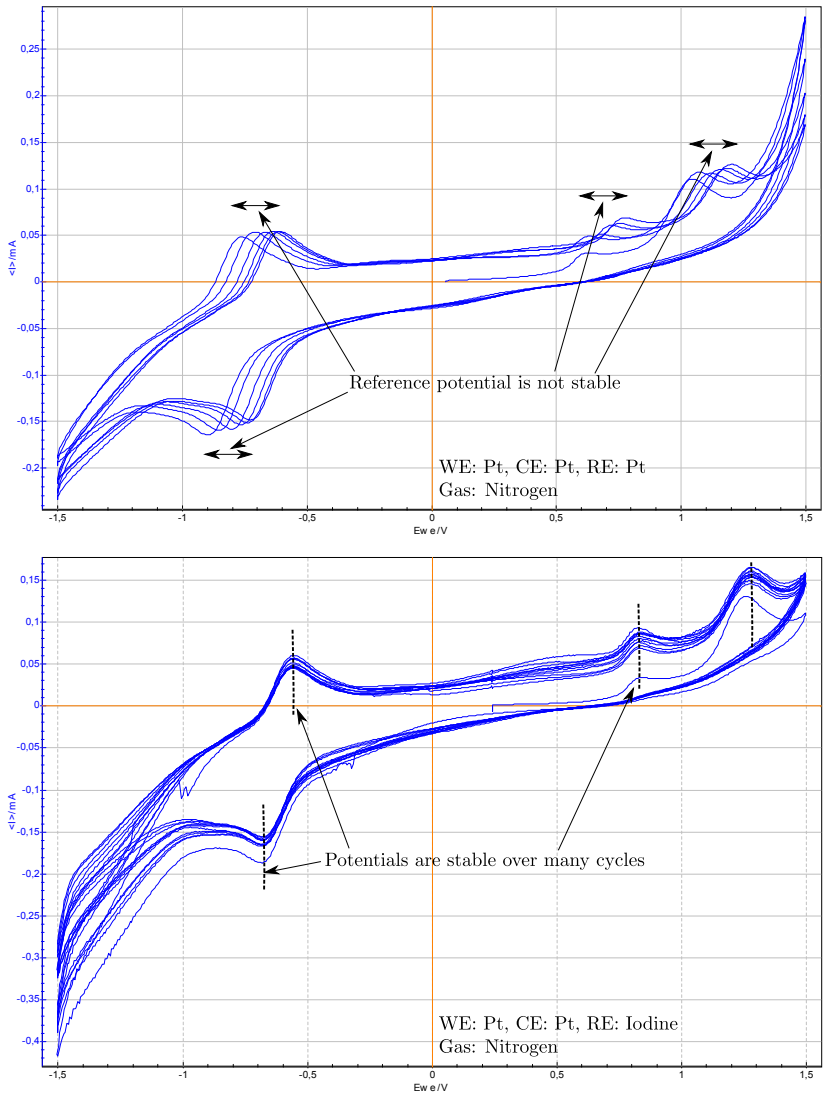

Figure 6.7: Cyclic voltammograms of nitrogen dissolved in [EMI][TFSI] at 90°C (363 K) over a Pt working electrode. The top graph shows an experiment using a Pt wire as a "quasi" reference electrode. The repeated cycles show that this reference electrode performs poorly since the electrochemical features drift around. This in stark contrast to the bottom graph, which shows the same experiment, but this time using a homemade iodine-based reference electrode. In this case the features occur at highly stable potentials.

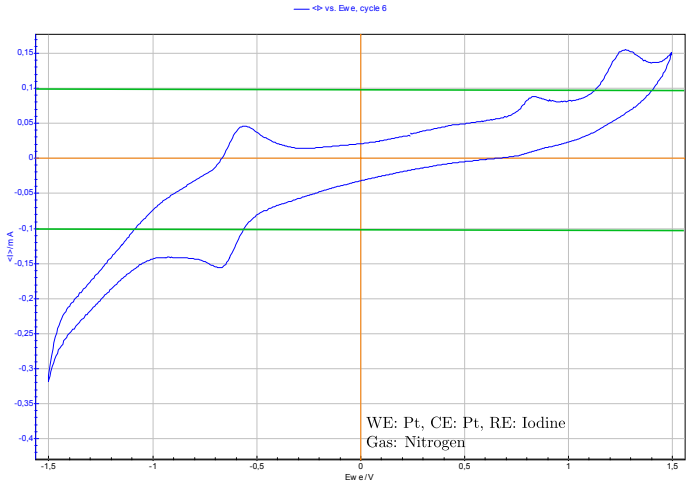

(a) CV of dissolved N_2

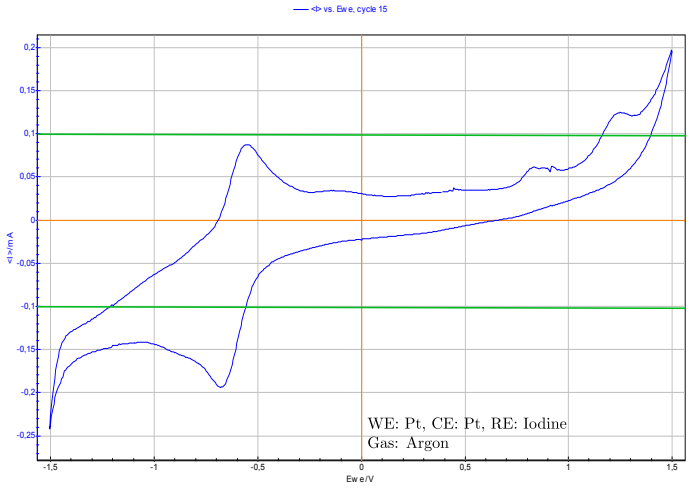

(b) CV of dissolved Ar

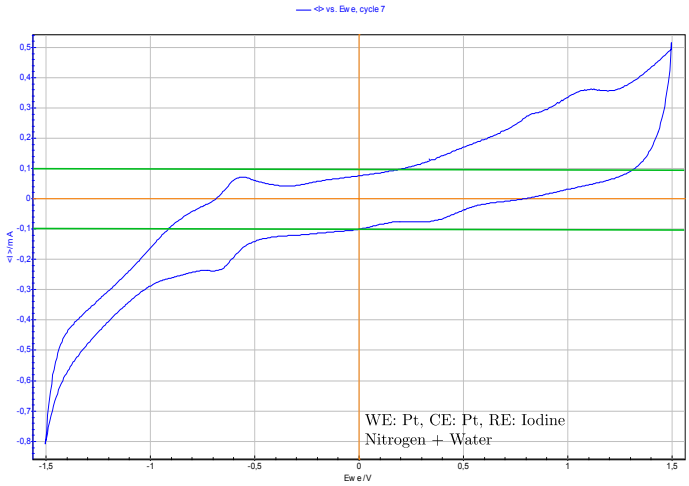

(c) CV of dissolved Water and N_2

Figure 6.8

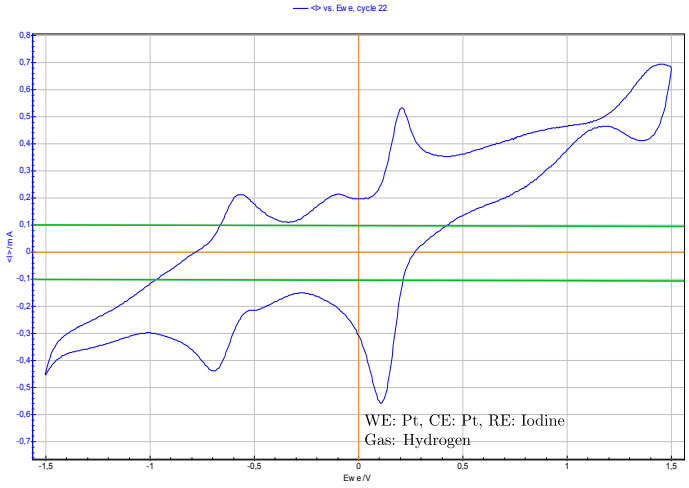

(d) CV of dissolved H_2

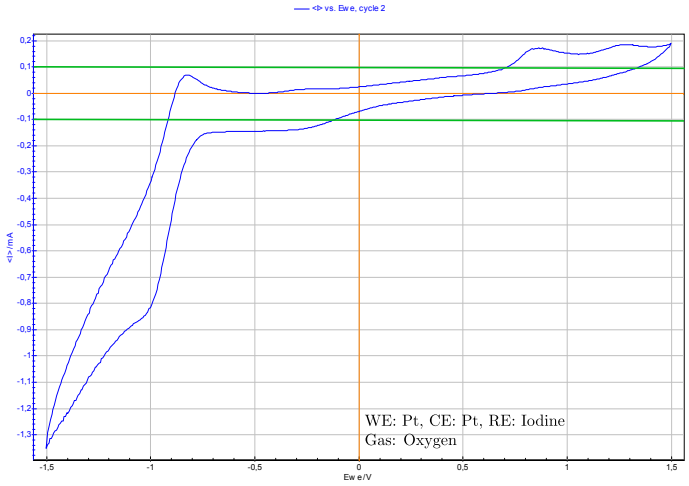

(e) CV of dissolved O_2

Figure 6.8: Cyclic voltammograms of various gasses (and water) dissolved in [EMI][TFSI] at ambient pressure. Working and counter electrodes are both Pt. The reference is I^-/I_3^-/Pt. Temperature in all cases is around 90°C (363 K). The green lines are drawn at $I = \pm 0.1$ mA, to aid the eye in comparing the order of magnitude of the current in the various cases.

All CVs were recorded with the ionic liquid temperature of about 90°C (363 K) and using the iodine reference electrode. All the CVs show a common pseudo-reversible feature at -0.55 V in the anodic sweep and -0.65 V in the cathodic sweep. What causes this feature is not clear, but is most likely some redox-active impurity in the ionic liquid - or perhaps the ionic liquid itself. Another interesting observation is that the feature is stronger (in absolute terms) when the electrolyte is saturated with argon (Fig. 6.8b) than when it is saturated with nitrogen (Fig. 6.8a). When a bit of water (0.1%) is dropped into the ionic liquid (Fig. 6.8c) current goes up significantly with respect to the nitrogen case. At low potentials it looks as if the capacitance of the cell has increased and when a large bias is applied (either positive of negative) current is much higher than in the "dry" nitrogen case. Presumably, water is electrolyzed when the WE-CE voltage becomes significantly higher than 1.23 V (Faradayic current). Unfortunately, no clear new feature in the CV occurs in the presence of water, so a CV cannot be used to prove (or disprove) that the electrolyte is contaminated with water. Figure 6.8d, which shows the CV when the electrolyte is saturated with hydrogen, is an entirely different story. In this case there is a new semi-reversible feature in the CV at +0.2 V (anodic sweep) and +0.12 V (cathodic sweep). It is tempting to think that this corresponds to the hydrogen underpotential-deposition region (UPD) (well known for hydrogen on platinum in aqueous electrolytes). In that case the reversible absorption of hydrogen which starts at (∼0.25 V) above the reversible potential for HER (0.0 V at pH = 0). Since the potential window of the CV is large, and since both the WE and the CE is Pt (over which the $2H^+ + 2e^- \rightleftarrows H_2$ reactions both run essentially reversibly at low current densities), one would expect the cell to exhibit an ohmic resistive character as a proton conductor. This is evidenced by the overall slope in the CV. The mobility of the protons is highly temperature dependent and therefore so too is the slope of the CV. In chronoamperometry experiments (with hydrogen in the cell) at different pressures I found that upon decreasing temperature from 125°C (398 K) to 108°C (379 K) the steady state current will go down by a factor of 3. By 100°C (373 K) it is a factor of 10 and by 75°C (348 K) the current is about 17 times lower. Figure 6.8e indicates that oxygen is very redox active in the ionic liquid. At potentials around −0.75 to −0.7 V vs. I^-/I_3^- a comparatively large cathodic current is observed. Comparison with the potential of the "new" redox features in the presence of H_2 (+0.12 to +0.2 V) makes the potential for oxygen reduction seem strange. In aqueous electrolytes, ORR occurs about 0.6 V *anodic* of the H-UPD region, but in the ionic liquid ORR seems to occur at 0.9 V *cathodic* of what I speculated to be H-UPD. One possible explanation could be that the cathodic stability of the [EMI] cation is lower in the presence of oxygen and the reaction giving rise to the cathodic current could be something like: $[EMI]^+ + e^- \rightleftarrows [EMI]$ and the (electronegative) oxygen "removing" product via: $[EMI] + O_2 \rightarrow [EMI]\text{-}O_2$ shifting the former equilibrium to the right. This would also help explain the numerically high value of the cathodic current in this experiment, which is twice any current measured in the H_2 saturated experiment, despite the fact that HER/HOR are much faster reactions than OER/ORR on Pt and also despite the fact that H_2 should diffuse faster (giving higher transport-limited currents than O_2).

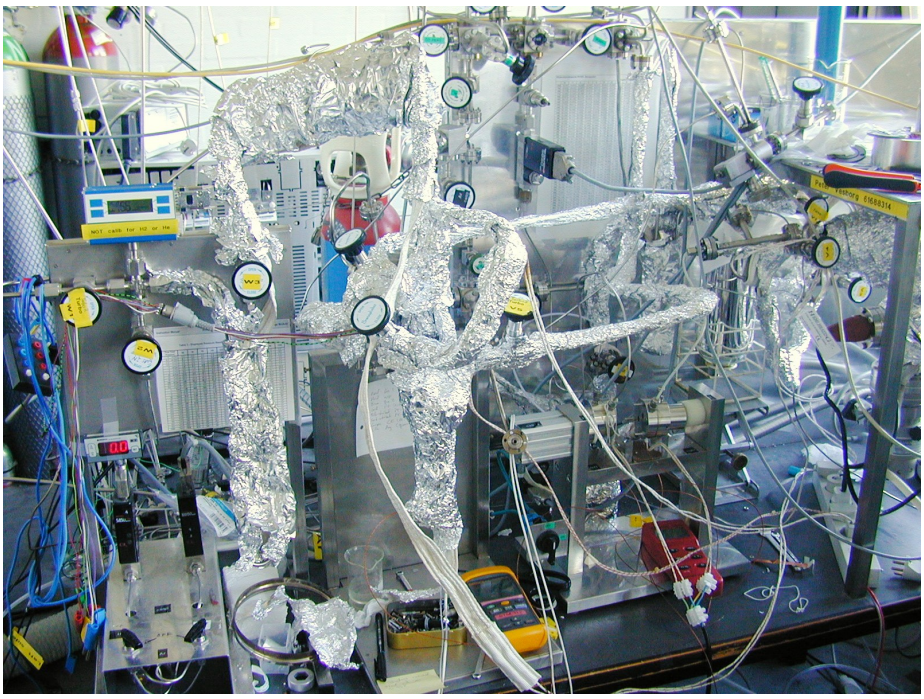

Figure 6.9: Photograph of the new ammonia setup. Everything that is wrapped in aluminium foil is part of the Ammonia setup (and everything that is not is part of our PEMFC setup). The setup has recently been moved to our new lab and is now considerably less confusing to look at, although it remains essentially unchanged.

6.5 Current setup

After the encouraging results in table 6.1 had been obtained with the infrared detector it was decided to try to measure the ammonia product with a mass spectrometer, in order to confirm that it really was ammonia. I first tried a few experiments running the old cell in conjunction with the QMS [9]. I only did a couple of these experiments, since significant amounts of water were being caught in the freeze trap and, since large water signals also interfere with ammonia detection in a QMS, it was clear that a whole new - much more airtight setup would be needed for these experiments.

The "new" ammonia setup evolved and gradually grew in complexity. Starting from a generation which used Swagelok-style compression fittings to connect tubing and without any provisions for pumping out lines and eventually becoming "UHV"-compatible. In the current system (seen in Fig.6.9 and schematically in Fig. 6.10), all fittings and connections are either VCR-style or Conflat-style employing single-use Cu-gaskets. All tubes are stainless steel and most are 1/4

[9]The way I did this was to connect the QMS to the freeze-trap (which is a stainless steel tube) and put entry and exit valves on the freeze trap. In this way I could run a normal experiment at 1 bar using the silicone tubing setup, and then seal off and evacuate the freeze trap before thawing it into the QMS for product detection.

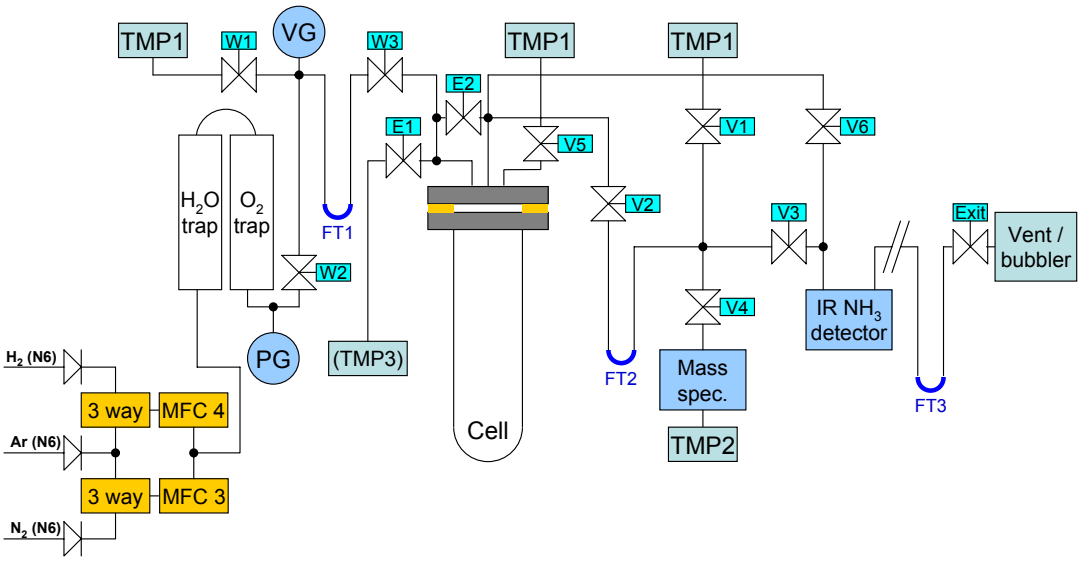

Figure 6.10: The new "UHV-style" electrochemical ammonia setup. 99.9999% N_2, H_2 and Ar are available via two MFCs. The gas is further cleaned by commercial GC-traps, one for water and one for oxygen and potentially also by a freeze trap (FT 1), before entering the cell at a pressure which is monitored by a capacitive pressure gauge (PG). The cell may or may not be fitted with an internal glass tube so the gas entering the cell is bubbled through the ionic liquid electrolyte. Gas leaves the cell and goes through FT 2, which is the main freeze trap for capturing product ammonia before it leaves the system via the infrared NH_3 detector and six meters of 1/8-inch tube, which severs the purpose of preventing back-diffusion. All parts of the system may be pumped by TMP1 (a turbo molecular pump) and the pressure in the gas supply region can be monitored by a vacuum gauge (VG). All major components including the cell and electrolyte can be baked.

inch in outer diameter to increase pumping speeds. All valves are of the "bellows" type (marked "W", "V" or "E" in Fig. 6.10). The cell itself is a 1.5 inch glass tube with a glass dome in one end and a Conflat flange in the other. This flange mates with a fixed flange, which is fitted with a commercial electrical feedthrough (eight individual feedthroughs [10]) and three 1/4 inch tubes for gas connections (inlet, outlet and pumping port). The system now contains no less than three freeze traps (FT) shown as blue semicircles in Fig. 6.10. FT 1 is situated before the cell. Gas from the gas supply system (which has already passed a molecular-sieve based water trap and a Cu-based oxygen trap) may be further cleaned (from water) by cooling FT 1. When thawing FT 1 after an experiment, closing W3 and W2 while opening W1 allows any water trapped in FT 1 to be pumped out by the turbo molecular pump (TMP1), without

[10] The large number of feedthroughs might seem excessive for two- or three-electrode experiments, but it has proven highly useful for auxiliary reference electrodes and for heaters during in-situ catalyst deposition (section 6.6).

contaminating the cell or other downstream components. FT 2, together with the cell, is the heart of the system. It is here that products are captured during an experiment. After an experiment V2 and V3 are closed and V1 is opened for a minute or so to pump FT 2 down to a reasonable vacuum before V1 is closed and the FT 2 thawed. Finally, V4 is slowly opened allowing products to enter the QMS. FT 3 is used as a "first line of defence" against water from the vent diffusing into the system. This is particularly important during periods where there is no flow (such as when the cell is being pumped out via V5) [11].

Nearly all of the experiments carried out in the new setup have been of the batch type with product capture in FT 2. In this respect the experimental parameters are very similar to the experiments in the old setup (total pressure in the cell of 1 bar, Pt counter electrode, [EMI][TFSI] electrolyte at 80 to 120°C (353 to 393 K) and chronoamperometry carried out at a WE-CE potential of about −2 V). The iodine reference electrode is quite bulky so rather than making a smaller version to fit the new cell, I decided to use an Ag-wire based quasi-reference electrode instead. The reference potential of this is not quite as stable as the iodine reference, but it is much better than a Pt-based quasi-RE.

At about the same time as the new setup became truly operational it was suggested by Sergey Dobrin (former Post Doc. at CAMd) that barium nitride (Ba_3N_2) was an interesting candidate as a cathode material. Therefore I shifted away from molybdenum nitride and started working out how to make barium nitride electrodes for the new cell (section 6.6). I did a very large number of full-day experiments in the new cell and on occasion I saw what *could* be interpreted as ammonia hiding in an ever present (albeit small) background of water, but again, the evidence was just too weak to support any conclusions - much less publications.

I think that the new electrochemical setup is a versatile and useful tool for any non-aqueous electrochemical experiment where oxygen must be avoided. The failure, so far, to observe any convincing ammonia signals in the QMS is not, I believe, due to any inherent shortcoming of the system and I think that an attempt at using high surface-area Mo_2N prepared by the single source method (section 6.6) would indeed be worth its while.

6.6 Selected catalyst synthesis methods

In this section, I will present some of the different ways of preparing catalyst which I have used in the ammonia project.

6.6.1 Molybdenum nitride

Mo_2N is said to be quite stable in air - at least in bulk (but probably the all-important surface will be oxygen covered). It can be made quite easily by

[11] To avoid a situation of stagnant gas in the exit tube (in which water or oxygen might back-diffuse into the system) every time V2 and V3 are closed, to thaw FT 2, I added a "bypass"-tube from the cell directly to the exit (via V6). By opening V6, a flow can be maintained constantly during regular experiments.

treating MoO_3 with ammonia at temperatures between 750 and 950°C (1023 to 1223 K), which will reduce the oxide to Mo_2N (temperatures below 700°C (973 K) give MoN), and it can also be made by treating the oxide with nitrogen at between 700 and 800°C (973 to 1073 K) [84]. This method of conversion of a thermally grown oxide was the method by which the foil samples used in the early experiments with the IR-NH_3 detector were made.

After some time Ib and I decided that it would probably be better to use nanoparticulate Mo_2N on some conductive support (to get higher surface area). If possible, the catalyst should be prepared in-situ (inside the cell in an oxygen free environment), to avoid oxidation. I found a paper which described a single-source thermal route to Mo_2N starting from HMT-Mo [12] [85], which I prepared by precipitating a solution of ammonium heptamolybdate with a solution of hexamine. Upon heating this salt to 550°C (823 K) in an inert atmosphere (I used the tube furnace and an argon-flow) decomposes to Mo_2N via the reaction [85]: $H_{44}C_{12}N_{12}Mo_7O_{26} \rightarrow 12CO + 14H_2O + 5.33NH_3 + 1.583N_2 + 3.5Mo_2N$. Figure 6.11 shows XRD data of a small amount of sample prepared in this way. Apart from a narrow, unexplained, peak at $2\theta = 41°$ and a broader one at $2\theta = 54°$ the sample looks like pure-phase Mo_2N (ref. pattern 00-025-1366) and with a crystallite size of 2 to 3 nm [13]. I think that this single-source thermal decomposition method is a very convenient way of preparing molybdenum nitride of high surface area and that ammonia synthesis over a cathode prepared this way deserves a try.

6.6.2 Barium nitride

Barium nitride was suggested, by Sergey Dobrin to be a good candidate for a cathode electrocatalyst at about the same time as the new UHV-style cell became operational. Unfortunately, barium and its nitride are both exceedingly reactive, so various strategies for in-situ synthesis the the nitride were tried out. One disadvantage of preparing catalyst inside the cell is that there are no characterization tools available so it is hard to ascertain whether the synthesis is successful. In any case, the first couple of attempts were based on evaporating Ba from a commercial "getter" source onto a piece of carbon paper (the kind we use for PEM-fuel cells, and which we know from XPS, to be quite clean). The carbon paper was held by a small "alligator"-clip made from nickel-plated steel and held in place by a small Nd-B-Fe magnet outside the cell. After deposition the idea was to lower the carbon paper with the barium nitride coating into the ionic liquid electrolyte using the external magnet as an external handle. Electrical connection to the clip (and hereby the carbon paper) was established through a thin Cu-wire, which was annealed between experiments to keep it ductile. During warm-up of the getter the carbon paper was shielded by an internal shutter, which was held in place by a second Nd-B-Fe magnet, and which could be removed once the getter was at deposition temperature for a certain

[12] Using "HMT" as shorthand for hexamethylenetetraamine (hexamine) the salt is: HMT-Mo = $(HMT)_2(NH_4)_4Mo_7O_{24}$. This corresponds to $H_{44}C_{12}\mathbf{N_{12}Mo_7}O_{26}$ - i.e., a large surplus of N to Mo.

[13] Recently, Wei Tang (Post Doc. at CASE who has inherited the ammonia project) has repeated the synthesis using some of my old precursor and seen particles in SEM of about 3 nm in size.

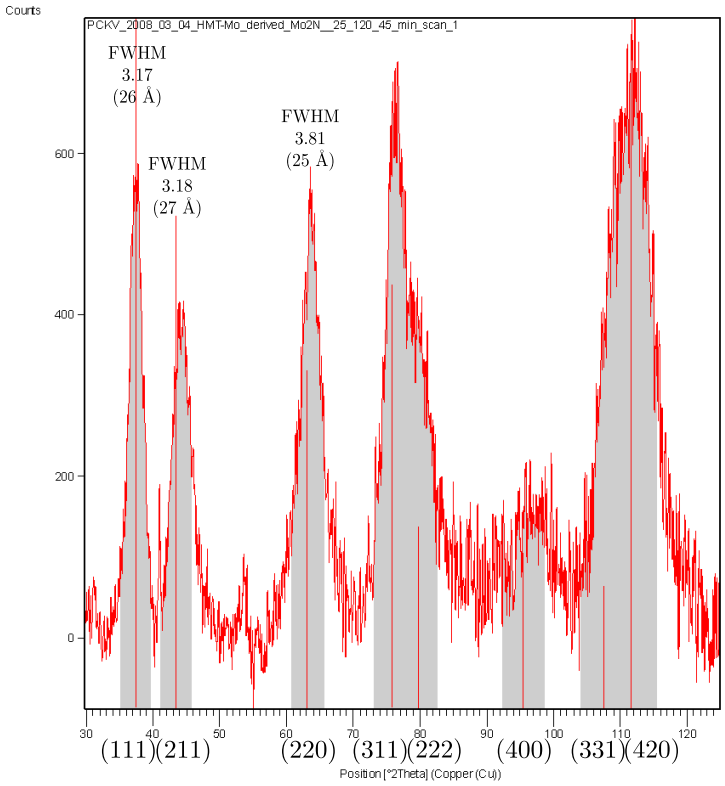

Figure 6.11: XRD measurement of a small amount of Mo_2N prepared by the thermal decomposition route [85]. In the Debye-Scherrer calculations of crystallite size I used K=0.9.

deposition time. In order to carry out this experiment a third (auxiliary) turbo pump was installed on the system, as close as possible to the cell to maintain the best possible vacuum at all times (TMP3 in Fig. 6.9). This was not very successful. Despite pumping with all three available turbo pumps, the pressure rose quickly upon heating of the Ba-source. Mass scans revealed that this was primarily due to CO_2 which probably originated from a carbonate precursor in the getter: $BaCO_3 \rightarrow BaO{+}CO_2(g)$, $BaO{+}Ni \leftrightarrows Ba{+}NiO$, $Ba \rightarrow Ba(g)$.

After a couple of attempts with commercial Ba-getter sources I switched to trying to use Ba-metal as the Ba-source. I made an evaporation boat by spot welding a piece of thin Ta-foil (bent to hold an irregular piece of barium of a few millimeters in size) to a Ta filament (0.5 mm in diameter), which in turn was spot-welded to 1 mm Ta leads. Again, carbon paper was the used as electrode substrate in this evaporation experiment and the same pumping measures as in the getter experiment were used. The biggest problem with this

setup was a practical one: Once the vial containing a suitable piece of barium under argon was opened, and the metal transferred to the tantalum boat, the clock was ticking, very fast [14]! It was therefore a race against time to assemble the entire cell (keeping the electrode in place by continually moving the magnet counter to the movement of the glass vessel) while avoiding short-circuiting any of the seven other electrical feedthroughs with the folded thin Cu-lead. Getting the six bolts tightened to compress the Cu-gasket and then pump down the system quickly was tricky - particularly because in order to avoid that dissolved gasses in the ionic liquid would cause it to "boil" explosively, there is a limit to how quickly the pressure can be brought down. (Any splash of ionic liquid hitting the tantalum boat, due to such boiling phenomena, would spell disaster as it would ruin the vacuum during heating due to gaseous decomposition products.) Often, by accident, something (e.g., the inner wall of the glass vessel) would touch one on the Ta-leads, or the boat, causing the Ba-piece to drop into the electrolyte in which case the whole procedure had to be started all over again.

In spite of these problems, on a few occasions whole assembly procedure worked and an experiment could be conducted. The Ba-particle would naturally always be partially oxidized, and therefore not in good thermal contact with the tantalum boat. The result was that the boat could be heated red-hot before the barium would melt, but as soon as it did, it would evaporate within a couple of seconds. Then I would cool down the boat and slowly re-pressurize with nitrogen to let the nitride form. A number of experiments were carried out using a cathode prepared in this way, but no clear activity was observed.

The final method I came up with for making barium nitride in-situ is the best, by far. Inspired by the ease of the single-source thermal route to molybdenum nitride, I wondered if something similar could be done with barium. The answer, as it turned out, is yes. I found a paper where it is shown that under refluxing in high-boiling organic solvents barium azide ($Ba(N_3)_2$) [86], which is stable in air, decomposes thermally to Ba_3N_4 and then further to Ba_3N_2 and N_2 at 200°C (573 K) or above. I thought that, since my ionic liquid is essentially stable at those temperatures, I could thermally decompose the azide directly on the carbon paper and avoid explosive decomposition [15] by soaking the whole thing in my ionic liquid. The problem was how to obtain sodium-free barium azide. I found a synthesis based on neutralizing a barium hydroxide solution with hydrazoic acid gas ($HN_3(g)$ (!!)) which is made by adding sulphuric acid to sodium azide. Not being a trained chemist, I did not want to attempt this synthesis, so I got help from a chemist [87] to synthesize suitable amount of the salt for me. My approach, then, was to apply an amount of a saturated solution to the carbon paper and evaporate away the water, then wet the carbon paper

[14] One can literally see the layer of oxide/carbonate growing on the Ba surface. After 10 minutes in air a 1 mm piece transforms completely into white dust.

[15] In common with the famous azide compounds like sodium azide, lead azide and silver azide barium azide will detonate upon heating. To get a feel for the sensitivity I tried heating small specks (few milligrams) of the salt on a lab hotplate and around 150 to 180°C (423 to 453 K) the speck would typically disappear with a report. Interestingly enough, on a clean (oxidized) silicon wafer surface I managed to heat the dry azide above 350°C (623 K) without explosion or indeed any visible decomposition. In a drop of ionic liquid (in which the azide has low solubility - at least at room temperature) the white azide gives off gas (N_2 no doubt) above a certain temperature and the product is black (presumably the nitride).

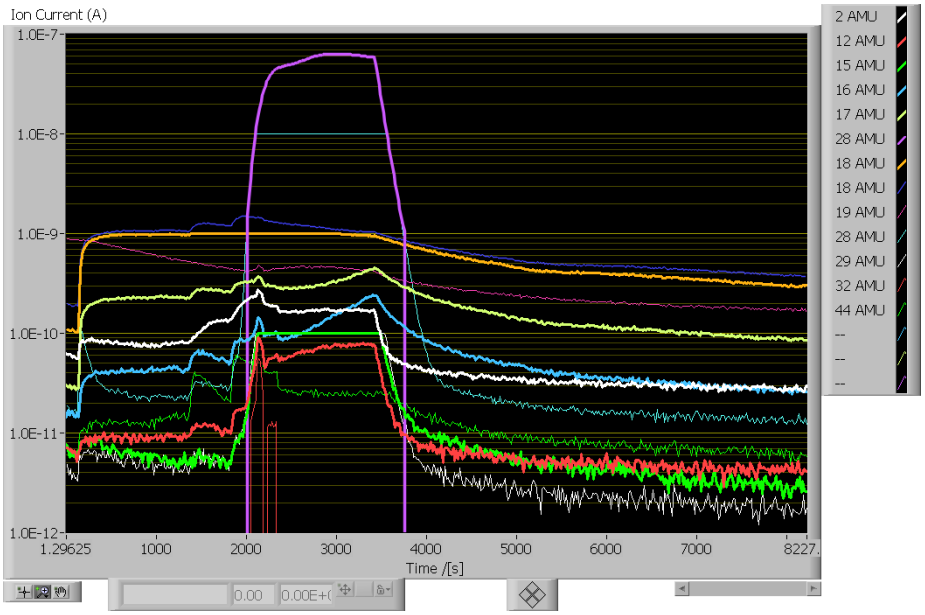

Figure 6.12: QMS screen dump from the first synthesis of barium nitride from barium azide. The thin blue trace shows the water signal and it shows that power on the lamp (temperature) was increased at times 200 s, 1400 s and 1800 s and turned off at 3600 s. The thick purple nitrogen signal very clearly shows the azide decomposing from about 2000 s and until the heating is switched off. Note also that m/Z = 16 and 17 go up during azide decomposition, while the water signal drops. This actually looks like ammonia somehow evolving during the azide decomposition.

with ionic liquid and mount the carbon paper in the cell above the level of the electrolyte, again using a magnet. In order to heat the lower part of the carbon paper (impregnated with the azide precursor) to above 200°C (473 K), I decided that an optical approach would be most elegant, hence I used a quartz-halogen lamp and a focussing lens mounted outside the glass cell, pumped down the cell (using the mass spectrometer) and started increasing the filament current of the lamp. Figure 6.12 shows how the QMS recorded the experiment. It is easy to see the azide decomposing and that there is a peak in decomposition rate approximately 800 seconds after the first N_2 is measured. There is also an indication that small amounts of ammonia evolve during the decomposition, as evidenced by the increasing m/Z = 16 and 17 signals while the water signal is dropping. There is no sign of severe decomposition of the ionic liquid (as evidenced by the fluorine signal or the sulphur signal). After decomposition, the carbon paper had visibly turned darker (more matte) where the azide had been (before heating, the azide gave the carbon paper a milky shade and after heating the color was darker (more black) than virgin carbon paper).

6.7 Conclusions and recommendations for future work

In-situ catalyst preparation followed by exotic electrochemistry in non-aqueous electrolytes in sealed setups equipped with turbo molecular pumps and a mass spectrometer, is an interesting and educating experience for any experimentalist. It can also be frustrating at times.

Keeping an electrochemical cell *free* of water is exceedingly difficult if not impossible and doing so using syringes, flexible tubing and so on is probably next to impossible. I think the present cell is about "as good as it gets" in terms of providing low oxygen and water concentrations, but the cleanliness comes at the expense of flexibility (which nearly killed the Ba-metal evaporation experiments (section 6.6)), and it rules out any characterization (e.g., optical or X-ray) of the catalyst. Perhaps if a catalyst which is active towards hydrogenation of nitrogen and which can survive exposure to air can be found (potentially molybdenum nitride) then experiments could be done in the liquid-ready μ-reactors (section 4.5, page 59) in a version that would accommodate the ionic liquid electrolyte.

I think that mass spectrometry has proven a hard technique to use in the batch reactor, due to the ubiquitous water background so perhaps other methods deserve (re-)consideration. The infrared detector can detect signals down to about $\sim 10^{15}$ ammonia molecules in practice and should not be ruled out in future work because of its ease of use (although it still must be proven that the signal *is* ammonia). An alternative detection method which is well-suited for batch experiments, is a GC - ideally fitted with a Nitrogen-Phosphorous Detector (NPD) [16]. If the GC were equipped with an autosampler the freeze trap (FT 2) would ideally be a cooled part of the sampling loop. This would be an elegant method and a strong proof of ammonia formation and it would be quantifiable for optimization purposes. A final (more exotic option) could be photoacoustic detection of ammonia in the electrochemical cell itself. This approach has the advantage that the cell itself serves as the trap (the experiment would be conducted with the cell sealed off - not with a gas flow like the freeze trap experiments).

With regards to catalysts I think the most obvious experiment would be to try using an electrode coated with Mo_2N prepared with the thermal decomposition technique. The high surface area should make it possible to obtain reasonably large ammonia signals to make detection easier. Finally I think that future experiments should try to minimize the cathode-anode distance (to obtain high currents) and minimize the total volume of electrolyte (because ammonia is quite soluble in [EMI][TFSI]).

[16] A Nitrogen-Phosphorous Detector (also sometimes called a TID (ThermIonic Detector)) resembles a Flame Ionization Detector (FID) in that the column carrier gas is mixed with hydrogen and burned, but in the NPD a heated ceramic bead containing cesium (or rubidium) is exposed to the combustion products. Products of partial combustion of nitrogen (or phosphorous) absorb on the surface and lower the work function and since the bead is cathodically biased, an increase in thermionic emission current results. (The true working mechanism is not really understood.) An NPD can detect nitrogen and phosphorous below 10^{-12} g i.e., below 10^{11} ammonia molecules [26].

Chapter 7

Conclusion and outlook

Overview

Many different topics have been touched upon in the previous chapters. These include:

- Overview of current global energy supply and the potential for the future solar supply.
- Gas-phase photooxidation of CO (and methanol) over various TiO_2-based photocatalysts.
- Photoreduction of water over surface modified silicon photocathodes.
- Synthesis of photocatalytic materials including TiO_2 nanotubes and $TaOxNy$ materials.
- The use of novel, highly sensitive, silicon μ-reactors for quantitative photocatalytic measurements.
- Electrochemical synthesis of ammonia in an ionic liquid electrolyte.

Useful results and outlook

Some of the sub-projects have been particularly successful while others have not. I am particularly satisfied with the progress made with the μ-reactors, where the last two years have seen the development of many technologies such as: Argon flushing of the manifold O-rings to eliminate air diffusion leakage, locally cooled anodic bonding for sensitive samples, on-lid RTD for temperature measurement during heterogeneous catalysis experiments, improved, UHV-compatible gas manifold, vastly improved gas supply infrastructure for the μ-reactors with LabVIEW control of flows, pressure, temperature, illumination etc., incremental improvements of the new μ-reactors including the on-chip mixing structure and new placement of the capillary. And, on top of all this, we are now very close to opening a new front within μ-reactors - namely electrochemical and photoelectrochemical μ-reactors. (Main people behind all this are Toke, Jakob,

Ib, Ole[1], Adam[2] and myself.) I am also very satisfied with the photocatalytic measurements of CO oxidation, as a function of illumination intensity and wavelength and the development of quantitative measurements in the μ-reactors, which enabled the APPE and IPPE calculations.

The TiO_2 nanotube project also resulted in a very interesting and technologically useful result, namely that molecular oxygen enhances the growth speed of the film, and that this may be used to grow large uniform films over non-conductive surfaces in a single step. This discovery was made by Su-il. The subsequent struggle to *understand* the nature of the effect was less successful, unfortunately, despite creative input and ideas of a number of people (i.e., the authors of [Paper I]).

The project with cubane-modified silicon photocathodes (lead by Billie and Hou) has been the most exciting project in our group in recent months. Our current understanding of why it works is very limited, but we now have a large body of data showing that cubane modification really does increase photocurrent significantly, so this is something we will continue to investigate intensively.

The least successful projects have been the TaO_xN_y photoanode project and the ammonia project. I am quite optimistic that photoanodes based on tantalum can be made (also with reactive sputtering), but given the scarcity of tantalum any working PEC technology based on this material would hardly be deployable on the requisite multi GW-scale. The ammonia project is still alive and there are new ideas on how to proceed.

[1] Associate Professor Ole Hansen at DTU Nanotech
[2] Former Post Doc. Adam Monkowski at DTU Nanotech

Bibliography

[1] U.S. Census Bureau. *Historical Estimates of World Population*, 2009 (Accessed December 10, 2009). URL www.census.gov/ipc/www/worldhis.html.

[2] Wikipedia. *World Population*, 2009 (Accessed December 10, 2009). URL en.wikipedia.org/wiki/World_population.

[3] BP. Statistical review of world energy. BP, June 2009. URL www.bp.com/statisticalreview.

[4] Petersen, E. L. & Sørensen, J. N. *Engineering challenges - energy, climate change & health*, chapter Wind energy researc: crucial for takeoff, pages 30–39. Technical University of Denmark (DTU), 2009.

[5] Mk Hubbert. Energy from fossil fuels. *Science*, 109(2823):103–109, 1949. ISSN 0036-8075.

[6] M. K. Hubbert. Nuclear energy and the fossil fuels. Presented before the Spring Meeting of the Southern District, American Petroleum Institute, March 1956.

[7] Energy Information Administration (EIA). *Crude Oil Production and Crude Oil Well Productivity, 1954-2008*, 2009 (Accessed December 19, 2009). URL www.eia.doe.gov/emeu/aer/txt/ptb0502.html.

[8] Pseodonym. *Oil Production is Reaching its Limit: The Basics of What This Means*, 2009 (Accessed December 11, 2009). URL www.theoildrum.com/node/5969#more.

[9] Jan Harley Andersen. *Den årlige produktion fra 1972 til 2008*, 2009 (Accessed December 19, 2009). URL www.ens.dk/da-DK/UndergrundOgForsyning/Olie_og_gas/Data/AarligProduktion/Sider/Forside.aspx.

[10] C. A. S. Hall and J. W. Day. Revisiting the limits to growth after peak oil in the 1970s a rising world population and the finite resources available to support it were hot topics. interest faded-but it's time to take another look. *American Scientist*, 97(3):230–237, May 2009.

[11] American Society for Testing and Materials. *Reference Solar Spectral Irradiance: Air Mass 1.5*, astm g173-03 edition, 2009 (Accessed December 10, 2009). URL rredc.nrel.gov/solar/spectra/am1.5/.

[12] Martin A. Green. The path to 25% silicon solar cell efficiency: History of silicon cell evolution. *Progress in Photovoltaics: Research and Applications*, 17(3):183–189, 2009. URL http://dx.doi.org/10.1002/pip.892.

[13] R. S. Ohl. *Light sensitive electric device*, 1941. Patent: US240252.

[14] R. S. Ohl. *Light-sensitive electric device including silicon*, 1941. Patent: US2443542.

[15] Syanne Olson. *Sharp accomplishes 35.8% solar cell efficiency*, 2009 (Accessed December 19, 2009). URL www.pv-tech.org/news/_a/sharp_accomplishes_35.8_solar_cell_efficiency/.

[16] R. Hezel. *High-Efficient Low-Cost Photovoltaics*, chapter Commercial High-Efficiency Silicon Solar Cells, pages 95–100. Springer, 2009. URL http://dx.doi.org/10.1007/978-3-540-79359-5_7.

[17] Lawrence Kazmerski. *Best Reseach-Cell Efficiencies*. NREL, 2009 (Accessed December 10, 2009). URL www.dotyenergy.com/Markets/PV_Solar.htm.

[18] Photovoltaic Geographical Information System (PVGIS). *Geographical Assessment of Solar Resource and Performance of Photovoltaic Technology*, 2010 (Accessed January 09, 2010). URL re.jrc.ec.europa.eu/pvgis/.

[19] Solar Energies Industry Association. *Photovoltaic Solar Resource: United States and Germany*, 2010 (Accessed January 10, 2010). URL www.seia.org/galleries/default-file/PVMap_USandGermany.pdf.

[20] Martin A. Green. Improved estimates for Te and Se availability from Cu anode slimes and recent price trends. *Progress in Photovoltaics: Research and Applications*, 14(8):743–751, 2006. URL http://dx.doi.org/10.1002/pip.703.

[21] Martin A. Green. Estimates of Te and In prices from direct mining of known ores. *Progress in Photovoltaics: Research and Applications*, 17(5):347–359, 2009. URL http://dx.doi.org/10.1002/pip.899.

[22] Guilinger. Assessment of Critical. Thin Film Resources. Tellurium. RAF-9-29609. World Industrial Minerals, April 1999. URL www.nrel.gov/pv/thin_film/docs/telluriumworldindustrialminerals2000.doc.

[23] Björn A. Andersson. Materials availability for large-scale thin-film photovoltaics. *Progress in Photovoltaics: Research and Applications*, 8(1):61–76, 2000. URL http://dx.doi.org/10.1002/(SICI)1099-159X(200001/02)8:1<61::AID-PIP301>3.0.CO;2-6.

[24] H. A. Gasteiger, J. E. Panels, and S. G. Yan. Dependence of PEM fuel cell performance on catalyst loading. *Journal of Power Sources*, 127(1-2):162–171, March 2004. ISSN 0378-7753. URL http://www.sciencedirect.com/science/article/B6TH1-4BP9K7R-1/2/48a85d630d0e1447ec1ff5b32b531b33.

[25] I. Chorkendorff and J.W Niemantsverdriet. *Concepts of modern catalysis and kinetics*. John Wiley and Sons Ltd., 2003.

[26] D. A. Skoog, F. J. Holler, and T. A. Nieman. *Instrumental Analysis*. Brooks/Cole, 1998.

[27] H. Gerischer. The impact of semiconductors on the concepts of electrochemistry. *Electrochimica Acta*, 35(11-12):1677–1699, November 1990. ISSN 0013-4686. URL http://www.sciencedirect.com/science/article/B6TG0-44XW0TN-K3/2/13c635619c03230f74af8f06121c0472.

[28] Nathan S. Lewis. Progress in understanding electron-transfer reactions at semiconductor/liquid interfaces. *The Journal of Physical Chemistry B*, 102 (25):4843–4855, June 1998. ISSN 1520-6106. URL http://dx.doi.org/10.1021/jp9803586.

[29] F. Thebault, B. Vuillemin, R. Oltra, J. Kunze, A. Seyeux, and P. Schmuki. Modeling of growth and dissolution of nanotubular titania in fluoride-containing electrolytes. *Electrochem. Solid-State Lett.*, 12(3):C5–C9, March 2009. URL http://link.aip.org/link/?ESL/12/C5/1.

[30] Hideki Masuda and Kenji Fukuda. Ordered metal nanohole arrays made by a two-step replication of honeycomb structures of anodic alumina. *Science*, 268(5216):1466–1468, 1995. ISSN 00368075. URL http://www.jstor.org/stable/2887752.

[31] V. Zwilling, M. Aucouturier, and E. Darque-Ceretti. Anodic oxidation of titanium and TA6V alloy in chromic media. An electrochemical approach. *Electrochimica Acta*, 45(6):921–929, December 1999. ISSN 0013-4686. URL http://www.sciencedirect.com/science/article/B6TG0-3XWJFRV-9/2/59135694d395143ed961eede2e272f50.

[32] V. Zwilling, E. Darque-Ceretti, A. Boutry-Forveille, D. David, M. Y. Perrin, and M. Aucouturier. Structure and physicochemistry of anodic oxide films on titanium and TA6V alloy. *Surface and Interface Analysis*, 27(7):629–637, 1999. URL http://dx.doi.org/10.1002/(SICI)1096-9918(199907)27:7<629::AID-SIA551>3.0.CO;2-0.

[33] D. Gong, C. A. Grimes, O. K. Varghese, W. C. Hu, R. S. Singh, Z. Chen, and E. C. Dickey. Titanium oxide nanotube arrays prepared by anodic oxidation. *Journal of Materials Research*, 16(12):3331–3334, December 2001.

[34] Jan M. Macak, Hiroaki Tsuchiya, Luciano Taveira, Saule Aldabergerova, and Patrik Schmuki. Smooth anodic tio2 nanotubes. *Angewandte Chemie International Edition*, 44(45):7463–7465, 2005. URL http://dx.doi.org/10.1002/anie.200502781.

[35] Maggie Paulose, Karthik Shankar, Sorachon Yoriya, Haripriya E. Prakasam, Oomman K. Varghese, Gopal K. Mor, Thomas A. Latempa, Adriana Fitzgerald, and Craig A. Grimes. Anodic Growth of Highly Ordered TiO_2 Nanotube Arrays to 134 μm in Length. *The Journal of Physical Chemistry B*, 110(33):16179–16184, August 2006. ISSN 1520-6106. URL http://dx.doi.org/10.1021/jp064020k.

[36] Gopal K. Mor, Oomman K. Varghese, Maggie Paulose, Karthik Shankar, and Craig A. Grimes. A review on highly ordered, vertically oriented tio2

nanotube arrays: Fabrication, material properties, and solar energy applications. *Solar Energy Materials and Solar Cells*, 90(14):2011–2075, September 2006. ISSN 0927-0248. URL http://www.sciencedirect.com/science/article/B6V51-4K48N9K-1/2/aed2141fda94a9882ef5936bb23fa567.

[37] K. Shankar, G. K. Mor, H. E. Prakasam, S. Yoriya, M. Paulose, O. K. Varghese, and C. A. Grimes. Highly-ordered TiO2 nanotube arrays up to 220 mu m in length: use in water photoelectrolysis and dye-sensitized solar cells. *Nanotechnology*, 18(6):065707, February 2007.

[38] Arthur J. Nozik and Rudiger Memming. Physical Chemistry of Semiconductor-Liquid Interfaces. *The Journal of Physical Chemistry*, 100 (31):13061–13078, January 1996. ISSN 0022-3654. URL http://dx.doi.org/10.1021/jp953720e.

[39] T. Bak, J. Nowotny, M. Rekas, and C. C. Sorrell. Photo-electrochemical hydrogen generation from water using solar energy. materials-related aspects. *International Journal of Hydrogen Energy*, 27(10):991–1022, October 2002. ISSN 0360-3199. URL www.sciencedirect.com/science/article/B6V3F-45BRNPN-2/2/0303ba83a9c0a716924b02cba60404f0.

[40] Michikazu Hara, Go Hitoki, Tsuyoshi Takata, Junko N. Kondo, Hisayoshi Kobayashi, and Kazunari Domen. TaON and Ta3N5 as new visible light driven photocatalysts. *Catalysis Today*, 78(1-4):555–560, February 2003. ISSN 0920-5861. URL http://www.sciencedirect.com/science/article/B6TFG-47CH5X3-N/2/2876f0ff54b82d5379b517e27bc29af6.

[41] N. Hara, G. Hitoki, T. Takata, J. N. Kondo, H. Kobayashi, and K. Domen. Ta3N5 and TaON as novel photocatalysts responding to visible light. *Science and Technology In Catalysis 2002*, 145:169–172, 2003.

[42] Kazuhiko Maeda and Kazunari Domen. New non-oxide photocatalysts designed for overall water splitting under visible light. *The Journal of Physical Chemistry C*, 111(22):7851–7861, June 2007. ISSN 1932-7447. URL http://dx.doi.org/10.1021/jp070911w.

[43] Michikazu Hara, Eisuke Chiba, Akio Ishikawa, Tsuyoshi Takata, Junko N. Kondo, and Kazunari Domen. Ta3N5 and TaON Thin Films on Ta Foil: Surface Composition and Stability. *The Journal of Physical Chemistry B*, 107(48):13441–13445, December 2003. ISSN 1520-6106. URL http://dx.doi.org/10.1021/jp036189t.

[44] Akio Ishikawa, Tsuyoshi Takata, Junko N. Kondo, Michikazu Hara, and Kazunari Domen. Electrochemical Behavior of Thin Ta3N5 Semiconductor Film. *The Journal of Physical Chemistry B*, 108(30):11049–11053, July 2004. ISSN 1520-6106. URL http://dx.doi.org/10.1021/jp048802u.

[45] G. Brauer, J. Weidlein, and J. Strahle. Uber Das Tantalnitrid Ta3N5 Und Das Tantaloxidnitrid TaON. *Zeitschrift Fur Anorganische Und Allgemeine Chemie*, 348(5-6):298–308, 1966.

[46] M. I. Gavrilyuk, V. T. Ershova, and V. A. Konstantinov. Interaction of tantalum with nitrogen and air. *Metal Science and Heat Treatment*, 8(12):998–1000, December 1966. URL http://dx.doi.org/10.1007/BF00653000.

[47] Stuart J. Henderson and Andrew L. Hector. Structural and compositional variations in Ta3N5 produced by high-temperature ammonolysis of tantalum oxide. *Journal of Solid State Chemistry*, 179(11):3518–3524, November 2006. ISSN 0022-4596. URL http://www.sciencedirect.com/science/article/B6WM2-4KFT891-4/2/6a37f9fe583fd81db3aa0313f249c229.

[48] Bjerrum, N. J. and Christensen, E. *Hycycle*, 2010 (Accessed January 10, 2010). URL www.hycycle.dk.

[49] Berit Hinnemann, Poul Georg Moses, Jacob Bonde, Kristina P. Jorgensen, Jane H. Nielsen, Sebastian Horch, Ib Chorkendorff, and Jens K. Norskov. Biomimetic Hydrogen Evolution: MoS2 Nanoparticles as Catalyst for Hydrogen Evolution. *Journal of the American Chemical Society*, 127(15): 5308–5309, April 2005. ISSN 0002-7863. URL http://dx.doi.org/10.1021/ja0504690.

[50] Thomas F. Jaramillo, Kristina P. Jorgensen, Jacob Bonde, Jane H. Nielsen, Sebastian Horch, and Ib Chorkendorff. Identification of Active Edge Sites for Electrochemical H2 Evolution from MoS2 Nanocatalysts. *Science*, 317(5834): 100–102, July 2007. URL http://www.sciencemag.org/cgi/content/abstract/317/5834/100.

[51] Thomas F. Jaramillo, Jacob Bonde, Jingdong Zhang, Bee-Lean Ooi, Klas Andersson, Jens Ulstrup, and Ib Chorkendorff. Hydrogen Evolution on Supported Incomplete Cubane-type [Mo3S4]4+ Electrocatalysts. *The Journal of Physical Chemistry C*, 112(45):17492–17498, November 2008. ISSN 1932-7447. URL http://dx.doi.org/10.1021/jp802695e.

[52] J. Bonde, P. G. Moses, T. F. Jaramillo, J. K. Norskov, and I. Chorkendorff. Hydrogen evolution on nano-particulate transition metal sulfides. *Faraday Discussions*, 140:219–231, 2008.

[53] K. Osseo-Asare, Dawei Wei, and Kamal K. Mishra. Dissolution Windows for Wet Chemical Processing of Silicon and Silicon Dioxide: Potential-pH Diagrams for the Si-F-H_2O System. *J. Electrochem. Soc.*, 143(2):749–751, February 1996. URL http://link.aip.org/link/?JES/143/749/1.

[54] R. Parsons. The Rate of Electrolytic Hydrogen Evolution and the Heat of Adsorption of Hydrogen. *Transactions of the Faraday Society*, 54(7): 1053–1063, 1958.

[55] Jeff Greeley, Thomas F. Jaramillo, Jacob Bonde, Ib Chorkendorff, and Jens K. Norskov. Computational high-throughput screening of electrocatalytic materials for hydrogen evolution. *Nat Mater*, 5(11):909–913, November 2006. ISSN 1476-1122. URL http://dx.doi.org/10.1038/nmat1752.

[56] Poul G. Moses. *Transition metal sulphide catalysts: A DFT study of structure and reactivity*. PhD thesis, DTU, Physics (CAMd), 2008.

[57] Konrad Herbst, Magda Monari, and Michael Brorson. Facile formation of a heterobimetallic cluster with a cubane-like [mo3s4cu]5+ core. *Inorganica Chimica Acta*, 357(3):895–899, February 2004. ISSN 0020-1693. URL http://www.sciencedirect.com/science/article/B6TG5-49CT19B-9/2/fcf0b518069efe3ce5fcb60700311ac8.

[58] S. R. Elliot. *The Physics and Chemistry of Solids*. Wiley, 1998.

[59] T. Tiedje, E. Yablonovitch, G. D. Cody, and B. G. Brooks. Limiting Efficiency of Silicon Solar-cells. *IEEE Transactions On Electron Devices*, 31 (5):711–716, 1984.

[60] Raymond N. Dominey, Nathan S. Lewis, James A. Bruce, Dana C. Bookbinder, and Mark S. Wrighton. Improvement of photoelectrochemical hydrogen generation by surface modification of p-type silicon semiconductor photocathodes. *Journal of the American Chemical Society*, 104(2):467–482, January 1982. ISSN 0002-7863. URL http://dx.doi.org/10.1021/ja00366a016.

[61] Bunsho Ohtani. Preparing articles on photocatalysis - beyond the illusions, misconceptions, and speculation. *Chemistry Letters*, 37(3):216–229, 2008.

[62] S. Johansson, E. Fridell, and B. Kasemo. Microreactor for studies of low surface area model catalysts made by electron-beam lithography. *Journal Of Vacuum Science & Technology A-Vacuum Surfaces And Films*, 18(4): 1514–1519, July 2000.

[63] P. W. Jacobs, S. J. Wind, F. H. Ribeiro, and G. A. Somorjai. Nanometer size platinum particle arrays: catalytic and surface chemical properties. *Surface Science*, 372(1-3):L249–L253, February 1997. ISSN 0039-6028. URL http://www.sciencedirect.com/science/article/B6TVX-3YYVGSW-1/2/994325b3f4b8835f725cdc899ad6cba3.

[64] G. Wallis and D.I. Pomerantz. Field assisted glass-metal sealing. *Journal Of Applied Physics*, 40(10):3946–3949, 1969.

[65] K. M. Knowles and A. T. J. van Helvoort. Anodic bonding. *International Materials Reviews*, 51(5):273–311, October 2006.

[66] Thomas R. Anthony. Anodic bonding of imperfect surfaces. *Journal of Applied Physics*, 54(5):2419–2428, 1983.

[67] H. Einaga, M. Harada, S. Futamura, and T. Ibusuki. Generation of Active Sites for CO Photooxidation on TiO_2 by Platinum Deposition. *The Journal of Physical Chemistry B*, 107(35):9290–9297, September 2003. ISSN 1520-6106. URL http://dx.doi.org/10.1021/jp0343638.

[68] T. A. Egerton and C. J. King. The influence of light intensity on photoactivity in TiO_2 pigmented systems. *J. Oil Col. Chem. Assoc.*, 62:386, 1979.

[69] Yoshihisa Ohko, Kazuhito Hashimoto, and Akira Fujishima. Kinetics of photocatalytic reactions under extremely low-intensity uv illumination on titanium dioxide thin films. *The Journal of Physical Chemistry A*, 101(43): 8057–8062, October 1997. ISSN 1089-5639. URL http://dx.doi.org/10.1021/jp972002k.

[70] José Peral and David F. Ollis. Heterogeneous photocatalytic oxidation of gas-phase organics for air purification: Acetone, 1-butanol, butyraldehyde, formaldehyde, and m-xylene oxidation.

Journal of Catalysis, 136(2):554–565, August 1992. ISSN 0021-9517. URL http://www.sciencedirect.com/science/article/B6WHJ-4CJTXK3-HF/2/024979e3c64959417b317058dc8a948b.

[71] M.A. Aguado, M.A. Anderson, and C.G. Hill Jr. Influence of light intensity and membrane properties on the photocatalytic degradation of formic acid over TiO2 ceramic membranes. *Journal of Molecular Catalysis*, 89(1-2):165–178, April 1994. ISSN 0304-5102. URL http://www.sciencedirect.com/science/article/B6W91-44074H7-111/2/5201d2961059e06cb091c769447b2e98.

[72] Sangman Hwang, Myung Churl Lee, and Wonyong Choi. Highly enhanced photocatalytic oxidation of CO on titania deposited with Pt nanoparticles: kinetics and mechanism. *Applied Catalysis B: Environmental*, 46(1):49–63, October 2003. ISSN 0926-3373. URL http://www.sciencedirect.com/science/article/B6TF6-48N3H9T-2/2/e4f1719434f221b5f885a5e5afe9d01e.

[73] K. Domen, S. Naito, M. Soma, T. Onishi, and K. Tamaru. Photocatalytic Decomposition of Water-vapor On An NiO-SrTiO3 Catalyst. *Journal of the Chemical Society-chemical Communications*, (12):543–544, 1980.

[74] C. N. Rusu and J. T. Yates. Photochemistry of NO Chemisorbed on TiO2(110) and TiO2 Powders. *The Journal of Physical Chemistry B*, 104 (8):1729–1737, March 2000. ISSN 1520-6106. URL http://dx.doi.org/10.1021/jp992239b.

[75] Takuya Goto and Yasuhiko Ito. Electrochemical reduction of nitrogen gas in a molten chloride system. *Electrochimica Acta*, 43(21-22):3379–3384, July 1998. ISSN 0013-4686. URL http://www.sciencedirect.com/science/article/B6TG0-3TXCKNF-15/2/8d8ac8e07d1b52c748b5409a4dbed269.

[76] Tsuyoshi Murakami, Tokujiro Nishikiori, Toshiyuki Nohira, and Yasuhiko Ito. Electrolytic synthesis of ammonia in molten salts under atmospheric pressure. *Journal of the American Chemical Society*, 125(2):334–335, January 2003. ISSN 0002-7863. URL http://dx.doi.org/10.1021/ja028891t.

[77] A. Logadottir, T. H. Rod, J. K. Nørskov, B. Hammer, S. Dahl, and C. J. H. Jacobsen. The brønsted-evans-polanyi relation and the volcano plot for ammonia synthesis over transition metal catalysts. *Journal of Catalysis*, 197(2):229–231, January 2001. ISSN 0021-9517. URL http://www.sciencedirect.com/science/article/B6WHJ-45BCCNR-C5/2/807a518cd5b99090c171fdeed1578264.

[78] G. Marnellos and M. Stoukides. Ammonia synthesis at atmospheric pressure. *Science*, 282(5386):98–100, October 1998.

[79] V. Kordali, G. Kyriacou, and C. Lambrou. Electrochemical synthesis of ammonia at atmospheric pressure and low temperature in a solid polymer electrolyte cell. *Chemical Communications*, (17):1673–1674, 2000.

[80] David L. Boucher, Julian A. Davies, Jimmie G. Edwards, and Abdelkader Mennad. An investigation of the putative photosynthesis of ammonia on iron-doped titania and other metal oxides. *Journal of Photochemistry and Photobiology A: Chemistry*, 88(1):53–64, May 1995. ISSN 1010-6030. URL http://www.sciencedirect.com/science/article/B6TGY-40324DT-Y/2/b114383b0ca03bc9d11f2ee9a1cf863d.

[81] Jimmie G. Edwards, Julian A. Davies, David L. Boucher, and Abdelkader Mennad. An Opinion on the Heterogeneous Photoreactions of N_2 with H_2O. *Angewandte Chemie International Edition in English*, 31(4):480–482, 1992. URL http://dx.doi.org/10.1002/anie.199204801.

[82] Michel Armand, Frank Endres, Douglas R. MacFarlane, Hiroyuki Ohno, and Bruno Scrosati. Ionic-liquid materials for the electrochemical challenges of the future. *Nat Mater*, 8(8):621–629, August 2009. ISSN 1476-1122. URL http://dx.doi.org/10.1038/nmat2448.

[83] Ohno, H. & Katayama, Y. *Electrochemical Aspects of Ionic Liquids*, chapter 3, pages 29–33. Wiley-Interscience, 2005.

[84] S. T. Oyama, editor. *The Chemistry of Transition Metal Carbides and Nitrides*, chapter Synthesis of thin films of Cr, Mo and W carbides and nitrides, pages 274–281. Chapman & Hall (Springer), 1996.

[85] Pavel Afanasiev. New Single Source Route to the Molybdenum Nitride Mo2N. *Inorganic Chemistry*, 41(21):5317–5319, October 2002. ISSN 0020-1669. URL http://dx.doi.org/10.1021/ic025564d.

[86] Y. Okamoto and J. C. Goswami. Preparation and Properties of Barium Pernitride Ba3N4. *Inorganic Chemistry*, 5(7):1281–&, 1966.

[87] Theis Brock-Nannestad. Department of Chemistry, University of Copenhagen.

Paper I

Paper I
Controlled Directional Growth of TiO_2 Nanotubes
Su-il In, Yidong Hou, Billie L. Abrams, Peter C. K. Vesborg and Ib Chorkendorff
Accepted - Journal of The Electrochemical Society (2010).

Controlled Directional Growth of TiO_2 Nanotubes

*Su-Il In, Yidong Hou, Billie L. Abrams, Peter C.K. Vesborg, and Ib Chorkendorff**

Technical University of Denmark, Department of Physics, Center for Individual Nanoparticle Functionality, Building 312, 2800 Kgs, Lyngby, Denmark

E-mail: ibchork@fysik.dtu.dk

ABSTRACT: We demonstrate how the anodization direction and growth rate of vertically-aligned, highly-ordered TiO_2 nanotube arrays can be controlled and manipulated by the local concentration of O_2. This leads to the growth of highly active TiO_2 nanotube arrays directly on non-conducting substrates in a single step. By controlling the oxygen concentration the electrical contact to the Titanium film can be preserved until the entire film is anodized. The role of molecular oxygen on the anodization and the means necessary for controlling the growth direction were investigated through use of labeled oxygen and concentration gradient experiments.

KEYWORDS: TiO_2, nanotubes, photocatalysis, oxygen

INTRODUCTION

Highly-ordered, large-aspect ratio TiO_2 nanotubes (NTs) [1-7] offer new possibilities in the area of sustainable energy due to enhanced photocatalytic water-splitting activity [2,8] and applications in solar cells [9-12]. This is because they allow for fast separation of electron-hole pairs while at the same time exposing a high surface area where photocatalytic reactions take place. Another important use is in self-cleaning or environmental remediation technology where TiO_2 NTs may have a high activity for photooxidation of organics [13,14]. Specifically, formation of optically transparent TiO_2 NTs onto non-conducting substrates allows access to new photocatalytic environments i.e., gas phase photocatalysis using glass, polymer, or ceramic substrates. Here, we demonstrate how the growth direction and rate of these NT arrays can be controlled by the local O_2 concentration allowing single-step growth of TiO_2 NT directly onto non-conducting substrates. We also show how molecular oxygen affects the growth mechanism through isotopic labeling experiments and concentration gradients.

Generally, planar TiO_2 films can be prepared using the sol-gel method [15,16] or by sputtering (either dc or rf) [17,18] resulting in reasonably reactive surface areas. Attempts to enhance the surface area of TiO_2 have been explored by synthesizing TiO_2 nanotubes using a template process [19,20]. Recently, vertically-oriented, highly-ordered TiO_2 nanotube (NT)-array thin films made by anodization of titanium metal have received much attention because of their high surface area nano-structure [2,6,7,21]. Anodization of Ti using a fluoride-containing polyhydric alcohol such as ethylene glycol (EG) as the electrolyte results in ordered TiO_2 NT-arrays [22,23]. The anodization process depends critically on pH, F^- concentration, as well as EG and water concentration [22-24]. Various mechanisms have been proposed to account for the TiO_2 NTs forming [23,25], but the role of the individual components is not completely understood.

It has been reported that anodization of single-layer titanium films onto non-conducting glass substrates is not possible as the metal layer in contact with the electrolyte surface is rapidly etched away as shown in Figure 1a [21]. Mor et al. have reported that this problem may be circumvented by a two-step process or "bi-layer" approach which involves anodization down to a thin "first layer" of Ti metal, so that the electrical contact is not broken. This first thin Ti layer is subsequently oxidized thermally, leading to a transparent TiO_2 nanotube film on top of a conventional TiO_2 thin film. This approach does produce TiO_2 NTs onto non-conducting substrates but involves a multistep approach and there is a dense oxide film between the support and the NT layer [21]. The method presented here, which involves controlling the NT-array growth direction through the molecular oxygen concentration, also alleviates the contact-loss problem by ensuring that the contact point is the last part (Figure 1b) to be anodized – a principle that may also be used for other anodization processes as well. This approach also allows for the formation of the TiO_2 nanotubes onto a nonconducting substrate in a one-step process where the nanotubes are in direct contact with the non-conducting (i.e., Pyrex glass) substrate.

EXPERIMENTAL

Formation of TiO_2 Nanotubes (NTs)

The substrate was Pyrex glass coated with thermally deposited metallic titanium. First, a titanium film (400 nm thick) was deposited on 4 inch Pyrex wafers (JINSOL) via E-beam deposition (Wordentec QCL800). Prior to Ti film deposition, the Pyrex wafers were cleaned using sulphuric acid with ammonium peroxydisulfate at 80 ^{o}C for 10 min, rinsed with water for 10 min and dried at 250 ^{o}C overnight. The purity of the Ti target used was 99.995%. The base chamber pressure was approximately 5×10^{-7} mbar. The deposition rate was 10 Å/s. Prior to anodization, the titanium metal film was cleaned with acetone and ethanol followed by a deionized water rinse. The anodization was performed using a two-electrode cell with titanium deposited on Pyrex as the working electrode and carbon paper as the counter electrode. Anodizations were carried out for about 1.5 hours at a constant applied voltage of 10V at room temperature in an electrolyte mixture of 0.3 wt.% NH_4F (98%, ACS reagent, Sigma Aldrich) and 2 vol. % H_2O in ethylene glycol (ReagentPlus® , ≥ 99%, Aldrich). Note, as expected, there was no significant ohmic drop across the sample at any time during the process. The temperature of the electrolyte solution was 298 K. To convert the amorphous TiO_2 nanotube array film into anatase, the as-prepared sample was annealed at 450 °C for 2 hours in air (30 ml/min).

Measurement of Oxygen Concentrations in solution

The dissolved oxygen present in the electrolyte during the anodization was monitored by an OxySense 210T non-invasive oxygen determination (NIOD) instrument. This technique utilizes the effect of oxygen on the fluorescence lifetime of a Ruthenium (Ru) complex that is excited by a blue LED with a wavelength between 400-500 nm. The Ru complex is immobilized in a stable polymer and placed in the form of a 5mm diameter dot on the inner wall of the container submerged in the electrolyte in the same depth as the sample being anodized and 20 mm from the sample. The excitation light source/detector is placed outside the container but within a 5 mm distance of the dot in order to measure the O_2 concentration. We noticed that the oxygen diffusion is somewhat higher than what would be expected for a standard diffusion constant of D_{O2}=1.97*10^{-5} cm^{-2}/s. This is ascribed to the non-ideal conditions under which these experiments were performed for measuring diffusion and was not pursued further as the establishment of a strong gradient in the oxygen concentration was successful.

Oxygen Isotope Labeling Experiment: SIMS

Ion probe analysis was performed at Danchip, DTU, using a quadrupole SIMS, ATOMIKA 4000. Sputter etching of the surface was accomplished with 5 KeV Cs^+ ions raster scanned over 300 μm (I = 10 nA) at 20^{o} impact angle from normal incidence. The main chamber base pressure was about 10^{-10} Torr. Oxygen isotopes were analyzed as O^- ions produced by a bombardment by a Cs^+ primary beam (10 nA intensity) of around 15 μm in diameter. The Oxygen isotopes were subsequently measured in a single channeltron plate.

UV-Vis Measurements

UV-Vis spectra were collected using a Cary 1e spectrophotometer operated in dual beam mode and with an uncoated Pyrex sample in the reference beam.

Photocatalytic Activity

The photocatalytic oxidation of acetone over TiO_2 thin films was performed in a 440 ml steel reactor with a quartz window at ambient temperature. A circulating gas pump was set up between the reactor and gas chromatograph (Perkin Elmer Claus 500 GC, Porapak® QS 80/100 mesh, 2 m × 1/8 in.). A 4-inch diameter Pyrex wafer coated with TiO_2 NTs was placed in the reactor. 1 µL liquid acetone was injected into the reactor. Inside the reactor the acetone vaporized and was allowed to reach adsorption equilibrium with the catalyst in the reactor prior to an experiment, the initial concentration of acetone after the adsorption equilibrium was about 720 ± 20 ppmv. A 4 W UV lamp (UVP® UVGL-15) with a dominant emission at 345-365 nm was used as an excitation light source. Figure S6 shows the UV light source spectrum. Integrated UV intensity measured with a UV radiometer was 1.75 mW/cm^2.

RESULTS and DISCUSSION

The realization that molecular oxygen enhances the anodization process makes it important to establish well-defined oxygen concentration gradients. The oxygen concentration profile can be established in numerous ways but here we shall demonstrate two of the more common designs in detail. In the first approach, termed the "bottom contact" method, the entire closed system containing the electrolyte, headspace and anode is first de-aerated with Argon. The anode is then submerged into the electrolyte mounted vertically with the electrical contact to the Ti layer at the largest possible distance from the surface as shown in the diagram of Figure 2. After the electrolyte is saturated with Ar the headspace is exchanged with atmospheric air and the anodization process is initiated.

In this manner an oxygen concentration gradient is established in the electrolyte being highest at the surface which is in contact with air. Figures 2 a, b and c show the process of forming the nanotube arrays in this manner where the anodization was stopped after 3760 sec, *i.e.* when the top part of the sample is getting transparent, but before the entire Ti-film (400 nm) is completely converted into NT which for this type of sample usually takes ~4400 sec. Cross-sectional Scanning Electron Microscopy (SEM) images of a sample were taken from each part of the anode corresponding to 1 cm, 2 cm and 3 cm below the electrolyte surface, respectively. Figure 2a shows the fully anodized upper part of the anode where there is no Ti metal layer remaining. Figure 2b is the middle part of the anode, which still has some Ti metal layer remaining (~30 nm) and Figure 2c shows the bottom part of the anode, which has more Ti metal layer left (~50 nm). Typically we start with a Ti metal layer 400 nm in thickness which usually leads to a NT layer of about the same length accompanied by a variable volume expansion on the order of 1 to 1.2. This expansion is somewhat less than what is reported in literature [26,27]. The nanotubes shown in this work have tube lengths of about 400 nm with O.D. ~ 30 nm and I.D. ~ 20 nm. Viewed from the side the nanotubes look thin and elongated. From the top, they are hollow and highly-ordered.

The oxygen concentrations were measured with an oxygen sensor (OxySense) which is based on measuring the fluorescence lifetime of a

ruthenium-based complex in a so-called Oxydot. Three Oxydots were mounted on the inside of the container in the electrolyte at depths corresponding to the SEM locations. The oxygen concentration profiles as a function of time for each portion of the TiO_2 NT film are plotted in Figure 2d.

Initially, the system was de-aerated by purging N60 Argon until the oxygen concentration reading by the three Oxydots, each corrected for their individual offsets, gave constant readings corresponding to the detection limit (< 0.18 % of saturation). Oxydots monitor oxygen diffusion to the different portions of the sample during anodization. Figure 2e is the measured anodization rate extracted from Figures 2a-2c versus the average oxygen concentration at each position. It is observed that the rate increases with increasing oxygen concentration, although the enhancement due to oxygen is modest. It should be mentioned that performing the same experiments without oxygen above the electrolyte or a saturated electrolyte in contact with air, would lead to random initiations of the anodization and usually premature loss of contact. Since oxygen obviously enhances the anodization process the NT-formation can be controlled to proceed from the top towards the bottom contact with no loss of contact.

It is also possible to control the oxygen concentration gradient without the use of air if desired. For example a localized source of oxygen can be established by electrolysis on a gold wire under the anode in a de-aerated container. Note, it is not desired to have oxygen bubbling uncontrollably, but rather bubbles adhering to the wire as a diffusion-source of oxygen. If +5 V is applied to the Au wire (with respect to a carbon paper counter electrode) until small oxygen bubbles cover the Au wire as indicated in Figure 3a an oxygen gradient away from the Au wire will develop. In this case the growth direction can be manipulated to grow from the bottom towards the contact point at the top. Other geometries (i.e, horizontal) and sources of oxygen (i.e., electrolysis and air-tubes) have been performed, all clearly demonstrating that the directional growth can be manipulated by the oxygen concentration, see Figure 3b. In this case the Au wire is placed at one end of the anode, opposite to the contact side. Numerous other configurations were tested consistently demonstrating that the process can be controlled by the oxygen gradient. It is crucial to avoid oxygen evolution near the contact point itself, which is at +10 V, since that would enhance anodization locally leading to premature loss of contact. Thus the choice of wire material used to make electrical contact is important. They must consist of self-passivating materials such as Ti or Al suppressing oxygen evolution, while oxygen evolving materials like gold (Au) or platinum (Pt) must be excluded.

To elucidate the mechanism experimentally we used ^{18}O-isotope labeled molecular oxygen and water see in order to trace the oxygen location and determine its role in NT formation. Two different samples were prepared in a (initially) de-aerated electrolyte, T1: 2 vol. % of H_2O (standard electrolyte) and T2: 2 vol. % of H_2O with a bubble of ^{18}O labeled O_2 held near the anode. The T1 sample constitutes the reference sample and is only

displaying the ^{16}O isotope (Figure 4a, blue line). When an ^{18}O-labeled oxygen bubble is suspended near the anode (T2) during anodization, ^{18}O remains absent in the depth profile (Figure 3a black line). We do, however, see an increased ^{16}O signal in the SIMS profile (Figure 3a red line). The enhanced SIMS signal could be due to a geometric effect in the SIMS measurement. For example, if the NTs grown under the influence of O_2 have slightly different geometries (*i.e.*, wall thickness/diameter ratio) than those grown without O_2, the oxygen ion yield would be affected. Similar effects are observed when the ^{16}O bubble was provided near the anode (T4, see Figure 3b). From this it is concluded that oxygen from O_2 is not implemented in the TiO_2 to any significant degree.

Beyond the experiment shown in Figure 3a showing that no $^{18}O_2$ was implemented in the TiO_2 NT we also performed experiments using ^{18}O labeled water (samples T3 and T4). These samples were prepared like T1 and T2 but with the following modifications: T3: 2 vol. % of ^{18}O labeled $H_2{}^{18}O$, and T4; 2 vol. % of ^{18}O labeled $H_2{}^{18}O$ and an unlabeled O_2 bubble near the anode. In this case both ^{16}O and ^{18}O were clearly present in the film (Figure 3b). Given the isotopic purity of the labeled water (> 97% ^{18}O, CK gas products Ltd) and size of the ^{16}O signal there can be no doubt that oxygen from ethylene glycol is also being incorporated into the TiO_2 nanotubes as there is no other source of ^{16}O present. It has been considered that water is the main oxygen source in forming TiO_2 NTs [25], but the availability of oxygen from organic solutions has also been suggested [23]. The current data also provides experimental support that EG does indeed donate oxygen to the nanotube structures. From this result (Figure 3b) it seems that water and EG could be acting as competing oxygen sources during anodization with EG leading in the very beginning. But eventually the dominant oxygen contribution is from water despite the ~ 16:1 molar ratio of EG to water. We believe that mass transport of reactants down through the growing film (of high aspect ratio nanotubes) may account for this since the smaller water molecules are likely to diffuse faster than EG.

In order to explain how O_2 enhances anodization without being implemented in the oxide we propose the mechanism illustrated in Figure 5. The model is based on the following two assumptions: 1) That above some critical break-down field strength across the oxide, oxygen vacancies form at the electrolyte-surface/interface Figure 5a, a phenomenon also reported by Zhang *et al.* [28]. 2) That this vacancy (*i.e.*, for geometric reasons) cannot accommodate a water molecule but can accommodate an O_2 molecule (Figure 5b). Using these assumptions, we suggest that a partial oxidation of the adsorbed O_2 molecule by the strongly anodic-biased oxide can occur. This yields an electrostatic attractive force between the outermost O-atom of the adsorbed molecule and anions or dipoles in the surroundings. Fluoride ions cannot readily donate electrons but water molecules (or potentially hydroxyl ions) can. Figures 5c and 5d illustrate the process where the H-atoms of a water molecule donate electrons to the surface via the adsorbed oxygen - effectively filling the surface vacancy and liberating a new O_2 molecule (Figure 5e). The net (anodic) reaction in this case remains:

$$TiO + H_2O\ (+ O_2) \rightarrow TiO_2 + 2\ H^+\ (+ O_2) + 2e^- \quad (1)$$

This is in accordance with the general picture accepted in the literature of water acting as the main oxygen source [3]. In an isotope-labeled experiment using an ^{18}O-labeled suspended bubble to initiate the anodization (*i.e.* experiment T2 above) one would expect, that near the very top of the nanotubes corresponding to initial growth there should be an enrichment of ^{18}O in the film. The reason may be seen in Figure 5b where we find that the oxygen atom filling the vacancy comes from the O_2 molecule and as such has a probability of donating an ^{18}O-atom of $p = 2^{-n}$, where n is the number of times the molecule has previously catalyzed the reaction. Within the sensitivity of our SIMS data we do not see such an initial hump in the ^{18}O signal in the T2 profile. This is, however, expected since the total expected ^{18}O amount only should be about a monolayer to begin with and furthermore chemical dissolution of the nanotubes during growth will mostly etch the top of the tubes whereby the labeled oxygen is lost.

In order to demonstrate that such NT-growth on insulating material have the desired optical properties and catalytic activity (400 nm) we measured the absorbance and photocatalytic activity of the TiO_2 NTs. They were grown on 4-inch Pyrex wafers and compared to P25 TiO_2 spin-coated on similar wafers for similar thickness as shown in Figure 6a. As-anodized TiO_2 NTs were amorphous and were thus annealed at 450^{o}C in order to convert them to anatase (See XRD and XPS data in Figures S4 and S5, respectively). The absorbance spectra of annealed TiO_2 NT-array film were compared with those of the same thickness P25 TiO_2 coated film. The data of Figure 6b clearly shows that the nanotube films are much more transparent over the entire visible spectrum relative to the P25 TiO_2 powder, which exhibits much higher scattering loss and a dull grey appearance as seen in the photographs Figure 6a.

The photocatalytic activity was evaluated by the oxidation of gaseous acetone under UV light irradiation utilizing a batch reactor with principles of operation similar to that described by Yu *et al.* [29,30]. Here, however, a GC was used to evaluate evolution of any possible organic intermediates. Figure 6c shows the acetone concentration and subsequent evolved CO_2 as a function of time. Apart from the decay of the acetone only the final products for complete mineralization of acetone, CO_2, was observed in an almost stoichiometric ratio 1:3. The photocatalytic activity for acetone degradation over the TiO_2 NT film (318 ppmv/h, corresponding to ~1.04×10^{15} acetone molecules/sec) was similar or better than that of the commercial 400 nm thick P25 TiO_2 for similar conditions.

CONCLUSION

In this work, we showed that it was possible to control the growth rate and thus direction of TiO_2- nanotube arrays by manipulating the oxygen concentration gradient. This has the advantage that such nanotubes can be grown from a metallic titanium film deposited on an insulating material in a one step procedure over large areas (>= 4 inch wafer). We demonstrated that the nanotube arrays made here maintain the desired properties concerning mineralization of organic compounds for self-cleaning purposes and optical properties *i.e.*, transparency. The procedure described here is versatile and

promising for large-scale production of transparent nanotube arrays on insulating media – an effect that may also be pursued for anodization of other materials. An autocatalytic model is proposed based on the fact that labeled oxygen ^{18}O was not implemented in the NT-array as judged by SIMS analysis. It was, however, found that oxygen from the labeled water was implemented in the nanotubes in competition with oxygen from the ethylene glycol.

ACKNOWLEDGMENT: We thank John Larsen for his help in XPS experiments. The Center for Integrated Nanoparticle Functionality is funded by the National Danish Research Council. This work was also funded by the Clean Catalytic Surfaces project through the Danish Innovations konsortium.

REFERENCES

[1] D. Gong, C. A. Grimes, O. K. Varghese, W. C. Hu, R. S. Singh, Z. Chen, and E. C. Dickey, *Journal of Materials Research* **16,** 3331-3334 (2001).

[2] C. A. Grimes, *Journal of Materials Chemistry* **17,** 1451-1457 (2007).

[3] G. K. Mor, O. K. Varghese, M. Paulose, K. Shankar, and C. A. Grimes, *Solar Energy Materials and Solar Cells* **90,** 2011-2075 (2006).

[4] O. K. Varghese, D. W. Gong, M. Paulose, C. A. Grimes, and E. C. Dickey, *Journal of Materials Research* **18,** 156-165 (2003).

[5] O. K. Varghese, D. W. Gong, M. Paulose, K. G. Ong, E. C. Dickey, and C. A. Grimes, *Advanced Materials* **15,** 624-627 (2003).

[6] V. Zwilling, M. Aucouturier, and E. Darque-Ceretti, *Electrochimica Acta* **45,** 921-929 (1999).

[7] V. Zwilling, E. Darque-Ceretti, A. Boutry-Forveille, D. David, M. Y. Perrin, and M. Aucouturier, *Surface and Interface Analysis* **27,** 629-637 (1999).

[8] G. K. Mor, K. Shankar, M. Paulose, O. K. Varghese, and C. A. Grimes, *Nano Letters* **5,** 191-195 (2005).

[9] M. Gratzel, *Nature* **421,** 586-587 (2003).

[10] J. R. Jennings, A. Ghicov, L. M. Peter, P. Schmuki, and A. B. Walker, *Journal of the American Chemical Society* **130,** 13364-13372 (2008).

[11] T. S. Kang, A. P. Smith, B. E. Taylor, and M. F. Durstock, *Nano Letters* **9,** 601-606 (2009).

[12] K. Lee, S. W. Park, M. J. Ko, K. Kim, and N.-G. Park, *Nature Materials* **8,** 665-671 (2009).

[13] Z. Liu, X. Zhang, S. Nishimoto, M. Jin, D. A. Tryk, T. Murakami, and A. Fujishima, *Journal of Physical Chemistry C* **112,** 253-259 (2008).

[14] Z. Y. Liu, X. T. Zhang, S. Nishimoto, T. Murakami, and A. Fujishima, *Environmental Science & Technology* **42,** 8547-8551 (2008).

[15] J. Medina-Valtierra, J. Garcia-Servin, C. Frausto-Reyes, and S. Calixto, *Applied Surface Science* **252,** 3600-3608 (2006).

[16] Y. F. Zhu, L. Zhang, W. Q. Yao, and L. L. Cao, *Applied Surface Science* **158,** 32-37 (2000).

[17] A. Karuppasamy and A. Subrahmanyam, *Journal of Applied Physics* **101** (2007).

[18] A. Mills, J. S. Wang, M. Crow, G. Taglioni, and L. Novella, *Journal of Photochemistry and Photobiology a-Chemistry* **187,** 370-376 (2007).

[19] P. Hoyer, *Langmuir* **12,** 1411-1413 (1996).

[20] P. Hoyer, *Advanced Materials* **8,** 857-& (1996).

[21] G. K. Mor, O. K. Varghese, M. Paulose, and C. A. Grimes, *Advanced Functional Materials* **15,** 1291-1296 (2005).

[22] J. M. Macak and P. Schmuki, *Electrochimica Acta* **52,** 1258-1264 (2006).

[23] K. S. Raja, T. Gandhi, and M. Misra, *Electrochemistry Communications* **9,** 1069-1076 (2007).
[24] K. S. Raja, M. Misra, and K. Paramguru, *Electrochimica Acta* **51,** 154-165 (2005).
[25] J. M. Macak, H. Tsuchiya, A. Ghicov, K. Yasuda, R. Hahn, S. Bauer, and P. Schmuki, *Current Opinion in Solid State & Materials Science* **11,** 3-18 (2007).
[26] D. J. LeClere, A. Velota, P. Skeldon, G. E. Thompson, S. Berger, J. Kunze, P. Schmuki, H. Habazaki, and S. Nagata, *Journal of the Electrochemical Society* **155,** C487-C494 (2008).
[27] A. Valota, D. J. LeClere, T. Hashimoto, P. Skeldon, G. E. Thompson, S. Berger, J. Kunze, and P. Schmuki, *Nanotechnology* **19** (2008).
[28] L. Zhang, D. D. Macdonald, E. Sikora, and J. Sikora, *Journal of the Electrochemical Society* **145,** 898-905 (1998).
[29] J. G. Yu, Y. R. Su, and B. Cheng, *Advanced Functional Materials* **17,** 1984-1990 (2007).
[30] J. G. Yu, J. C. Yu, M. K. P. Leung, W. K. Ho, B. Cheng, X. J. Zhao, and J. C. Zhao, *Journal of Catalysis* **217,** 69-78 (2003).

Figure 1

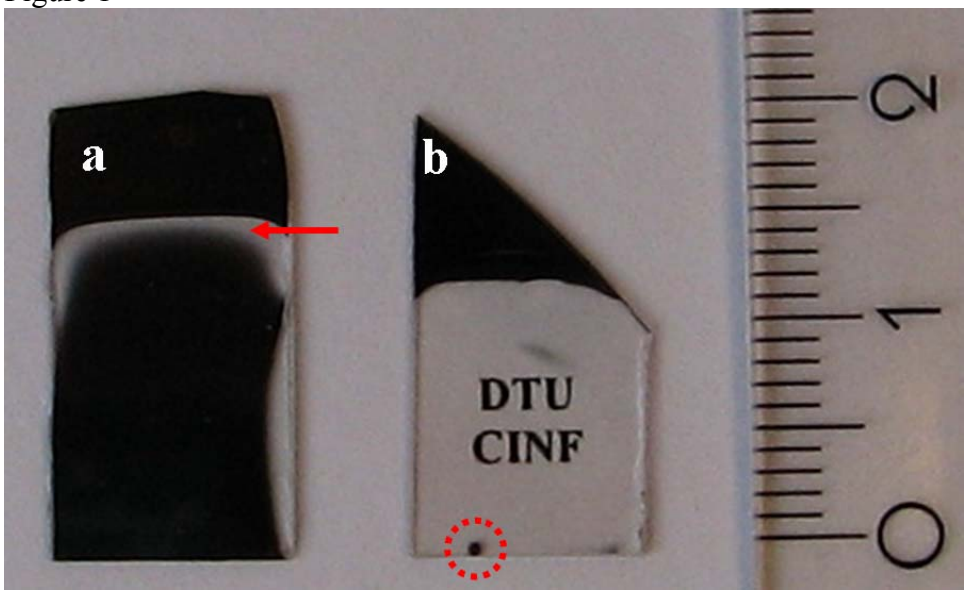

Figure 2

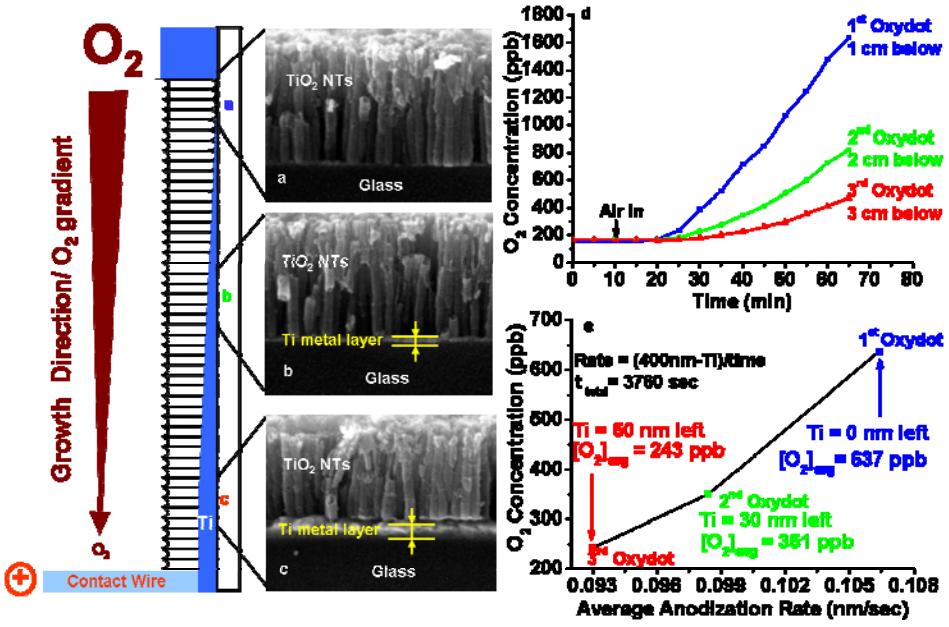

Figure 3

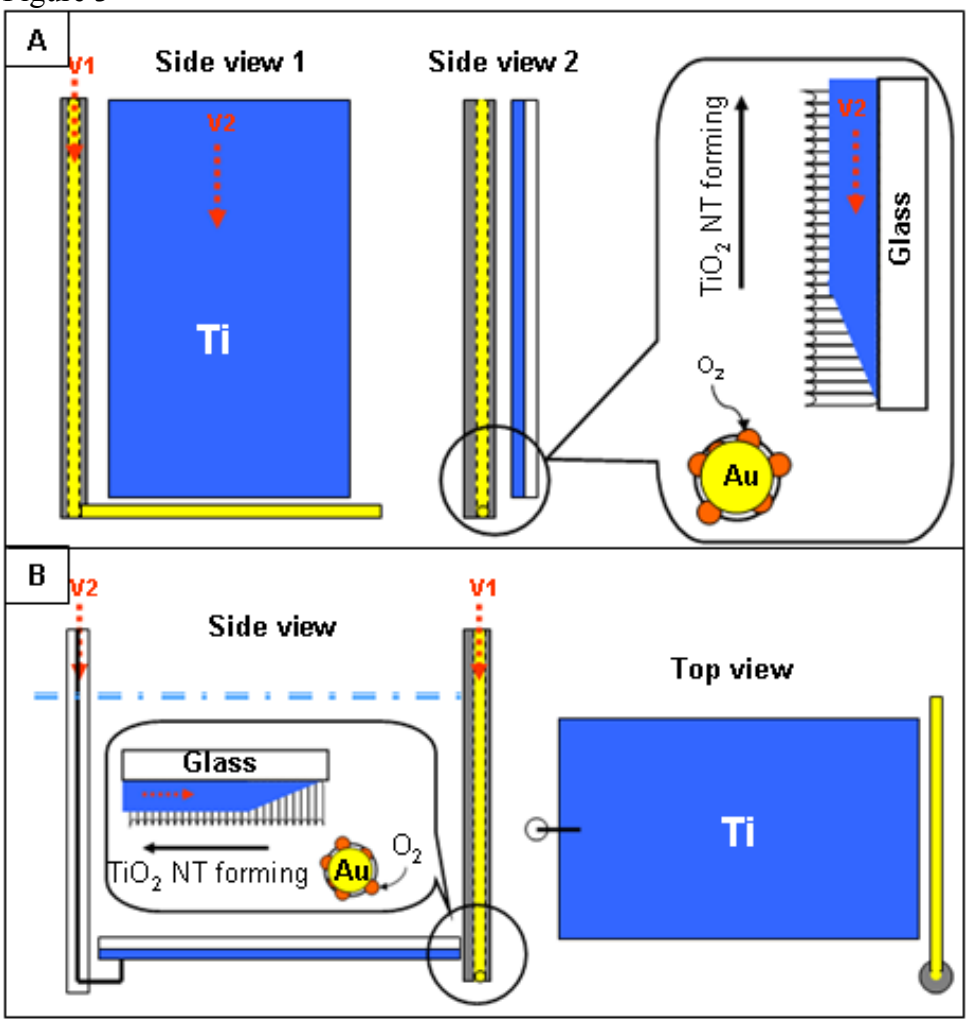

Figure 4

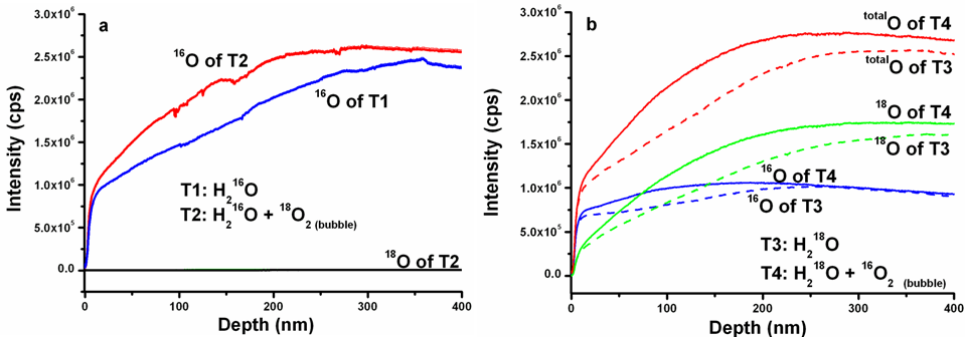

Figure 5.

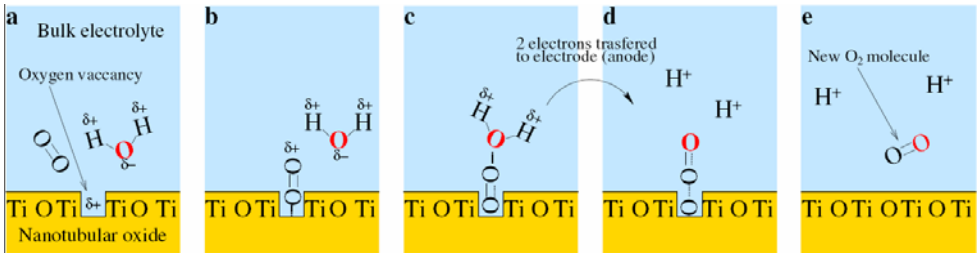

Figure 6.

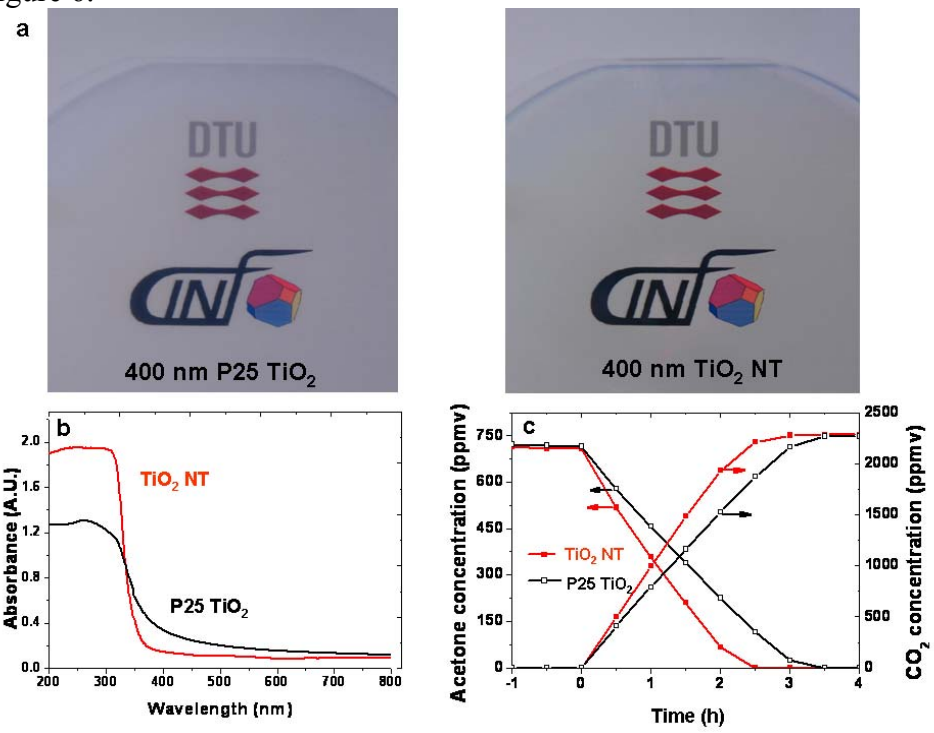

Figure Captions

Figure 1 A digital photograph showing (a) unsuccessful anodization of single-layer Ti film onto a non-conducting glass substrate (Red arrow points out rapidly etched part consequently causing electric disconnection) (b) Successful direct anodization of single-layer Ti film onto a non-conducting glass substrate by a "bottom contact" method (Black letters are clear and the bottom contact point is remaining).

Figure 2. Schematic diagram and corresponding SEM image of "bottom contact" method of anodization process generating a 400 nm thick TiO_2 NT-array thin film. The dark red arrow shows the direction forming TiO_2 NTs as a result of the enhanced anodization rate. The enhanced rate is due to higher oxygen concentration at the top. SEMs were taken at 1 cm, 2 cm, and 3 cm depths at different stages of the anodization process. (a) The corresponding SEM image at 1 cm shows no Ti metal remaining consistent with this part being transparent *i.e.* completely anodized. (b) At 2 cm the presence of a thin Ti metal layer is indicated by the yellow arrows between the TiO_2 NTs and the glass substrates. (c) Near the contact point (3 cm) resides the thickest Ti metal layer remaining since it is the last region to be fully converted to NTs, (d) O_2 concentration as a function of time for each position of the SEM images. (e) Average anodization rate at various average oxygen concentrations, corresponding to the SEM images of parts a, b, and c.

Figure 3. Schematic diagrams of the experimental setups used for growing TiO_2 NT-array films by controlling oxygen concentration. (A) A voltage V1 of 5 V is applied to the Au wire until oxygen covers the Au wire and then 10 V is applied to V2 from the top of the anode. (B) The anode is placed horizontally under the electrolyte solution. 10 V is applied to V2 at the point furthest away from the Au wire. Both principles have been demonstrated successfully.

Figure 4. (a) SIMS data showing oxygen depth profiles of TiO_2 NTs prepared with isotopically labeled molecular oxygen. T1 is without labeled O_2 (the control - blue line). T2 is the experiment utilizing ^{18}O labeled O_2 bubble held near the anode (red and black lines). The total oxygen flux in both cases is similar to ^{16}O flux from TiO_2 NTs. ^{18}O is negligible. (b) SIMS data showing depth profiles of TiO_2 NTs of isotope labeled water experiment. The solid lines represent labeled water with $^{16}O_2$ bubble present. The dotted lines represent experiments without $^{16}O_2$ bubble present. The upper red lines represent the total oxygen flux, the second set of green lines represent the ^{18}O flux, and the third set of blue lines represent the ^{16}O flux from TiO_2 NTs growth.

Figure 5. Autocatalytic mechanism for O_2 anodization enhancement. (a) Initial situation where the strong anodic bias has created an oxygen vacancy at the surface. (b) O_2 is adsorbed in the vacancy. (c) Electrostatic attraction between the adsorbed O_2 molecule attracts a (polar) water molecule (with its O-atom shown in red). (d) The H atoms of the water molecule are oxidized via the adsorbed O_2 molecule and the donated electrons give rise to the anodization current. (e) The O-atom from the water molecule covalently

bonds to the outer O-atom of the adsorbed O_2 molecule causing a scission of the original O-O bond leaving the vacancy annihilated and forming a (new) O_2 closing the cycle.

Figure 6. Activity and absorbance measurements comparing TiO_2 NTs and P25 TiO_2 for the same thickness (400nm) on a Pyrex glass substrate. (a) Left: Spin-coated P25 TiO_2 on a 4-inch Pyrex wafer (See Figure S7 for SEM). Right: Transparent TiO_2 NTs formed on the 4-inch Pyrex wafer. (b) Optical absorbance spectra of TiO_2 NTs (red curve) and P25 TiO_2 (black line). (c) Photocatalytic activity measurements comparing TiO_2 NTs to P25 TiO_2. Changes in acetone (left axis) and CO_2 concentrations (right axis) are plotted as a function of time in the presence of a TiO_2 NT-array film (red lines, filled boxes) and a P25 thin film (black line, open boxes) under UV irradiation.

Paper II

Highly sensitive silicon microreactor for catalyst testing
Toke R. Henriksen, Jakob L. Olsen, Peter C. K. Vesborg, Ib Chorkendorff, and Ole Hansen
Review of Scientific Instruments **80**, 124101 (2009).

Highly sensitive silicon microreactor for catalyst testing

Toke R. Henriksen,[1,2] Jakob L. Olsen,[2] Peter Vesborg,[2] Ib Chorkendorff,[2] and Ole Hansen[1,2,a)]

[1]*Department of Micro- and Nanotechnology, Technical University of Denmark, DTU Nanotech Building 345 East, DK-2800 Kgs. Lyngby, Denmark*

[2]*Department of Physics, Danish National Research Foundation's Center for Individual Nanoparticle Functionality (CINF), Technical University of Denmark, Building 312, DK-2800 Kgs. Lyngby, Denmark*

(Received 14 July 2009; accepted 6 November 2009; published online 7 December 2009)

A novel microfabricated chemical reactor for highly sensitive measurements of catalytic activity and surface kinetics is presented. The reactor is fabricated in a silicon chip and is intended for gas-phase reactions at pressures ranging from 0.1 to 5.0 bar. A high sensitivity is obtained by directing the entire gas flow through the catalyst bed to a mass spectrometer, thus ensuring that nearly all reaction products are present in the analyzed gas flow. Although the device can be employed for testing a wide range of catalysts, the primary aim of the design is to allow characterization of model catalysts which can only be obtained in small quantities. Such measurements are of significant fundamental interest but are challenging because of the low surface areas involved. The relationship between the reaction zone gas flow and the pressure in the reaction zone is investigated experimentally. A corresponding theoretical model is presented, and the gas flow through an on-chip flow-limiting capillary is predicted to be in the intermediate regime. The experimental data for the gas flow are found to be in good agreement with the theoretical model. At typical experimental conditions, the total gas flow through the reaction zone is around 3×10^{14} molecules s^{-1}, corresponding to a gas residence time in the reaction zone of about 11 s. To demonstrate the operation of the microreactor, CO oxidation on low-area platinum thin film circles is employed as a test reaction. Using temperature ramping, it is found that platinum catalysts with areas as small as 15 μm^2 are conveniently characterized with the device. © *2009 American Institute of Physics.*
[doi:10.1063/1.3270191]

I. INTRODUCTION

In heterogeneous catalysis, the discovery, characterization, and optimization of catalysts require extensive experimentation and are critical steps in the development of new chemical processes. Traditionally, macroscale chemical reactors such as the idealized plug flow reactor have been used for catalyst testing.[1] As a supplement to these traditional reactors, microfabricated reactors have, in recent years, shown promise as versatile analytical tools for measuring catalytic activity. Microfabricated reactors, also known as microreactors, are chemical reactors with dimensions in the micrometer range. Pioneered by, among others, Jensen *et al.*, microreactors have been shown to offer a number of advantages compared to conventional macroscale reactors.[2–6] The temperature of a microreactor can be varied easily and quickly because of the small size. Due to the high surface-to-volume ratio, heat transfer to and from the reaction zone is greatly enhanced. This reduces thermal gradients in the reactor and makes accurate control of temperature possible, even for strongly exothermic reactions. Furthermore, the small dimensions of the reactor improve mass transfer and reduce concentration gradients. Small thermal and concentration gradients are favorable when determining kinetic data. Reaction parameters such as pressure, residence time, and flow rate are more easily controlled in reactions that take place in small volumes. In addition to these advantages, the small scale of the reactor improves safety of use for explosive mixtures and greatly reduces reactant gas consumption. Finally, it is possible to integrate heaters and sensors directly into microreactors using microfabrication technology.

Fundamentally, a microreactor consists of a system of microchannels in which the reactants will flow and react. The flow through the microchannels is mostly laminar, resulting in predictable and well-controlled flow patterns. Due to the small dimensions, the residence time of the reactant gas in the catalyst bed is typically low. Consequently, high space velocities can be obtained.

In combination with an appropriate instrument for gas composition analysis, it is possible to design microreactors which facilitate detection of very small amounts of gas phase products. This is a consequence of the low flow rate through the microchannel system. High sensitivity product detection under atmospheric pressure is useful in several respects. When investigating new, nonoptimized catalysts, the catalytic activity might be low, necessitating detection of small amounts of substances. Furthermore, some model catalysts, such as mass selected clusters and catalysts fabricated using electron-beam lithography (EBL), can only be obtained in small quantities. Thus, a sensitive experimental arrangement is required for measuring the catalytic activity of such samples.[7–9]

a)Electronic mail: ole.hansen@nanotech.dtu.dk.

A few microreactors for low-area catalyst characterization with gas-phase reactions have been reported in literature. Johansson *et al.*[9] demonstrated a Pyrex flow microreactor for measuring catalytic activity of nanofabricated model catalysts at atmospheric pressure. The microreactor had a reaction chamber volume of around 100 mm^3, a reaction zone gas flow of about 4×10^{16} molecules s^{-1}, and a gas residence time in the reaction zone of approximately 60 s. They observed CO oxidation on a platinum wire with a surface area of 0.3 mm^2. Jacobs *et al.*[10] measured ethylene hydrogenation at atmospheric pressure in a closed tank reactor. They detected catalytic activity on an EBL-nanofabricated platinum model catalyst with a total active surface area of 4 mm^2.

Our research group has previously fabricated microreactors and applied them in experiments concerning catalysis and surface science.[11–14] In this paper, we present a novel continuous-flow microreactor with a highly improved sensitivity for measurements of catalytic activity. The device is intended for gas-phase reactions at pressures in the range of 0.1–5.0 bar. The gas composition is analyzed using a quadropole mass spectrometer (QMS). As a characteristic feature, the microreactor presented here directs the entire reaction zone gas flow to enter the mass spectrometer. This increases the sensitivity considerably compared to traditional microreactors where only a small fraction of the gas flow is analyzed.

The microreactor is designed as an analytical tool for catalyst testing. In this context, the term *catalyst testing* covers measurements of catalytic activity, turnover frequency, apparent activation energy, and surface area, as a result of temperature programmed desorption and experiments with conversion rate as a function of temperature and gas phase stoichiometry. The high sensitivity of the reactor makes it especially well-suited for fundamental catalytic activity studies of model catalysts with low surface areas. A particularly important application is the characterization of mass selected metal clusters with a narrow size distribution. Such measurements are of significant interest for the purpose of correlating size and catalytic activity of clusters.[15–17] Often, a low density of clusters is desirable in these studies to suppress sintering effects. Ensembles of metal clusters can be produced with a magnetron sputtering cluster source, but only in small quantities per unit time, since the cluster beam intensity decreases with reduced spread in the cluster size. Thus, a highly sensitive measurement technique, like the one presented here, could substantially reduce the time consumption of such experiments.

Although the high sensitivity is particularly advantageous for fundamental studies involving small quantities of model catalysts, the microreactor is not restricted to such experiments. In addition to deposition from a cluster source, catalyst samples can be introduced into the reactor using a variety of other methods, including flame spray deposition,[18] dip-coating, spin coating, or manual deposition with a pipette. During catalyst deposition, a shadow mask can be used to confine deposition to the reaction chamber area. Any catalyst, which can be deposited with these methods and which can fit in the reaction chamber, can be tested with the device.

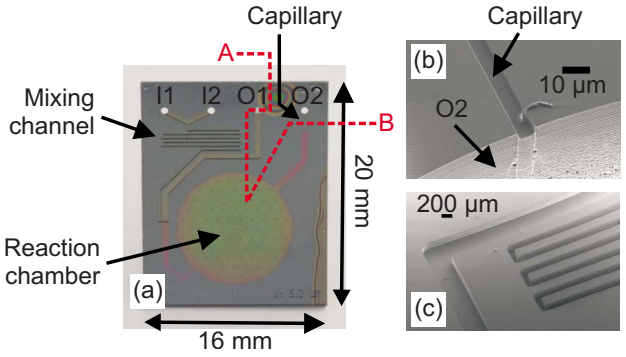

FIG. 1. (Color online) (a) Photograph of reactor showing the two inlets I1 and I2 and the two outlets O1 and O2. The dashed red line signifies the cross section shown in the process flow in Fig. 2. (b) Scanning electron micrograph of the junction between the capillary and the outlet O2. (c) Scanning electron micrograph of the mixing channel.

For example, many industrial catalysts with promoters, metal alloys, oxides, and supports can be conveniently tested with the microreactor.

In the work presented here, CO oxidation on circular platinum thin films of different areas is employed as a test reaction. The aim of these experiments is to demonstrate the operation of the reactor and the ability to characterize low-area catalysts. While platinum thin films are not used as CO oxidation catalysts for practical purposes, they are often used as model systems and for test reactions in fundamental catalysis studies.[19,20] Platinum thin films produced using electron-beam (e-beam) physical vapor deposition (PVD) and a lift-off process in acetone are used in this work because this is a convenient way of preparing catalysts with well controlled surface areas in the range 10–10 000 μm^2. The relation between the area of the catalyst circle and the lowest temperature at which catalytic activity can be detected in the QMS is investigated with reference to determining the sensitivity of the microreactor.

II. EXPERIMENTAL

A. Microreactor design

The microreactor directs the entire gas flow through the catalyst bed to a QMS, ensuring that almost all reaction products are present in the analyzed gas flow. Thus, unnecessary dilution of products is avoided, resulting in a high sensitivity. This concept places the following demands on the microreactor design: (1) the flow rate through the catalyst bed must be small, since gas can only be allowed to enter the QMS at a low rate. (2) Because of the low gas flow rate, the reaction zone volume must be small to ensure a relatively short gas residence time.

The microreactor consists of a microchannel system which has been formed in a silicon chip using reactive ion etching (RIE) and deep RIE (DRIE). DRIE is a technique with which deep and narrow structures with vertical sidewalls can be etched in silicon.[21] The chip has dimensions of 16×20 $mm^2\times350$ μm, as shown in Fig. 1. The channel system includes two inlets (I1 and I2), through which two different reactant gas mixtures can be introduced and mixed on-chip. In addition, two outlets (O1 and O2) are included in

the chip. The inlets and outlets all consist of 600 μm diameter holes which extend from the front side to the back of the chip. The two inlets are connected to a mixing channel of depth 250 μm. To make certain that the two reactant gas mixtures are properly mixed when entering the reaction zone, the mixing channel has a long meander structure and a width of only 150 μm. The mixing channel connects to O1 through a channel with the same depth as the mixing channel. To achieve a high flow conductance, this channel has a width of 500 μm. The gas flow through the mixing channel enters the chip through I1 and I2 and leaves the microreactor through O1. This gas flow is typically on the order of 10 Nml min^{-1} (4.1×10^{18} molecules s^{-1}).

A channel leads from the mixing channel to a circular reaction chamber with a diameter of 1.0 cm, and another channel leads from the reaction chamber to O2. These two channels as well as the reaction chamber all have depths of only 3 μm. In experiments, the catalyst is contained within the reaction chamber, and the chemical reaction occurs here. Gas flows from the mixing channel into the reaction chamber and proceeds to O2. The low depth yields a reaction chamber volume of only 240 nl. The purpose of the shallow channel connecting the mixing channel to the reaction chamber is to limit back-diffusion of reaction products to the mixing channel. O2 is connected to a QMS, which analyzes the composition of the gas leaving the reaction chamber. Thus, the entire gas flow through the reaction chamber, and consequently almost all reaction products, enter this QMS. Only reaction products which might back diffuse from the reaction chamber into the mixing channel can elude the QMS.

The QMS is a vacuum system from which gas can only be pumped at a limited pumping speed. For this reason, the connection between the reaction chamber and O2 includes an on-chip flow-limiting capillary with a low flow conductance. The capillary has a width of 5 μm, a depth of 3 μm, and a length of 1500 μm. To facilitate optimal detection, these dimensions of the capillary have been chosen to obtain a gas flow through the reaction chamber of around 3×10^{14} molecules s^{-1} and a resulting QMS pressure of around 10^{-7} mbar under typical experimental conditions.

In the experimental setup, the absolute pressure at O1 can be varied in the range of 0.1–5.0 bar. The absolute pressure at O2 is at vacuum level since this outlet is connected to the QMS. It follows that there is a pressure difference of the order of 1 bar across the system. Since the flow conductance of the capillary is much lower than the conductance of any other part of the channel system, almost the entire pressure drop occurs across the capillary. Consequently, the pressure in the reaction chamber is expected to be very close to the controlled pressure at O1.

The gas flow through the reaction chamber is only around 0.01% of the flow through the mixing channel because the flow resistance of the capillary is much higher than that of the mixing channel. This difference in magnitudes of the gas flows is desirable for the following reasons. Since the gas flow through the reaction chamber constitutes the entire flow entering the QMS, this flow determines the pressure in the QMS. Only when the reaction chamber gas flow has an approximate magnitude of 10^{14} molecules s^{-1} will the QMS pressure be compatible with mass spectrometer operation. Concerning the mixing channel, such a low gas flow would be difficult to control with off-the-shelf mass flow controllers (MFCs) and highly impractical when changing the composition of the gas mixture introduced through the inlets. The volume of the exterior gas supply system connected to I1 and I2 in the experimental setup is much larger than the volume of the microchannel system itself. When changing the composition of the gas entering the chip, one, therefore, has to wait for the old gas to be fully washed away from the exterior tubing by the new gas. Until then, the composition of the gas entering the chip does not resemble the one specified by the user. Thus, a relatively high mixing channel gas flow is required to ensure a short gas residence time in the exterior tubing and a practical time-scale for changes of the gas mixtures. For these reasons, O1 has been included in the chip to generate a bypass gas flow on the order of 10^{18} molecules s^{-1}. A gas flow of this magnitude can readily be controlled with off-the-shelf MFCs.

In summary, reactant gases are introduced into the reactor through the two inlets. The reactant gas mixture flows through the mixing channel to O1, where it is vented to the atmosphere. However, around 0.01% of the mixing channel gas flow proceeds to the reaction chamber, where the reactants can react and form products under influence of the catalyst. The resulting gas mixture flows from the reaction chamber through the capillary and enters the QMS, where the gas composition is analyzed.

The large area of the reaction chamber increases the amount of catalyst which can fit at the floor of the reaction chamber for a given density. This is favorable for the purpose of obtaining a reasonably high reaction rate when the turnover frequency is low or when a low catalyst density is required to avoid sintering. The circular shape is an advantage since it makes confinement of the catalyst deposition to the reaction chamber easier than it would be, if for instance a long, narrow meander geometry of the same large area were used. When depositing metal clusters from a magnetron sputtering cluster source, the large, circular shape makes it fairly easy to align a shadow mask. When depositing a catalyst manually with a pipette, the high area and circular shape also ease the process. In addition, with a circular design liquid catalyst suspensions deposited in the reactor form a relatively uniform loading. Finally, the circular shape allows easy use of the "locally cooled anodic bonding" method which has been developed for low-temperature sealing of the microreactor.[22] This bonding method is very useful for catalysts, such as gold clusters, which are likely to sinter at elevated temperatures.

After deposition of catalyst in the catalyst bed, the reactor is sealed with a Pyrex lid, using anodic bonding.[23] During the bonding process, the Pyrex-lid and the floor of the reaction chamber will be attracted toward each other by a strong electrostatic force. Because of the low depth-to-diameter ratio of the reaction chamber, the attractive force might cause the Pyrex-lid to get into intimate contact with the floor of the reaction chamber during the anodic bonding. If this happens, attractive surface forces will quickly cause the entire reaction chamber to collapse, permanently bonding the lid to the re-

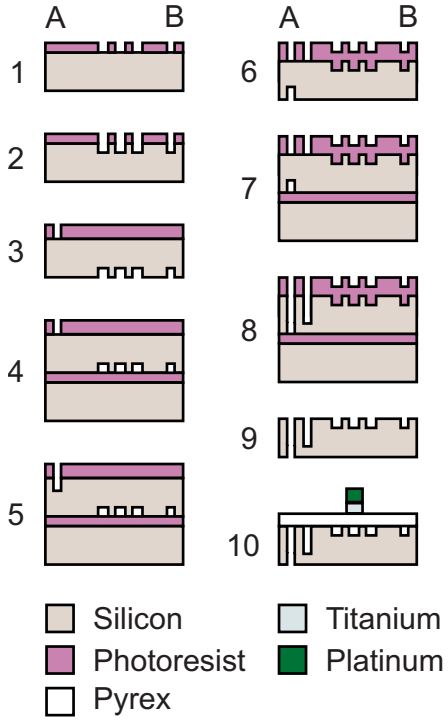

FIG. 2. (Color online) Fabrication sequence for the microreactor. (1) Reaction chamber, shallow channels, and capillary are defined in photo resist; (2) etching of the reaction chamber, shallow channels, and capillary; (3) inlet and outlet holes are defined in photoresist from back; (4) handle wafer mounting; (5) etching of inlet and outlet holes; (6) inlet and outlet holes and mixing channel are defined from front side; (7) handle wafer mounting; (8) etching of inlet and outlet holes and mixing channel; (9) removal of remaining photoresist and handle wafer; and (10) reactor sealed with Pyrex lid with integrated temperature detector using anodic bonding.

action chamber floor.[24–26] To avoid such a collapse, the reaction chamber contains 200 μm diameter silicon pillars which are spaced 1 mm apart. These pillars prevent the lid from getting into contact with the reaction chamber floor during the bonding process.

B. Microreactor fabrication

The microreactor is fabricated using micromanufacturing batch techniques. With these processes, large numbers of reactors can be produced in a short time and at relatively low cost. The silicon chips are fabricated using ultraviolet (UV) lithography, RIE, and DRIE. These are all standard microfabrication processes. The fabrication sequence for the silicon chips is shown in Fig. 2. The starting point is a 350 μm thick silicon wafer. First, what will later become the substrate front side is covered with a 1.5 μm thick layer of AZ5214 photoresist (a photosensitive, etch resistant polymer). A pattern containing the reaction chamber and the capillary is then defined in the polymer using UV lithography, and the wafer is etched to a depth of around 3.0 μm through a RIE process. This pattern also includes the two microchannels leading from the mixing channel to the reaction chamber and from the reaction chamber to the capillary, respectively. After etching the low flow part of the channel system, the polymer mask is removed in acetone. A 9.5 μm thick layer of AZ4562 photoresist is then applied to the back of the wafer, and a pattern containing the in- and outlet holes is defined using UV lithography. Now, the front of the wafer is bonded to a handle wafer using photoresist as an adhesive. This is done to protect this side of the wafer, which might otherwise become damaged along the edge during the subsequent DRIE process. The pattern is then etched using DRIE to a depth of around 100 μm, followed by removal of the remaining photoresist and the handle wafer in acetone. The front of the wafer is now covered with a 9.5 μm thick layer of AZ4562 photoresist, and a pattern containing the mixing channel is defined using UV lithography. Again, before the subsequent DRIE process, the side of the wafer not covered by photoresist is bonded to a handle wafer. At this point in the process flow, the handle wafer is required since the in- and outlet holes will now be etched all the way through the wafer. In the DRIE tool helium gas is used to cool the back of the wafer during etching. If no handle wafer were used, the helium gas would leak into the plasma chamber through the in- and outlet holes. The mixing channel pattern is now etched using DRIE until it reaches the in- and outlet holes at a depth of approximately 250 μm. Afterwards, the remaining photoresist and the handle wafer are removed in acetone. As a final fabrication step, the chip is thermally oxidized with an oxide thickness of 50 nm. The wafer is sawn into small chips, each containing one microreactor.

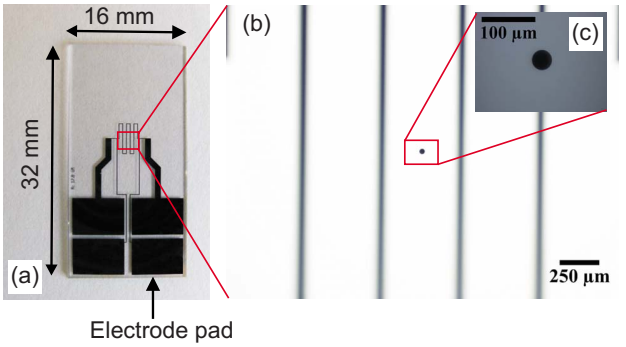

FIG. 3. (Color online) (a) Photograph of the Pyrex lid with integrated platinum thin film RTD. The temperature is determined with a four-point-probe measurement of the resistance of the meander path in the center of the lid. (b) Magnification of the center of the meander path. The platinum catalyst circle is visible in the center. (c) Magnification of the catalyst circle. This particular circle has a diameter of 36 μm.

To prepare the microreactor for a catalyst test experiment, a catalyst material can be deposited in the reaction chamber using one of the deposition methods described earlier. The microchannel system is subsequently sealed with a Pyrex lid using anodic bonding. This concludes the preparation procedure, and catalyst testing can be initiated. The total preparation time before measurements can be commenced depends on the catalyst deposition method, but is usually around one hour. In the experimental results presented in this article, the catalyst is incorporated on the Pyrex lid surface as a thin film. Thus, no additional catalyst is deposited in the reaction chamber prior to bonding in these specific experiments.

The side of the Pyrex-lid facing the silicon chip includes a circular platinum thin film, as seen in Fig. 3. This platinum circle acts as a catalyst in the test reaction. A number of

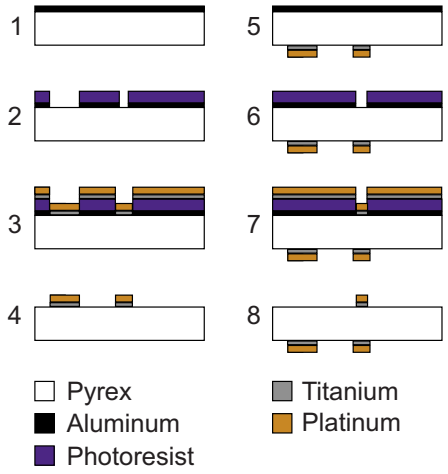

FIG. 4. (Color online) Fabrication sequence for the Pyrex lid. (1) Aluminum thin film deposition on front side; (2) RTD is defined in photoresist and aluminum; (3) titanium and platinum thin film deposition; (4) lift-off of titanium and platinum and removal of aluminum; (5) aluminum thin film deposition on back; (6) catalyst circle is defined in photoresist and aluminum; (7) titanium and platinum thin film deposition; and (8) lift-off of titanium and platinum and removal of aluminum.

different lids with platinum circle areas ranging from 15 μm^2 to 5000 μm^2 is fabricated. By performing measurements with different platinum circle areas, it is possible to investigate the relation between the catalyst area and the lowest temperature at which catalytic activity can be detected. The other side of the lid is equipped with an integrated four-point probe resistive temperature detector (RTD) consisting of a structured platinum thin film. The positions of the RTD and the catalyst circle both match with the center of the reaction chamber. The Pyrex lid has dimensions of 16×32 $mm^2 \times 500$ μm.

The lid is fabricated using UV lithography, PVD, and lift-off processes in acetone. These are all standard microfabrication processes. The fabrication sequence for the lid is shown in Fig. 4. The starting point is a 500 μm thick Pyrex wafer. First, what will later become the RTD side of the lid is covered with a 10 nm thick aluminum thin film using e-beam PVD. The aluminum layer acts to promote adhesion between photoresist and the wafer. In addition, the aluminum layer reflects UV light and thus prevents reflections from the chuck in the exposure tool during the lithography process. This is important since the Pyrex wafer is transparent to UV light. A 1.5 μm thick layer of AZ5214 photoresist is now spun on top of the aluminum, and a pattern containing the RTDs is subsequently defined in the polymer using UV lithography. As a part of the lithography-process the photoresist is developed in an aqueous NaOH-solution. During this development process, the aluminum below the exposed parts of the photoresist is also etched away. A 10 nm thick titanium thin film is then deposited on the RTD side using e-beam PVD. This titanium layer serves as an adhesion layer between the Pyrex substrate and the platinum thin film which is deposited next. Now, a 100 nm thick platinum thin film is deposited using e-beam PVD. The polymer mask and the metal on top of it are subsequently lifted off in acetone using ultrasound. This is followed by removal of the remaining aluminum in an aqueous solution of NaOH. The RTD has now been formed on top of the Pyrex lid. Afterwards, the catalyst circle is formed on the opposite side of the lid. This is done by processing the back of the wafer in exactly the same way as the front side, while using a different mask when exposing the polymer to UV light. Hence, the catalyst circle consists of a 100 nm thick platinum thin film in addition to a 10 nm thick titanium thin film in between the platinum and the Pyrex substrate. Finally, the Pyrex wafer is sawn into small chips, each containing one lid. Before the measurements, the RTDs are annealed at 400 °C.

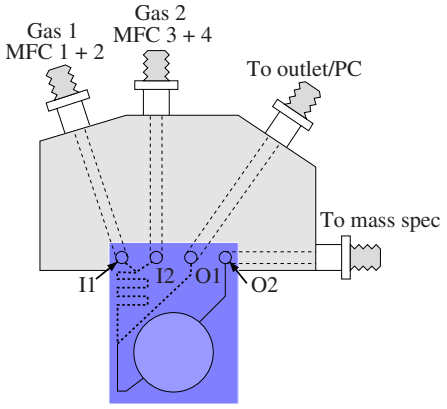

FIG. 5. (Color online) Sketch of the stainless steel manifold fixture for the microreactor. Gas lines machined in the interior of the fixture connect the inlets and outlets of the microreactor to MFCs, a PC, and a QMS.

C. Experimental setup

The gas handling system is made from 1/4 in. stainless steel tubing with welded VCR® (Swagelok) fittings as connections. The microreactor is mounted in a stainless steel manifold fixture with welded VCR® fittings, and the gas lines are connected to the microreactor through this fixture. A sketch of the arrangement is shown in Fig. 5. The gas lines are machined in the interior of the fixture, and tight connections between the steel block and the microreactor are ensured by using Kalrez perfluoroelastomer O-rings.

Since the O-rings are made from an elastomer, a small amount of gas diffusion from the surrounding air into the system is unavoidable, particularly at elevated temperatures. This gives rise to unwanted background signals of O_2 and N_2, complicating analysis of the reaction products and source gas species. To mitigate this problem, a continuous flow of argon is introduced in the volume surrounding the O-rings. Thus, any unwanted background due to diffusion through O-rings will be in the form of argon.

The reactor is heated from the silicon side using an external resistive heating element covering the outline of the reaction chamber. The temperature is measured with four point measurements of the resistance of the integrated RTD. The gas flow to the two inlets is controlled by four MFCs allowing mixing of up to four different gases. Outlet 1 is connected to a pump via a pressure controller (PC). This makes experiments at absolute pressures from 0.1 to 5.0 bar possible. The gas flows, the PC, and the temperature are all controlled with a LabVIEW program. The temperature is

controlled using a PID algorithm, allowing temperature changes of up to 1 K/s and constant temperatures within 0.1 K. Time resolved gas detection is performed with a QMS (Balzers QMA 125) equipped with a secondary electron multiplier.

III. RESULTS AND DISCUSSION

A. Gas flow

The pressure difference between the reaction chamber and O2 gives rise to a gas flow through the capillary, and the magnitude of the gas flow depends on the exact value of the reaction chamber pressure as well as the temperature. The absolute gas flow through the capillary is an essential design parameter for the following reasons. The reaction chamber and the capillary are connected in series, so the flows through them are the same. Consequently, the residence time of the gas in the reaction chamber can be derived from the capillary flow. Furthermore, knowledge of the gas flow is important for interpretation of experimental results, for instance for determining absolute reaction rates. Finally, when designing the microreactor, the capillary dimensions must be chosen carefully to ensure that the flow to the QMS facilitates optimal gas composition analysis. Gas flows through narrow capillaries with vacuum pressure at one end are nontrivial since the small cross sectional dimensions might be comparable to the mean free path of the gas, resulting in a nonviscous flow regime. It follows that it is of interest to measure the capillary gas flow using an absolute method.

To characterize the relation between the pressure in the reaction chamber and the gas flow through the capillary, a microreactor is mounted in the manifold fixture to allow flow from a fixed volume to the QMS. This is done by sealing up the gas lines in the interior of the fixture from the external pump system. Thus, a fixed volume constituted by the microchannel system in the reactor and the gas lines in the interior of the fixture is hermetically sealed. The only path by which gas can leave the volume is by entering the QMS through the on-chip capillary. In this experiment, a Baratron (MKS Inc. type 211, 0–1 bar range), which measures the pressure inside the fixed volume, is installed in the fixture. At the onset of the experiment, the fixed volume contains atmospheric air at atmospheric pressure, and the QMS is at vacuum pressure. The fixed volume is 11.2 ml, and the experiment is carried out at room temperature. The pressure is plotted as a function of time in Fig. 6(a). As gas flows through the capillary, the pressure in the fixed volume decreases, and the flow is obtained from

$$\dot{N}(t) = \frac{V}{k_B T}\frac{dp_v(t)}{dt}, \tag{1}$$

where $\dot{N}(t)$ is the net number of gas molecules crossing a cross section of the capillary per unit time, $p_v(t)$ is the pressure in the fixed volume, V is the volume, k_B is the Boltzmann constant, T is the temperature of the fixed volume, and t is time. In the experiment the microreactor has a capillary depth of 3.0 μm. In Fig. 6(b), $\dot{N}$ is plotted as a function of the pressure in the fixed volume.

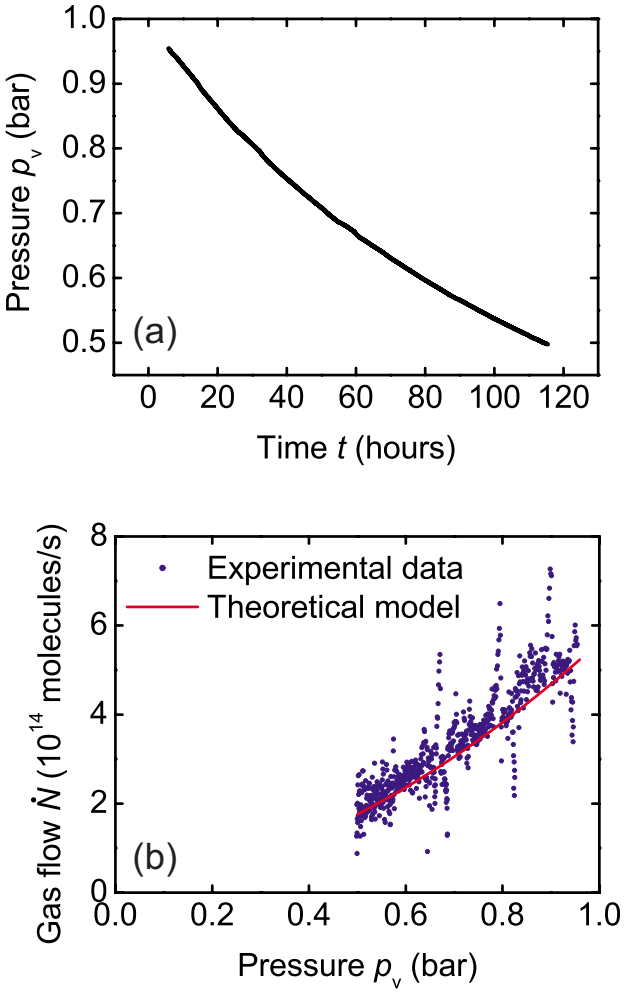

FIG. 6. (Color online) (a) Measured pressure p_v in the fixed volume as a function of time. (b) Experimentally measured flow as a function of the reaction chamber pressure p_v (blue circles). The red curve is the theoretically predicted flow as a function of p_v.

The gas flow through the capillary is now described with a theoretical model for comparison with the experimental results. The width of the capillary is very small compared to the widths of the channel leading from the mixing channel to the reaction chamber and the channel leading from the reaction chamber to the capillary. Consequently, the flow resistances of the latter two channels as well as that of the reaction chamber can be safely neglected when predicting the flow entering the QMS. Thus, in this discussion only the flow resistance of the capillary is considered.

Gas flow in a tube of characteristic cross sectional width d can be characterized by the Knudsen number λ/d, where λ is the mean free path of molecules in the gas. If $\lambda/d < 0.0091$, the flow is viscous, if $0.0091 < \lambda/d < 1$, the flow is intermediate, and if $\lambda/d > 1$, the flow is molecular.[27,28] The capillary has a rectangular cross section with dimensions 5×3 μm^2. However, when attempting to predict the relation between the capillary gas flow and the pressure in the reaction chamber, it is convenient to treat the capillary as having a circular cross section. The advantage of this approximation is that for a circular cross section analytic expressions for the flow exist for all three flow regimes. In

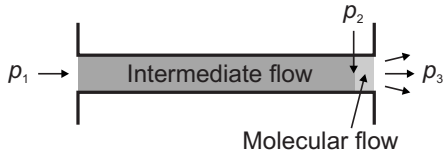

FIG. 7. Sketch of the capillary showing the reaction chamber side (left) and the QMS side (right). The reaction chamber pressure is p_1, and the QMS pressure is p_3. The regions with intermediate and molecular flow are indicated. At the position where the pressure is p_2, the gas flow changes from intermediate to molecular.

this discussion, a circular cross section of diameter $d=4.4\ \mu$m and thus of the same area as the actual rectangular cross section will be assumed.

For air at room temperature, the mean free path is given by[27]

$$\lambda = \frac{6.7 \times 10^{-3}\ \text{Pa m}}{p}, \tag{2}$$

where p is the pressure. For a capillary diameter of 4.4 μm, this means that the flow is intermediate at atmospheric pressure, and that the transition from intermediate to molecular flow occurs at a pressure of around 1.5×10^3 Pa. In Fig. 7, the capillary is shown schematically with the two flow regimes. The inlet pressure is p_1, and at the pressure p_2 the flow changes from intermediate to molecular. The pressure in the QMS is denoted p_3.

In the intermediate flow regime, the gas flow through a tube of length ℓ with circular cross section is[27]

$$\dot{N} = c\frac{p_1 - p_2}{k_B T}, \tag{3}$$

with

$$c = \frac{\pi}{128}\frac{\bar{p}d^4}{\eta\ell} + \frac{1}{3}\sqrt{\frac{\pi}{2}}\frac{d^3}{\ell v}\frac{1+\frac{dv\bar{p}}{\eta}}{1+1.24\frac{dv\bar{p}}{\eta}}, \tag{4}$$

where η is the viscosity of the gas, $\bar{p}=(p_1+p_2)/2$, $v=\sqrt{m/(k_B T)}$, and m is the mass of a single gas molecule. In the molecular flow regime[29]

$$\dot{N} = \frac{1}{3}\sqrt{\frac{\pi}{2}}\frac{d^3}{\ell v}\frac{p_2 - p_3}{k_B T}. \tag{5}$$

Using Eq. (2), the expressions Eqs. (3) and (5) can be combined to obtain an analytical expression for the flow that includes both the intermediate and the molecular flow regimes. In addition, an analytical expression for the fraction of the capillary length where the flow is intermediate can be obtained. For atmospheric air at $T=295$ K and at $p_v>0.5$ bar, the flow is intermediate in more than 98% of the length of the capillary, according to this calculation. In Fig. 6(b), the theoretically predicted gas flow as a function of the pressure in the fixed volume is plotted with $T=295$ K, $\eta=17.8\times10^{-6}$ Pa s, and $m=4.81\times10^{-26}$ kg (the average molecular mass in the air). Both the intermediate and the molecular flow regimes are taken into account when calculating this gas flow. A good agreement with the experimental data is observed. It is emphasized that the expected gas flow plotted in Fig. 6(b) is generated from a purely theoretical model, and that the experimental data are not considered when making this prediction. Thus, the theoretical model presented here is not a fit to experimental data but rather a prediction based entirely on the capillary dimensions, the temperature, and the properties of the gas.

Based on these results, the capillary gas flow at typical experimental conditions can be inferred. It appears from Fig. 6(b) that, at approximately atmospheric pressure in the reaction chamber, the capillary gas flow is around 6×10^{14} molecules s^{-1} at room temperature. At the same pressure and a typical reactor temperature of 250 °C, the theoretical model predicts a flow of around 3×10^{14} molecules s^{-1}, corresponding to a gas residence time in the reaction chamber of around 11 s.

During operation, gas is pumped out of the QMS by a turbo pump. In steady state, the amount of gas flowing through the capillary equals the amount pumped by the turbo pump. The pressure p_{ms} in the QMS is then given by

$$p_{\text{ms}} = \frac{k_B T_{\text{ms}}}{S}\dot{N}, \tag{6}$$

where T_{ms} is the temperature of the gas in the QMS, $\dot{N}$ is the number of gas molecules pumped by the turbo pump per unit time, and S is the gas volume pumped by the turbo pump per unit time. S is referred to as the pumping speed. It is clear from Eq. (6) that the gas flow through the capillary determines the pressure in the QMS. Since the gas flow in turn is determined by the capillary dimensions, these dimensions must be chosen to facilitate a suitable QMS pressure. During the experiment, p_{ms} is continuously measured with an ion gauge and is in the range $2-10\times10^{-7}$ mbar. These pressures are well-suited for QMS analysis suggesting that the capillary dimensions are appropriate. Using Eq. (6), the effective pumping speed is determined to be approximately 38 l/s. This is reasonable, since the geometric pump aperture is about 9 cm^2 giving a maximum theoretical pumping speed of ~106 l/s.

Although the experimental data in Fig. 6(b) are in good agreement with the theoretical prediction, pronounced deviations appear at $p_v=67$ kPa, $p_v=80$ kPa, and $p_v=90$ kPa. These deviations derive from the numerical differentiation of the pressure with respect to time in Eq. (1). The deviations are caused by distinct periods of time in the originally measured values of $p_v(t)$ characterized by a relatively abrupt increase of about 200 Pa in p_v followed by a corresponding decrease back to the original level 5–8 h later. These "bumps" in the measured values of $p_v(t)$ are caused by unstable performance of the Baratron. In spite of this effect, the quantitative agreement between experimental data and the theoretical prediction clearly suggests that the gas flow can be understood in terms of the theoretical model outlined above.

It is noted that other desired values of the capillary flow resistance can easily be obtained by fabricating microreactors with other capillary dimensions. This could be favorable for some experiments. For a constant inlet pressure, an in-

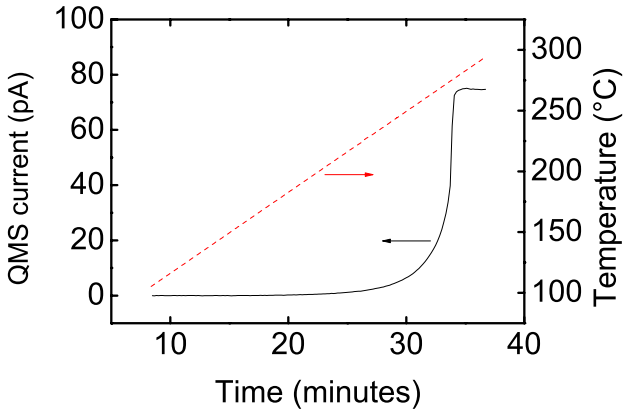

FIG. 8. (Color online) Experimental data from oxidation of carbon monoxide in the microreactor using a platinum thin film catalyst. The measured temperature (red, dashed curve, right ordinate axis) and the CO_2 signal in the QMS (black, solid curve, left ordinate axis) are plotted as a function of time. The catalyst area is 515 μm^2, and the CO_2 content is measured using the mass 44 signal in the QMS.

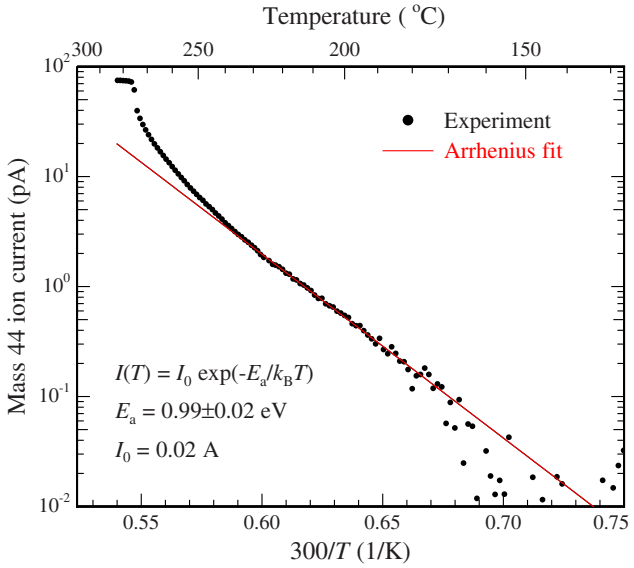

FIG. 9. (Color online) Arrhenius plot of the mass 44 (CO_2) signal plotted in Fig. 8 (black circles). The catalyst area for this experiment is 515 μm^2 platinum. A linear fit of the part of the experimental data, where the reaction exhibits Arrhenius behavior, is also shown (red line). The slope of the fit corresponds to an apparent activation energy of 0.99 eV.

crease of the capillary width would for example result in a shorter reaction chamber residence time.

B. Oxidation of carbon monoxide

To demonstrate the operation of the microreactor, CO oxidation on platinum thin film circles is used as a test reaction. In particular, the experiments are performed to test the ability to measure catalytic activity of catalysts with low surface areas. Since the main purpose of the reactor design is to improve sensitivity to enable studies on low density mass selected clusters, this is essential information on reactor performance. A gas mixture consisting of CO and O_2 is used, and the platinum circles have different areas ranging from 15 to 5000 μm^2. The reaction is run at a pressure of 1.00 bar in a surplus of oxygen, with an O_2:CO ratio of 20:1 and with a total flow rate of 8.4 Nml min^{-1} through the mixing channel. After mounting in the manifold fixture, the reactor is heated to 400 °C in the reaction gas, until any organic contaminants have been burned away, and the gas system has stabilized. The experiments consist of repeatedly ramping the temperature from 80 to 350 °C at a rate of 400 K/h, activating the CO oxidation

$$2CO(g) + O_2(g) \rightarrow 2CO_2(g). \tag{7}$$

Figure 8 shows the temperature and the CO_2 signal in the QMS, both as a function of time, during a single temperature ramp. This experiment is carried out with a catalyst area of 515 μm^2, and the CO_2 content in the QMS is measured using the mass 44 signal. As the temperature is increased, the CO_2 signal rises exponentially until a "light off" phenomenon is seen, and full conversion of CO to CO_2 takes place. In Fig. 8, the background of CO_2 from reactions on the filament in the QMS has been subtracted. The CO and O_2 signals are measured simultaneously with the CO_2 signals at mass 28 and 32, respectively. Both signals drop as the CO_2 content increases in accordance with the stoichiometry of the reaction.

At low conversion, the CO_2 reaction rate $\dot{N}_{CO_2}$ (the number of CO_2 molecules produced in the reaction chamber per unit time) is[1]

$$\dot{N}_{CO_2} \simeq A r_0(p_{CO}, p_{O_2}, p_{CO_2}) \exp\left(\frac{-E_a}{k_B T}\right), \tag{8}$$

where A is the area of the platinum circle, E_a is the apparent activation energy, and p_{CO}, p_{O_2}, and p_{CO_2} are the partial pressures in the reaction chamber of CO, O_2, and CO_2, respectively. $r_0(p_{CO}, p_{O_2}, p_{CO_2})$ is a parameter which depends on the partial pressures and the catalyst. The data from Fig. 8 are shown as an Arrhenius plot in Fig. 9. Here, it can be seen that at low temperature and low conversion the rate follows an Arrhenius behavior as expected, with an apparent activation energy E_a of 0.99 eV. For all the samples, the reactivity exhibited Arrhenius behavior with apparent activation energies in the range 0.91–1.40 eV with the highest values found for the measurements with smaller catalyst areas. Contreras *et al.*[30] performed experiments with CO oxidation on a 15 nm thick platinum thin film deposited using PVD on a silicon(100) wafer with native oxide. At temperatures below "light off," these authors measured an apparent activation energy of 1.17 eV, within range of the values found in this work.

The microreactor and the corresponding experimental arrangement are designed to facilitate high sensitivity characterization of catalytic reactions. The sensitivity of the setup is now evaluated by considering the smallest catalyst area for which catalytic activity can be detected. The criterion for detection of catalytic activity is that the product QMS current I_p must be distinguishable from the background in the QMS. Thus, I_p must be higher than some threshold value I_t, which is determined by the QMS background. For the CO oxidation measurements described here, I_t is defined to be 1.0 pA,

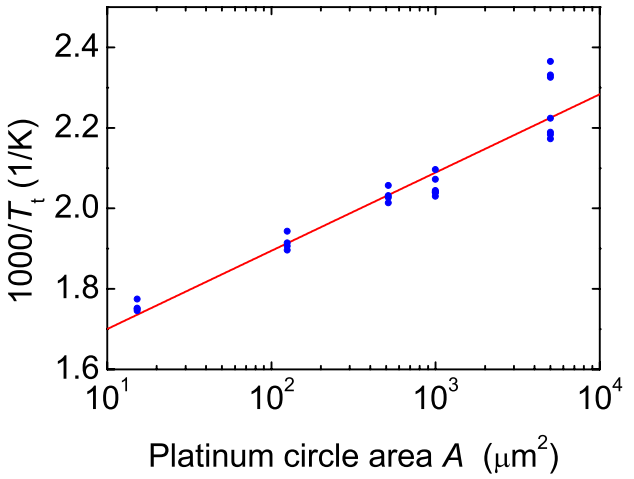

FIG. 10. (Color online) The inverse of the lowest temperature at which CO oxidation can be detected plotted as a function of catalyst area. Experimental data from all measured samples are shown (blue circles). The abscissa axis has logarithmic scale. The linear fit (red line) yields an apparent activation energy of 1.02 eV.

since this is significantly higher than the background. The product current increases linearly with the reaction rate $\dot{N}_p$ in the reaction chamber. It follows that the criterion for detection is satisfied when

$$\dot{N}_p > \dot{N}_t, \tag{9}$$

where $\dot{N}_t$ is the reaction rate which causes a product current I_t.

From Eqs. (8) and (9), it follows that for a given area the temperature must exceed a certain threshold temperature T_t before product formation can be detected. T_t is the temperature which causes a reaction rate $\dot{N}_t$. Only if the temperature is higher than T_t, will the catalytic activity be high enough to cause a QMS product signal distinguishable from the background. In view of Eqs. (8) and (9), the threshold temperature can be predicted.

$$\dot{N}_t = Ar_0 \exp\left(\frac{-E_a}{k_B T_t}\right) \Rightarrow \frac{1}{T_t} = \frac{k_B}{E_a}\left(\ln A - \ln\frac{\dot{N}_t}{r_0}\right). \tag{10}$$

Assuming that $\dot{N}_t/r_0$ may be considered constant, only A and T_t vary in the CO oxidation experiments. Thus, the inverse threshold temperature plotted against the logarithm of the area should yield a straight line with a slope of k_B/E_a. Figure 10 shows the experimental data from CO oxidation in the microreactors. The inverse of the lowest temperature at which CO_2 formation can be detected is plotted against the platinum circle area (logarithmic scale). In the data evaluation, the threshold current I_t is defined to be 1.0 pA, which is significantly above the background (see Fig. 9). From the slope of the best linear fit to the data, an apparent activation energy of 1.02 eV is found. This is within range of the values found from the individual Arrhenius plots.

It appears from Fig. 10 that even for the smallest catalyst area of 15 μm^2, conversion into CO_2 can be detected at a temperature of ~300 °C. This temperature can easily be reached with the experimental setup. An area of 15 μm^2 is considerably lower than catalyst areas for other high-sensitivity chemical reactors reported in literature.[9,10] The experimental data thus demonstrate the high sensitivity of the microreactor and the capability to measure reactivity of small amounts of catalyst.

IV. CONCLUSIONS

The microfabricated chemical reactor presented here facilitates highly sensitive catalyst testing. An integrated capillary limits the gas flow through the catalyst bed to around 3×10^{14} molecules s^{-1} at typical experimental conditions, making it possible to direct the entire reaction zone gas flow to enter a QMS. This prevents unnecessary dilution of the reaction products and causes almost all the products to enter the gas analysis tool, thus ensuring a high sensitivity. The microreactor can be employed as a platform for testing of a wide variety of different catalysts, including industrial catalysts. However, the primary aim of the device is to allow measurements of catalytic activity and surface kinetics of model catalysts, which can only be obtained in small quantities, thus necessitating high sensitivity to low surface areas. In particular, the reactor is well-suited for characterization of mass selected metal clusters from a sputtering cluster source.

The relationship between the reaction zone gas flow and the pressure in the reaction chamber has been investigated with a theoretical model, which predicts the gas flow in the capillary to be in the intermediate flow regime. The theoretical model is in good agreement with experimental results. CO oxidation on low-area platinum thin films was carried out in the reactor as a test reaction to demonstrate the operation of the device. The experimental data show that for this reaction and under the conditions used in these experiments, catalysts with surface areas as low as 15 μm^2 can be conveniently characterized with the microreactor. This catalyst area is considerably lower than for other high-sensitivity chemical reactors reported in literature.

ACKNOWLEDGMENTS

Center for Individual Nanoparticle Functionality (CINF) is sponsored by The Danish National Research Foundation.

[1] I. Chorkendorff and J. Niemantsverdriet, *Concepts of Modern Catalysis and Kinetics* (Wiley, New York, 2003)
[2] K. F. Jensen, Chem. Eng. Sci. **56**, 293 (2001).
[3] S. K. Ajmera, C. Delattre, M. A. Schmidt, and K. F. Jensen, Sens. Actuators B **82**, 297 (2002).
[4] G. Kolb and V. Hessel, Chem. Eng. J. **98**, 1 (2004).
[5] K. Jähnisch, V. Hessel, H. Lowe, and M. Baerns, Angew. Chem. Int. Ed. **43**, 406 (2004).
[6] L. Kiwi-Minsker and A. Renken, Catal. Today **110**, 2 (2005).
[7] K. Wong, S. Johansson, and B. Kasemo, Faraday Discuss. **105**, 237 (1996).
[8] A. S. Eppler, G. Rupprechter, L. Guczi, and G. A. Somorjai, J. Phys. Chem. B **101**, 9973 (1997).
[9] S. Johansson, E. Fridell, and B. Kasemo, J. Vac. Sci. Technol. A **18**, 1514 (2000).
[10] P. W. Jacobs, S. J. Wind, F. H. Ribeiro, and G. A. Somorjai, Surf. Sci. **372**, L249 (1997).
[11] U. Quaade, S. Jensen, and O. Hansen, Rev. Sci. Instrum. **75**, 3345 (2004).
[12] O. Younes-Metzler, J. Svagin, S. Jensen, C. H. Christensen, O. Hansen, and U. Quaade, Appl. Catal., A **284**, 5 (2005).
[13] O. Younes-Metzler, J. Johansen, S. Thorsteinsson, S. Jensen, O. Hansen, and U. Quaade, J. Catal. **241**, 74 (2006).
[14] R. Z. Sørensen, A. Klerke, U. Quaade, S. Jensen, O. Hansen, and C. H.

Christensen, Catal. Lett. **112**, 77 (2006).
[15] U. Heiz and E. L. Bullock, J. Mater. Chem. **14**, 564 (2004).
[16] K. Judai, S. Abbet, A. S. Worz, U. Heiz, and C. R. Henry, J. Am. Chem. Soc. **126**, 2732 (2004).
[17] D. W. Goodman, Nature (London) **454**, 948 (2008).
[18] S. Thybo, S. Jensen, J. Johansen, T. Johannessen, O. Hansen, and U. Quaade, J. Catal. **223**, 271 (2004).
[19] S. Johansson, E. Fridell, and B. Kasemo, J. Catal. **200**, 370 (2001).
[20] M. Roumanie, C. Delattre, F. Mittler, G. Marchand, V. Meille, C. de Bellefon, C. Pijolat, G. Tournier, and P. Pouteau, Chem. Eng. J. **135**, S317 (2008).
[21] A. M. Hynes, H. Ashraf, J. K. Bhardwaj, J. Hopkins, I. Johnston, and J. N. Shepherd, Sens. Actuators, A **74**, 13 (1999).
[22] P. C. K. Vesborg, J. L. Olsen, T. R. Henriksen, I. Chorkendorff, and O. Hansen, "Anodic bonding with cooling of heat sensitive areas," Rev. Sci. Instrum. (submitted).
[23] G. Wallis and D. I. Pomerantz, J. Appl. Phys. **40**, 3946 (1969).
[24] W. P. Shih, C. Y. Hui, and N. C. Tien, J. Appl. Phys. **95**, 2800 (2004).
[25] P. Mao and J. Y. Han, Lab Chip **5**, 837 (2005).
[26] K. M. Knowles and A. T. J. van Helvoort, Int. Mater. Rev. **51**, 273 (2006).
[27] A. Roth, *Vacuum Technology*, 3rd ed. (Elsevier, Amsterdam, 1990).
[28] U. Quaade, S. Jensen, and O. Hansen, J. Appl. Phys. **97**, 044906 (2005).
[29] J. O'Hanlon, *A User's Guide to Vacuum Technology*, 3rd ed. (Wiley, Hoboken, New Jersey, 2003).
[30] A. M. Contreras, X. M. Yan, S. Kwon, J. Bokor, and G. A. Somorjai, Catal. Lett. **111**, 5 (2006).

Paper III

Anodic bonding with cooling of heat-sensitive areas
Peter C. K. Vesborg, Jakob L. Olsen, Toke R. Henriksen, Ib Chorkendorff, and Ole Hansen
Review of Scientific Instruments **81**, 016111 (2010).

Note: Anodic bonding with cooling of heat-sensitive areas

Peter C. K. Vesborg,[a] Jakob L. Olsen, Toke R. Henriksen,[b] Ib Chorkendorff, and Ole Hansen[b]
Department of Physics, CINF, Technical University of Denmark (DTU), Building 312, Fysikvej, DK-2800 Kgs. Lyngby, Denmark

(Received 26 August 2009; accepted 3 December 2009; published online 26 January 2010)

Anodic bonding of silicon to glass always involves heating the glass and device to high temperatures so that cations become mobile in the electric field. We present a simple way of bonding thin silicon samples to borosilicate glass by means of heating from the glass side while locally cooling heat-sensitive areas from the silicon side. Despite the high thermal conductivity of silicon, this method allows a strong anodic bond to form just millimeters away from areas essentially at room temperature. © *2010 American Institute of Physics.* [doi:10.1063/1.3277117]

The highly useful phenomenon—that silicon (with a thin oxide layer) may form an impressively strong bond to glass when the two materials are brought into intimate contact under the influence of strong electric fields and high temperature, anodic bonding (also known as "Mallory bonding," named after the company where it was invented and patented[1])—has been known and used for many years.[2]

The process is particularly useful for microelectromechanical system (MEMS) pressure sensors and other transducers and in weather sealing of solar cells because the bond hermetically seals the surfaces together.[3] In our research group we use the process for sealing μ-reactors for catalyst characterization;[4] however for this application the high temperatures needed for successful anodic bonding may cause catalysts to sinter or otherwise lose activity. An example of this is Au-based catalysts, which are notorious for deactivating since activity is dependant on very small Au particle size. This paper describes a practical way to overcome this issue by locally cooling the chip while the rest of it bonds. This method has proven practical and reliable in our implementation and could be useful for many other MEMS applications.

In brief, anodic bonding works by applying a large (~kV) negative bias on the glass with respect to the silicon while at the same time heating the stack such that cations in the glass become somewhat mobile. The electric field set up over the interface causes migration of ions (typically Na^+ for normal glass types) away from the interface, which sets up an intrinsic electrostatic attraction between the silicon and the glass. No external force is therefore required as the internal forces set up by this field are very strong (pressure in the GPa range).[3,5] True chemical bonds are formed between the Si and the glass permanently bonding the two surfaces. A schematic of the process is shown in Fig. 1. The downside of the technique is the inherent necessity of elevated temperatures to give the cations reasonable mobility in the glass.[6] In some applications a typical bonding procedure for borosilicate-type glass (e.g., Pyrex) to silicon (e.g., 30 min at 350 °C) may well exceed the thermal budget of parts of the device. In such cases the traditional remedy is to use glass types that conduct at lower temperatures. A typical strategy might be a lithium doped glass-ceramics,[7] but generally the process still does not work below perhaps 160 °C),[7,8] and differences in thermal expansion coefficients might be problematic for these glass types, while conventional borosilicate glass is well matched to Si. Another method is low-temperature soldering with, e.g., In/Sn eutectic mixtures;[9] however necessary measures to avoid oxidation of the solder make this method unsuited for general use in open air, and the minimum temperature for this method is also ~160 °C. Devices may also be sealed with adhesives, but (un)cleanliness and leakage makes this unattractive.

Conventional (hot) anodic bonding is shown in Fig. 1, while the locally cooled-bonding method we have developed may be seen in cross section in Fig. 2. There are a few key differences to note. First, since it is the glass (not the silicon) that needs to be warm we apply heat from the glass side. The heater also serves as high tension cathode. Second, the heater only touches the glass where bonding is needed and heat is acceptable. Third, we have introduced a heat sink (cold finger), which also serves as electrical connection to ground, and the heat sink only touches the silicon in the areas where low temperature (and not bonding) is needed. In our setup, the cold finger supporting the silicon and the hole in the heater are both cylindrical, giving the advantage of radial symmetry (no corners with stress concentration) when parts of the system heat and cool.

As a practical method for heating the top electrode, we use two commercial 150 W incandescent lamps with quartz envelopes (Osram) embedded in holes in the top electrode, which is made of aluminum for its high thermal conductivity. Quartz is insulating well above the relevant temperatures, so the power supply for the filaments does not need galvanic isolation and is indeed grounded in our setup. The heat sink is machined from copper and has internal channels for coolant flow. It is kept at a constant temperature (typically 6–12 °C, but this could well be lower if needed) using a commercial circulating cooling bath. Thermal contact between the silicon and the Cu pillar may be assured with conventional heat sink compounds or a thin indium foil. For our conditions (1 kV potential drop and 475 °C cathode temperature), bonding is normally complete within 20–25 min.

[a]Electronic mail: peter.vesborg@fysik.dtu.dk.
[b]Also at Dept. of Micro- and Nanotechnology, Technical University of Denmark, DTU Nanotech Building 345 East, DK-2800 Kgs. Lyngby, Denmark.

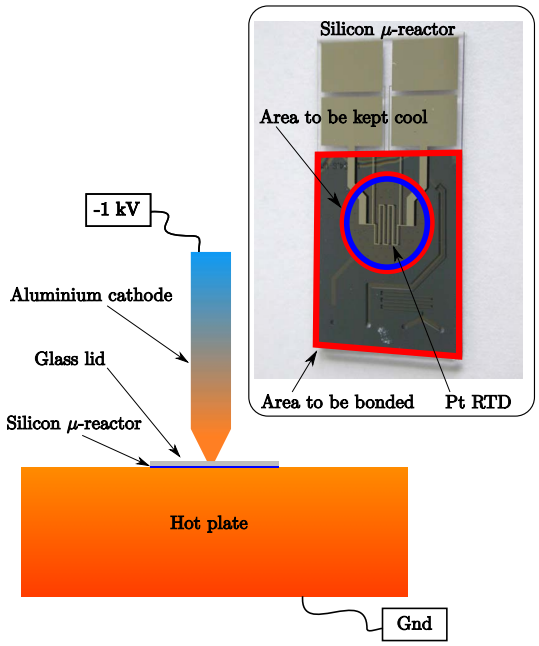

FIG. 1. (Color online) Cross section of a typical hot anodic bonding setup. The glass-silicon assembly is supported on a grounded hotplate and is contacted by a high tension cathode from above. The inset shows a photograph of our μ-reactor and highlights the areas to be bonded as well as the central reactor area, which is to be kept cold during bonding (inner blue circle). In the center of the circle (and reactor), the meander platinum RTD structure on the inside of the glass lid may be seen.

In order to find out what the temperature inside the reactor is during bonding, we have performed a direct measurement inside the reactor using resistive temperature detection (RTD) and also carried out a finite-element-type

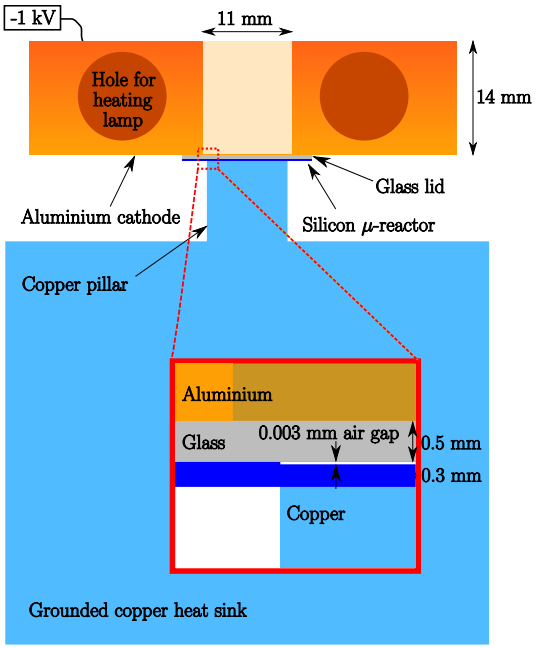

FIG. 2. (Color online) Cross-sectional view showing the locally cooled-bonding setup. The grounded Cu pillar is kept cold and acts as a heat sink during bonding, while the cathode is kept at high temperature so that it simultaneously supplies the high voltage and heats the glass. Over the Cu cold finger a cylindrical hole is drilled in the cathode, so only a minimum of heat is transferred to the central (reactor) part of the chip.

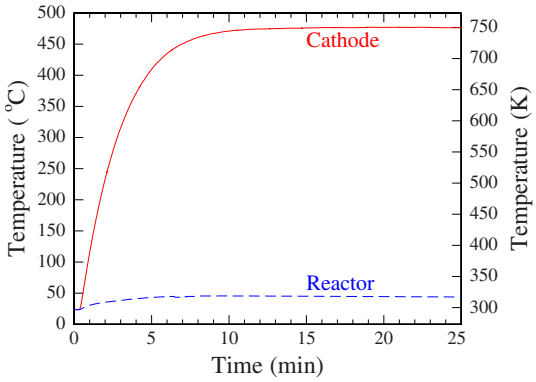

FIG. 3. (Color online) Thermocouple measurement of the aluminum cathode temperature and RTD measurement of the reactor chamber temperature.

calculation using the COMSOL MULTIPHYSICS 3.5 software package. For the four-point RTD measurement, we have used our standard RTD μ-reactor lids, which incorporate a 100 nm thick platinum four terminal resistor structure and contact pads for making the four connections, as may be seen in Fig. 1 and detailed in Ref. 4. For the purpose of measuring the temperature inside the μ-reactor during bonding, we turned the lid "upside down" so that the Pt RTD was inside the μ-reactor. As a result, the measured RTD temperature corresponds to the temperature inside the reactor. The temperature of the aluminum top cathode was also recorded using a K-type thermocouple. The measurements are plotted in Fig. 3. It is seen that the cathode stabilizes at ~475 °C, while the RTD temperature inside the reactor only reaches 45 °C.

In the finite element analysis (FEA), the real bonding arrangement was approximated with an axially symmetric geometry similar to the actual setup.The steady state temperature distribution was computed. The geometry of the FEA and the predicted temperature distribution are shown in Fig. 4. In the bonding setup a thermal contact resistance is expected between the aluminum and Pyrex. This was represented in the simulations by a narrow subdomain along the aluminum-Pyrex interface, giving rise to a thermal contact resistance of 5×10^{-5} m^2 K W^{-1}. In the FEA a constant tem-

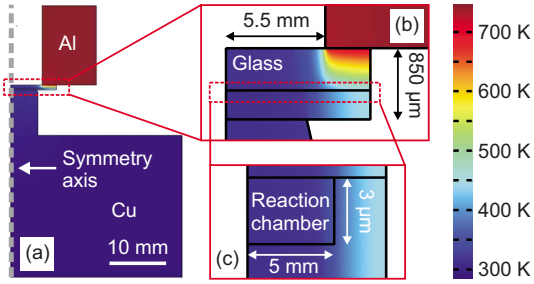

FIG. 4. (Color online) Geometry and color plot of the calculated steady state temperature distribution from the FEA. The geometry is an axially symmetric approximation of the real cooled-bonding setup. (a) The entire geometry with equal scale on both coordinate axes. The vertical dashed gray line signifies the symmetry axis. The silicon and the glass chip are stacked between the aluminum cathode and the copper heat sink. (b) Magnification of the silicon and glass chip. A high temperature gradient is observed in the part of the Pyrex lid outside the reaction chamber. (c) Magnification of the reaction chamber. The temperature in the chamber is seen to be close to room temperature as a result of the cooled-bonding fixture. Note that in (b) and (c) the scaling of the x-axis and the y-axis is different.

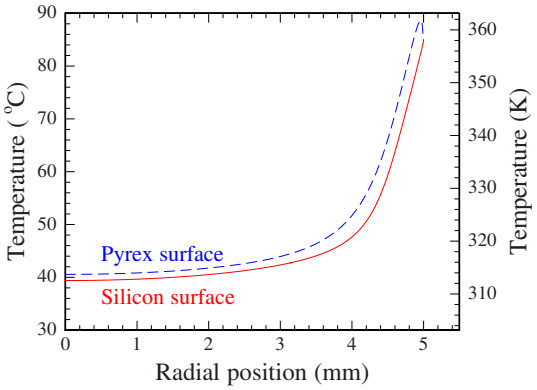

FIG. 5. (Color online) Steady state temperature distribution in the reaction chamber as computed in the FEA. The temperature in the chamber as a function of radial position is shown. The radial position is the distance from the center axis of the chamber (the symmetry axis). In the plot, the temperature in the top of the chamber adjacent to the Pyrex is shown (blue dashed curve) as well as the temperature in the bottom of the chamber adjacent to the silicon (red full curve).

perature of 475 °C was applied to the right boundary of the aluminum block. The bottom of the copper block was set to a constant temperature of 12.5 °C, and the reaction chamber was treated as containing atmospheric air. The FEA gives detailed information about the thermal gradients from which, e.g., heat fluxes and thermal expansion can be extracted. Figure 5 shows the temperature in the reaction chamber as a function of radial position according to the FEA. It is seen that the predicted temperature is below 90 °C everywhere and below 50 °C within the central 8 mm diameter circle in the chamber. In the center of the chamber the FEA predicts a temperature of around 40 °C, which is in good agreement with the experimental result 45 °C (Fig. 3).

For evaluation of the scalability of the method, it is useful to consider a design where the radial distance between heater and cold finger edges is sufficient to ensure that a region (outside the cooled air-gap region) of purely radial heat flow exists. In the present system such a region would be the cylindrical cross section with a radius of ~5.2 mm (to good approximation). In that region the ratio of heat flows in glass $P_{G,r}$ and silicon $P_{Si,r}$ is $P_{G,r}/P_{Si,r}=(\varkappa_G h_G)/(\varkappa_{Si} h_{Si})$, while the total heat flow is $P_{tot}=P_{G,r}+P_{Si,r}$; here and below $\varkappa_i$ and h_i are the thermal conductivities and material thicknesses, respectively. Then, by continuity, in the reactor region the heat flow in the glass will be directed through the air film in the reactor and cause a (mean) temperature difference $\Delta T=P_{G,r}h_{air}/(\varkappa_{air}\pi a^2)$ between top and bottom of the reactor; a is the radius of the reactor chamber. It follows that ΔT will increase approximately linearly with reactor height; in the present design $\Delta T \simeq 4$ K at $h_{air}=3$ μm, and if arbitrarily the upper acceptable limit is $\Delta T_{max}=60$ K, then the upper limit on the reactor chamber height is $h_{air} \leq 45$ μm, with all other parameters unchanged. The limit on reactor chamber height may be lifted if forced convection cooling is applied to the glass lid surface through the center bore of the heater.

An increase in the thickness of the glass wafer is also seen to cause an increase in ΔT, but at the same time the heater temperature must be increased since $P_{Si,r}$ must be maintained to keep the temperature T_B at the bonding interface fixed.

In the heater and cold finger regions, the heat flow is three-dimensional. The transition to a radial heat flow in the heater region takes place on a length scale that is approximately h_G+h_{Si}, while at the cold finger the transition takes place on a length scale of approximately h_{Si} since here, the main heat flow is in silicon. It follows that the radial distance between heater and cold finger edges must fulfill $\Delta r_{hc} \gtrsim h_G+2h_{Si}$. Moreover, in the region directly above the cold finger, the length scale of the temperature variation is h_{Si}, and thus the cold finger radius must fulfill $r_{Cu} > h_{Si}$, say, $2h_{Si}$. A minimum applicable chip size could then be estimated from $2r_{min} \sim 2(2h_{Si}+h_G+2h_{Si}+w_H)$, where w_H is the width of the glass-heater contact; this probably has to fulfill $w_H > h_G+h_{Si}$, making $2r_{min} \sim 2(5h_{Si}+2h_G)=5.5$ mm with a cold finger radius $r_{Cu}=0.7$ mm. This design was verified by FEA.

With the current design, the temperature T_{Rc} in the center of the reactor (on the silicon side) is almost entirely controlled by the Cu cold finger $T_{Rc} \simeq T_L+R_{Cu}P_{tot}$, where T_L is the cold finger temperature (we have used $T_L=12$ °C) and $R_{Cu}=L_{Cu}/(\varkappa_{Cu}\pi r_{Cu}^2)+1/(4\varkappa_{Cu}r_{Cu})$ is the thermal resistance of the cold finger of length L_{Cu} including thermal spreading resistance to the Cu bulk. It follows that the reactor temperature is linearly dependent on the cold finger temperature, linearly dependent on the total heat flow, and strongly dependent on the cold finger geometry. This also emphasizes the importance of ensuring good thermal contact between silicon and the cold finger; thus we use thermogrease at that junction.

By heating from the glass side of the glass-silicon stack and providing efficient local cooling, we have shown that silicon may be anodically bonded to glass successfully while keeping small (<1 cm) areas at ambient temperatures. This is highly useful for any MEMS or lab-on-a-chip devices, which contain heat-sensitive components such as polymeric structures or coatings, antibodies, or other biomolecules or sensitive metallic structures. The method may be scaled down to bond individual chips as small as ~5.5 mm in diameter while keeping 1.4 mm diameter regions cold. Even smaller dimensions are possible with thinner silicon and Pyrex. Cavities up to ~45 μm deep may be used in the existing setup, while still keeping the reactor temperature below 100 °C. Finally, it should be possible to locally cool multiple areas/chips simultaneously when bonding whole wafers.

CINF is funded by the Danish National Research Foundation.

[1] P. R. Mallory, U.S. Patent No. 3397278 (1969).
[2] G. Wallis and D. Pomerantz, J. Appl. Phys. **40**, 3946 (1969).
[3] K. M. Knowles and A. T. J. van Helvoort, Int. Mater. Rev. **51**, 273 (2006).
[4] T. R. Henriksen, J. L. Olsen, P. C. K. Vesborg, I. Chorkendorff, and O. Hansen, Rev. Sci. Instrum. **80**, 124101 (2009).
[5] T. R. Anthony, J. Appl. Phys. **54**, 2419 (1983).
[6] K. B. Albaugh, J. Electrochem. Soc. **138**, 3089 (1991).
[7] S. Shoji, H. Kikuchi, and H. Torigoe, Sens. Actuators, A **64**, 95 (1998).
[8] Y. Huang, Z. Cui, G. Xiping, L. Changjiu, and G. Zhenan, J. Non-Cryst. Solids **354**, 1407 (2008).
[9] C. Lee, W. Huang, and J. Shie, Sens. Actuators, A **85**, 330 (2000).

Paper IV

Gas phase photocatalysis in μ-reactors

Peter C. K. Vesborg, Jakob L. Olsen, Toke R. Henriksen, Ib Chorkendorff, and Ole Hansen

Submitted

Gas phase photocatalysis in μ-reactors

Peter C. K. Vesborg [a,*] Jakob L. Olsen [a] Toke R. Henriksen [a,b]
Ib Chorkendorff [a] Ole Hansen [a,b]

[a] *CINF, Dept. of Physics,*
Building 312, Fysikvej
Technical University of Denmark, DTU
DK-2800 Kgs. Lyngby, Denmark

[b] *Dept. of Micro- and Nanotechnology,*
Technical University of Denmark, DTU Nanotech
Building 345 East, DK-2800 Kgs. Lyngby, Denmark

Abstract

Gas-phase photocatalysis experiments may benefit from the high sensitivity and good time response in product detection offered by μ-reactors. We demonstrate this by carrying out CO oxidation and methanol oxidation over commercial TiO_2 photocatalysts in our recently developed high sensitivity reactors. We demonstrate that the system exhibits great versatility in terms of photocatalyst, illumination source and target reaction.

Key words: microreactor, nanoreactor, photocatalysis, photooxidation, methanol oxidation, CO oxidation, TiO2, P25, W 2730X

1 Introduction

Photocatalysis is the conversion of chemicals to other chemicals over a semiconducting catalyst which is activated by band-gap excitation as opposed to conventional catalysis where reactions are thermally activated. Photocatalysis may be used for eliminating of unwanted chemicals such as pollutants in air or waste water by mineralizing e.g. organics down to CO_2 and H_2O [1–3]. The second main use of photocatalysis is (solar) energy harvesting since a photocatalyst, unlike a thermal catalyst, may convert reactants to products of

* Corresponding author
Email address: peter.vesborg@fysik.dtu.dk (Peter C. K. Vesborg).

higher energy thereby storing some of the energy from the absorbed photons [4].

The merits of μ-reactors in the study of catalysis have been broadly demonstrated [5–7], but only comparatively little work has been done to use the benefits of μ-reactors in the study of photocatalytic reactions [8–11]. We have recently reported the development of a new μ-reactor fabricated in silicon and sealed with a Pyrex lid [12]. Compared to previously published photochemical "micro"-reactors which typically are based on one or more channels of 10-1000 μm in depth and width [10] our reactors are quite different with their large frontal area combined with their *very* shallow chambers (3 μm depth) and resulting small volumes. This new design features a large frontal area of 0.78 cm^2 - useful for photocatalyst illumination - while keeping the total reactor volume down to $\sim$ 240 nl giving very short time constants and high sensitivity due to the integrated direct quadropole mass spectrometer (QMS) interface. In this paper we demonstrate that these μ-reactors can be very useful in characterizing photocatalysts.

Focusing on the technique two commercial photocatalysts, P25 and W 2730X TiO_2-catalysts (both from Evonik formerly known as Degussa) are used and use these to photooxidize CO and methanol. CO oxidation has previously been established as a useful probe reaction for gas-phase photocatalysis [13,14] and methanol is a commonly used sacrificial reductant in photoelectrochemical studies [2].

2 Experimental

The μ-reactor system (fabrication, gas handling system, QMS detection, etc.) has been described in a previous publication [12]. Briefly, the reactors are planar (16 by 20 mm^2 by 0.35 mm (+0.5 mm Pyrex lid)) with a circular active area of 10 mm diameter and a reactor volume of roughly 240 nl. Up to four simultaneous gas streams can be led to the reactor via two inlets (I1 and I2, Fig. 1 C) and the reactor effluent is led to a quadropole mass spectrometer (QMS) for detection via O2. The bypass flow which never enters the circular reactor area exits via O1. This bypass flow is normally chosen to be on the order of 10 sccm to get good regulation using off-the-shelf mass flow controllers.

Fig. 1 A and B are cross-sections of the μ-reactor showing the two basic ways photocatalyst may be loaded into the reactor and that they allow for both front-side and back-side illumination. The light sources available range from

small, cheap LEDs directly over the reactor to a large Xe-arc broadband source (Newport model 66942 1 kW OF) which may or may not be filtered or passed through a monochromator before light is guided to the reactor with a fiber bundle terminated with a collimating optic. In the present paper we excite the photocatalysts using a small 4 W Hg lamp (UVP model UVGL-15). Regardless of the light source used the incident spectrum and intensity is recorded by replacing the reactor with the measurement head of a calibrated spectroradiometer (International Light model RPS-900R). The measured spectrum incident on the reactors in the present paper is shown in Fig. 2. Since some of the light is lost passing through the Pyrex lid due to reflection and absorption for the deeper UV we include the transmittance spectrum of the 0.5 mm Pyrex lids used to seal our reactors in Fig. 3. Even though Pyrex starts absorbing light at $\sim$ 330 nm the lids are sufficiently transparent that experiments down to well below 300 nm are possible.

For the experimental examples presented in this paper the P25 and W 2730X photocatalysts are loaded onto the Pyrex lids which is subsequently bonded to the silicon reactor. This corresponds to sketch B of Fig. 1 and the photocatalyst is effectively illuminated from "behind". One advantage of depositing the photocatalyst on the glass lid is that it may be characterized by transmission UV-VIS spectroscopy before measurements begin. The catalyst is deposited by spin coating. The suspension is made by sonication and the Pyrex area for deposition (circular, 8 mm diameter) is masked by "Blue Tape" (SWT20, Nitto Scandinavia AB). The thickness of the catalyst layer is controlled by the concentration of the suspension and the number of depositions in the spin coater. Once the catalyst is deposited (and possibly characterized by UV-VIS or other techniques) the lid is anodically bonded to the reactor [15,12]. During anodic bonding the temperature of the catalyst is kept well below 100°C using a special "Cold-bonding" method [16].

Once the reactor is bonded it is mounted in the gas manifold fixture and the target gas mixture flow is started. It takes a while for the reactor and catalyst to dry (as evidenced by the m/Z=18 signal in the QMS) and since trace water in our experience inhibits CO oxidation over TiO_2 care is taken that the chip is dry before experiments. Sometimes cycles of illumination and/or heating to $\sim$ 100°C are used to speed up the drying process. For methanol oxidation careful drying is not relevant since the reaction itself evolves water.

In general, the experiment consists of supplying the relevant reactant gas mixture to the μ-reactor and pulsing the light on and off while monitoring the relevant masses with the QMS. This procedure is conducted for all wavelengths and intensities of interest. Generally, illumination causes only negligible (< 3

K) increase in reactor temperature, since the metallic gas manifold to which the reactor is clamped acts as a massive heat sink.

This method is also suited for long-term stability testing by leaving the light source on for prolonged periods before pulsing the light to measure photo activity. The setup is automated with LabVIEW (National Instruments) so that light sources, gas pressure and feed gas composition may be automatically scanned during longer experiments.

3 Photooxidation experiments

The photooxidation experiments presented in this letter serve to exemplify the method. For these experiments two reactors were prepared. Each was spin coated three times (6000 RPM, 10 s) with a $5\%_{\mathrm{mass}}$ suspension in water (18 MΩcm, "Milipore") of P25 and W 2730X respectively. The resulting thickness was estimated by cross-sectional scanning electron microscopy to be approximately 400 nm on average in the case of the P25 catalyst and since the tapped density of P25 according to the data sheet is 130 g/l this corresponds to an upper limit of about $400 \times 10^{-7} \times 0.4^2 \times \pi$ cm$^3 \times 0.13$ g/cm$^3 = 2.6$ μg of P25 in total in the μ-reactor.

CO photooxidation over P25

Oxidation of CO is a very simple reaction: $\mathrm{CO}(g) + \frac{1}{2}\mathrm{O}_2(g) \rightarrow \mathrm{CO}_2(g)$. Fig. 4 shows time traces of the main components of the CO oxidation reaction gas: m/Z = 4 (He used as internal reference), m/Z = 28 (CO), m/Z = 32 (O_2), m/Z = 44 (CO_2). The nominal feed gas composition is 6:6:2 (He, O_2, CO) by volume and the total pressure is fixed at 1 bar. It is obvious from the time trace in Fig. 4 when the light is switched on and off. The reason that m/Z = 44 does not drop to zero when the light is off is background reaction on the filament of the mass spec - not dark reaction in the reactor. Fig. 5 shows the another experiment where the QMS is sampling mass 44 at 10 Hz and the light is toggled every 10 seconds. It is seen that the system reaches 90% of steady-state level in less than 2 seconds after the light is toggled. This high time resolution is a key feature inherent in our μ-reactor design and allows for e.g. very fast experiments where illumination wavelength is scanned.

In order to ensure that it is really photooxidation going on heating the loaded

reactors up to about 100°C in the dark was also tried, but no measurable dark activity was seen for these catalysts. As a further check, an empty reactor (without photocatalyst) was also tested and as expected this had no activity whatsoever under heating or illumination.

Methanol photooxidation

Methanol oxidation is slightly more complicated (and interesting) than CO oxidation. For instance it may be oxidized completely (mineralized): $CH_3OH(g) + \frac{3}{2}O_2(g) \rightarrow CO_2(g) + 2H_2O(g)$ Or it may oxidize partially to methanal ("formaldehyde" - CH_2O) or to methanoic acid ("formic acid" - HCOOH). In order to carry out the methanol photooxidation experiments a bubbler made of stainless steel filled with 2 ml of HPLC-grade methanol (Sigma-Aldrich) was inserted after one of the four MFCs supplying gas to our μ-reactor. The concentration of methanol is then conveniently adjusted by the ratio of clean helium to methanol-saturated helium (at the bubbler temperature which is monitored) controlled by the two corresponding MFCs. For the measurements presented in Fig. 6 and 7 the nominal ratio of partial pressures in the feed are 6:6:0.085 (He, O_2, MeOH) corresponding to about $0.7\%_{\text{volume}}$ of methanol. An experiment with about five times higher methanol concentrations was also tested, but resulted in a similar turnover as estimated by the m/Z = 44 signal and is omitted here. For all experiments the methanol signal is monitored by the strongest feature in the cracking pattern at m/Z = 31.

Figures 6 and 7 both show methanol oxidation data, but with P25 and W 2730X and long and short wave illumination respectively. The data clearly demonstrates that the photooxidation of methanol under these conditions takes *much* more time to reach steady state when the light is toggled than it does with CO-oxidation. The methanol signal and particularly the water signal both take many minutes to fully respond when the light is toggled. Another clear feature of the data is the apparent photo-desorption (and re-adsorption) of methanol when the light is toggled although it is less pronounced with the W 2730X reactor (Fig. 7). This phenomenon can only be resolved thanks to the fast time resolution of the μ-reactor so even for this (somewhat slow to reach steady state) reaction the time resolution is a useful feature.

A mass scan from m/Z of 1 to 50 was also carried out to look for other (by)products and intermediates of methanol oxidation (such as formic acid), but nothing (that could not be assigned to cracking of water, methanol or CO_2) was detected in noteworthy concentrations so methanol seems to mineralize fully under these conditions.

4 Conclusion

We have shown that gas-phase photochemistry may be conveniently investigated using our silicon μ-reactors due to the transparency of the Pyrex lids in the relevant wavelength range. We carried out mineralization of methanol as a general representative of such reactions, but in principle anything of interest that has a practical vapor pressure could be substituted for methanol in the bubbler. The photocatalytic oxidation of CO has become the "standard" test reaction in our group since it is convenient to do and has near-instant response to illumination which allows for mass-transport studies in thick, mesoporous systems.

To our knowledge the combination of excellent time-resolution (which gives mechanistic information on absorption/desorption and mass transport) and versatile high-sensitivity detection offered by on-line QMS is far better than anything achievable with more conventional "macro" reactors with $\sim 10^6$ larger reactor volumes and gas chromatograph product detection.

Acknowledgements

CINF is funded by the Danish National Research Foundation.

Figures

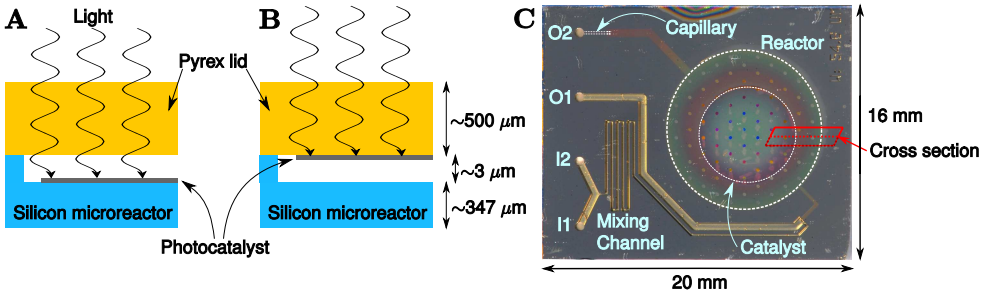

Fig. 1. Partial cross sections of two different μ-reactors loaded in two different ways and a photograph of a μ-reactor. Sketch A shows that when photocatalyst is deposited on the silicon reactor the illumination is frontal - i.e. light is incident from the same side as the reactants - while sketch B shows that photocatalyst deposited on the Pyrex lid (as in the examples in this paper) is effectively illuminated from behind. Sketch C shows a top view of the reactor where main parts are indicated. Gas is let in via I1 and I2 and out via O1 and O2. O1 goes to a pressure controller and O2 leads from the reactor to the mass spectrometer. The location of the cross sectional cut shown in A and B is also indicated in C.

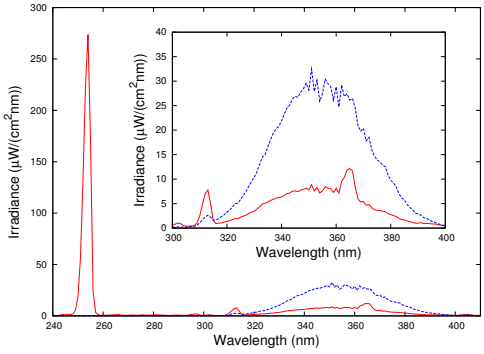

Fig. 2. Measured irradiation on the μ-rectors from the 4 W Hg lamp used in this paper. The lamp can be used in "short" wave mode (solid, red curve) and in "long" wave mode (dashed, blue curve). In the "short" wave mode it the spectrum is dominated by the narrow Hg-line at 253.6 nm

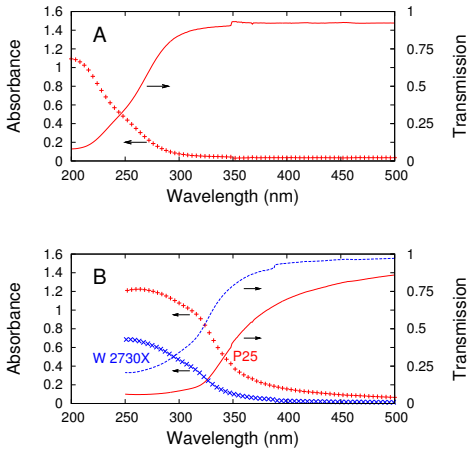

Fig. 3. A: Measured absorbance and resulting transmission of a Pyrex lid. Above ∼ 330 nm transmission is essentially flat at 0.92. B: Absorbance and transmission of the TiO_2 samples studied measured against a blank Pyrex lid in the reference beam (A). The P25-based sample (red curves) has more absorption and scattering than the W 2730X-based sample (blue curves). The increased scattering of P25 is most pronounced at the higher wavelengths.

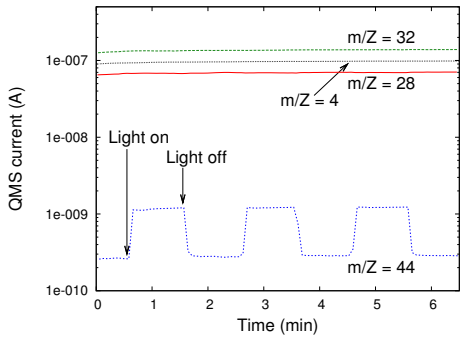

Fig. 4. Representative photooxidation experiment using "long" wave illumination (Fig. 2). QMS-current as a function of time. He, CO, O_2 and CO_2 (m/Z: 4, 28, 32, 44) each sampled at 0.5 Hz are plotted. The CO_2 signal increases when the light is on and vice versa. The other channels are almost unaffected due to low turnover (<1%).

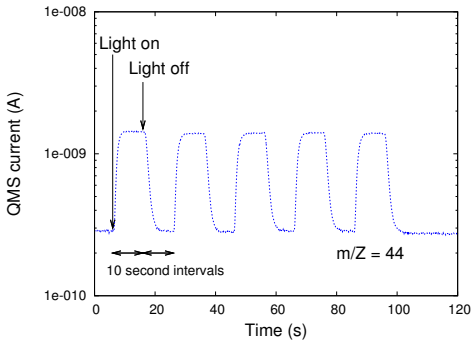

Fig. 5. Time trace of CO_2 signal sampled at 10 Hz and 10 s light on-off cycles using "short" wave illumination (Fig. 2). The very fast time response of the reactor is evident.

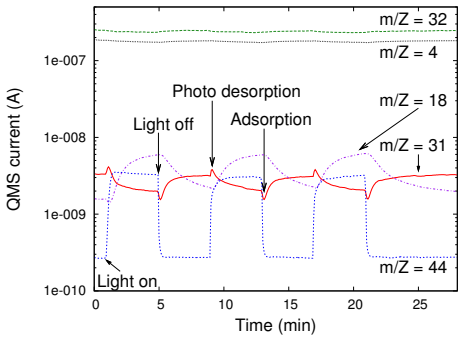

Fig. 6. Photooxidation of methanol over P25 photocatalyst using "long" wave illumination (Fig. 2). m/Z = 31 is the main signal from methanol and m/Z = 18 is the main peak from water. It is clear, that while the CO_2 signal responds quickly to illumination the metanol signal - and the water signal in particular takes much longer to respond. Notable photo desorption (and re-adsorption upon switching off the light) of methanol is observed.

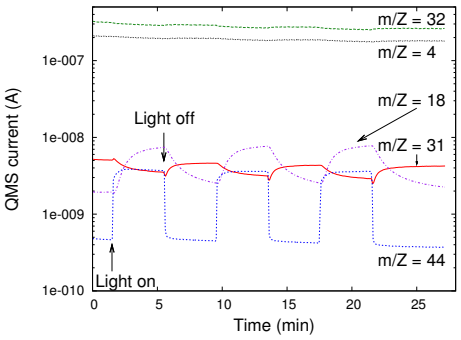

Fig. 7. Photooxidation of methanol over W 2730X photocatalyst using "short" wave illumination (Fig. 2). The overall picture is very similar to the P25 data (Fig. 6). However the phenomenon of photo desorption and re-adsorption is much less pronounced.

References

[1] U. Diebold, The surface science of titanium dioxide, Surface Science Reports 48 (5-8) (2003) 53 – 229.

[2] O. Carp, C. L. Huisman, A. Reller, Photoinduced reactivity of titanium dioxide, Progress in Solid State Chemistry 32 (1-2) (2004) 33 – 177.

[3] A. Fujishima, X. Zhang, D. A. Tryk, Tio2 photocatalysis and related surface phenomena, Surface Science Reports 63 (12) (2008) 515 – 582.

[4] A. Fujishima, K. Honda, Electrochemical photolysis of water at a semiconductor electrode, Nature 238 (5358) (1972) 37–38.

[5] K. F. Jensen, Microreaction engineering - is small better?, Chemical Engineering Science 56 (2) (2001) 293–303.

[6] S. K. Ajmera, C. Delattre, M. A. Schmidt, K. F. Jensen, Microfabricated cross-flow chemical reactor for catalyst testing, Sensors And Actuators B-Chemical 82 (2-3) (2002) 297–306.

[7] P. Mao, J. Y. Han, Fabrication and characterization of 20 nm planar nanofluidic channels by glass-glass and glass-silicon bonding, Lab On A Chip 5 (8) (2005) 837–844.

[8] R. Gorges, S. Meyer, G. Kreisel, Photocatalysis in microreactors, Journal of Photochemistry and Photobiology A: Chemistry 167 (2-3) (2004) 95 – 99.

[9] Y. Matsushita, T. Ichimura, N. Ohba, S. Kumada, K. Sakeda, T. Suzuki, H. Tanibata, T. Murata, Recent progress on photoreactions in microreactors, Pure And Applied Chemistry 79 (11) (2007) 1959–1968.

[10] E. E. Coyle, M. Oelgemoeller, Micro-photochemistry: photochemistry in microstructured reactors. The new photochemistry of the future?, Photochemical & Photobiological Sciences 7 (11) (2008) 1313–1322.

[11] Y. Matsushita, N. Ohba, S. Kumada, K. Sakeda, T. Suzuki, T. Ichimura, Photocatalytic reactions in microreactors, Chemical Engineering Journal 135 (Supplement 1) (2008) S303 – S308, microreaction Technology IMRET 9: Proceedings of the Ninth International Conference on Microreaction Technology - IMRET9 Special Issue.

[12] T. R. Henriksen, J. L. Olsen, P. C. K. Vesborg, I. Chorkendorff, O. Hansen, Highly sensitive silicon microreactor for catalyst testing, Submitted.

[13] A. Linsebigler, G. Lu, J. Yates, Photocatalysis On TiO2 Surfaces - Principles, Mechanisms, And Selected Results, Chemical Reviews 95 (3) (1995) 735–758.

[14] J. T. Yates Jr., Photochemistry on TiO2: Mechanisms behind the surface chemistry, Surface Science 603 (10-12) (2009) 1605 – 1612, special Issue of Surface Science dedicated to Prof. Dr. Dr. h.c. mult. Gerhard Ertl, Nobel-Laureate in Chemistry 2007.

[15] G. Wallis, D. Pomerantz, Field assisted glass-metal sealing, Journal Of Applied Physics 40 (10) (1969) 3946–3949.

[16] P. C. K. Vesborg, J. L. Olsen, T. R. Henriksen, I. Chorkendorff, O. Hansen, "Cold" anodic bonding: Performing anodic bonding while cooling heat sensitive areas, Submitted.

Paper V

Quantitative measurements of photocatalytic CO-oxidation as a function of light intensity and wavelength over TiO_2 nanotube thin films in μ-reactors

Peter C. K. Vesborg, Su-il In, Jakob L. Olsen, Toke R. Henriksen, Billie L. Abrams, Alan Kleinman-Shwarsctein, Ole Hansen and Ib Chorkendorff

Submitted

Quantitative measurements of photocatalytic CO-oxidation as a function of light intensity and wavelength over TiO_2 nanotube thin films in μ-reactors

Peter C. K. Vesborg,* Su-il In, Jakob L. Olsen, Toke R. Henriksen,† Billie L. Abrams, Yidong Hou, Alan Kleinman-Shwarsctein, Ole Hansen,† and Ib Chorkendorff
CINF, Dept. of Physics,
Building 312, Fysikvej
Technical University of Denmark, DTU
DK-2800 Kgs. Lyngby, Denmark
(Dated: January 17, 2010)

Gas-phase photooxidation of CO over TiO_2 catalysts (P25 and TiO_2 nanotubes) in μ-reactors with quantitative product detection was used to study turnover as a function of illumination intensity over four orders of magnitude. Turnover was found to be of order 0.84 in illumination intensity. A CO photooxidation action spectrum was also recorded for TiO_2 nanotubes. The action spectrum was used to calculate both the Incident Photon to Product Efficiency (IPPE) and the Absorbed Photon to Product Efficiency (APPE). The wavelength dependence of the IPPE was found to follow the absorption spectrum while the APPE peaks around 345 nm with a value of about 0.8%.

PACS numbers:

I. INTRODUCTION

In photoelectrocatalysis it is a well established practice to measure photocurrent to estimate activity. Provided that it can be *proved* which reaction takes place at the photoelectrode and counter electrode (e.g. evolution of oxygen and hydrogen in the common case of water splitting) the current measured by the potentiostat gives a highly sensitive and convenient measure of photoactivity. However, in the case of photocatalysis where chemicals are converted into other chemicals on the photocatalyst surface the absence of external current makes it much more problematic to quantify the photocatalytic activity. For both liquid and gas phase reactions it is necessary to quantify product molecules which is much harder than measuring a current. The problem of product detection is particularly difficult when e.g. the activity dependence on wavelength (action spectrum) is sought. Many wavelengths must be tested to give a reasonable resolution in the action spectrum and monochromatic sources tend to be weaker than broad band light sources which makes the measurement very time consuming.

In this paper we demonstrate how our μ-reactor system presents a novel and superior alternative to the traditional approach to such measurements. The traditional procedure is to place a macroscopic amount (1 to 1000 mg) of photocatalyst in a macroscopic (batch)reactor (1 to 1000 ml) made of glass, quartz or metal and use a gas chromatograph (GC) to analyze small samples of the reactor content at suitable time intervals under illumination [1, 2]. Some groups even employ reactors of several liters and other detection schemes (e.g. photoacoustic) [3, 4]. Other groups use flow (single pass) reactors, but these are also typically larger than 100 ml [5].

Some groups have studied photocatalysis in small (mm size) flow-reactors [6–9] and our group has recently developed a μ-reactor with quadropole mass spectrometer (QMS) detection [10] and shown its suitability for (thermal) heterogeneous catalysis as well as photocatalysis [11]. In the following we present:

- How quantitative photocatalytic experiments may be carried out using our μ-reactor platform.
- How the large dynamic range of the reactor and QMS detector allows fast studies of photocatalytic turnover rate as a function of illumination intensity over 4 orders of magnitude and discuss how the results relate to the literature.
- How the μ-reactor system can be used to record a detailed action spectrum of a photocatalyst in an automated fashion in only 2 hours and calculate quantum efficiencies (Incident Photon to Product Efficiency - IPPE) and (Absorbed Photon to Product Efficiency - APPE).

II. QUANTITATIVE MEASUREMENTS IN μ-REACTORS

A. The μ-reactor

There is no general consensus about what the term μ-reactor covers. We use the term to cover "chemical reactors with dimensions in the μm range" whose

*Electronic address: peter.vesborg@fysik.dtu.dk
†Also at Dept. of Micro- and Nanotechnology, Technical University of Denmark, DTU Nanotech Building 345 East, DK-2800 Kgs. Lyngby, Denmark

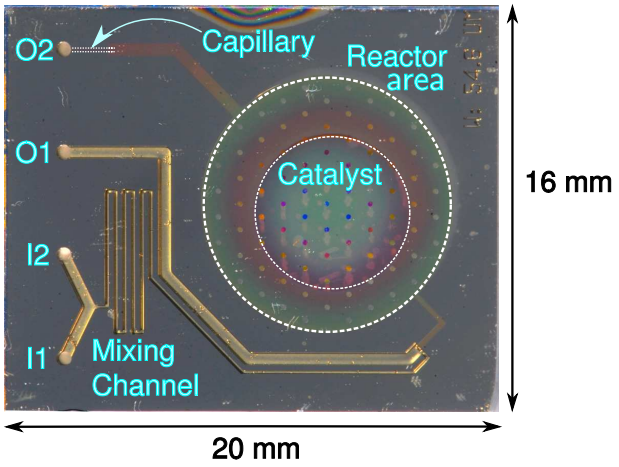

FIG. 1: Photograph of a μ-reactor. I1 and I2 are gas inlets and O1 is the outlet for the main flow. A small amount of gas (5×10^{14} or 5×10^{15} molecules/s depending on the type of reactor) is continually removed from the reactor area via the flow-limiting capillary through O2 to the mass spectrometer for detection.

general merits have been demonstrated by other groups [12, 13]. Our μ-reactors seen in Fig. 1 (described in detail elsewhere [10]), briefly, are 16 by 20 mm^2 chips fabricated from 350 μm thick silicon substrates and permanently sealed with a 500 μm thick Pyrex lid using anodic bonding [14] with local cooling of the catalyst [15] (the catalyst is kept well below 100°C during bonding). Each chip contains a circular reactor area of 0.78 cm^2 yet it has a total volume of only 240 nl (3 μm depth). Gas is continually led from the reactor area via a flow limiting capillary to a QMS for instantaneous detection. This combination of a large area for illumination with fast time response and high sensitivity is well suited for gas-phase photocatalytic studies [11]. Two kinds of chips with different capillary widths are available. These have an order of magnitude different flow conductance so that the flow through the reactor can be either $\sim 5 \times 10^{14}$ or $\sim 5 \times 10^{15}$ molecules/s depending on the experiment. The gas source which feeds the reactor with this tiny flow is the main flow channel. This can accommodate up to 20 ml/min enabling conventional mass flow controllers to be used for gas supply [10] and the reactor flow is independent of the main channel flow (it depends only on the main channel pressure which is fixed by a pressure controller within the useful range 0.05 to 5 bar). In the experiments presented in this paper the pressure is fixed at 1.00 bar and the feed gas composition is 3:3:1 (He:O_2:CO) by volume.

In this study the samples are prepared by depositing the photocatalyst on the Pyrex lid (of the μ-reactor) before it is bonded onto a silicon chip to complete the loaded μ-reactor. The sample μ-reactor is then mounted in a gas manifold fixture and the reactant gas mixture flow is started. The μ-reactor is then heated to ~100°C until it is completely dry as evidenced by the water signal at m/Z = 18 and no experiments are carried out before the water signal has reached a steady background level and the photoactivity has stabilized. This is important because we find photooxidation of CO to be inhibited by water as also reported by Einaga et al. [16]. In general, once the samples have been mounted and dried the photocatalytic performance is very stable over time and reproducible - even if the reactor is dismounted and then remounted months later. The typical experiment consists of toggling a light source on and off while recording all relevant masses with the QMS as a function of time since the μ-reactor is a flow reactor.

B. Calibration procedures

The raw data obtained from the μ-reactor setup consists of time series of currents - one for each m/Z-value being scanned. The key is the ability to convert from QMS currents to molecular flows (Ampere $\rightarrow$ molecules/s). There are four steps to this procedure, but step 1 must in principle only be done once and then only steps 2-4 (which are very quick) have to be repeated with every new μ-reactor:

1. Measure the molecular flow of a "reference" μ-reactor by pumping down a known volume fitted with a baratron through the capillary of the reference μ-reactor. Call this flow R_{flow}. The unit is [molecules/s]. The details of this procedure may be found in [10].

2. Find the molecular flow of the sample μ-reactor, S_{flow} [molecules/s]. This is conveniently done by comparing the QMS current of a suitable gas component (this *inert* internal reference is typically He measured at m/Z = 4) of the sample μ-reactor with the reference μ-reactor using the same gas mixture. This gives the relation

$$S_{\text{flow}} = R_{\text{flow}} \frac{S_{QMS}(inert)}{R_{QMS}(inert)} \quad (1)$$

   where $\frac{S_{QMS}(inert)}{R_{QMS}(inert)}$ is the ratio of measured QMS currents [Ampere/Ampere] of the inert gas in the sample μ-reactor to the reference μ-reactor. This simple method of swapping the sample with the reference reactor is much faster and more convenient than doing a pump-down experiment (step 1) with every sample μ-reactor.

3. Measure the QMS signal for every interesting component, n, in a known gas mixture to find a set of calibration constants, C_n, (sensitivity factors):

$$C_n = S_{\text{flow}} \frac{f(n)}{S_{QMS}(n)} \quad (2)$$

where $f(n)$ is the fraction of the n$^{\text{th}}$ component of the gas ($\sum f(n) = 1$ where summation is over all components) and $S_{QMS}(n)$ is the QMS current measured for the n$^{\text{th}}$ component. Each calibration constant is the ratio of the molecular flow to the measured QMS current of a given gas, n. They capture differences in ionization probabilities etc. In general, they are equal within 50% of each other - except for He which has a low ionization cross section.

4. Now the molecular flow of each gas component, n, is given by

$$S_{flow}(n) = C_n S^*_{QMS}(n) \tag{3}$$

where $S^*_{QMS}(n)$ is the QMS signal that has been corrected for background in the QMS (including cracking and reaction on the filament). In the case of CO (photo)oxidation this is easy since in the dark there is no reaction (verified in separate experiments) so the dark CO_2 signal (m/Z = 44) is the background and in the above equation $S^*_{QMS}(\mathrm{CO_2}) = S_{QMS}(\mathrm{CO_2}) - S_{QMS-\mathrm{dark}}(\mathrm{CO_2})$

The order of magnitude for molecular chip flow is 5×10^{14} molecules/s - i.e. 10^{-9} moles/s for μ-reactors with the small capillary and an order of magnitude higher for μ-reactors with the large capillary. Implicit in the calibration is the assumption that the QMS is linear (i.e. a 10 times reduction in pressure of a given gas component in the QMS results in a signal that is exactly 10 times lower). A linearity calibration of the mass spectrometer has been carried out and we have no reason to suspect any non-linearity leading to a systematic instrumental error. We also note that we generally see mass balance for carbon and oxygen: CO + CO_2 = constant and 2 O_2 + CO + 2 CO_2 = another constant.

III. SAMPLES AND SAMPLE PREPARATION

Sample "A" was simply P25 (AEROXIDE P25, Evonik (formerly Degussa)) spin coated in a masked 8 mm disc on a Pyrex lid by the method given in [11]. The resulting film thickness was estimated to be 225 ± 25 nm by SEM on similarly prepared samples. After transmission UV-VIS characterization (not included for brevity) the lid was bonded (as explained in section II) to a wide-capillary silicon chip to complete the μ-reactor.

Sample "B" consisted of an 8 mm diameter disc of TiO_2 nanotubes (TiO_2 NTs) formed on the Pyrex lid by potentiostatic anodization of a metallic titanium film [17, 18] (400 nm thick, 8 mm diameter) which was deposited on the Pyrex lid using electron beam evaporation. Prior to anodization, the samples were cleaned with acetone and ethanol followed by a deionized water rinse. The anodization was performed using a two-electrode cell with the titanium film as the working electrode and carbon paper as the counter electrode. The anodization was carried out for about 1 hour at a constant applied voltage of 10 V at room temperature in an electrolyte mixture of 0.3 $\%_{\text{mass}}$ NH_4F (98% + ACS reagent, Sigma Aldrich) and 2 $\%_{\text{volume}}$ H_2O in ethylene glycol (99%, Sigma-Aldrich) [19]. In order to get complete anodization without loss of electrical contact the so-called "bottom contact" method [20] was used. After growing the TiO_2 NT film the lid was annealed in a furnace at 723 K for 2 hours. The resulting film consisted of ordered arrays of nanotubes of about 400 nm length (thickness of the film) ∼30 nm in outer diameter and ∼20 nm in inner diameter (estimated from scanning electron micrographs of similarly prepared samples). X-ray diffraction (XRD) peaks in the annealed film were all be assigned to anatase, but of course XRD cannot rule out that some TiO_2 could remain amorphous after annealing [21].

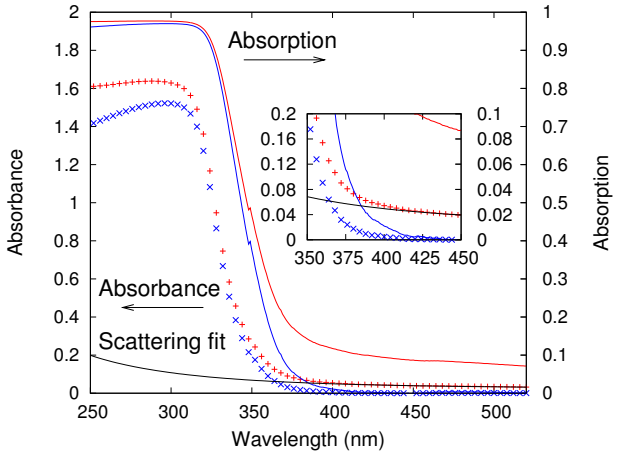

FIG. 2: Absorbance ($A = \log(I_0/I)$) of sample "B" - red plus signs, left ordinate - measured against a blank Pyrex lid in the reference beam. The black curve is a fit ($A_{\text{scattering}} = C_1/\lambda^4 + C_2$) to the data above 400 nm as a simple model of the the scattering losses. Subtraction of the fit from the absorbance is plotted with blue crosses and represents the "scattering corrected" absorbance. The right ordinate is the resulting absorption ($1 - I/I_0$) - red and blue solid curves. Again, the blue curve is the "scattering corrected" data. The inset shows a close-up of the band edge region. For instance it can be read off the blue curve that only below 385 nm does the nanotube film absorb more than 2% of the incident photons. Scattering (black line) is probably overestimated at short wavelengths since scattered photons have a high absorption probability due to short absorption length, but the error due to this is insignificant since raw and corrected absorbance remain essentially equal at short wavelengths (both above 95 %).

Fig. 2 shows the UV-VIS spectrum of the TiO_2 NT sample "B" measured (with a Cary model 1E spectrophotometer) against a blank Pyrex lid. Thus the resulting

apparent absorption is only due to absorption and scattering of the TiO_2 film - the absorption due to the Pyrex itself is therefore contributing negligibly to the measured absorbance in the figure. Fig. 2 also shows a simple fit of the scattering background and the resulting "corrected" absorption data for the sample. This will be needed for the discussion of absorbed photon to product efficiency and action spectra (section VI). After UV-VIS characterization the lid was bonded to a narrow-capillary silicon chip. The samples both have the photocatalyst sitting on the glass lid so they are both illuminated "from behind" with respect to the reactant gas mixture flowing through the reactor as explained in [11].

IV. LIGHT SOURCES

Two very different light sources were used in this work. The first is a high-power UV-LED source (Hamamatsu model LC-L2) fitted with a focusing lens assembly (Hamamatsu L10561-220) suited for areas of 8 mm in diameter. The peak wavelength is ∼367 nm and the FWHM is ∼9 nm. In our setup an average irradiance on the sample μ-reactor of ∼645 mW/cm^2 at full power was measured using a calibrated spectroradiometer (International Light model RPS-900R). The LED unit may be electronically tuned down to 10% of full power. Combined with simple neutral density (ND) filters of optical density 1.0 and 2.0 (Newport corp.) a few extra orders of magnitude in light intensity become available. A range of combinations of filters and power settings were measured using the spectroradiometer to calibrate for the exact extinction of the individual ND filters (which at 367 nm is not equal to their nominal values).

The second light source is shown in Fig. 3. The main components include an (ozone free) 1 kW Xe-arc source (Newport model 66924) equipped with a water filter to eliminate unwanted long-wave light and for this study it was fitted with a monochromator (Newport Cornerstone 260) and appropriate optics for F-number matching. The output is coupled via a quartz fiber bundle through a collimating lens onto the sample μ-reactor.

The μ-reactor and catalyst is kept at room temperature in all experiments since the μ-reactor is clamped to a metallic gas interface manifold which acts as a heat sink.

V. INTENSITY DEPENDENCE

A. Motivation

The high sensitivity of the μ-reactor system which enables flow experiments where steady state conditions can be ensured is a great advantage compared to batch reactors. This merit in combination with the fact that the QMS offers a very wide dynamic range (ratio

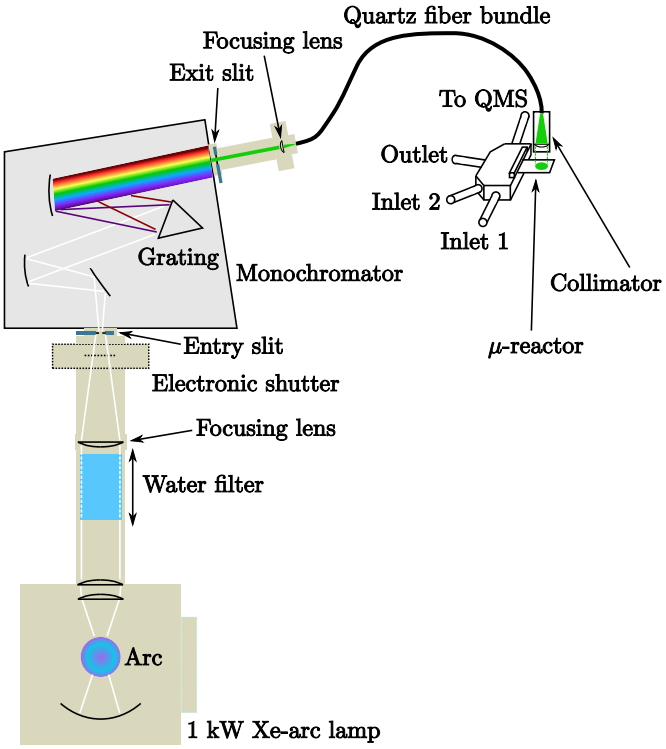

FIG. 3: Schematic of the monochromated Xe-arc source used for measuring action spectra. The irradiance of the system at all relevant settings (choice of wavelength, slits and grating) is measured by putting the measuring head of a calibrated spectroradiometer (International Light model RPS-900R) in the place of the μ-reactor. This irradiance measurement is carried out immediately before or after the actual measurement on the μ-reactor.

of minimum detectable signal to maximum practical conversion which is limited by "full conversion") makes the μ-reactor platform highly suited for investigations of how the photocatalytic conversion scales with illumination intensity. It is of interest to know how well a given photocatalyst performs as a function of illumination intensity for at least three reasons. The first is practical: In a given photocatalytic converter where higher conversion is needed will it be more economical to increase photocatalyst amount/surface area - or would a more powerful light source with the same photocatalyst amount be the better choice? The second reason is that when trying to characterize the photocatalytic performance as a function of illumination wavelength (action spectrum) it may be important to correct measured turnover for intensity variation when the tunable light source does not provide the same irradiance at different wavelengths. For example, when using an Xe-arc lamp with a monochromator to record action spectra, as is commonly done in many labs and as we do in section VI, the irradiance on the sample will often vary by an order of magnitude or more as the wavelength is scanned such that effectively two parameters

(wavelength *and* irradiance) are scanned simultaneously; if the turnover is not linear in irradiance for a given sample the action spectrum must be corrected for that. The third reason for measuring intensity dependence is that it gives mechanistic insight about the sample. For example, it is often claimed that in the limit of low light intensity (where mass transport is not a limiting factor) turnover should scale linearly with incident photon flux. Furthermore, it is claimed that at higher irradiance levels turnover becomes proportional to $(\text{irradiance})^{0.5}$ due to substantial carrier recombination. Experimental support for this was found by Egerton and King [22] by oxidizing isopropanol to acetone over rutile TiO_2 and commercial pigments in the liquid phase while varying irradiance over five orders of magnitude. Later, however, Ohko et al. [1] studied the same reaction in gas phase over a TiO_2 thin film at very low light intensities (45 μW/cm^2 down to 36 nW/cm^2 - the latter corresponding to only 6.6×10^{10} photons/(cm^{2}s)) and found over their 3.5 orders of magnitude in irradiance turnover to be proportional to $(\text{irradiance})^{0.8}$ as long as the isopropanol concentration was above 10 ppmv.

Given that our μ-reactor setup uses a mass spectrometer (as opposed to a gas chromatograph) for detection and that one should always choose to use probe reactions with a well defined stoichiometry [21] we have chosen photooxidation of CO. Photooxidation of CO has previously been established as an interesting probe reaction over TiO_2. It has been studied over single crystals at low temperatures [23] and over powders at room temperature [16, 24]. For plain TiO_2 Einaga et al. [16] observe that water vapor inhibits photooxidaiton of CO. We have also observed this inhibiting effect [11] and therefore take great care to dry our reactors until activity is stable before performing any measurements as explained in section II. In addition to pure TiO_2 references [16, 23, 24] also study platinized TiO_2 and in the case of [16] also the effect of water vapor and of light intensity and find that platinized systems are less sensitive to water than plain TiO_2.

B. Results

In order to be able to study illumination intensity dependence over a large range of intensities we have used our Hamamatsu LED unit (section IV) because it is fairly monochromatic at 367 nm and that it can provide a high irradiance over the reactor area.

Two μ-reactors, "A" with P25 and "B" with TiO_2 NTs (section III) were used for the experiments. For both samples the light intensity is almost constant over the thickness of the sample due to the thin layers used and the proximity of the 367 nm central wavelength to the band edges. Particularly for the nanotube μ-reactor its absorption edge is at ~380 nm so in simple transmission only about 10% is absorbed at 365 nm (see Fig. 2). This means that for both samples the excitation rate should be approximately constant everywhere in the photocatalyst layers. Figure 4 shows data for measured CO_2 production measured as the m/Z = 44 QMS current where the constant background signal has been subtracted as a function of measured irradiance (centered at 367 nm) for the two different μ-reactors from 90 μW/cm^2 to 645 mW/cm^2. For comparison, integration of the AM1.5G spectrum (ASTM G173-03 solar spectrum) in the 10 nm interval from 365 to 374 nm gives 0.67 mW/cm^2. The data are presented in a log-log plot so if turnover were proportional to illumination intensity the data would fall on lines of slope 1. For the nanotube μ-reactor it is remarkable that the turnover vs. intensity falls on a straight line over four orders of magnitude (of course as a substantial fraction of the available CO is converted in the final couple of data points the linearity fails). Turnover is *not* proportional to irradiance (slope $\neq$ 1), but rather to irradiance raised to the 0.84 power (the reaction is of order 0.84 in irradiance). For P25 the same slope is seen at moderate irradiance up to about 1 mW/cm^2,

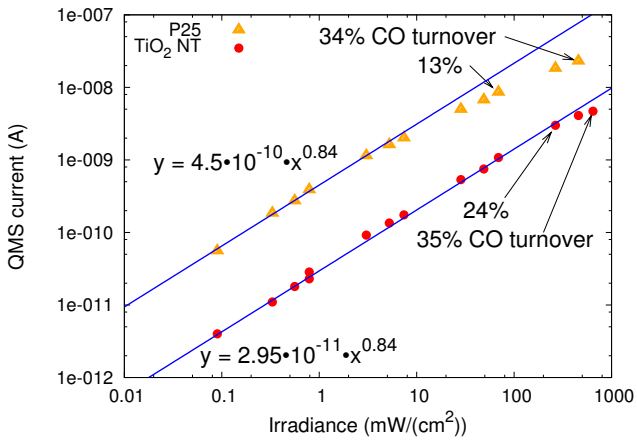

FIG. 4: Background-corrected m/Z = 44 (CO_2) QMS signal as a function of measured irradiation on the reactor with $\lambda = 367$ nm peak wavelength. For the nanotube μ-reactor it is seen that except for the highest illumination intensities where the effective feed gas composition is altered by high turnover in the reactor (final two data points where well over 10% of the CO is photooxidized to CO_2) the turnover vs. illumination intensity is very well described by a power function. The apparent slope (power) is 0.84 meaning that a doubling of the light intensity only results in a factor 1.79 times more turnover. This relation holds true over four orders of magnitude of light flux - from moderate to very high flux (90 μW/cm^2 to 645 mW/cm^2 = 1.7×10^{14} to 1.2×10^{18} photons/(cm^{2}s)). Also in the case of P25 it seems that the turnover is proportional to illumination intensity to the power of about ~0.84. At intensities above ~5 mW/cm^2 the power law fails (or changes to a lower power), but it cannot be ruled out that this is due to transport limitations in the P25 film.

but above 5 mW/cm^2 the slope is lower. This could be due to a change in mechanism, but it could just as well be due to transport limitations.

To ensure that the slope of 0.84 is not somehow an artifact of the illumination wavelength being close to the band edge a similar experiment (not shown) was conducted at 254 nm (strong line in the Hg spectrum) with the nanotube sample although the illumination could only be varied over one order of magnitude for practical reasons. The result was that the turnover seemed proportional to irradiance to the 0.75 ± 0.06 power.

C. Discussion

As mentioned in the above motivation the non-linearity of photocatalytic conversion in irradiance for CO oxidation and other gas (and liquid) phase photocatalytic reactions over TiO_2 have previously been reported in literature. Peral and Ollis [25] note for acetone oxidation in gas phase that $r \propto I^{0.7\pm0.1}$ (I is irradiance and r is rate) over one order of magnitude and conclude that they are in the "transition regime" between the values of 0.5 (recombination dominated) and 1.0 (light limited). Aguado et al. [26] report that for one of three different colloids they test for formic acid decomposition in liquid phase they find that $r \propto I^{0.78\pm0.2}$ (the two other colloids have even lower exponents). Einaga et al. [16] studying CO oxidation at high light intensities ($\sim$ 1 to 10 W/cm^2) find that $r \propto I^{\sim0.7}$ for TiO_2 (and $r \propto I^{\sim0.5}$ for platinized TiO_2). Hwang et al. [27] find $r \propto I^{0.73\pm0.1}$ for CO oxidation over platinized TiO_2 ($\sim$ 0.03 to 3 mW/cm^2). Even Ohko et al. [1] who measure isopropanol oxidation in the gas phase over three orders of magnitude at what they call "Extremely low" light intensities and arrive at $r \propto I^{0.8\pm0.04}$ conclude that they are in a "transition region" between the two asymptotic values.

Considering that Ohko et al. [1] measure $r \propto I^{0.8\pm0.04}$ with I from 36 nW/cm^2 to 45 μW/cm^2 and that we measure $r \propto I^{0.84\pm0.03}$ with I from 90 μW/cm^2 to 645 mW/cm^2 (albeit for a different kind of TiO_2 film and a different reaction) it seems unreasonable that the combined seven orders of magnitude in light intensity where $r \propto I^{\sim0.8}$ is just a "transition region" between the low light limit where supposedly $r \propto I^1$ and the recombination dominated region where supposedly $r \propto I^{0.5}$. A related question is whether anyone has really ever measured $r \propto I^{1.0}$. Egerton and King [22] show that only one pigment (out of the three commercial pigments and rutile that they test) shows $r \propto I^1$ at low light intensities, and this conclusion is based on only two data points - the rest of the data for that pigment at higher intensities shows $r \propto I^{\sim0.5}$ as does the data for the other two pigments. We hesitate to conclude that turnover can never be truly proportional to incident photon flux, but it appears that it is hard to find a (TiO_2-based) photocatalyst and a probe-reaction where this can be measured in practice.

VI. ACTION SPECTRA

Another great benefit of the fast response and low detection limit offered by the μ-reactor platform in photocatalysis is the collection of action spectra. "Chemical", photocatalytic action spectra are useful and complement traditional "electrical", photoelectrocatalytic action spectra. This is because reactivity is measured under true zero-bias conditions without the influence of the solid-liquid junction on band structure and without possible artifacts due to non-Faradayic photocurrent.

Most tuneable and monochromatic sources provide only modest irradiation levels, thus the measurement of photocatalytic action spectra with traditional large volume (batch) photoreactors and gas chromatographic product detection can take many hours of illumination to obtain a quantifiable product concentration at every wavelength. This long time scale can complicate the measurements due to adsorption of both reactants and products during the measurement - not least because of the unfavorable ratio between active catalyst area and reactor inner surface area that is typical of large reactors. In the case of the μ-reactor the same measurement can be quite fast because the μ-reactor has sufficient sensitivity that flow-experiments are possible. In this section we present an action spectrum for the TiO_2 nanotube sample "B" measured from 290 nm to 400 nm in 5 nm intervals - all recorded in 135 minutes using an automated LabVIEW program.

The raw measurements of the monochromated output of the Xe light source at every wavelength used in the study are presented in Fig. 5 (for a description of the light source, see section IV). With this instrumental configuration the FWHM is on the order of 9 nm and the peak irradiance is around 40 μW/cm^{2}nm for central wavelengths in the relevant range ($\sim$300 - 370 nm). As a reference, AM1.5G is also shown in Fig. 5 and it is seen that its irradiance is of the same order of magnitude. No effort was made to keep irradiance constant over the wavelength interval. Given the results from the previous section such extra refinements might be relevant for careful characterization, but for the purpose of demonstrating the technique it was considered unnecessary - not least because irradiance is constant to within a factor of two in the 310 nm to 370 nm interval.

For photon-to-product molecule efficiency calculations it is the number of incident photons (not incident power) that is the interesting parameter. The conversion, photon flux = power flux / (energy/photon), has been carried out and the result is plotted in Fig. 6 which also

includes the integrated photon flux density for every monochromator setting in units of photons/(cm^2s). The light output from the monochromator is moderate - for example at 350 nm the integrated flux density of 6×10^{14} photons/cm^2s corresponds to 325 μW/cm^2 (Fig. 6).

Having calibrated photon fluxes the next step is to mount a μ-reactor and measure turnover at each monochromator setting. The resulting time trace of the m/Z = 44 channel is plotted in Fig. 7. In this case the light is on for six minutes, off for six minutes and the wavelength is changed every 12 minutes. Raw data such as those shown in Fig. 7 may be converted to more useful units of CO_2 molecules/s vs. wavelength by applying the QMS calibration procedure explained in section II. Doing this and taking an average figure for CO_2 turnover at each wavelength gives the data presented in Fig. 8. This figure shows the calibrated CO_2 turnover at every wavelength and, for convenience, also integrated incident photons/s and the estimated number of absorbed photons at each monochromator setting (both right ordinate). The integrated incident photons is, of course, just the data from Fig. 6 multiplied by the geometric area of the photocatalyst in the μ-reactor - in this case $\pi(0.4\text{ cm})^2 = 0.50\text{ cm}^2$. The number of absorbed photons is calculated as the incident photons multiplied by the probability that a photon (that has made it through the Pyrex lid) is absorbed. The latter is estimated as the "scattering corrected" absorbance of the Pyrex lid TiO_2 film as explained in section III and corrected for the fraction of photons absorbed in the Pyrex itself (the Pyrex lid transmits $> 90\%$ down to about 330 nm and $\sim$80% at 290 nm [11]). The only step left to get an action spectrum is to divide the CO_2 production by the photon count at every wavelength (and possibly by an intensity correction term if $r \not\propto I^1$ (see section V) *and* if the output from the monochromator varies a lot (e.g. 10x) over the wavelength interval).

The result is shown in Fig. 9 (no intensity correction) which shows the Incident Photon to Product Efficiency (IPPE) as well as the Absorbed Photon to Product Efficiency (APPE). The IPPE - the *apparent* quantum yield - is really the photocatalytic (chemical) equivalent of the photoelectrocatalytic (photocurrent) action spectrum. For the catalyst tested here it takes about 220 incident photons (of $\lambda \lesssim 340$ nm) to make one CO_2 molecule (IPPE of 0.45 %). Above 340 nm the IPPE rapidly drops off, reflecting that photons close to the absorption edge have a high probability of penetrating the film without being absorbed (Fig. 2). The APPE is the same as the intrinsic quantum yield except that it includes no corrective factor for the number of photons ($e^- + h^+$ pairs) needed for the reaction. In the present case the APPE reaches a maximum of about 0.8% to 0.9% (corresponding to one CO_2 molecule for every $\sim$120 absorbed photons) for wavelengths in the interval 330 nm to 355 nm. At lower wavelengths there is a drop-off in the APPE down to about 0.55% below 315 nm. We suspect that this is due to the decreased average penetration length of high energy photons. At 315 nm, for example, 60% of the photons are absorbed within the bottom 100 nm of the 400 nm TiO_2 nanotube film (this may be derived from the Absorbance data in Fig. 2) and since the sample is illuminated from the back, with the respect to the reactants, it seems reasonable that high energy photons result in less CO_2 than lower energy photons - given that they are absorbed (APPE). At 350 nm less than 50% of the photons are absorbed by the entire 400 nm of the film so for $\lambda > 350$ nm the excitation is nearly homogenous. The reason for the drop in APPE at higher wavelengths is less obvious. One possibility is that even though photons are absorbed some may only excite localized interband defect states where the electron-hole pair is not free to migrate to the surface as opposed to "real" above-band gap excitation where the charge carriers have a chance to reach the surface and induce CO-oxidation. This could explain the drop in APPE above 350 nm. We have not calculated APPE above 370 nm since the uncertainty of the estimate would be very large because both the numerator (turnover) and the denominator (absorbed photons) tend toward zero for higher wavelengths (Fig. 8).

VII. CONCLUSIONS

We have demonstrated that μ-reactors may be a convenient alternative to macroscopic reactors for obtaining quantitative information about photocatalytic performance. Specifically, we have investigated photooxidaiton of CO over TiO_2 thin films (P25 and nanotubes) at room temperature and found turnover to be proportional to irradiance to the power of 0.84 ± 0.03 over four orders of magnitude in irradiance (moderate to high irradiance). We have also determined the action spectrum for the TiO_2 nanotubes and found the Incident Photon to Product Efficiency to be essentially zero above 375 nm, that it has a small peak around 330 and that it is almost constant below 320 nm. This corresponds closely to the (scattering corrected) absorbance of the sample. We also estimated the Absorbed Photon to Product Efficiency which is peaked around 345 nm - a significantly higher wavelength than the IPPE.

Acknowledgments

CINF is funded by the Danish National Research Foundation.

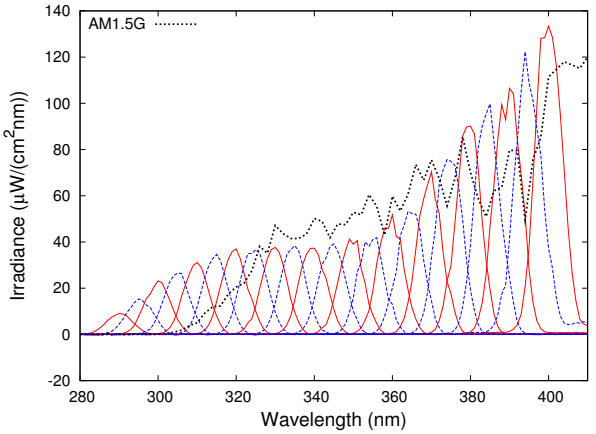

FIG. 5: Irradiance spectra measured at the μ-reactor surface for all the monochromator settings used for recording action spectrum. For clarity, every other wavelength measurement $(290, 300, 310, \ldots)$ is plotted with solid, red and every other wavelength $(295, 305, 315, \ldots)$ in dashed, blue. Note that in the wavelength interval (310 to 370 nm) the irradiance is constant within a factor 2. AM1.5G (dotted, black line) is included for comparison.

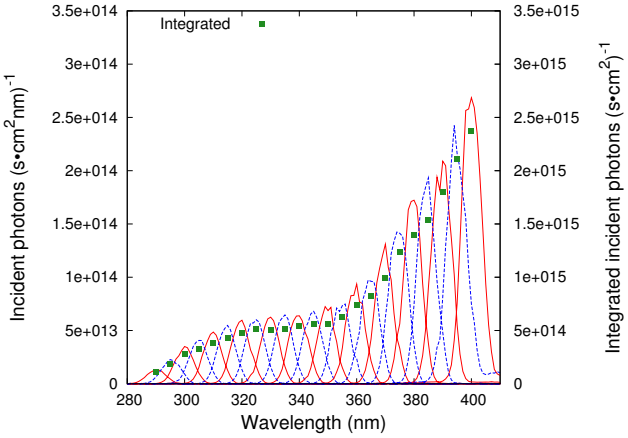

FIG. 6: Data from Fig. 5, but converted to photon flux density (instead of energy flux density). The green squares show the integrated photon flux density at each monochromator setting (second ordinate). This flux density is on the order of $5 \times 10^{14}/(\mathrm{cm}^2\ \mathrm{s})$ in the relevant wavelength range < 375 nm.

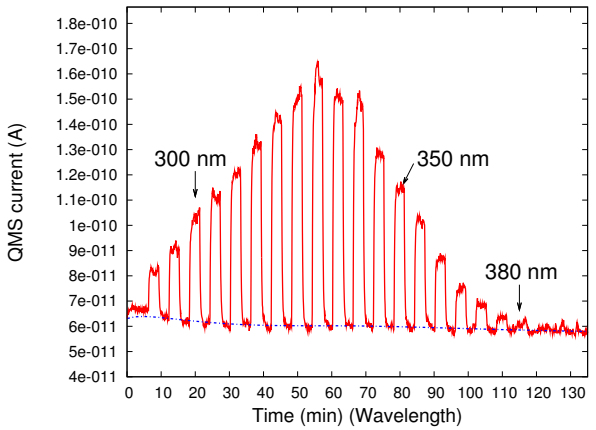

FIG. 7: Raw CO_2 (m/Z = 44) action spectrum data. The wave length is incremented in 5 nm steps from 290 nm every 12 minutes while the shutter is toggled every 6 minutes. The dashed blue line shows the fitted background signal in the QMS.

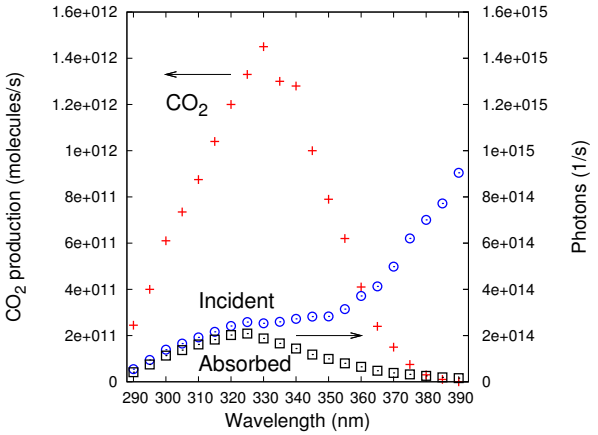

FIG. 8: Background corrected CO_2 (From Fig. 7) converted to units of molecules/s as described in section II (red + symbols). Also shown (right ordinate) is the integrated incident and absorbed photons/s (data from Fig. 6 multiplied by the active photocatalyst area).

[1] Y. Ohko, K. Hashimoto, and A. Fujishima, The Journal of Physical Chemistry A **101**, 8057 (1997), ISSN 1089-5639, URL `http://dx.doi.org/10.1021/jp972002k`.

[2] O. K. Varghese, M. Paulose, T. J. LaTempa, and C. A. Grimes, Nano Letters **9**, 731 (2009), ISSN 1530-6984, URL `http://dx.doi.org/10.1021/nl803258p`.

[3] J. Yu, J. C. Yu, M. K. P. Leung, W. Ho, B. Cheng, X. Zhao, and J. Zhao, Journal of Catalysis **217**, 69 (2003), ISSN 0021-9517, URL `http://www.sciencedirect.com/science/article/B6WHJ-4899VXD-1/2/a6bada31c832c95843af2f0b47b7971c`.

[4] J. Yu, Y. Su, and B. Cheng, Advanced Functional Materials **17**, 1984 (2007), URL `http://dx.doi.org/10.1002/adfm.200600933`.

[5] S. In, A. Orlov, F. Garcia, M. Tikhov, D. S. Wright, and R. M. Lambert, Chemical Communications pp. 4236–4238 (2006).

[6] R. Gorges, S. Meyer, and G. Kreisel, Journal of Photochemistry and Photobiology A:

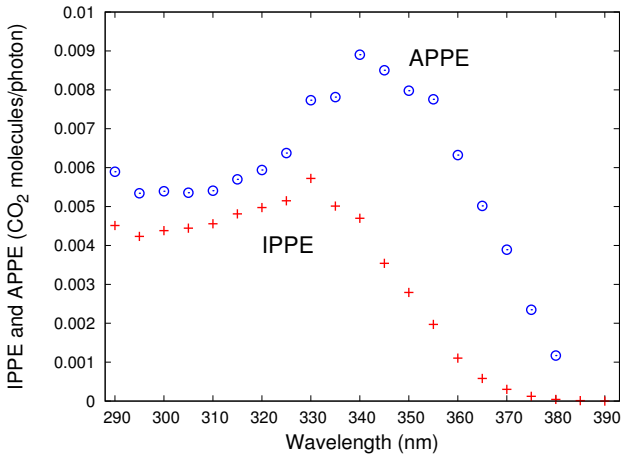

FIG. 9: Incident Photon to Product Efficiency (IPPE) and Absorbed Photon to Product Efficiency (APPE). Up to ∼340 nm one CO_2 molecule results for every ∼200 photons incident on the reactor. At wavelengths above about 340 nm the IPPE quickly drops off reflecting the fact that many photons pass the TiO_2 nanotube layer unabsorbed. Considering only the fraction of photons absorbed, the APPE, it is clear that higher wavelength may well induce turnover - up to about 380 nm. The APPE has a broad maximum at 345 ± 15 nm where the efficiency is about 0.8%. The APPE data at 290 nm and particularly above 370 nm is very uncertain. This is because it is calculated as conversion divided by absorbed photons and in the extremes of the plot both denominator and numerator are close to zero.

Chemistry **167**, 95 (2004), ISSN 1010-6030, URL http://www.sciencedirect.com/science/article/B6TGY-4CP6BYF-1/2/557ec89f8275251cd5fcd7f1571df549.

[7] Y. Matsushita, T. Ichimura, N. Ohba, S. Kumada, K. Sakeda, T. Suzuki, H. Tanibata, and T. Murata, Pure And Applied Chemistry **79**, 1959 (2007), ISSN 0033-4545.

[8] E. E. Coyle and M. Oelgemoeller, Photochemical & Photobiological Sciences **7**, 1313 (2008), ISSN 1474-905X.

[9] Y. Matsushita, N. Ohba, S. Kumada, K. Sakeda, T. Suzuki, and T. Ichimura, Chemical Engineering Journal **135**, S303 (2008), ISSN 1385-8947, microreaction Technology IMRET 9: Proceedings of the Ninth International Conference on Microreaction Technology - IMRET9 Special Issue, URL http://www.sciencedirect.com/science/article/B6TFJ-4P6M68R-6/2/c6426b1f31abd7666aed12afe271d21f.

[10] T. R. Henriksen, J. L. Olsen, P. C. K. Vesborg, I. Chorkendorff, and O. Hansen, Accepted - Review Of Scientific Instruments (2009).

[11] P. C. K. Vesborg, J. L. Olsen, T. R. Henriksen, I. Chorkendorff, and O. Hansen, Submitted (2009).

[12] K. F. Jensen, Chemical Engineering Science **56**, 293 (2001).

[13] S. K. Ajmera, C. Delattre, M. A. Schmidt, and K. F. Jensen, Sensors And Actuators B-Chemical **82**, 297 (2002).

[14] G. Wallis and D. Pomerantz, Journal Of Applied Physics **40**, 3946 (1969).

[15] P. C. K. Vesborg, J. L. Olsen, T. R. Henriksen, I. Chorkendorff, and O. Hansen, Submitted (2009).

[16] H. Einaga, M. Harada, S. Futamura, and T. Ibusuki, The Journal of Physical Chemistry B **107**, 9290 (2003), ISSN 1520-6106, URL http://dx.doi.org/10.1021/jp0343638.

[17] D. Gong, C. A. Grimes, O. K. Varghese, W. C. Hu, R. S. Singh, Z. Chen, and E. C. Dickey, Journal of Materials Research **16**, 3331 (2001).

[18] M. Paulose, K. Shankar, S. Yoriya, H. E. Prakasam, O. K. Varghese, G. K. Mor, T. A. Latempa, A. Fitzgerald, and C. A. Grimes, The Journal of Physical Chemistry B **110**, 16179 (2006), ISSN 1520-6106, URL http://dx.doi.org/10.1021/jp064020k.

[19] K. Shankar, G. K. Mor, H. E. Prakasam, S. Yoriya, M. Paulose, O. K. Varghese, and C. A. Grimes, Nanotechnology **18**, 065707 (2007).

[20] S.-I. In, Y. Hou, B. L. Abrams, P. C. K. Vesborg, and I. Chorkendorff, Submitted (2009).

[21] B. Ohtani, Chemistry Letters **37**, 216 (2008).

[22] T. A. Egerton and C. J. King, J. Oil Col. Chem. Assoc. **62**, 386 (1979).

[23] A. Linsebigler, G. Lu, and J. Yates, Chemical Reviews **95**, 735 (1995), ISSN 0009-2665.

[24] A. V. Vorontsov, E. N. Savinov, G. B. Barannik, V. N. Troitsky, and V. N. Parmon, Catalysis Today **39**, 207 (1997), ISSN 0920-5861, URL http://www.sciencedirect.com/science/article/B6TFG-3SH48TB-2S/2/a1e8a74aee1b2656db84d2f711434e11.

[25] J. Peral and D. F. Ollis, Journal of Catalysis **136**, 554 (1992), ISSN 0021-9517, URL http://www.sciencedirect.com/science/article/B6WHJ-4CJTXK3-HF/2/024979e3c64959417b317058dc8a948b.

[26] M. Aguado, M. Anderson, and C. Hill Jr., Journal of Molecular Catalysis **89**, 165 (1994), ISSN 0304-5102, URL http://www.sciencedirect.com/science/article/B6W91-44074H7-111/2/5201d2961059e06cb091c769447b2e98.

[27] S. Hwang, M. C. Lee, and W. Choi, Applied Catalysis B: Environmental **46**, 49 (2003), ISSN 0926-3373, URL http://www.sciencedirect.com/science/article/B6TF6-48N3H9T-2/2/e4f1719434f221b5f885a5e5afe9d01e.